Gravitational Lensing in *Herschel*-ATLAS

Thesis

Gravitational Lensing in *Herschel*-ATLAS

Author:

Simon Amber

Department of Physical Sciences,
The Open University

Supervisors:

Dr. Mattia Negrello

INAF, Osservatorio
Astronomico di Padova

Dr. Stephen Serjeant

Department of Physical Sciences
The Open University

DATE OF SUBMISSION: 31 MARCH 2015
DATE OF AWARD: 13 NOVEMBER 2015

Abstract

This thesis presents the samples and investigation of strong gravitational lenses identified with the Herschel Space Observatory using the H-ATLAS survey.

A flux-limited lens candidate selection is applied to the complete H-ATLAS area, $\sim 600\text{deg}^2$, and following the inspection of shallow optical and radio survey data the sources are classified into the predicted populations. A bootstrap analysis of the lens candidates is presented and compared to theoretical models which are in broad agreement and support a maximum magnification of the lensed sub-millimetre galaxy (SMG) population as $\mu_{max} \sim 20 - 30$.

Low resolution spectra, obtained from two cycles of observation at the New Technology Telescope (NTT), are reduced and analysed for 57 lens candidates. The distribution of estimated redshifts fail to support models predictions compiled from three different halo mass functions.

Finally, snapshots obtained as part of a collaborative Hubble Space Telescope (HST) campaign are reduced and the first lens models of isolated, robust lens counterparts are presented, which on their own provide compelling evidence that the majority of this sample are lensed by early-type galaxies at higher redshifts than existing gravitational lens surveys.

Glossary

ACS	Advanced Camera for Surveys
AGN	Active Galactic Nucleus
CIB	Cosmic Infrared Background
CMB	Cosmic Microwave Background
EFOSC2	Second ESO Faint Object Spectrograph and Camera
ESO	European Southern Observatory
FIR	Far Infrared ($8 - 1000\mu$m)
FIRST	Faint Images of the Radio Sky at Twenty centimeters (Survey)
FWHM	Full Width Half Maximum
GAMA	Galaxy and Mass Assembly
H-ATLAS	Herschel Astrophysical Terahertz Large Area Survey
HALOS	H-ATLAS Lensed Object Selection
HerMES	Herschel Extra-galactic something
HST	Hubble Space Telescope
IDL	Interactive Data Language
IRAF	Image Reduction and Analysis Facility
IRAS	Infrared Astronomy Satellite
ISM	Interstellar Medium
KIDS	Kilo Degree Sky Survey
L_{FIR}	Far infrared luminosity
LAS	Large Area Survey
NED	NASA Extragalactic Database

NFW	Navarro-Frenk-White
NGP	Northern Galactic Pole
NIR	Near Infrared
NTT	New Technology Telescope
NVSS	National Radio Astronomy Observatory Very Large Array Sky Survey
POSS-II	Second Palomar Sky Survey
PSF	Point Spread Function
PyRAF	Python-based command language for IRAF
S_{FIR}	Far infrared flux
SCUBA	Sub-millimetre Common User Bolometer and Camera
SDP	Science Demonstration Phase
SDSS	Sloan Digital Sky Survey
SED	Spectral Energy Distribution
SFR	Star Formation Rate
SGP	Southern Galactic Pole
SIE	Singular Isothermal Ellipsoid
SIS	Singular Isothermal Sphere
SLACS	Sloan Lens ACS Survey
SMG	Sub-millimetre Galaxy
SNR	Signal-to-Noise Ratio
SPIRE	Spectral and Photometric Imaging Receiver
SPT-SZ	South Pole Telescope Sunyaev-ZelĎovich Survey
UKIDSS	UKIRT Infrared Deep Sky Survey
UKIRT	United Kingdom Infrared Telescope
ULIRG	Ultra Luminous Infrared Galaxy
VIKING	VISTA Kilo Degree Infrared Galaxy Survey
VISTA	Visible and Infrared Survey Telescope
WFC3	Wide Field Camera 3

Acknowledgements

My thanks to my supervisors for their understanding and support during the low points I've experienced during the past three years. Mattia for his continued support from abroad and the warm hospitality afforded to me on my visit to Padova. Stephen for his guidance and faith in my ability to complete this work.

My thanks go out to all who have been present at *Cosmology Coffee Club*: Aleksi, Chris, David, Glenn, Helen, Jeronimo, Jon and Lucia. Every Thursday morning was a pleasant opportunity to see the wider picture and share in your work. Additional thanks to Lucia for her assistance with redshift fitting and proposal planning. A special thank you to Jon for his friendship and reassuring discussions over the occasional coffee, it helped immensely.

Thank you to my parents for their support and I am also grateful for the STFC funding that gave me the opportunity to pursue this work.

List of Publications

- Ivison et al. (2013): Herschel-ATLAS: A Binary HyLIRG Pinpointing a Cluster of Starbursting Protoellipticals.

  First H-ATLAS publication to use a reduced HST F110W snapshot. Snapshot of HATLAS J084933 used in figure 1 and for J-band photometry estimates of three objects within the system. Feedback and description of reduction method provided to the primary author.

- Negrello et al. (2013): Herschel-ATLAS: deep HST/WFC3 imaging of strongly lensed submillimeter galaxies.

  Feedback and discussion of HST/WFC3 reduction methods with the primary author.

- Bussmann et al. (2013): Gravitational Lens Models Based on Submillimeter Array Imaging of Herschel-selected Strongly Lensed Sub-millimeter Galaxies at $z > 1.5$.

  Multiple reduced HST F110W snapshots used in the paper. Fifteen reduced J-band snapshots used in figure 2 and used to identify the nature of the gravitational lens in the cases of multiply imaged sub-mm sources. Feedback and description of reduction method provided to the primary author.

- Negrello et al. (2014): Herschel-ATLAS: deep HST/WFC3 imaging of strongly lensed submillimetre galaxies.

  H-ATLAS ticket used for co-authorship on a paper related to the work within the thesis. Feedback provided to the primary author.

- Dye et al. (2014): Herschel-ATLAS: modelling the first strong gravitational lenses.

H-ATLAS ticket used for co-authorship on a paper related to the work within the thesis. Feedback provided to primary author.

- Messias et al. (2014): Herschel-ATLAS and ALMA. HATLAS J142935.3-002836, a lensed major merger at redshift 1.027.

  Reduced HST F110W snapshot used in conjunction with multi-wavelength data to investigate the edge-on spiral lens J142935. Snapshot used in figure 1 and featured in the ESO press release[1] publicizing the paper. Feedback and description of reduction method provided to the primary author.

- González-Nuevo et al. (2014): Herschel-ATLAS/GAMA: SDSS cross-correlation induced by weak lensing.

  H-ATLAS ticket used for co-authorship on a paper. Interest in the cross-correlation method while performing the cross-matching of NIR sources to lens candidates as discussed in Chapter 4. Feedback provided to primary author.

- Calanog et al. (2014): Lens Models of Herschel-selected Galaxies from High-resolution Near-IR Observations.

  H-ATLAS ticket used for co-authorship. Companion paper to the data described in Chapter 5, discussed with the primary author the H-ATLAS sources in the paper and HST/WFC3 features and differing lens classifications present in the paper.

Herschel-ATLAS operates a ticketing system to recognise the contribution made by members whose work assists the consortia without being directly involved in publications. Such tickets are awarded to those who, for example, have been instrumental in reducing the raw Herschel data, compliling the source catalogs or maintaining the consortium website. Tickets can be redeemed for co-authorship on H-ATLAS papers with the approval of the author and consortium executive. Four tickets were awarded for producing the source follow-up databases/websites which were developed to improve on the wiki-based system. The database and websites are described in appendix C.

[1] http://www.eso.org/public/unitedkingdom/news/eso1426/

Contents

List of Figures

List of Tables

Chapter 1

Gravitational Lensing

"Do not Bodies act upon Light at a distance, and by their action bend its Rays; and is not this action strongest at the least distance?"

- Isaac Newton, *Optiks (1704)*

Gravitational lensing is the observed effect when an intervening mass deflects the light of a background source (figure 1.1). This chapter introduces the subject with a short historical perspective, the general principles, terminology and application, concluding with a summary of notable lens samples. The principles of lensing are discussed using simple models to introduce the core concepts and key terminologies. The extensive literature of e.g Petters et al. (2001) and reviews by Blandford & Narayan (1992); Narayan & Bartelmann (1996); Bartelmann (2010) provide a comprehensive treatment of lensing.

1.1 A Short History of Lensing

With hindsight it is remarkable that, given the above quote, Newton did not pursue this apparent insight. However, when taken in context and as the title of the source implies, it was the effects of reflection, refraction and diffraction rather than gravity that were being considered. Despite this, the quote represents the starting thought experiment that leads to understanding the phenomenon of gravitational lensing. Early investigations are attributed to Michell, Cavendish and von Soldner in the late 18th century (see Valls-Gabaud (2006) for a complete historical examination). It is in von Soldner's 1801 paper

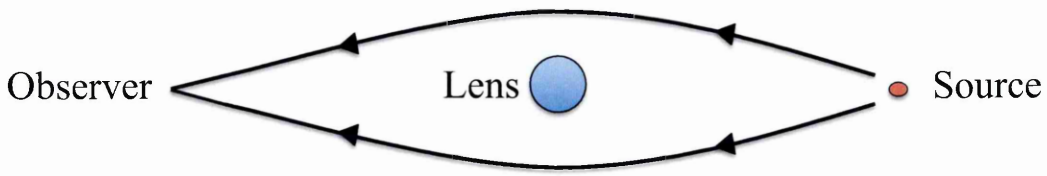

Figure 1.1: Simple gravitational lens schematic. The mass of the lens deflects the light of the background source.

(Jaki (1978) for the english translation) that, using Newtonian dynamics, he calculates the deflection angle experienced by starlight grazing the surface of the sun as $\alpha = 0''.84$. Aside from this result the field would lay dormant for another century until its revival by Einstein.

The General Theory of Relativity predicts a deflection of starlight grazing the surface of the sun as $\alpha = 1''.7$, an observable displacement with the technology of the time during a solar eclipse. The fascinating story of the attempted observations culminated with those obtained by Eddington during the 1919 solar eclipse providing the first observations of gravitational lensing and the spectacular validation of General Relativity (Dyson et al., 1920). Predictions of the observable effects of different lensing scenarios were considered. Einstein (1936) concludes that the lensed effect of a star-star lensing was too small (~milli-arcseconds) to be resolved. In contrast Zwicky (1937) concludes 'gravitational lens effects among nebulae [galaxies] should have been long since discovered'. But it was not until 1979 that the first gravitational lens system was discovered by chance, Walsh et al. (1979), observing two quasars with approximately equal spectra at a redshift $z = 1.41$ propose that both are images lensed by a foreground galaxy at $z = 0.36$. A decade later Soucail et al. (1987) and Lynds & Petrosian (1989) independently discover galaxies distorted into giant arcs about clusters of galaxies and consider gravitational lensing in their conclusions.

Advances in technology and ever increasing sky coverage has meant the discipline no

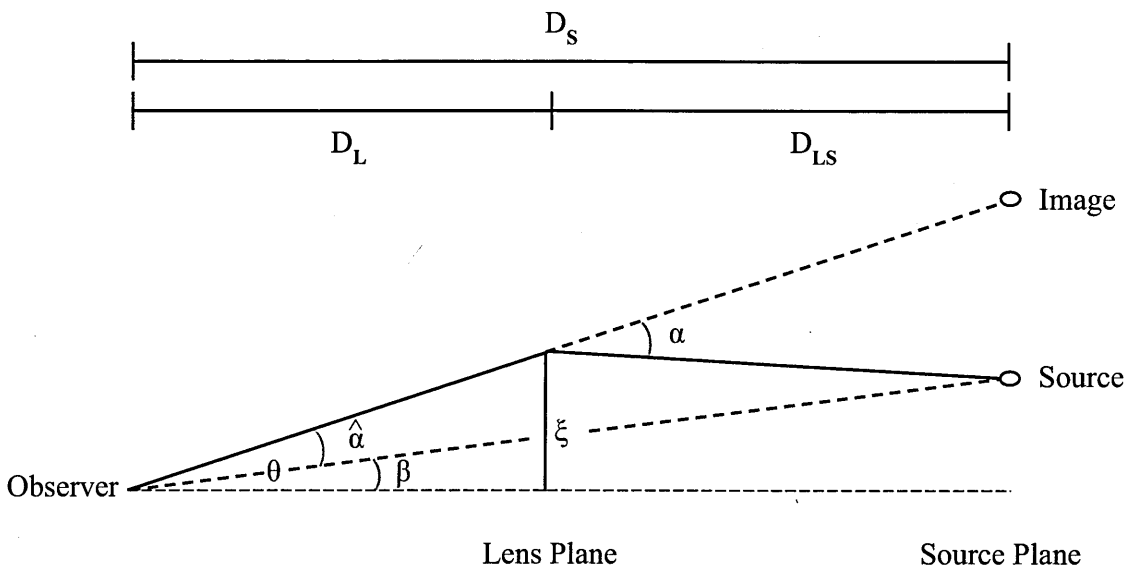

Figure 1.2: General gravitational lensing geometry. In general $D_S \neq D_L + D_{LS}$.

longer relies on such chance discoveries rather systematic searches are responsible for the ongoing detection of hundreds of known gravitational lenses.

1.2 The Principles of Lensing

To introduce the concepts and terminology of lensing a simple system of a point mass lens is considered. The complexities of real systems can also be reduced under two assumptions (1) The *thin lens* approximation: the distance over which deflection occurs is small in comparison to the overal distances. In this approximation any mass density of a lens is represented as the two-dimensional projection on a lens plane. (2) The gravitational potential (Φ) is small in comparison to c^2, this *weak-field limit* simplifies the non-trivial derivation of the small deflection angle (α) experienced by a photon at the distance of closest approach or *impact parameter* (ξ), which for the simplest case of a point mass (M):

$$\alpha = \frac{4GM}{c^2 \xi} \tag{1.1}$$

The relatively simple geometry of a lensing system is shown in figure 1.2. The optical axis is drawn from the observer to the lens, defining the perpendicular source and lens planes. The path of a photon emitted from point source, S, offset from the optical axis

by angle (β) experiences the deflection (α) resulting in the observer detecting the source image, I, offset by angle (θ). The distances between the observer and lens, observer and source and lens and source are D_L, D_S and D_{LS} respectively and are the *angular diameter* distances such that:

$$\theta D_S = \beta D_S - \hat{\alpha} D_{LS} \tag{1.2}$$

It is clear from the geometry that:

$$\beta = \theta - \hat{\alpha} \ , \tag{1.3}$$

which is defined as the lens equation. The observed deflection, also known as the *reduced deflection angle*, is related to the photon deflection (1.1) by:

$$\hat{\alpha} = \frac{D_{LS}}{D_S}\alpha \ , \tag{1.4}$$

which by substituting (1.1) becomes:

$$\hat{\alpha} = \frac{D_{LS}}{D_S}\frac{4GM}{c^2\xi} \tag{1.5}$$

The small angle approximation ($\theta = \xi/D_L$) and substitution into the lens equation (1.3) yields:

$$\beta = \theta - \frac{D_{LS}}{D_L D_S}\frac{4GM}{c^2\theta} \ , \tag{1.6}$$

which relates the source angular position (β) to the image angular position (θ). Starting from the simple geometry the relation between source and image has been derived and is dependent not only on the position of the source relative to the optical axis but on the distances/redshifts of the source and lens. The special case for a source aligned on the optical axis, $\beta = 0$, defines the Einstein radius:

$$\theta_E = \sqrt{\frac{D_{LS}}{D_L D_S}\frac{4GM}{c^2}} \tag{1.7}$$

Where $\beta \neq 0$, in this ideal point mass lensing system, the image positions, $\theta_\pm$ can be

found by, substitution of (1.7) into (1.6):

$$\beta = \theta - \frac{\theta_E^2}{\theta} \,, \tag{1.8}$$

and solving for θ:

$$\theta_\pm = \frac{1}{2}\left(\beta \pm \sqrt{\beta^2 + 4\theta_E^2}\right) \tag{1.9}$$

The case of $\beta \neq 0$ in the point mass lens system results in two images, separated by $\sqrt{\beta^2 + 4\theta_E^2}$, one within ($\theta_- < \theta_E$) and the other outside ($\theta_+ > \theta_E$) the Einstein radius.

For this idealised example the effect of lensing is to either produce a ring or two opposing images for any position of the source relative to the optical axis. The creation of the images or re-distribution of photons arising from lensing does not alter the surface brightness of the source (a non-trivial consequence of Liouville's theorem). A consequence is that images are magnified by the ratio of their size to that of the source:

$$\mu = \frac{\theta}{\beta}\frac{d\theta}{d\beta} \tag{1.10}$$

Differentiating (1.8) the magnifications of the images are defined as:

$$\mu_\pm = \left(1 - \left(\frac{\theta_E}{\theta_\pm}\right)^4\right)^{-1} \,, \tag{1.11}$$

where $\mu_- < 0$ for $\theta_- < \theta_E$, the negative magnification corresponding to an inverted image. Although this idealised case implies that there will always be two images regardless of the source position (β), the results of (1.9) and (1.11) imply that as $\beta \to \infty$ $\theta_+ \to \beta$, $\mu_+ \to 1$ and $\theta_- \to 0$, $\mu_- \to 0$. As a source is moved further away the inverted image within the Einstein radius approaches the optical axis becoming increasingly de-magnified as the outer image eventually approaches the source position and experiences no magnification.

Extending the point mass model to more realistic lens mass distributions is performed by projecting the mass density (ρ), onto the lensing plane:

$$\Sigma(\xi) = \int \rho(\xi, r)\, dz \tag{1.12}$$

The thin screen approximation still applies as the size of any lensing mass is negligible

compared to the the overall distances. The deflection of a photon at a particular impact parameter, ξ_i, is therefore the resultant contribution of all mass elements in the lens plane ($\Sigma(\xi)\ d\xi$):

$$\vec{\alpha}(\xi_i) = \frac{4G}{c^2} \int \Sigma(\vec{\xi})\ \frac{\xi - \xi_i}{|\xi - \xi_i|^2}\ d\vec{\xi} \tag{1.13}$$

In the case of spherically symmetric distributions the mass effectively contributing to the deflection angle is that enclosed within the impact parameter:

$$M(\xi_i) = 2\pi \int_0^{\xi_i} \Sigma(\xi)\xi\ d\xi \tag{1.14}$$

$$\alpha = \frac{4GM(\xi_i)}{c^2 \xi_i} \tag{1.15}$$

For the special case of a lens of constant surface density, Σ, the mass enclosed reduces to $\Sigma\pi\xi_i^2$ and under the small angle approximation leads to an observed deflection:

$$\hat{\alpha} = \frac{4\pi G\Sigma}{c^2} \frac{D_L D_{LS}}{D_S} \theta \tag{1.16}$$

This causes the lens equation (1.3) to be linear, $\beta \propto \theta$, and defines the *critical density*:

$$\Sigma_{cr} = \frac{c^2}{4\pi G} \frac{D_S}{D_L D_{LS}} \tag{1.17}$$

This ideal, critical, lens results in $\beta = 0$, where the source is perfectly focused for the observer. Naturally there is no such perfect mass distribution however the general case is if $\Sigma > \Sigma_{cr}$ is found for a lens then multiple images will be formed.

The trivial derivation of the aforementioned quantities is due to the simple, symmetric and idealised properties of the lens. Real lenses (galaxies) exhibit complex substructures and a wide range of morphologies. The general formalism for more complex lenses introduces further terminology used in the discipline. A lens is fully described by its gravitational potential (Φ) which leads to the definition of the *effective lensing potential*, a dimensionless projection onto the lens plane (recalling the small angle approximation so the impact parameter is reduced to the image angle $\vec{\theta}$):

$$\phi(\vec{\theta}) = \frac{D_{LS}}{D_L D_S} \int \Phi(D_L\vec{\theta}, z)\ dz\ , \tag{1.18}$$

where the gradient with respect to θ is the observed deflection angle, $\vec{\nabla}_\theta \phi = \vec{\hat{\alpha}}(\vec{\theta})$, and the Laplacian is proportional to the surface mass density:

$$\nabla^2_\theta \phi = \frac{2}{c^2} \frac{D_L D_S}{D_{LS}} 4\pi G \Sigma(\vec{\theta}) \tag{1.19}$$

Recalling (1.17), the critical density, defines *convergence*:

$$\kappa(\vec{\theta}) = \frac{\Sigma(\vec{\theta})}{\Sigma_{cr}} \tag{1.20}$$

Therefore the Laplacian of the effective lensing potential is twice the convergence:

$$\nabla^2_\theta \phi = 2\kappa(\vec{\theta}) \tag{1.21}$$

In the general formalism the lens equation (1.3) is a vector mapping from source plane, $\vec{\beta} = [\beta_i, \beta_j]$, to image plane, $\vec{\theta} = [\theta_i, \theta_j]$, therefore any transformation is fully described by the Jacobian matrix:

$$A = \frac{\partial \beta}{\partial \theta} = \left(\delta_{ij} - \frac{\partial \vec{\hat{\alpha}}_i(\vec{\theta})}{\partial \theta_j} \right) \tag{1.22}$$

The relation between observed deflection angle and the effective lensing potential defines the *inverse magnification tensor*:

$$M^{-1} = A = \left(\delta_{ij} - \frac{\partial^2 \phi(\vec{\theta})}{\partial \theta_i \partial \theta_j} \right) \tag{1.23}$$

From (1.21) and defining the quantities:

$$\frac{\partial^2 \phi(\vec{\theta})}{\partial^2 \theta_i} - \frac{\partial^2 \phi(\vec{\theta})}{\partial^2 \theta_j} = 2\gamma(\vec{\theta}) \cos(2\omega(\vec{\theta})) \ , \tag{1.24}$$

$$\frac{\partial^2 \phi(\vec{\theta})}{\partial \theta_i \partial \theta_j} = \gamma(\vec{\theta}) \sin(2\omega(\vec{\theta})) \ , \tag{1.25}$$

(1.23) can be re-written in terms of two major components: the convergence (κ) and shear,

$$M^{-1} = (1 - \kappa(\vec{\theta})) \begin{pmatrix} 1 & 0 \\ 0 & 1 \end{pmatrix} - \gamma(\vec{\theta}) \begin{pmatrix} \cos 2\omega(\vec{\theta}) & \sin 2\omega(\vec{\theta}) \\ \sin 2\omega(\vec{\theta}) & -\cos 2\omega(\vec{\theta}) \end{pmatrix} \tag{1.26}$$

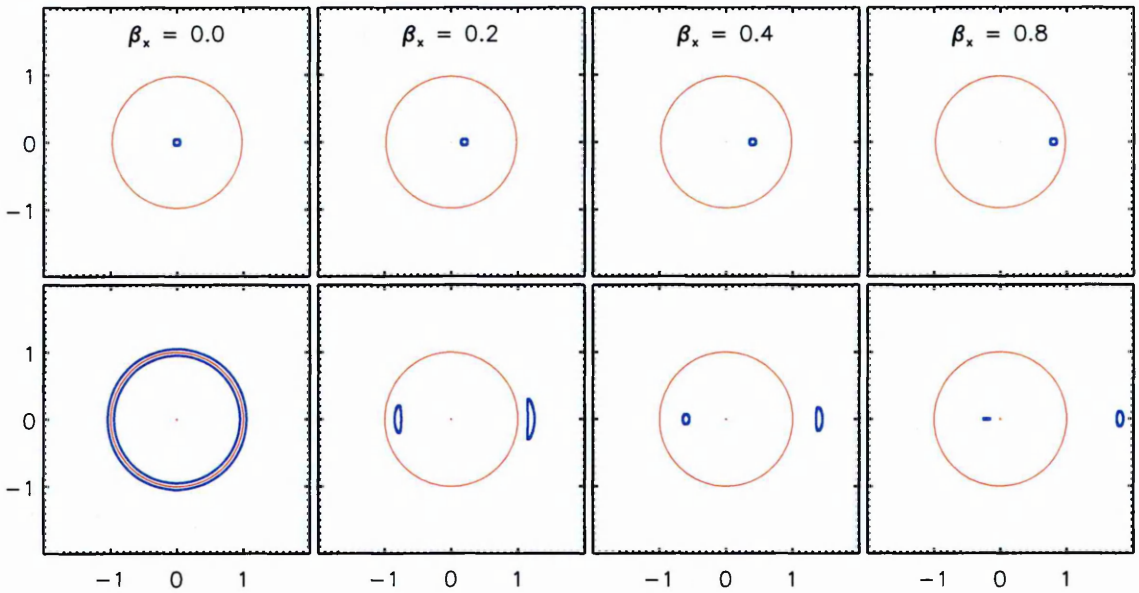

Figure 1.3: `gravlens` models for source plane (top) and image plane (bottom) for circular source, 0".05 in radius, for different positions, β, as lensed by a singular isothermal sphere (SIS). Caustic lines for the source plane and corresponding critical lines for the image plane are drawn in red.

where γ is the shear magnitude and ω is the shear orientation angle from the i-axis of the source/lens planes. The general transformation from source to image plane is described by an isotropic change in size (convergence, κ) and a deformation along a preferred orientation (shear, γ and ω) dependent on image position, $\vec{\theta}$. The transformation of a solid angle element on the source plane to the image plane defines the magnification as:

$$\mu = \frac{1}{\det A} = \det M = \frac{1}{(1-\kappa)^2 - \gamma^2} \tag{1.27}$$

Figures 1.3 and 1.4 show model examples produced using the `gravlens` software, Keeton (2001). The top panels represent the source plane and the circular source moved to larger β_x from left to right. The bottom panels represent the corresponding image plane and the resultant image(s) produced by the lensing mass. The mass distributions are spherical and elliptical with $e = 0.2$, respectively, for singular isothermal sphere/ellipsoid (SIS/SIE) in a system of $z_{lens} = 0.7$ and $z_{source} = 2.5$ with the lensing mass tailored to result in $\theta_E = 1''$. The figures include the *caustic* and *critical* lines in red, for the source and image planes respectively. The *critical* lines represent the location where $\det A = 0$ and $\mu = \infty$ (1.27), which in reality results in positive and negative magnification, corresponding to a reversed image, either side of these lines. *Caustic* lines are the corresponding

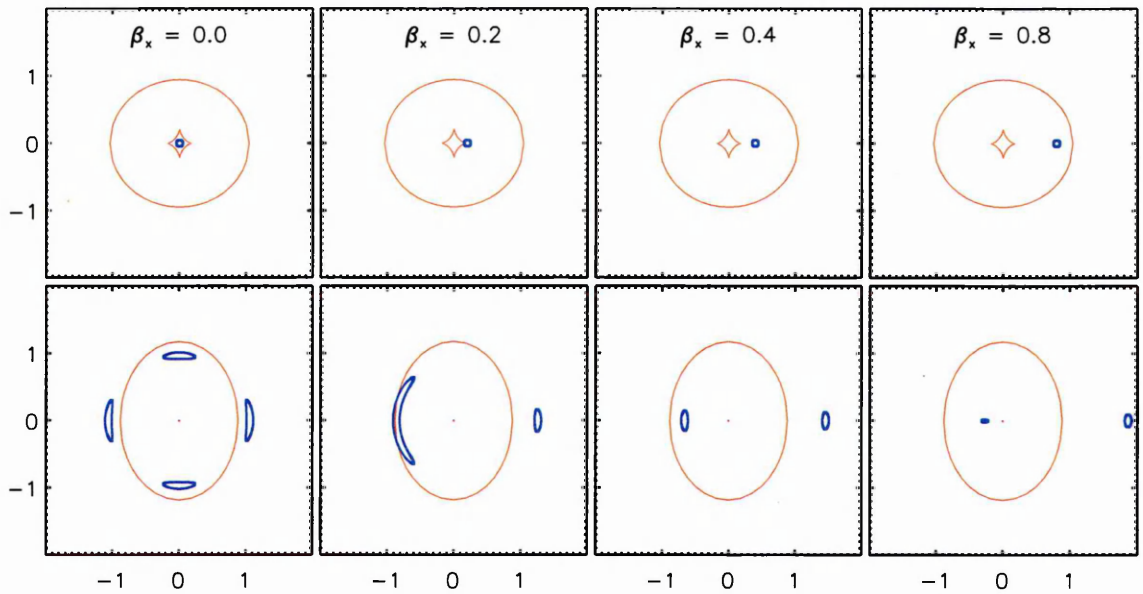

Figure 1.4: `gravlens` models for source plane (top) and image plane (bottom) for circular source, 0".05 in radius, for different positions, β, as lensed by a singular isothermal ellipsoid (SIE), $e = 0.2$. Caustic lines for the source plane and corresponding critical lines for the image plane are drawn in red.

locations on the source plane. For the symmetrical mass distribution the perfectly aligned source, $\beta_x = 0$ results in an Einstein ring or radius $\theta_E = 1''$ whereas for the elliptical lens this ring is broken into four images, otherwise known as an Einstein cross. Sources positioned close to the optical axis are in close proximity to the inner *caustic* (a point for the spherical lens) and the resultant images are tangentially elongated near the corresponding, outer, *critical*. As the sources are moved away from the optical axis they approach the outer *caustic* and the resultant images are radially elongated near the corresponding, inner, *critical*. While tangential images are clearly magnified as the source moves further from the optical axis the radial images produced are de-magnified ($|\mu| < 1$). Although unclear in the figures, there is an additional, highly de-magnified image located at the optical axis which represents the perfectly aligned photons which experience no net deflection.

The lensing phenomena arises from the geometry of the system, as such all lensing is *achromatic* (independent of wavelength).

1.2.1 Lensing Regimes

The definition of three lensing regimes follow by considering possible lensing scenarios:

- Strong: Extragalactic sources undergoing lensing by galaxy/cluster scale masses

where image separations are of the scale of arcseconds. Multiple images or $|\mu| > 2$ are often quoted to define the strong lensing regime.

- Micro: Extragalactic/galactic sources undergoing lensing by galactic objects with image separations on the scale of milli-arcseconds. As such these systems cannot be resolved but are identified by an increase in brightness caused by the magnification experienced when a lens passes between the source and observer.

- Weak: The presence of the lensing mass has only a minor effect on sources, resulting in a small shear effect. The detection of 'cosmic shear' by large scale structure in the universe requires a statistical analysis of the orientations of large samples of sources.

1.2.2 Strong Lens Models

For the strong lensing regime a huge variety of lens models exist, see e.g. Keeton (2001), however two models are most commonly used due to their simplicity and ability to reproduce observables. The singular isothermal sphere model used to produce figures 1.3 and 1.4 is derived by treating the 'particles' within a galaxy as an ideal gas with one-dimensional velocity dispersion, σ_v, it reproduces the observed, flat, rotation curves of galaxies:

$$\rho_{SIS}(r) = \frac{\sigma_v^2}{2\pi G r^2} \tag{1.28}$$

However the SIS model has infinite density at $r = 0$ and can be 'softened' by including a core radius, r_c, to avoid this singularity:

$$\rho_{SIS}(r) = \frac{\sigma_v^2}{2\pi G(r^2 + r_c^2)} \tag{1.29}$$

The Navarro-Frenk-White (NFW), Navarro et al. (1996), is found to be in good agreement to the simulations of a wide range ($M_H \sim 10^{11} - 10^{15} M_\odot$) of dark matter halos. Described by a single parameter, the characteristic density, δ_s, which is dependent on the halo mass and simulation parameters (e.g. Lapi et al. (2012) for the determination of δ_s):

$$\frac{\rho_{NFW}(r)}{\rho_c} = \frac{\delta_s}{(r/r_s)(1 + r/r_s)^2} \tag{1.30}$$

For galaxy-galaxy lensing an SIS/SIE model is found to be a good representation of the lensing mass, e.g. Bussmann et al. (2013) and Lapi et al. (2012) who show that the SIS profile is broadly similar to their intuitive composite model using a sérsic profile to describe the stellar/baryonic matter and a NFW profile for the dark matter component. For the larger scales of group/cluster lensing the dark matter halo, rather than the stellar component, is the dominant contributor and the mass is best described by NFW models, e.g. Sand et al. (2008); Zitrin et al. (2015).

1.3 Applications of Gravitational Lensing

Applications of strong gravitational lensing range from studies of individual systems to the statistical properties of large samples of lens systems for cosmology. The use of lenses as 'cosmic telescopes' allow observations of distant sources often magnified above a detection limit enabling investigation at otherwise inaccessible spatial scales for intrinsically faint populations, e.g. SMM J2135, the 'cosmic eyelash', at $z_{source} = 2.3$, Swinbank et al. (2010), observable at scales $\sim$ 100pc as a result of $|\mu| \sim 32$. Lensing is performed by the combined mass of the lens, dark and baryonic components and provide the means to directly infer the dark matter distribution of galaxy/cluster haloes, e.g. 1E0657 − 558 the 'bullet cluster', Clowe et al. (2006), where the gravitational potential is significantly offset from the baryonic matter, only explainable with the presence of dark matter. The different images for a gravitational lens system are subject to different path lengths and as such the light travel time differs depending on image position. Measurement of the time delay between variable lensed sources is a direct probe of the cosmography of the universe, allowing estimates of the major parameters, e.g. Chae (2003). Other such cosmological probes are the lensing optical depth (the probability of lensing), the redshift distribution of the lenses and number counts of lensed sources, see e.g. the theoretical treatments of Short et al. (2012); Eales (2015). Oguri et al. (2012) perform statistical analysis of 19 lensed quasars to constrain the cosmological constant, Ω_Λ, and the accelerating cosmic expansion. This sample highlights that it is the current number of gravitational lenses which limit their application, see Treu (2010). Despite hundreds of known lenses the variety of different samples and selection effects limits investigations to much smaller samples.

1.4 Gravitational Lens Surveys

Existing lens samples have progressed from the historical chance discoveries to targeted searches and data-mining surveys. The detection of the characteristic lensed images (arcs/rings) requires high-resolution data, e.g. the Cosmic All Sky Survey, CLASS, Myers et al. (2003) used sub-arcsecond radio snapshots with the Very Large Array (VLA) in a combination of automatic and manual inspection to identify 22 lenses from a sample of $\sim$ 16000. The Canada-France-Hawaii Legacy Survey (CFHTLS) Strong Lensing Legacy Survey (SL2S), Cabanac et al. (2007), uses the high resolution optical to automatically search for lensed arcs $> 2''$ finding $\sim$ 40 candidates in the initial 40deg^2 with the potential of hundreds in the final survey area of $\sim$ 170deg^2. The development of automated algorithms such as those used in SL2S is essential for an efficient prospect in lens finding for future wide-area high-resolution surveys such as Euclid with $\sim 10^5$ predicted lenses, Serjeant (2014).

An alternative search method is to data-mine large surveys for lens candidates, those sources which display possible indications of gravitational lensing. The Sloan Lens ACS survey, SLACS, Bolton et al. (2008), used the vast Sloan Digital Sky Survey, SDSS, archives to identify sources with incompatible spectral features characteristic of both low and high redshift sources within the same fibre, potentially a lens and a source. Follow-up observations with the Hubble Space Telescope (HST) Advanced Camera for Surveys (ACS) has revealed a sample of $\sim$ 80 robust lens systems including a rare double-lens, Gavazzi et al. (2008). This method has since been applied to the upgraded SDSS spectrograph and the Baryon Oscillation Spectroscopic Survey (BOSS) in the BOSS Emission-Line Lens Survey, BELLS, Brownstein et al. (2012), which revealed $\sim$ 30 lens systems confirmed with HST imaging. Also data-mined from the SDSS is the Sloan Lens Quasar Search, SLQS, Oguri et al. (2006), which identified candidates based on near-identical sources (the images) within close ($> 2''$) proximity, revealing 19 lensed quasars. A similar method to SLACS/BELLS is currently being applied to the GAMA spectroscopic survey, Holwerda et al. (2015) report the identification of $\sim$ 300 blended spectra as gravitational lens candidates. The identification of strong lenses in wide-area sub-mm surveys, later described in §2.4 and §4.1, is the primary focus of this work and has the potential to yield $\sim$ 1000

lenses in the $\sim 600\text{deg}^2$ of the Herschel-ATLAS survey.

Chapter 2

Lensing in the Sub-mm

The Herschel Space Observatory opened the far-infared/sub-mm wavelength regime to wide-area surveys in this under-explored part of the spectrum. Sensitive to the thermal emission of cool dust, Herschel is uniquely placed to detect dust-shrouded star formation at far-infrared wavelengths. At high redshift this emission is shifted to the longer sub-mm/mm wavelengths; distant and dusty sub-millimetre galaxies (SMGs) represent a population of sources that may be lensed by the presence of a foreground mass. In contrast to optical wavelengths, subject to dust extinction, the detection of the lensed SMG population is easily performed by Herschel. This chapter introduces SMGs and the fundamental implications of their discovery, the Herschel Space Observatory and H-ATLAS. The chapter concludes by describing the efficient lens selection that is performed at sub-mm wavelengths which forms the foundation for this thesis.

2.1 Sub-mm Galaxies

Observations with the InfraRed Astronomy Satellite, IRAS, Neugebauer et al. (1984), revealed a small population of ultra-luminous infrared galaxies (ULIRGs), with infrared luminosities, $L_{IR} \sim 10^{12} L_{\odot}$. Arising from intense star-formation (ULIRG luminosities imply star formation rates of $\sim 100 M_{\odot} yr^{-1}$) within molecular clouds; the UV light of massive young stars is absorbed by the dust which re-radiates at longer far-infrared wavelengths $(8 - 1000 \mu m)$, see e.g. the review by Sanders & Mirabel (1996). Subsequent investigations revealed the majority of these sources to be local mergers where the violent interactions

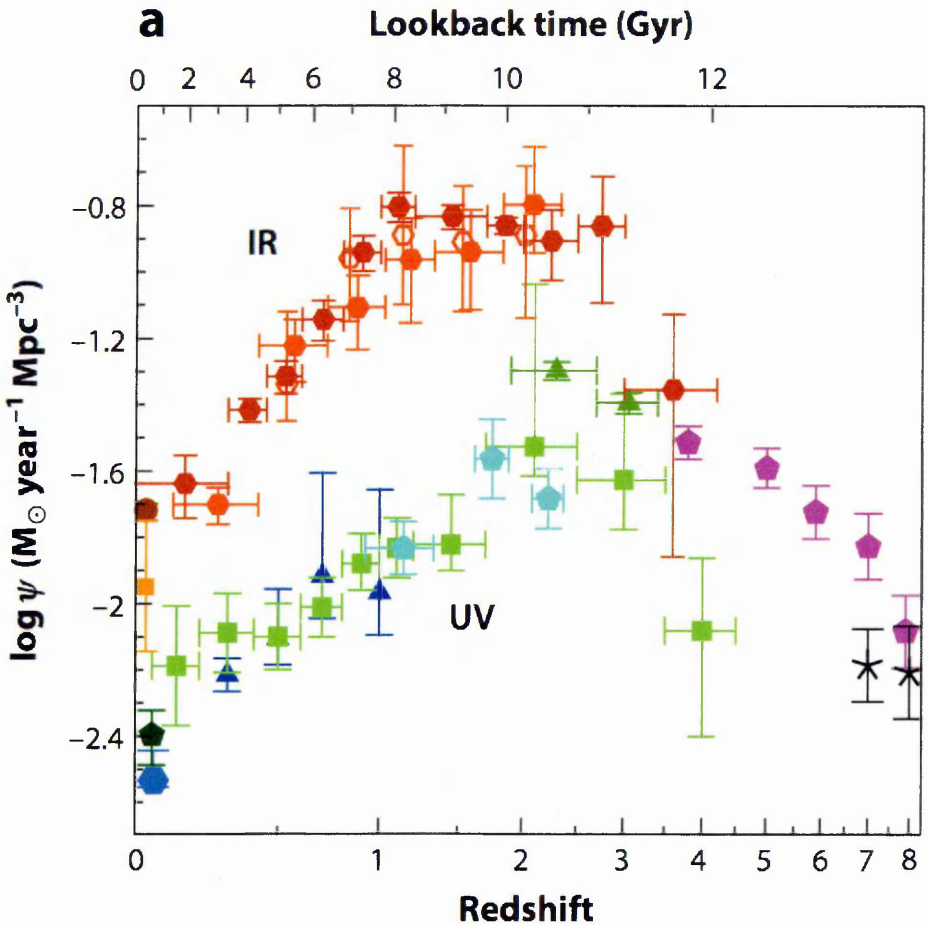

Figure 2.1: Star-formation rate density as a function of redshift. Credit: Madau & Dickinson (2014). Uncorrected rest-frame ultraviolet based SFR estimates are plotted in green and infrared in red.

had triggered a period of star formation (Hopkins et al., 2006). The detection of the hyper-luminous source IRAS 10214 + 4724, Rowan-Robinson et al. (1991), at a high redshift of $z = 2.286$ implied that a vast amount of dust and star formation must have been present in the very early universe, suggesting an evolving star formation rate.

Figure 2.1 presents the plot of star-formation rate as a function of redshift, figure from Madau & Dickinson (2014) and data points from references therein. The uncorrected UV-based estimates drastically fail to reproduce IR based estimates, this highlights that observations based solely on the UV must have accurate estimates of dust extinction to account for star-formation as traced by the dust emission. Prior to sub-mm observations attempts to measure the cosmic star-formation history were performed using deep optical

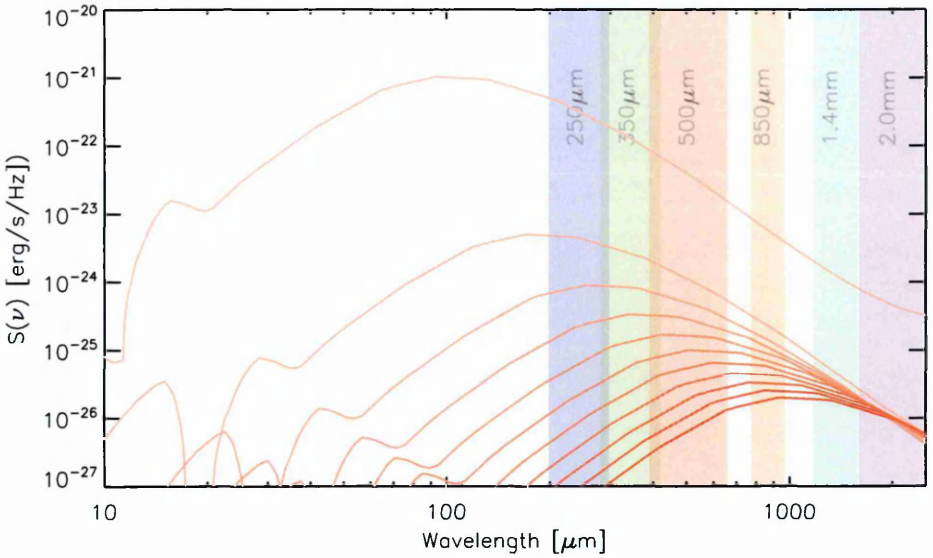

Figure 2.2: Far-infrared spectral energy distribution of SMMJ2135 'The Cosmic Eyelash'. Normalized to $L_{FIR} = 10^{13.5}$ $L_{\odot}$, redshifted at intervals z = 0.1, 1, 2, 3, 4, 5, 6, 7, 8, 9, 10 (redshift increasing with darker SED color). Sub-mm filter ranges overplotted in the background correspond to apparent fluxes in figure 2.3

images to detect the rest-frame UV emission to high redshifts, e.g. Connolly et al. (1997) in the Hubble Deep Field. These results of UV-based investigations were, however, drastically demonstrated to be underestimates by the first sub-mm observations.

The Submillimeter Common User Bolometer and Camera, SCUBA, on the James Clerk Maxwell Telescope, JCMT, was the first sub-mm instrument with the sensitivity to perform surveys capable of testing predictions of star formation at high redshift. Observations at sub-mm/mm wavelengths experience *negative k-correction*: as a source is redshifted spectral energy distribution (SED) sampled by a given filter changes, see figure 2.2 which plots the SED for the ULIRG SMMJ2135, the 'cosmic eyelash'. Figure 2.3 plots the corresponding fluxes observed across the different sub-mm/mm filters, the observed flux for ULIRGS at $z > 1$ in these bands remains broadly similar over a large range of redshifts. As a consequence SCUBA's 850μm observations were recognised to be ideal for the detection of ULIRGs over a range of high redshift. The first SCUBA surveys revealed a denser population of ULIRGs than predicted by rest-frame UV observations, Smail et al. (1997); Hughes et al. (1998) estimating that $< 80\%$ of star formation that is missed by optical observations alone.

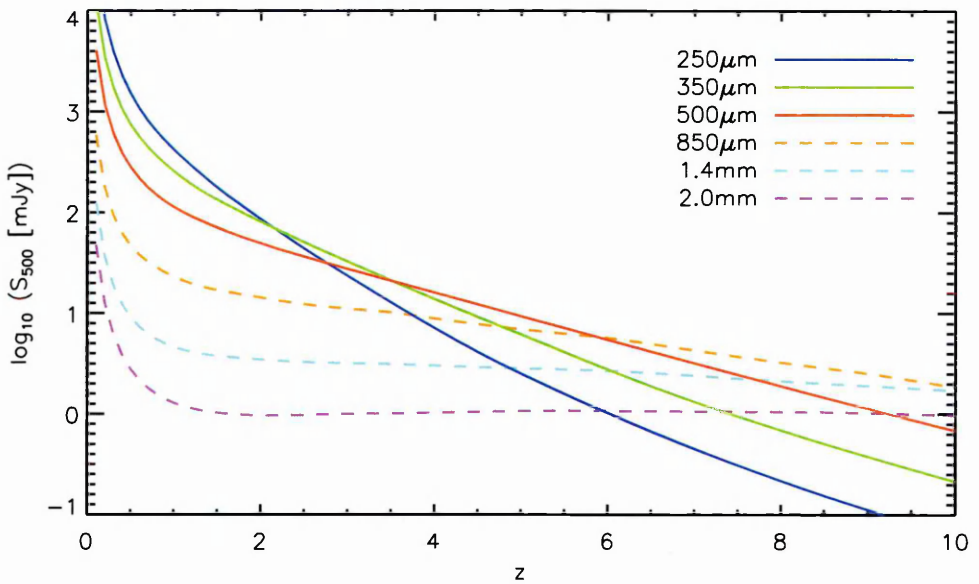

Figure 2.3: Apparent fluxes as a function of redshift for the above Cosmic Eyelash template SED for sub-mm/mm filters. Note the lack of detection at $S_{500} > 100$mJy for this 'model' unlensed ULIRG at $z > 1$. Also note the constant apparent flux for 1.4mm and and increase in apparent flux over the range $z = 1 - 10$.

SMGs represent the most luminous infra-red sources in the universe at the height of star formation, the magnification of lensing provides the opportunity to observe this important population at brighter fluxes and larger scales than otherwise possible. Such sources, which are exceptionally faint in the optical, can only be easily detected in the sub-mm which, until Herschel, had been restricted to small area surveys, e.g. 0.5 deg^2 of Mortier et al. (2005).

2.2 The Herschel Space Observatory

The Herschel Space Observatory (Pilbratt et al., 2010), conceived as the Far-InfraRed Space Telescope (FIRST) was proposed to the European Space Agency (ESA) in 1982, selected as the fourth 'cornerstone' of ESA's Horizon 2000 plan in 1993, and was renamed prior to construction in 2000 to honour William Herschel for his discovery of infrared radiation. Launched on 14^{th} May 2009 it was operational from June 2009 to April 2013 when the onboard cryogen was exhausted. *Herschel* spent over 23,000 hours observing the under-explored far-infrared / sub-millimeter radiation emitted by the 'cool' universe between $55 - 671\mu$m. Its elliptical orbit about the second (Sun-Earth) Lagrangian point

(L2) provided a stable location for the observatory and, importantly, a position where the Sun, Earth and Moon are in approximately the same location minimizing the area of incident thermal radiation from these bodies. The passive cooling provided by the solar shield maintained the temperature of the primary mirror at $\sim$ 85K ensuring minimal thermal radiation arising from the telescope. The focal plane and science instrument housing were actively cooled with a liquid helium cryostat maintaining a temperature a few Kelvin above absolute zero. The design of the observatory provided astronomers with a large, diffraction limited, low-emissivity telescope unrestricted by the atmospheric absorption experienced by ground based observations.

2.2.1 Instrument Overview

Three science instruments on *Herschel* provided photometry in six bands centered at approximately 70, 100, 160, 250, 350 and 500μm, spectral imaging over the wavelength range $55 - 671\mu$m and very high resolution spectroscopy over the ranges: $157 - 213\mu$m $240 - 625\mu$m. Accurate reduction of observations required precise flat-field information to account for the bright background noise of the telescope. Techniques of 'chopping/nodding' the telescope on and off target and 'scan-mapping' in which the telescope moves across the target area with overlapping scans at orthogonal orientations provided the efficient modes of observation.

PACS

The Photodetector Array Camera and Spectrograph, PACS, Poglitsch et al. (2010), is the first of the two general purpose instruments, designed with photometric and spectroscopic capabilities at the shorter wavelengths of the observatory. Photometry is performed using two out of three filters, either the 70μm (blue) or the 100μm (green) alongside the 160μm (red), in either point source or mapping mode. The rectangular field of view is 3.5' x 1.75' with projected pixel sizes of 3.2"/pix and 6.4"/pix for the short (blue/green) and long (red) filters respectively. Medium resolution imaging spectroscopy (R $\sim$ 1000 – 4000) covering the range $55 - 210\mu$m is provided by means of an integral field spectrometer (IFU) with a square field of view of 47" on a side projected onto 5 x 5 pixels.

SPIRE

The Spectral and Photometric Imaging REceiver, SPIRE, Griffin et al. (2010), is the second general purpose instrument, complementing PACS, providing photometric and spectroscopic capabilities at the longer wavelengths. Photometry is performed simultaneously for three filters, 250, 350 and 500μm (blue, green and red) in either point source, jiggle or scan mapping modes. The rectangular field of view is 4' x 8' with projected pixels sizes of 6, 10 and 14" for the blue, green and red filters respectively. An efficient parallel mode with both *PACS* (70/160μm or 100/160μm) and *SPIRE* (all filters) maps large areas of the sky in either slow (20"/s) or fast (60"/s) mode. Imaging spectroscopy by means of a Fourier Transform Spectrograph (FTS) operates at either medium (R $\sim$ 370 – 1300) or low (R $\sim$ 20 – 60) resolution in two overlapping wavelength ranges, 194 – 313μm and 303 – 671μm, with an approximate circular field of view of diameter $\sim$ 2.6'

HIFI

The Hetrodyne Instrument for the Far-Infrared, HIFI, de Graauw et al. (2010), provided very high resolution spectroscopy (R $\sim$ 10^6) over the wavelength ranges $\sim$ 157 – 213μm and $\sim$ 240 – 625μm using detection techniques akin to radio astronomy. Projected into the spectral dimension target beam sizes vary proportional to wavelength with Full Width Half Maximum (FWHM) ranging $\sim$ 11 – 45".

2.3 The Herschel ATLAS Key Project

The Herschel Astrophysical Terahertz Large Area Survey, H-ATLAS, Eales et al. (2010), was the largest key program under open time with Herschel, allocated $\sim$ 600hrs and covering $\sim$ 600deg^2. A photometric survey that used the efficient parallel observing mode of PACS and SPIRE to image $1/80^{th}$ of the sky in five bands: 100, 160, 250, 350 and 500μm. Survey depth was not a primary concern for the science being addressed, rather the largest possible survey area was most important, despite this the performance of the SPIRE instrument resulted in a survey remarkably close to the confusion limit at the longest wavelengths. A strength of H-ATLAS is the overlap with many existing or upcoming wide-area surveys at a variety of wavelengths, by exploiting all the available

data in the survey areas, H-ATLAS is uniquely placed to investigate important questions across multiple topics. Primarily conceived for studies of the local universe, the scope of the survey allows numerous science goals to be addressed. H-ATLAS involves 180+ members from 100+ institutions providing expertise across seven working groups within the consortium: local universe, H-ATLAS/Planck collaboration, lensing, rare objects/AGN, large scale structure, galactic dust/objects and high-z objects. An overview of the survey fields, multi-wavelength data and the science objectives are described in the following sections.

2.3.1 Survey Fields

The H-ATLAS area is divided into 5 separate fields, figure 2.4, the Northern Galactic Pole (NGP) field ($\sim$ 170deg^2) roughly centered at 13 hours right ascension and $+30°$ declination, three equatorial fields ($\sim$ 161deg^2 combined area), named for the GAMA survey areas they overlap, centered at 9, 12 and 15 hours right ascension, the Southern Galactic Pole (SGP) field ($\sim$ 273deg^2) centered at roughly 0 hours right ascension and $-30°$ declination. Located in regions of high galactic latitude, minimizing contamination from galactic cirrus, these fields were selected to complement existing and upcoming wide area spectroscopic and photometric surveys ensuring an enduring legacy value.

2.3.2 Multi-wavelength Coverage

Figure 2.4 displays the H-ATLAS fields and current/ongoing multi-wavelength complementary surveys. Overlapping spectroscopic surveys are: Sloan Digital Sky Survey, SDSS, York et al. (2000), the Galaxy and Mass Assembly, GAMA, Driver et al. (2011) and the 2dF Galaxy Redshift survey, 2dFGRS, Colless et al. (2001). In addition to SDSS photometric coverage is also provided in the optical and near-infrared by: UKIRT Infrared Deep Sky Survey Large Area Survey, UKIDSS LAS, Lawrence et al. (2007),the VISTA Kilo-degree Infrared Galaxy survey, VIKING, Emerson & Sutherland (2010) and the Kilo-degree Sky Survey, KIDS, de Jong et al. (2013). Table 2.1 details the filters and limiting (AB) magnitude of these photometric surveys.

	u	g	r	i	z	Z	Y	J	H	K
SDSS	22.0	22.2	22.2	21.3	20.5	-	-	-	-	-
KIDS	24.0	24.6	24.4	23.4	-	-	-	-	-	-
UKIDSS	-	-	-	-	-	-	20.9	20.6	20.3	20.1
VIKING	-	-	-	-	-	23.1	22.4	22.2	21.6	21.3

Table 2.1: Complementary survey AB magnitude limits.

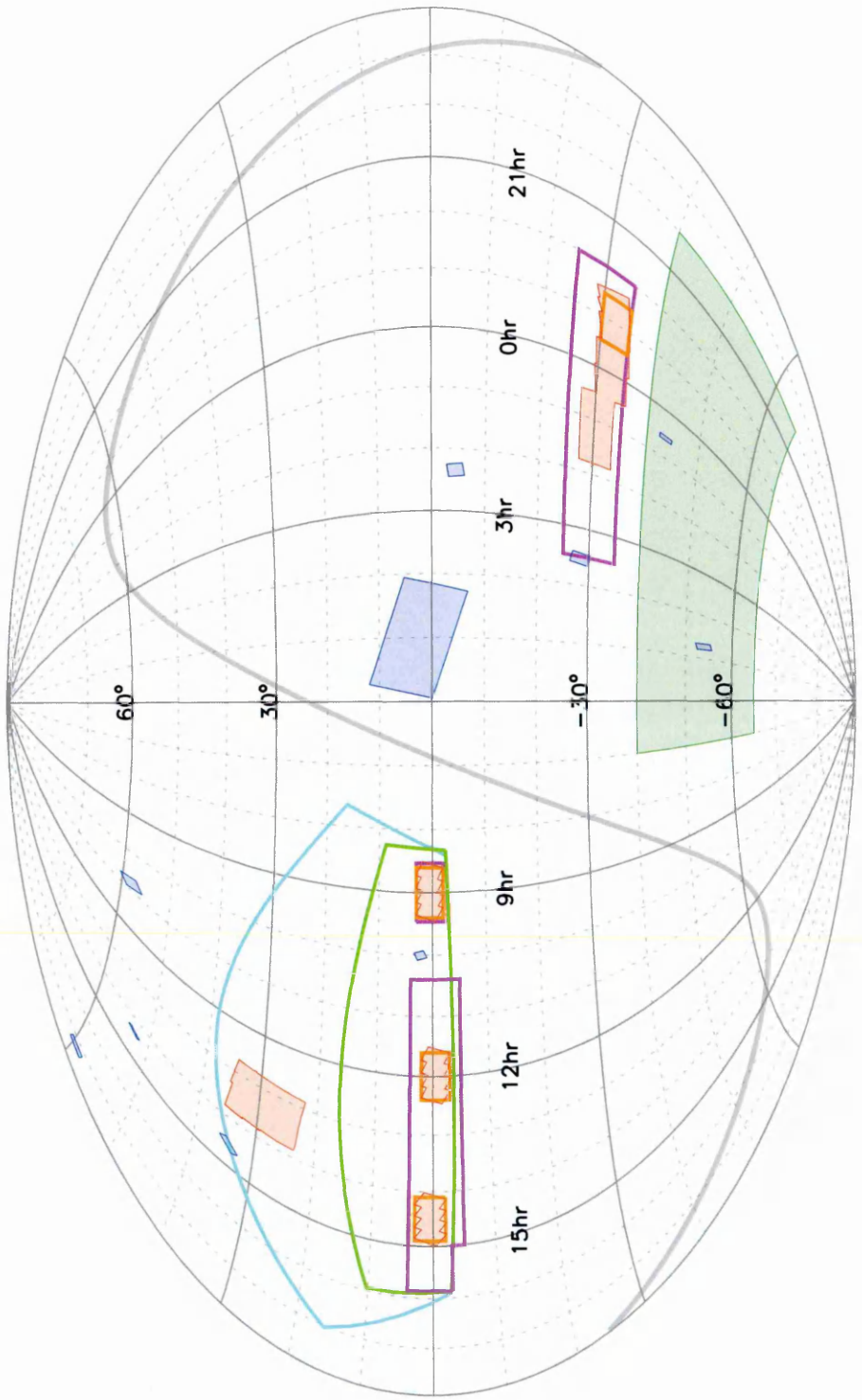

Figure 2.4: H-ATLAS survey fields and multi-wavelength coverage. Red shading: the five H-ATLAS fields, Northern Galactic Pole (NGP) at $+30°$, three equatorial GAMA regions located at 9, 12 and 15 hours, and the Southern Galactic Pole (SGP) at $-30°$. Cyan: SDSS stripes 9 – 25. Green: UKIDSS LAS. Magenta: VIKING and KIDS. Orange: GAMA spectroscopic survey. Also plotted are the HerMES fields (blue shading) and the SPT-SZ survey region (dark green shading). The galactic equator is represented in thick grey.

2.3.3 Science Objectives

Local Universe

The complete H-ATLAS has detected $\sim 40,000$ local galaxies ($z < 0.3$), of which the vast majority have spectroscopic redshifts, the combination of multi-wavelength and sub-mm photometry have allowed estimates of the intrinsic properties of local galaxies as a function of, e.g., environment, galaxy type, redshift; see e.g. Rowlands et al. (2012) for a blind sample, Rowlands et al. (2012) by morphological type. Such a sample size allows the stacking of objects to detect those which, individually, would be too faint to discern. Bourne et al. (2012) perform a comprehensive analysis stacking for optically selected sources investigating, e.g., dust mass evolution and contribution to the cosmic infrared background. The first estimates of the local sub-mm luminosity function, Dye et al. (2010) and the dust-mass function, Dunne et al. (2011). The volume sampled by H-ATLAS is vast in comparison to previous, comparable, surveys (e.g. SCUBA half-degree survey, SHADES, Coppin et al. (2006)) and has provided better estimates (in the aforementioned citations) of the obscured star formation and its evolution, allowing investigation of the radio-FIR correlation, Jarvis et al. (2010). The first investigations into the dust obscuration with large sample sizes at far-infrared wavelengths, Wijesinghe et al. (2011), are important to better understand empirically derived scaling laws, e.g. Calzetti et al. (2000).

Planck Collaboration

The Planck satellite (Tauber et al., 2010; Planck Collaboration et al., 2011), launched with Herschel, conducted an all sky survey with two instruments to map the Cosmic Microwave Background (CMB) at greater resolutions and sensitivities than precursor missions, Cosmic Background Explorer (COBE) and Wilkinson Microwave Anisotropy Probe (WMAP). The High Frequency Instrument (HFI) performed observations in six bands (350μm, 550μm, 850μm, 1.4mm, 2.1mm and 3mm) and detected more than the CMB: large scale galactic dust, point source emission for radio sources (longer wavelengths), dusty emission (shorter wavelengths) and the Sunyaev Zel'Dovich (SZ) effect of scattering of the CMB by galaxy clusters. With coverage of 1/80th of the sky in two shared wave-

lengths of much higher resolution (HFI beam $\sim 5 - 10$' compared to SPIRE ~ 30") there is an obvious synergy between the surveys. Source confusion is much more extreme for the large beam sizes of Planck, the effects of which manifest as uncertainties in position, overestimates of flux (Eddington bias) and spurious source detections. The overlapping H-ATLAS catalog, with improved positional and flux information, allows for better estimates of the necessary correction factors for the aforementioned effects. Herranz et al. (2013) demonstrate this with the first cross correlation between the Planck and H-ATLAS GAMA fields.

Gravitational Lensing and High-z

This science objective is intimately linked to this work, the selection of bright 500μm sources has been demonstrated as an efficient strong gravitational lens selection (see §2.4). The simple selection method and initial discovery of Negrello et al. (2010) has since been corroborated by the HerMES and SPT consortia, Wardlow et al. (2013); Vieira et al. (2013), respectively. The first H-ATLAS lenes discovered in the GAMA and NGP fields have resulted in follow-up observations to confirm their nature, e.g. Frayer et al. (2011); Harris et al. (2012); Lupu et al. (2012), including this work in §4 and §5). As well as the investigations made possible by the magnification of lensing, e.g. Omont et al. (2011); Valtchanov et al. (2011); Fu et al. (2012). The extension of the flux-limited selection (§4.1),proposed by González-Nuevo et al. (2012) and investigated in this work, has the potential to increase the number of strong gravitational lenses in H-ATLAS to $\sim$ 1000. Beyond the insights that lenses can provide on an individually basis the statistics of such a sample have the potential to independently constrain cosmological parameters (Short et al., 2012; Eales, 2015) and galaxy population statistics (§3). Based solely on the background source brightness H-ATLAS (flux-limited) lenses are unbiased towards the type of lens, with the potential to reveal rare configurations and more late-type lenses than existing surveys, e.g. Messias et al. (2014), Williams et al. (in prep).

Rare Objects and AGN

The observed correlation of central black hole mass and galactic stellar mass implies a connection between the cosmic star formation and black hole accretion which is reinforced

by the similarities between the cosmic star formation and quasar luminosity densities as functions of redshift (Franceschini et al., 1999). The final H-ATLAS sub-mm catalog will be uniquely placed to investigate the (sub-mm based) star formation properties of existing quasar samples, see the initial investigation by Bonfield et al. (2011). Serjeant et al. (2010) exploit the large coverage of H-ATLAS to perform a stacking analysis where individual quasars are not detected to provide statistical insights into the population as a whole.

Large scale structure

Galaxies are not uniformly distributed in space, residing in groups and clusters which in turn lie within long filaments of a cosmic web (Springel et al., 2006). The clustering of sources is a key statistical property of galaxy populations, quantifying the environment and characterised by a correlation function. The final H-ATLAS area contains $300,000+$ sources at a median redshift of $z \sim 1$ which, when complete, will allow investigation of large scale structure of $\sim$ 1000Mpc scales. Maddox et al. (2010) find the angular correlation function of the first 16deg^2 in agreement with models detecting weak clustering at low redshift increasing with redshift, van Kampen et al. (2012) performing a similar investigation of the clustering at low redshifts.. The overlapping multi-wavelength coverage allows for extensive photometric redshift estimates, e.g. Fleuren et al. (2012), which naturally extends investigations to the three dimensional two point correlation function to investigate source clustering. H-ATLAS sources have resolved only $\sim 15\%$ (Oliver et al., 2010) of the extragalactic background at the survey wavelengths. By modelling and removing the high signal to noise sources Thacker et al. (2013) investigate the angular power spectrum of the far-infrared background, estimate the average halo mass and occupancy for contributing sources and find their estimate of the density of dust in the universe in agreement with alternate methods.

Galactic Dust/Objects

Whilst serving as a good tracer of the Interstellar Medium (ISM) and star formation, galactic dust is a nuisance for extragalactic observations where corrections for extinction and reddening effects are essential. Galactic cirrus is be present in the H-ATLAS fields and mapped at a resolution of ~ 30", a factor of ~ 10 improvement over maps produced

by IRAS and at longer wavelengths and at wavelengths sensitive to colder (T$\sim$ 15K) dust. Bracco et al. (2011) investigate the SED, dust emissivity and power spectrum of the foreground cirrus in H-ATLAS which is a byproduct of the H-ATLAS map making and source extraction. Despite being extragalactic fields the survey will also detect high latitude galactic objects. The detection of the high latitude populations of dusty debris disks is investigated by Thompson et al. (2010) for the initial 16deg^2 of H-ATLAS with $\sim$ 10000 main sequence stars in the final catalogs a stacking analysis will extend this initial work to estimate the frequency of debris disks by spectral type.

2.4 A Flux-limited Lens Selection

2.4.1 Predictions

Previous lens surveys (§1.4) have relied on either the detection of lensed features (CLASS, CFHTLS-S2LS) and multiple images (SQLS) or the characteristic signatures of closely aligned, distinct sources (SLACS, BELLS). It has long been predicted (Blain, 1996; Negrello et al., 2007) that the steep source counts at sub-mm/mm wavelengths, e.g. Clements et al. (2010), are drastically affected by the presence of lensed galaxies. The magnification experienced by the handful of lensed sources flattens the tail of the source counts, this *magnification bias* results in a distinct lensed population above a bright flux-limit.

Figure 2.5 shows the model source counts of Cai et al. (2013) for the bright-end populations at 500μm. A selection of $S_{500} > 100$mJy sources will include the rarest and brightest of the un-lensed population (e.g. Ivison et al. (2013)), radio-loud blazars, local star-forming/dusty galaxies and the lensed population. The identification of the blazar and local populations is simply performed using shallow, wide-area radio and optical surveys (see §3) leaving a sample predicted to contain an overwhelming majority of lensed sources.

2.4.2 Confirmation

Prior to the H-ATLAS, HerMES and SPT-SZ surveys, the largest sub-mm (SCUBA) surveys covering only a few square degrees were too small to find a statistically signif-

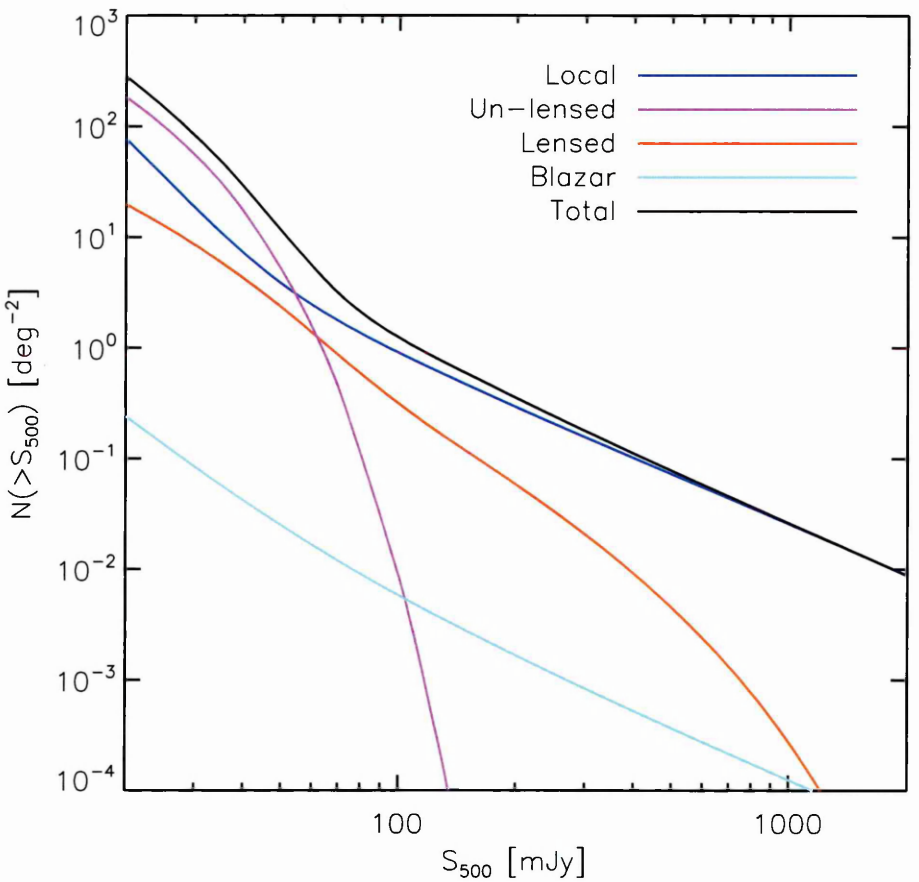

Figure 2.5: Predicted integral number counts of Cai et al. (2013). Blue: local spiral/starbursts, Magenta: un-lensed SMGs, Red: lensed SMGs, Cyan: Blazars, Black: total counts.

icant sample of lenses (see figure 2.5, predicted density of $> 1\text{deg}^{-2}$). Prospects for a comprehensive detection of the lensed population came with the advent of wide area sub-mm/mm surveys of areas $> 100\text{deg}^2$ with Herschel and the SPT (see figure 2.4 for the survey regions). Within each of these surveys the prospect of a simple lens selection was recognised and the three consortia had the potential to confirm the existance of a lensed SMG population. Operations began at the SPT in 2008 observing the first $\sim 87\text{deg}^2$, followed by the launch of Herschel, the first regions of H-ATLAS ($\sim 16\text{deg}^2$) and HerMES ($\sim 20\text{deg}^2$) were selected for observations in the Herschel Science Demonstration Phase (SDP) in 2009. The first SPT number counts, Vieira et al. (2010), hypothesized that the bright flux sources without an IRAS counterpart were likely to be strongly lensed SMGs. Similiarly the first H-ATLAS number counts, Clements et al. (2010), found that the bright-end number counts were in approximate agreement with the predictions of Negrello et al. (2007) and discounted models that do not favour a bright-end contribution from lensing. The first HerMES number counts, Oliver et al. (2010), do not explicity hypothesize a lensing contribution but do show an agreement with model predictions that include the lensed population.

The work of Negrello et al. (2010) was the first confirmation of strongly lensed galaxies detected in the sub-mm. The H-ATLAS SDP catalog (> 6600) contained 11 sources with $S_{500} > 100\text{mJy}$, of which four sources were identified as local spiral galaxies, one source as a radio bright quasar and an additional source as an extended galactic star-forming region. The remaining five sources were investigated with follow-up observations which, combined, identified them as strong gravitational lenses. A likelihood ratio (LR) analysis of optical counterparts (Smith et al., 2011) from the SDSS catalog identified foreground lens candidates unlikely to be random associations. The foreground lenses were observed with high resolution imaging on the Keck telescope and spectroscopy from the William Herschel Telescope (WHT) and Apache Point Observatory (APO), firmly establishing the nature of the lens and their redshifts. Blind redshift spectroscopy was obtained using the Z-Spec instrument on the Caltech Submillimeter Observatory (CSO) and Zpectrometer on the Green Bank Telescope (GBT), Lupu et al. (2012) and Frayer et al. (2011) respectively, and subsequently confirmed with PdBI observations. Sub-Millimeter Array (SMA) interferometric observations for two of the sources revealed the presence of

multiple images about the lens further confirming the source-lens nature of these sources as already established by the distinct redshifts for the sources/lenses. In a remarkable demonstration of co-ordinated follow-up with multiple facilities the H-ATLAS consortium confirmed the efficient ($\sim 100\%$) flux-limited selection within the first year of the survey.

This initial confirmation has since been supplemented by investigations from the HerMES and SPT consortia. Wardlow et al. (2013) investigate 13 candidates from nine HerMES fields ($\sim 95\mathrm{deg}^2$) and confirm lensing in nine sources (the nature of four remaining uncertain). Their supplementary sample lowers the flux limit to $S_{500} = 80 - 100\mathrm{mJy}$ finding a lower efficiency and the presence of at least one intrinsically bright un-lensed HyLIRG. Vieira et al. (2013) confirms the SPT sample of lens candidates (~ 20) with the early science configurations of the Atacama Large Millimeter Array (ALMA) demonstrating not only the higher redshifts (Weiß et al., 2013) of sources selected from mm surveys but the power of ALMA, which reveals the multiply imaged sources (Hezaveh et al., 2013) in only one minute on-source integration times.

Chapter 3

Herschel-ATLAS Lens Candidates

The combination of steep number counts and the magnification of lensing results in distinct populations of lensed and un-lensed SMGs at the brightest sub-mm wavelengths (§2.4 and figure 2.5). The work undertaken in this chapter investigates the bright sources ($S_{500} > 80$mJy) from the H-ATLAS NGP and SGP 'phase 1' catalogs. In combination with the bright source classifications of the GAMA catalogs, Negrello et al. (in prep), the first bright source number counts of the complete H-ATLAS are presented and compared to model predictions.

The chapter is organised as follows: Section 3.1 presents with an overview of the H-ATLAS 'phase 1' maps and catalogs, produced by the H-ATLAS consortium (multiple in prep.), and describes the source classification method performed in this work. Section 3.2 describes the photometric redshift estimation performed using a minimum-χ^2 SED template fitting to the SPIRE data of all bright sources. Section 3.3 describes the compilation of the bright source number counts for the local and lens candidate populations by applying a bootstrap resampling method. Section 3.4 provides an overview of the population models of Lapi et al. (2012) and Cai et al. (2013) and describes the reduced-χ^2 comparison to the number counts derived in this work. Section 3.5 concludes with a summary of the chapter; the conclusions and future work.

3.1 Source Classification

3.1.1 H-ATLAS Phase 1 Data

The data used in the compilation of source counts are the NGP and SGP phase 1 (December 2013, H-ATLAS internal release) PSF matched catalogs comprising of photometry for the three SPIRE bands. Source identification was performed for all three bands using the Multi-band Algorithm for source eXtraction (MADX, Maddox et al. (in prep)). The local background, predominantly galactic cirrus, was estimated from the histogram peaks of 30×30 pixel region. The background at each pixel was subequently estimated by fitting a bi-cubic interpolation to this coarse grid. The background subtracted maps were then match-filtered using the band PSF with pixel noise estimates dominated by the instrumental noise of the detectors. The catalog requires that a source is detected at a 5σ level in at least one of the SPIRE bands. Phase 1 map making reduction and subsequent source extraction is due to be described in Maddox et al. (in prep) and Valiante et al. (in prep) respectively. These methods are not anticipated to differ significantly from the SDP reductions of Pascale et al. (2011) and Rigby et al. (2011). These preliminary catalog releases have been recognised to underestimate the fluxes of extended objects (Valiante, priv. comm.).

3.1.2 Source Classification

Starting with the complete 'phase 1' catalogs for the H-ATLAS NGP and SGP a bright source subsample was extracted by selecting those sources with $S_{500} > 80$mJy. The bright source subsample comprised of 298 and 401 extracted sources in the NGP and SGP respectively. This initial sample of bright sources was first inspected to identify and discard duplicate extracted sources (present in cases of the most extended local galaxies where structure in the sub-mm emission was resolved by SPIRE). Following this first sanity check the sources were subsequently inspected with complementary data to classify each as one of the expected contaminant populations: local late-type galaxies, radio-loud galaxies/blazars, extremely local dusty stars or galactic cirrus. Any sources not classified as a contaminant are considered to be lens candidates subject to further investigation to confirm their nature. The selection of sources down to a limit of 80mJy takes into account

the uncertainty in flux, particularly important at this 'phase 1' stage where subsequent data reduction, source extraction and catalog compilation may alter the flux estimates of sources. This lower flux limit ensures sample completeness for true 'bright' sources of $S_{500} > 100$mJy.

The Aladin software, Bonnarel et al. (2000), was used to inspect each source, retrieving and displaying optical and radio images and overlaying extragalactic catalog information from the NASA Extragalactic Database (NED).

The identification of local late-type galaxies was performed using Sloan Digital Sky Survey, SDSS York et al. (2000), and second Palomar Sky Survey, POSS-II Reid et al. (1991), for the NGP and SGP respectively. Although shallower in depth the POSS-II images were sufficient to identify local sources and where coverage allowed the Z and Y band images of the VISTA Kilo-degree Infrared Galaxy Survey, VIKING Emerson & Sutherland (2010), complemented the optical images to support the classifications. Alongside the r-band imaging the NED catalog information provided spectroscopic redshifts for ~99% of the local galaxies which further reinforced the classification. Tables A.3 and A.4 detail the locally classified sources including, where appropriate, any alternative catalog name and the NED quoted spectroscopic redshift. Figures A.7 and A.8 are the postage stamps of all locally classified sources. All NGP stamps are composite SDSS r-band images whereas SGP sources are the deeper VIKING Z or Y band images where available and POSS-II r-band elsewhere, in each postage stamp the scale bar represents 30". The identification of radio contaminants was made using 1.4GHz imaging from the Faint Images of the Radio Sky at Twenty-cm, FIRST Becker et al. (1995), and the NRAO VLA Sky Survey, NVSS Condon et al. (1998), for the NGP and SGP respectively. NED catalog information also provided spectroscopic redshifts for ~60% of the radio-loud/blazar sources. Tables A.5 and A.6 detail the blazar classified sources including the NED quoted spectroscopic redshift and the 1.4GHz flux/beam obtained from the FIRST source catalog, White et al. (1997), and NVSS catalogs, Condon et al. (1998), for the NGP and SGP respectively.

Figure 3.1 shows the SPIRE 500μm source contours (100, 200 and 300mJy) overlaid on SDSS DR8 r-band (left) and FIRST 1.4GHz (right). The matched contours of the SPIRE emission to the extended optical source and to the bright, coincident radio emission of the radio source serve to highlight the relatively simple identification of these contaminant

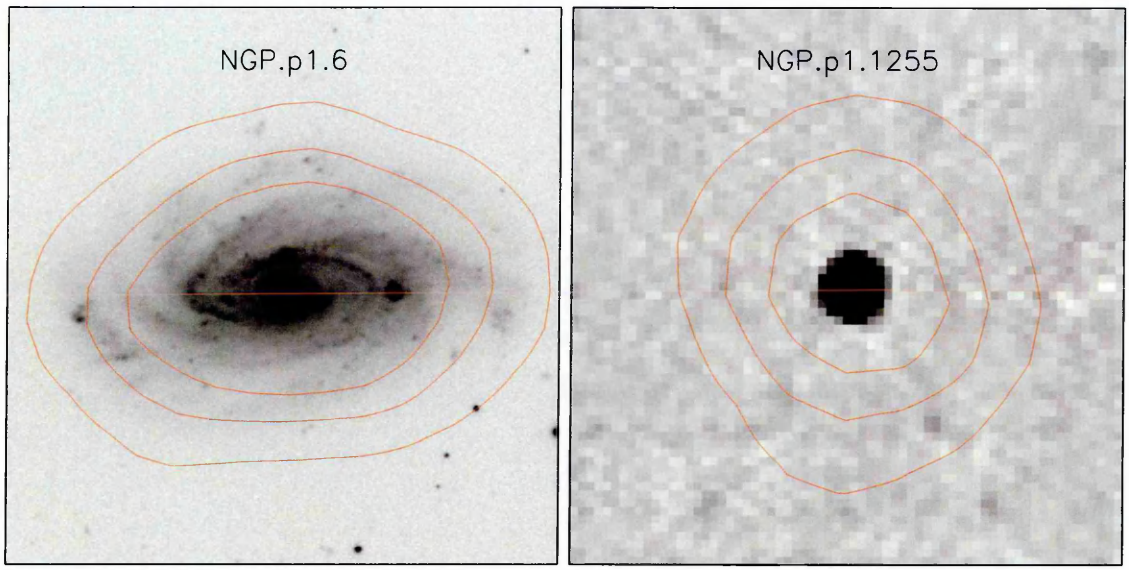

Figure 3.1: Postage stamps used for classification of sources, local (left) and blazar (right) examples in the NGP. Left: SDSS DR8 r-band image, 3' on a side. Right: FIRST 1.4GHz image scaled to a maximum intensity of 100mJy (black), 2' on a side. Red contours represent SPIRE 500μm emission at 100, 200 and 300 mJy.

populations.

In order to identify any spurious sources the Infrared Astronomy Satellite, IRAS Neugebauer et al. (1984), 60 and 100μm maps were inspected at the source positions. Bright extended structure present in the IRAS maps would be indicative of galactic cirrus and would have been removed from the sample, however no such sources were identified. Two sources in the SGP were co-incident with ~Jy level point sources in the IRAS maps and in very close proximity to bright stellar sources in optical imaging. Investigation with the ViZier catalog service, Ochsenbein et al. (2000), revealed these to be well studied stars with warm debris disks, Fomalhaut and R Sculptor, these sources were removed from the sample.

The remaining sources, without an obvious local or radio counterpart, were classified as lens candidates. Table 3.1 displays the number of sources classified per field. Optical and NIR postage stamps for the NGP and SGP lens candidates are respectively displayed in figures A.1, A.4 for $S_{500} > 100$mJy, figures A.2, A.5 for $90 > S_{500} > 100$mJy and figures A.3, A.6 for $80 > S_{500} > 100$mJy. Lens candidate fluxes, photometric redshift estimates (§3.2) and, where they exist, spectroscopic redshifts are displayed in tables A.1 and A.2.

	GAMA	NGP	SGP
Area [deg^2]	161.1	170.1	272.8
Contaminants			
N_{local}	167	175	177
N_{blazar}	0	6	6
N_{other}	1	0	2
Lens Candidates			
N($\geq$ 80)	156	104	190
N($\geq$ 100)	45	37	48
N($\geq$ 100) [deg^2]	0.28	0.22	0.18

Table 3.1: H-ATLAS field summary. GAMA data from priv. comm. courtesy of Negrello et al. (in prep.).

3.2 Photometric Redshift Estimates

Without the resolution to directly detect the signatures of strong lensing, any sample selected solely on sub-mm data will remain as lens candidates until additional observations can provide definitive evidence of lensing. This evidence is most striking where high resolution observations are sensitive enough to reveal the lensed source distorted into characteristic arcs, counterimages or rings. In the absence of high resolution imaging the detection of distinct source/lens redshifts can serve as confirmation of lensing.

The highly obscured nature of SMGs result in exceptionally faint optical/NIR emission at wavelengths dominated by the lens (e.g. Keck lens-subtracted i-band images for the 5 SDP lenses of Negrello et al. (2010)). Spectroscopy in this regime is exceptionally challenging for the source and while this traditional technique can provide accurate redshift estimates for the lens it is necessary to observe the longer, brighter mm/cm wavelengths to obtain source redshifts.

Wide bandwidth spectrometers have, for the past few years, demonstrated the ability to blindly measure CO emission redshifts. The discovery of an efficient lens selection was the motivation for some of the first observations with such instruments to obtain redshifts for the initial H-ATLAS and HerMES lenses. Key observatories/instruments including: the Green Bank Telescope (GBT) Zpectrometer, Caltech Submillimeter Observatory (CSO) Z-Spec, Combined Array for Research in Millimeter-wave Astronomy (CARMA), Institut

de Radioastronomie Millimétrique (IRAM) Plateau de Bure Interferometer (PdBI) contributed to identifying CO transitions for the first blind spectroscopic redshifts for sub-mm sources (Cox et al., 2011; Frayer et al., 2011; Riechers et al., 2011; Harris et al., 2012; Lupu et al., 2012). Of particular note is the large sample of SPT lenses observed with ALMA, Weiß et al. (2013) demonstrate that ALMA is ideally suited to observe large samples where exposure times are of the order of minutes opposed to the hours required on single dish telescopes.

For the large samples of lens candidates now being generated by sub-mm surveys it is unfeasible to expect spectroscopic observations to be made for all but a small percentage of the candidates. It has been shown that photometric redshifts, based soley on Herschel photometry, can be a reasonable estimate of the spectroscopic redshift, see e.g. the 5 SDP lenses in Negrello et al. (2010). The wavelength of the three SPIRE filters sample the peak of dusty emission for typical sub-mm bright sources, see §2.1 and figure 2.2 where the peak of emission falls between $250-500\mu$m for a redshift range $z \sim 1-3$. This coverage allows for a relatively simple template-fitting method to estimate photometric redshifts for H-ATLAS sources. The present number of spectroscopic redshifts for confirmed lens candidates provides a baseline to estimate the uncertainty of these simple photometric estimates.

3.2.1 Template Fitting

A minimum-χ^2 fitting of the SPIRE photometric data points to template SEDs was performed using IDL. Starburst/ULIRG templates: Arp220 and M82 from the `SWIRE` template library of Polletta et al. (2007) and the SMM J2135 (the Cosmic Eyelash) template from Lapi et al. (2011) as modelled with `GRASIL` (Silva et al., 1998) were redshifted ($z = 0 - 6$ over 201 bins):

$$S_{temp}(\lambda, z) \propto S_{temp}(\lambda_{z=0}/[1+z]) \tag{3.1}$$

Convolved with the SPIRE filters, where $T_{filter}(\lambda)$ is the filter transmission:

$$S_{temp,filter}(z) = \frac{\int T_{filter}(\lambda)\ S_{temp}(\lambda)\ d\lambda}{\int T_{filter}(\lambda)\ d\lambda} \tag{3.2}$$

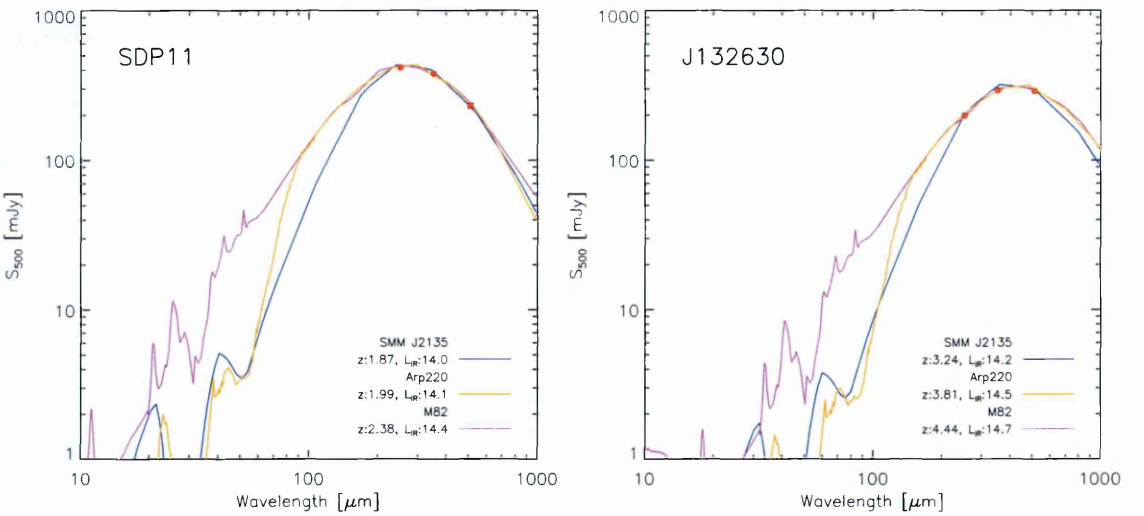

Figure 3.2: Best fit SEDs and parameters determined from the template fitting for two examples. Note that the error bars lie within the symbols. L_{IR} values are decimal logarithm in solar luminosity units.

And normalized to the data (S_{data}) and associated uncertainties (σ) across the three SPIRE filters($N_{filters}$):

$$a = \frac{\sum_{i=1}^{N_{filters}} \left(\frac{S_{temp,i}(z)\ S_{data,i}}{\sigma_i^2} \right)}{\sum_{i=1}^{N_{filters}} \left(\frac{S_{temp,i}(z)^2}{\sigma_i^2} \right)} \tag{3.3}$$

For each realisation the χ^2 was measured and the best fit redshift for that template taken as the minimum-χ^2:

$$\chi^2 = \sum_{i=1}^{N_{filters}} \left(\frac{S_{data,i} - aS_{temp,i}(z)}{\sigma_i} \right)^2 \tag{3.4}$$

By adopting a standard flat ΛCDM cosmology with $\Omega_M = 0.27$ and $H_0 = 70 \mathrm{kms}^{-1}\mathrm{Mpc}^{-1}$ the best fit photometric redshift is related to the luminosity distance (e.g. Peebles (1993)):

$$D_L = (1+z)\frac{c}{H_0}\frac{2(2-\Omega_M(1-z)-(2-\Omega_M)\sqrt{1+\Omega_M z})}{\Omega_M^2(1+z)} \tag{3.5}$$

Thereby providing an estimate of the far-infrared ($8\mu\mathrm{m} < \lambda < 1000\mu\mathrm{m}$) luminosity ($L_{IR}$) from the far-infrared flux of the best fit template ($S_{IR}(z)$):

$$L_{IR} = \frac{aS_{IR}(z)}{4\pi D_L^2} \tag{3.6}$$

Performing the above template fitting for a selection of sources with existing, robust spectroscopic redshifts allowed a statistical comparison to decide on the best template to use. Four samples of lens candidates with spectroscopic redshifts were combined: the 5 SDP lenses of Negrello et al. (2010), 7 robust HerMES lenses of Wardlow et al. (2013), 11 GAMA field lenses (excluding the SDP lenses) and 14 NGP lenses. Redshifts for the H-ATLAS sources were provided via H-ATLAS internal communications (publications in prep.) and Harris et al. (2012). The combined samples are summarized in table 3.2 and two examples of the minimum-χ^2 template fitting are shown in figure 3.2. Figure 3.3 shows the dispersion of the redshift estimates as a function of spectroscopic redshift and the best fit gaussion to the histogram of $(z_{phot} - z_{spec})/(1 + z_{phot})$.

Estimates using the template of M82 consistently overestimate the redshift of the sources whereas the templates of Arp220 and SMM J2135 are centrally dispersed. Taking the narrowest FWHM of the SMM J2135 sample as the best estimates dictate an error of ($\sigma = 0.208$) 20.8% of $(1+z)$ on the photometric redshifts quoted for the remainder of this work.

Each template routinely underestimates the redshift for sources $z \geq 3$. At this redshift the peak of emission is shifted into and beyond the 500μm filter and without longer wavelengths to constrain this peak the template fitting is unable to provide an accurate estimate. While the majority of sources are found to lie at $z \sim 2.5$ sources located at higher redshift will benefit from follow-up millimetre observations to provide a more accurate photometric estimate.

Photometric redshifts for the entire NGP and SGP bright ($S_{500} > 80$mJy) samples were estimated using the aforementioned minimum-χ^2 fitting with the SMM J2135 template. Figure 3.4 shows the histogram of redshifts for the two fields, both fields contain two distinct peaks representing the two dominant populations: local late-type galaxies and distant lens candidate sources. Figure 3.5 shows the histograms of the photometric redshifts for the lens candidate sample of each field including the GAMA field candidate sample. Table 3.3 provides the mean and standard error for all three fields, the mean redshift of the fields are all within their combined standard errors at $z \sim 2.6$.

Figures 3.6 shows the histograms of the photometric estimate and spectroscopic red-

Identifier	S_{250} [mJy]	S_{350} [mJy]	S_{500} [mJy]	z_{spec}	z_{phot} SMM/Arp220/M82	L_{IR}[4] SMM/Arp220/M82
SDP9	470.6 ± 6.8	342.7 ± 8.1	181.4 ± 8.8	1.577[1]	1.39 / 1.45 / 1.66	13.8 / 13.9 / 14.2
SDP11	417.0 ± 6.1	378.5 ± 7.4	232.1 ± 8.2	1.784[1]	1.87 / 1.99 / 2.38	14.0 / 14.1 / 14.4
SDP17	346.9 ± 6.8	338.9 ± 8.0	218.9 ± 8.8	2.305[1]	2.05 / 2.20 / 2.62	14.0 / 14.1 / 14.4
SDP81	137.9 ± 6.9	199.1 ± 8.2	174.3 ± 9.1	3.043[1]	3.03 / 3.48 / 4.08	14.0 / 14.2 / 14.4
SDP130	116.3 ± 6.1	140.0 ± 7.4	107.6 ± 8.2	2.626[1]	2.59 / 2.86 / 3.42	13.7 / 13.9 / 14.2
J083051	260.5 ± 7.0	321.3 ± 8.1	269.5 ± 9.0	3.634[3]	2.74 / 3.06 / 3.60	14.2 / 14.3 / 14.6
J084933	241.9 ± 7.0	292.9 ± 8.1	231.2 ± 9.0	2.410[3]	2.62 / 2.92 / 3.45	14.1 / 14.3 / 14.5
J085359	388.9 ± 6.9	381.4 ± 8.1	240.7 ± 9.2	2.089[3]	2.05 / 2.17 / 2.62	14.0 / 14.2 / 14.4
J091841	141.7 ± 6.8	175.3 ± 8.2	138.1 ± 8.9	2.581[3]	2.65 / 2.95 / 3.51	13.9 / 14.0 / 14.3
J113243	75.9 ± 6.8	120.4 ± 8.1	107.7 ± 8.9	2.578[3]	3.21 / 3.69 / 4.32	13.8 / 14.0 / 14.3
J113526	289.7 ± 6.9	295.2 ± 8.1	216.4 ± 8.8	3.128[3]	2.26 / 2.41 / 2.92	14.0 / 14.1 / 14.4
J114638	289.9 ± 6.1	356.4 ± 7.4	295.4 ± 8.1	3.259[3]	2.71 / 3.03 / 3.57	14.2 / 14.4 / 14.6
J115820	130.5 ± 6.4	142.9 ± 7.6	106.4 ± 8.3	2.191[3]	2.38 / 2.59 / 3.12	13.7 / 13.9 / 14.1
J141352	189.5 ± 6.9	240.2 ± 8.0	200.4 ± 8.8	2.478[3]	2.77 / 3.09 / 3.66	14.0 / 14.2 / 14.5
J142414	115.0 ± 6.9	191.7 ± 8.1	203.4 ± 8.8	4.243[3]	3.54 / 4.29 / 4.98	14.1 / 14.4 / 14.6
J142935	778.4 ± 6.2	467.0 ± 7.5	226.6 ± 8.1	1.026[3]	0.94 / 0.97 / 1.12	13.7 / 13.9 / 14.2
J125135	156.9 ± 5.7	207.3 ± 6.4	215.2 ± 7.5	3.675[3]	3.15 / 3.72 / 4.29	14.1 / 14.3 / 14.5
J125632	209.6 ± 5.6	285.7 ± 6.5	254.7 ± 7.6	3.565[3]	2.98 / 3.39 / 3.96	14.2 / 14.4 / 14.6
J125652	139.4 ± 5.7	168.1 ± 6.5	133.8 ± 7.8	2.792[3]	2.62 / 2.92 / 3.48	13.8 / 14.0 / 14.3
J132302	133.3 ± 5.6	152.2 ± 6.4	140.3 ± 7.7	2.194[3]	2.71 / 3.09 / 3.57	13.8 / 14.0 / 14.3
J132427	348.0 ± 5.6	378.3 ± 6.4	251.6 ± 7.6	1.676[3]	2.26 / 2.44 / 2.95	14.1 / 14.2 / 14.5
J132504	245.4 ± 5.5	237.6 ± 6.5	178.2 ± 7.7	1.836[3]	2.17 / 2.32 / 2.80	13.9 / 14.0 / 14.3
J132630	198.7 ± 5.6	293.0 ± 6.4	289.8 ± 7.8	2.951[3]	3.24 / 3.81 / 4.44	14.2 / 14.5 / 14.7
J132859	276.7 ± 4.7	311.9 ± 5.7	260.4 ± 6.8	2.778[3]	2.56 / 2.86 / 3.39	14.1 / 14.3 / 14.5
J133009	269.3 ± 5.4	284.5 ± 6.4	204.2 ± 7.5	3.111[3]	2.29 / 2.47 / 2.98	14.0 / 14.1 / 14.4
J133543	150.1 ± 5.5	158.5 ± 6.3	129.3 ± 7.5	2.685[3]	2.41 / 2.65 / 3.18	13.8 / 13.9 / 14.2
J133650	294.6 ± 4.9	282.8 ± 5.9	193.6 ± 7.2	2.202[3]	2.08 / 2.20 / 2.68	13.9 / 14.1 / 14.3
J133847	158.4 ± 5.7	181.1 ± 6.4	137.8 ± 7.9	2.341[3]	2.47 / 2.74 / 3.27	13.8 / 14.0 / 14.3
J133905	154.1 ± 5.9	158.8 ± 6.6	97.9 ± 7.8	2.390[3]	2.11 / 2.26 / 2.71	13.7 / 13.8 / 14.1
J134429	465.4 ± 5.7	474.1 ± 6.7	341.6 ± 7.7	2.301[3]	2.23 / 2.41 / 2.89	14.2 / 14.3 / 14.6
HBOOT01	158.0 ± 6.0	191.0 ± 7.0	160.0 ± 33.0	3.274[2]	2.59 / 2.95 / 3.54	13.9 / 14.1 / 14.3
HBOOT02	159.0 ± 6.0	196.0 ± 7.0	157.0 ± 33.0	2.804[2]	2.62 / 3.01 / 3.60	13.9 / 14.1 / 14.4
HBOOT03	323.0 ± 6.0	244.0 ± 7.0	140.0 ± 33.0	1.325[2]	1.48 / 1.54 / 1.75	13.7 / 13.8 / 14.1
HLOCK01	403.0 ± 7.0	377.0 ± 10.0	249.0 ± 7.0	2.958[2]	2.02 / 2.14 / 2.53	14.0 / 14.2 / 14.4
HLOCK03	114.0 ± 7.0	147.0 ± 10.0	114.0 ± 8.0	2.771[2]	2.71 / 3.01 / 3.57	13.8 / 14.0 / 14.2
HXMM01	180.0 ± 7.0	192.0 ± 8.0	132.0 ± 7.0	2.307[2]	2.26 / 2.44 / 2.92	13.8 / 13.9 / 14.2
HXMM02	92.0 ± 7.0	122.0 ± 8.0	113.0 ± 7.0	3.395[2]	3.01 / 3.42 / 3.99	13.8 / 14.0 / 14.2

[1] Negrello et al. (2010) and references therein.

[2] Wardlow et al. (2013) and references therein.

[3] Harris et al. (2012) and internal communication from H-ATLAS consortium.

[4] Decimal logarithm of luminosity in units of $L_{\odot}$

Table 3.2: Compilation of lens candidates with robust spectroscopic redshifts. Photometric redshift and infrared luminosity estimated from SED template fitting to the SPIRE data points.

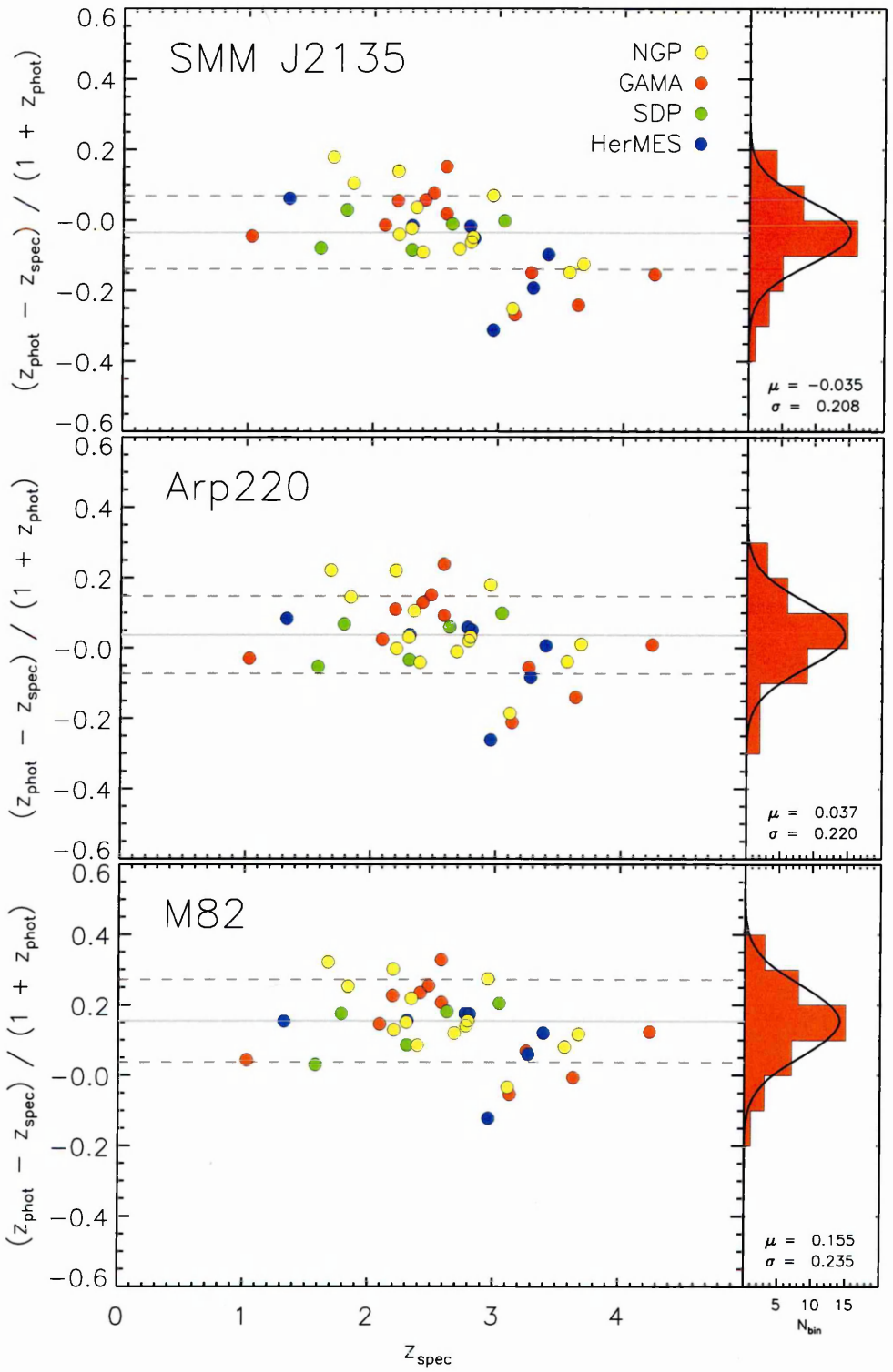

Figure 3.3: Photometric redshift error estimates for three templates: SMM J2135, Arp220 and M82. Data points represent the confirmed lens candidates with robust spectroscopic redshifts from the H-ATLAS SDP, GAMA, NGP, HerMES (Wardlow et al., 2013) and are summarized in table 3.2. Best-fit gaussians to the histogram of $(z_{spec} - z_{phot})/(1 + z_{phot})$ (black) provide 1σ error estimates for the different templates.

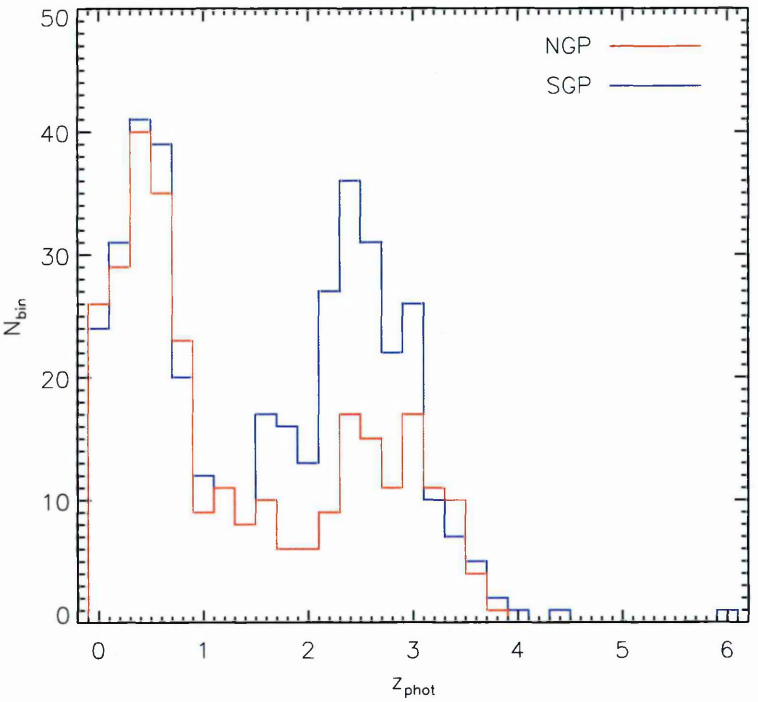

Figure 3.4: Photometric redshift estimates for all H-ATLAS phase 1 sources with $S_{500} > 80$mJy. NGP sources in red, SGP in blue.

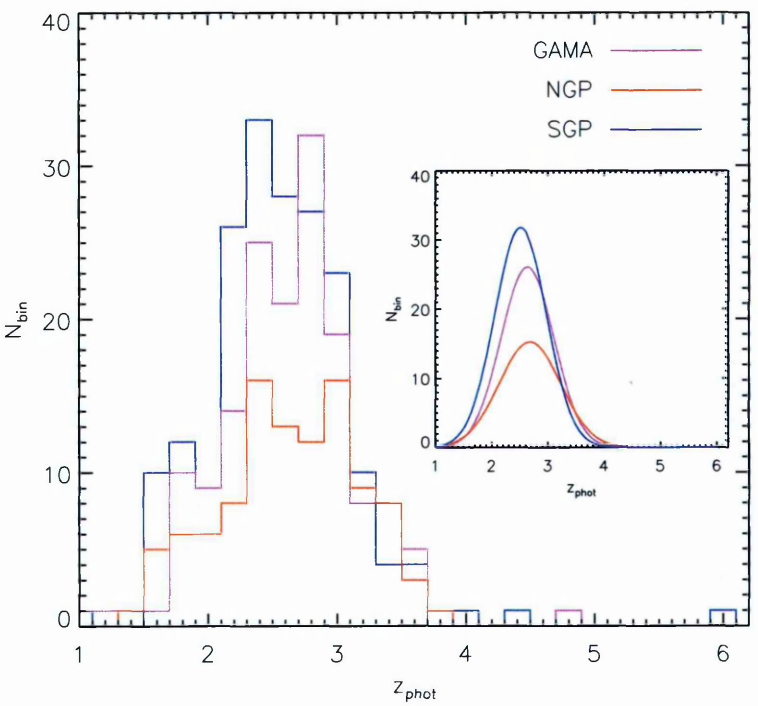

Figure 3.5: Photometric redshift histograms for sources classified as lens candidates. Inlay: best fit gaussian.

		GAMA	NGP	SGP
Data	$\overline{z}$	2.62 ± 0.04	2.64 ± 0.05	2.55 ± 0.04
	σ	0.52	0.54	0.57
Best fit Gaussian	χ^2	7.56	2.98	5.45
	$\overline{z}$	2.64 ± 0.08	2.68 ± 0.11	2.52 ± 0.08
	σ	0.55	0.64	0.54

Table 3.3: Photometric redshift statistics for complete H-ATLAS fields. Statistics calculated from data and best fit gaussian parameters.

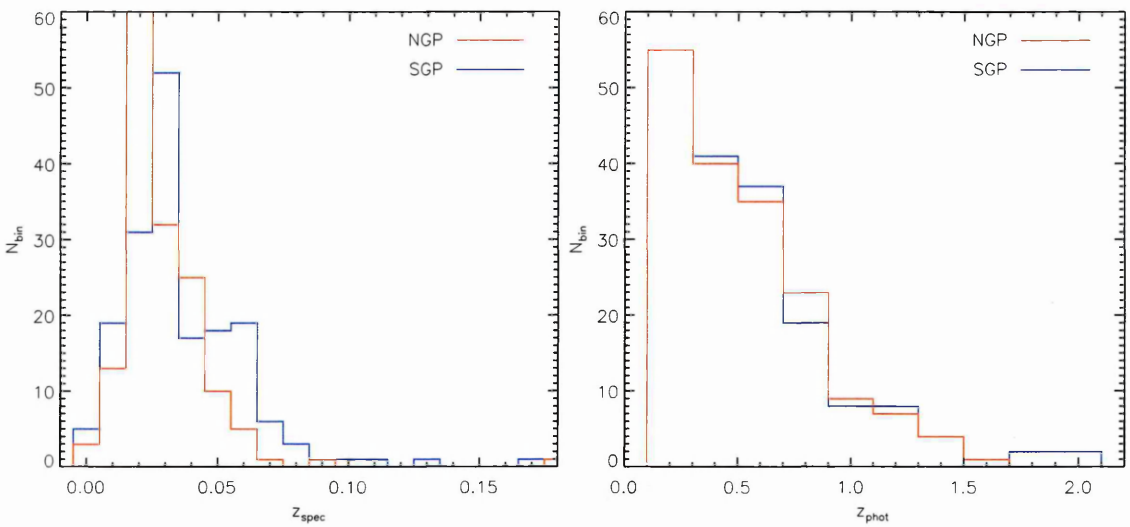

Figure 3.6: Spectroscopic (left) and photometric (right) redshift estimates for locally classified sources. Spectroscopic data obtained from NED and tabulated in A.3 and A.4.

shifts for the local sample. The large discrepancy between the two histograms demonstrates the importance of selecting a suitable template when performing photometric redshift fitting; clearly SMM J2135 does not represent a typical local late-type galaxy.

3.3 Bootstrapped Number Counts

The compilation of number counts follows from the classification of the bright sources. This 'blob counting' is a simple, yet powerful measure of a population distribution which can be compared to model predictions and fed back into such models to improve them.

Source counts (sources per flux bin) for equal, logarithmic bins of 80 – 1000mJy are presented in table 3.4 for the entire H-ATLAS bright sources of $S_{500} > 80$ mJy, included

Flux Bin	Lens candidates			Local sources		
$\log_{10}$[mJy]	GAMA	NGP	SGP	GAMA	NGP	SGP
1.955 ± 0.045	99	59	129	63	68	57
2.045 ± 0.045	25	21	31	37	32	50
2.136 ± 0.045	8	7	10	19	28	17
2.227 ± 0.045	2	1	6	15	13	9
2.318 ± 0.045	5	3	1	7	10	7
2.409 ± 0.045	4	3	0	5	8	14
2.500 ± 0.045	1	2	0	3	2	6
2.591 ± 0.045	0	0	0	3	3	3
2.682 ± 0.045	0	0	0	2	1	1
2.773 ± 0.045	0	0	0	3	2	1
2.864 ± 0.045	0	0	0	1	1	3
2.955 ± 0.045	0	0	0	1	0	1

Table 3.4: Raw source counts for lens candidate and locally classified sources.

are the GAMA field source lists of Negrello et al. (in prep.).

A bootstrap technique, see e.g. Feigelson & Jogesh Babu (2012), was used to estimate the distributions by re-sampling with replacement over a large number of realisations and taking the average distribution. Performed for each sample (two populations and three fields) a realisation (totalling the same number of sources as the original sample) was created by randomly drawing a source flux and the addition of its flux error multiplied by random, normal factor. Following the compilation of a realised sample the source count was calculated and stored, this was repeated 10000 times and the bootstrapped source counts taken as the average counts over the flux bins.

Prior work within the H-ATLAS and HerMES consortia support the assertion that the vast majority of sources with $S_{500} > 100$mJy are indeed lenses (see e.g. Negrello et al. (2010); Wardlow et al. (2013) and references therein). As the flux-limit is decreased the number of sources being selected from the un-lensed population increases (see figure 2.5) by taking sources with $S_{500} > 80$mJy the fainter sources considered in this work are likely to include un-lensed SMGs. To account for the uncertain nature of these fainter sources and reflect this uncertainty in the final lens candidate number counts the bootstrap method was performed for an inclusive sample ($S_{500} > 80$mJy) and an exclusive sample ($S_{500} > 100$mJy). The average of these samples was taken as the final differential and

integral counts which are presented in tables 3.5 and 3.6. Poisson errors were calculated and are quoted for all counts. The two faintest bins for the lens candidates counts, affected by the uncertainty in the nature of faint sources, are also quoted with the upper and lower limits derived from the inclusive and exclusive bootstrap samples (grey text), representing the extreme cases of all or no lensed sources below the $S_{500} > 100$mJy limit.

Integral ($N > S_{bin}$) and differential (dN/dS_{bin}) counts are presented (for GAMA, NGP and SGP fields respectively) in figures 3.7, 3.8 and 3.9 for the lens candidates and figures 3.10, 3.11 and 3.12 for the local sources.

	GAMA		NGP		SGP	
S_{500}	$N(>S_{500})$	dN/dS_{500}	$N(>S_{500})$	dN/dS_{500}	$N(>S_{500})$	dN/dS_{500}
$\log_{10}$[mJy]	[deg^{-2}]	[deg^{-2}]	[deg^{-2}]	[deg^{-2}]	[deg^{-2}]	[deg^{-2}]
1.955 ± 0.045	$0.527^{+0.064}_{-0.057}$	$2.641^{+0.521}_{-0.403}$	$0.370^{+0.053}_{-0.046}$	$1.662^{+0.418}_{-0.308}$	$0.364^{+0.039}_{-0.037}$	$2.006^{+0.338}_{-0.274}$
	$0.527^{+0.318}_{0.289}$	$2.641^{+2.927}_{-2.117}$	$0.370^{+0.215}_{-0.188}$	$1.662^{+1.889}_{-1.527}$	$0.364^{+0.235}_{-0.213}$	$2.006^{+2.260}_{-1.891}$
2.045 ± 0.045	$0.287^{+0.047}_{-0.043}$	$1.714^{+0.408}_{-0.346}$	$0.219^{+0.041}_{-0.037}$	$1.347^{+0.376}_{-0.284}$	$0.182^{+0.032}_{-0.024}$	$1.243^{+0.275}_{-0.216}$
	$0.287^{+0.091}_{0.078}$	$1.711^{+0.930}_{-0.712}$	$0.219^{+0.072}_{-0.058}$	$1.347^{+0.662}_{-0.569}$	$0.182^{+0.055}_{-0.048}$	$1.243^{+0.537}_{-0.471}$
2.136 ± 0.045	$0.131^{+0.034}_{-0.029}$	$0.574^{+0.243}_{-0.216}$	$0.096^{+0.028}_{-0.026}$	$0.449^{+0.248}_{-0.163}$	$0.069^{+0.021}_{-0.015}$	$0.448^{+0.174}_{-0.136}$
2.227 ± 0.045	$0.079^{+0.031}_{-0.020}$	$0.169^{+0.148}_{-0.120}$	$0.056^{+0.022}_{-0.020}$	$0.095^{+0.118}_{-0.084}$	$0.028^{+0.016}_{-0.009}$	$0.234^{+0.153}_{-0.088}$
2.318 ± 0.045	$0.064^{+0.025}_{-0.021}$	$0.404^{+0.251}_{-0.157}$	$0.047^{+0.023}_{-0.016}$	$0.190^{+0.192}_{-0.102}$	$0.007^{+0.010}_{-0.004}$	$0.073^{+0.114}_{-0.044}$
2.409 ± 0.045	$0.027^{+0.017}_{-0.014}$	$0.232^{+0.172}_{-0.139}$	$0.030^{+0.020}_{-0.013}$	$0.212^{+0.170}_{-0.124}$	$0.000^{+0.007}_{-0.000}$	$0.000^{+0.074}_{-0.000}$
2.500 ± 0.045	$0.006^{+0.015}_{-0.005}$	$0.066^{+0.160}_{-0.054}$	$0.010^{+0.017}_{-0.006}$	$0.106^{+0.194}_{-0.060}$	$0.000^{+0.007}_{-0.000}$	$0.000^{+0.074}_{-0.000}$
2.591 ± 0.045	$0.000^{+0.011}_{-0.000}$	$0.000^{+0.126}_{-0.000}$	$0.001^{+0.010}_{-0.001}$	$0.007^{+0.112}_{-0.007}$	$0.000^{+0.007}_{-0.000}$	$0.000^{+0.074}_{-0.000}$

Table 3.5: Integral and differential number counts estimated via the bootstrap method for sources classified as flux-limited gravitational lens candidates. Grey text represents the number with error limits implied from bootstrapping the inclusive and exclusive ($S_{500} < 100$mJy) samples.

	GAMA		NGP		SGP	
S_{500}	$N(>S_{500})$	dN/dS_{500}	$N(>S_{500})$	dN/dS_{500}	$N(>S_{500})$	dN/dS_{500}
$\log_{10}$[mJy]	[deg^{-2}]	[deg^{-2}]	[deg^{-2}]	[deg^{-2}]	[deg^{-2}]	[deg^{-2}]
1.955 ± 0.045	$0.905^{+0.077}_{-0.073}$	$2.717^{+0.520}_{-0.415}$	$0.928^{+0.074}_{-0.074}$	$3.437^{+0.528}_{-0.480}$	$0.604^{+0.048}_{-0.046}$	$1.981^{+0.320}_{-0.287}$
2.045 ± 0.045	$0.658^{+0.064}_{-0.064}$	$2.525^{+0.490}_{-0.411}$	$0.616^{+0.062}_{-0.059}$	$2.287^{+0.427}_{-0.405}$	$0.424^{+0.041}_{-0.038}$	$1.980^{+0.320}_{-0.286}$
2.136 ± 0.045	$0.428^{+0.058}_{-0.051}$	$1.462^{+0.359}_{-0.338}$	$0.408^{+0.053}_{-0.051}$	$1.863^{+0.429}_{-0.334}$	$0.243^{+0.032}_{-0.031}$	$0.783^{+0.202}_{-0.191}$
2.227 ± 0.045	$0.295^{+0.052}_{-0.040}$	$1.052^{+0.312}_{-0.289}$	$0.239^{+0.046}_{-0.035}$	$0.816^{+0.329}_{-0.205}$	$0.172^{+0.029}_{-0.025}$	$0.386^{+0.190}_{-0.108}$
2.318 ± 0.045	$0.200^{+0.041}_{-0.036}$	$0.540^{+0.276}_{-0.183}$	$0.164^{+0.038}_{-0.031}$	$0.624^{+0.299}_{-0.178}$	$0.137^{+0.025}_{-0.024}$	$0.287^{+0.148}_{-0.109}$
2.409 ± 0.045	$0.151^{+0.035}_{-0.032}$	$0.361^{+0.212}_{-0.167}$	$0.108^{+0.029}_{-0.027}$	$0.525^{+0.248}_{-0.186}$	$0.111^{+0.023}_{-0.021}$	$0.504^{+0.164}_{-0.158}$
2.500 ± 0.045	$0.118^{+0.034}_{-0.027}$	$0.206^{+0.199}_{-0.112}$	$0.060^{+0.024}_{-0.020}$	$0.137^{+0.163}_{-0.092}$	$0.065^{+0.020}_{-0.015}$	$0.263^{+0.171}_{-0.085}$
2.591 ± 0.045	$0.099^{+0.032}_{-0.024}$	$0.195^{+0.210}_{-0.101}$	$0.048^{+0.023}_{-0.017}$	$0.200^{+0.183}_{-0.111}$	$0.041^{+0.015}_{-0.013}$	$0.119^{+0.119}_{-0.064}$
2.682 ± 0.045	$0.081^{+0.028}_{-0.023}$	$0.175^{+0.229}_{-0.082}$	$0.029^{+0.020}_{-0.013}$	$0.048^{+0.165}_{-0.037}$	$0.031^{+0.013}_{-0.011}$	$0.053^{+0.080}_{-0.046}$
2.773 ± 0.045	$0.066^{+0.030}_{-0.018}$	$0.166^{+0.151}_{-0.117}$	$0.025^{+0.017}_{-0.013}$	$0.136^{+0.164}_{-0.091}$	$0.026^{+0.014}_{-0.010}$	$0.041^{+0.092}_{-0.034}$
2.864 ± 0.045	$0.050^{+0.024}_{-0.018}$	$0.074^{+0.152}_{-0.062}$	$0.013^{+0.015}_{-0.008}$	$0.074^{+0.139}_{-0.063}$	$0.022^{+0.013}_{-0.009}$	$0.120^{+0.119}_{-0.065}$
2.955 ± 0.045	$0.044^{+0.023}_{-0.016}$	$0.071^{+0.155}_{-0.059}$	$0.006^{+0.014}_{-0.005}$	$0.000^{+0.119}_{-0.000}$	$0.011^{+0.011}_{-0.006}$	$0.041^{+0.092}_{-0.034}$

Table 3.6: Integral and differential number counts estimated via the bootstrap method for sources classified as local contaminant sources.

3.4 Model Comparison

The compilation of lensed number counts allows a comparison to be made between measured data and model predictions. This section extends the work of Lapi et al. (2012) from five lensed sources in 15deg^2 to $>$ 400 lens candidates from the full $\sim$ 600deg^2 of H-ATLAS.

3.4.1 Model Summary

The prediction of the observables (image multiplicity, source magnification or, ultimately, the regime of lensing, strong or weak) for a particular lensing system properties of the source and lens with respect to the observer must be known to satisfy the equations introduced in §1. The extension of these equations from simple, single systems to general populations allows predictions to be made about the effects of lensing for models of sources and lenses.

Lapi et al. (2012) derive predictions of strongly (magnification, $\mu > 2$) lensed sub-mm number counts for three lens mass models: SIS, NFW and a two component SISSA[1] model. The SISSA model comprises of a NFW component for the dark matter halo and a three-dimensional Sersic profile for the stellar component. The three lens mass models are combined with (1) The distribution of sources, in terms of redshift and luminosity, as described by their luminosity function: the number of sources per luminosity interval. (2) The distribution of lenses, in terms of redshift and mass, as described by the halo mass function, the mass distribution of dark matter haloes as a function of redshift. Lapi et al. (2012) use the luminosity functions of Lapi et al. (2011) and adapt the halo mass function of Sheth & Tormen (1999), to consider only the case of single galaxy occupied halos in their calculations of the strong lensing probabilities. (3) Source sizes are the final essential ingredient in the prediction of number counts. The critical surface density, Σ_c, dictates the strong lensing effect; within the projected radius on the source plane where the lens surface density is critical ($\Sigma(r) \geq \Sigma_c$) is where the source experiences strong ($\mu > 2$) magnification. Source magnification is therefore greatest for compact sources

[1]Named after the Italian postgraduate teaching/research school: *Scuola Internazionale Superiore di Studi Avanzati*

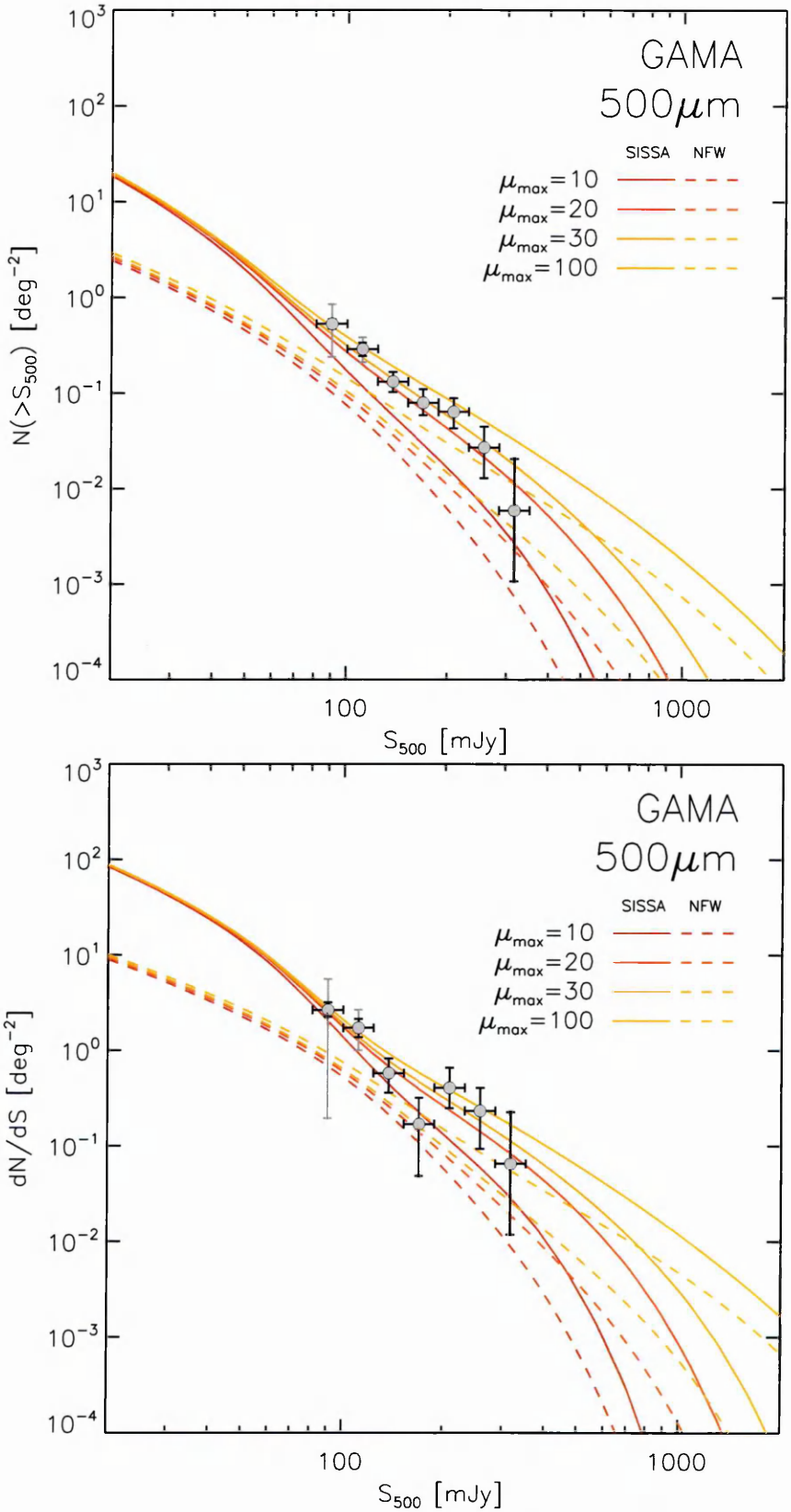

Figure 3.7: Candidate number counts for the GAMA fields. Upper panel: Integral number counts. Lower panel: Differential number counts. The solid lines represent the maximum magnifications of separate population predictions of Cai et al. (2013).

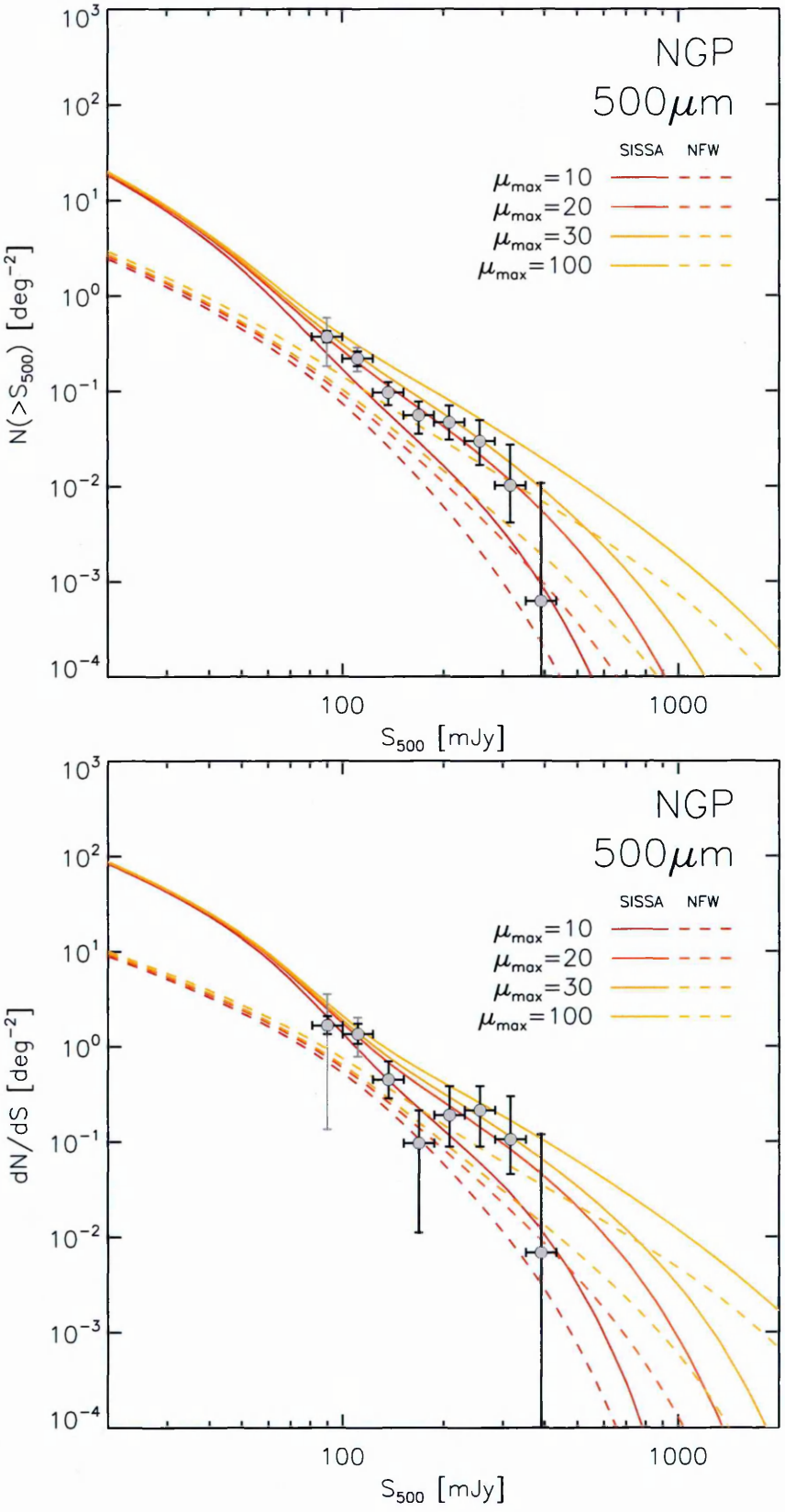

Figure 3.8: Candidate number counts for the NGP field. Upper panel: Integral number counts. Lower panel: Differential number counts. The solid lines represent the maximum magnifications of separate population predictions of Cai et al. (2013).

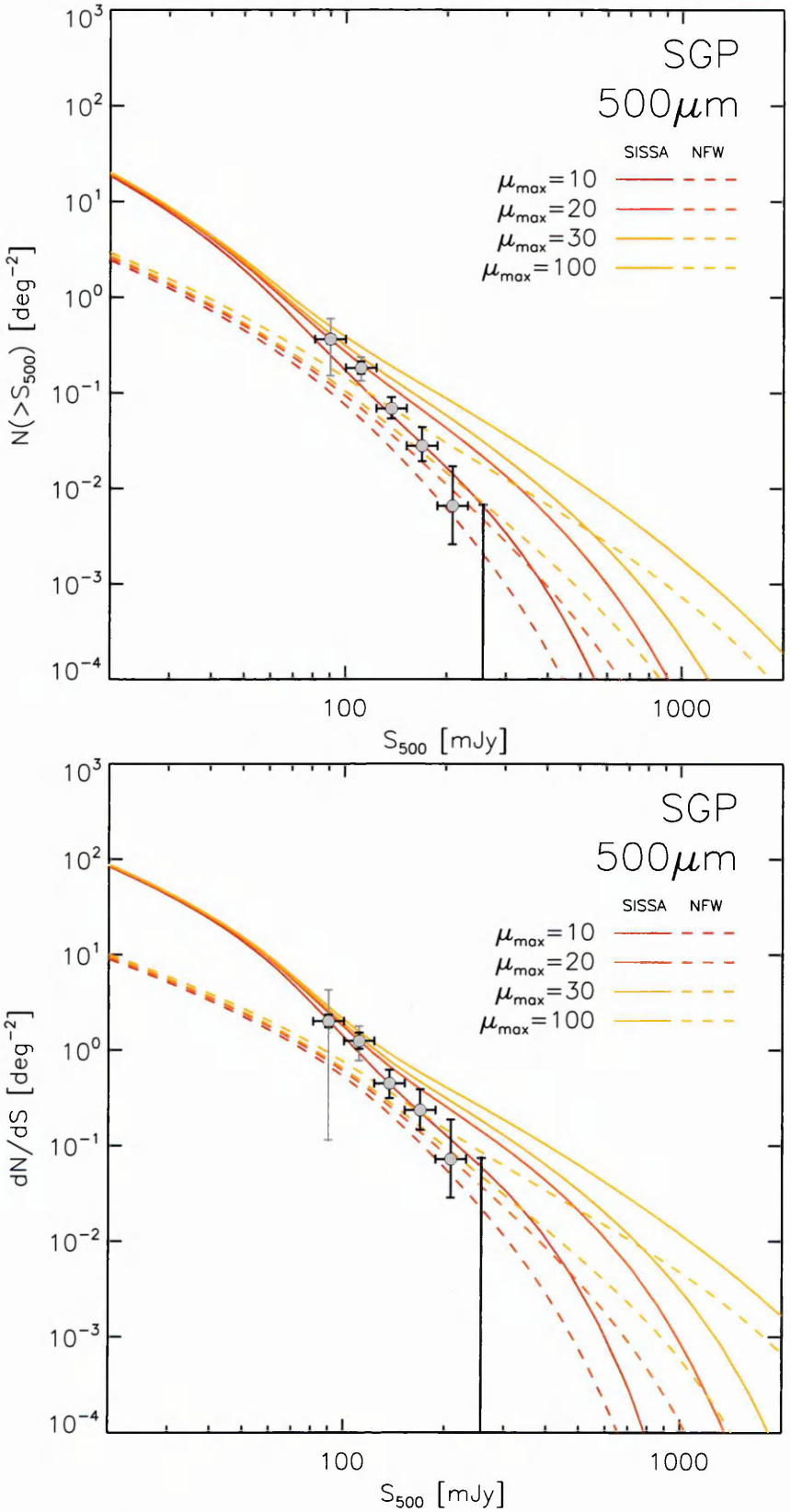

Figure 3.9: Candidate number counts for the SGP field. Upper panel: Integral number counts. Lower panel: Differential number counts. The solid lines represent the maximum magnifications of separate population predictions of Cai et al. (2013).

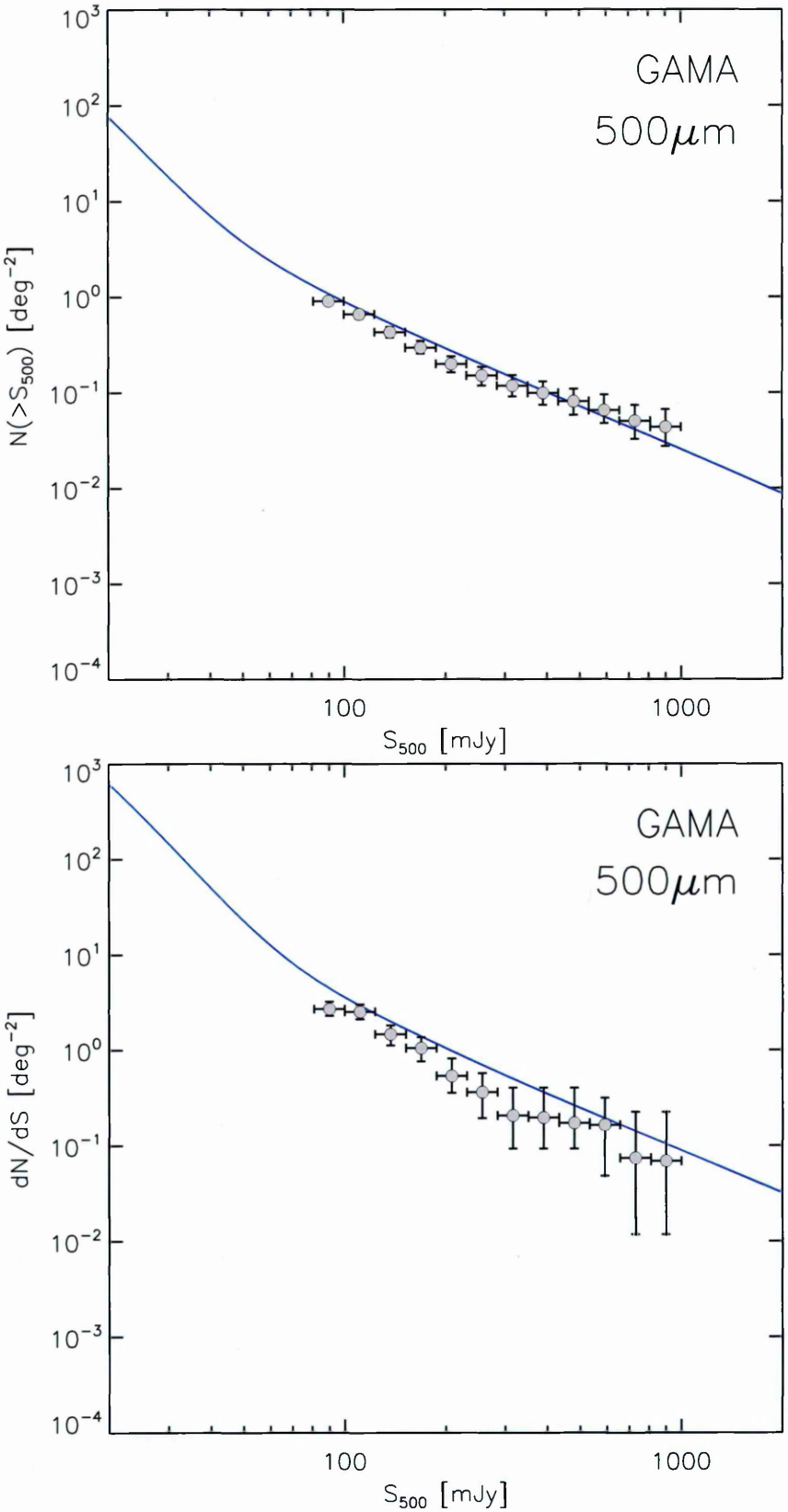

Figure 3.10: Local number counts in the GAMA fields. Upper panel: Integral number counts. Lower panel: Differential number counts. The solid blue line represents the total local population predictions from the models of Cai et al. (2013)

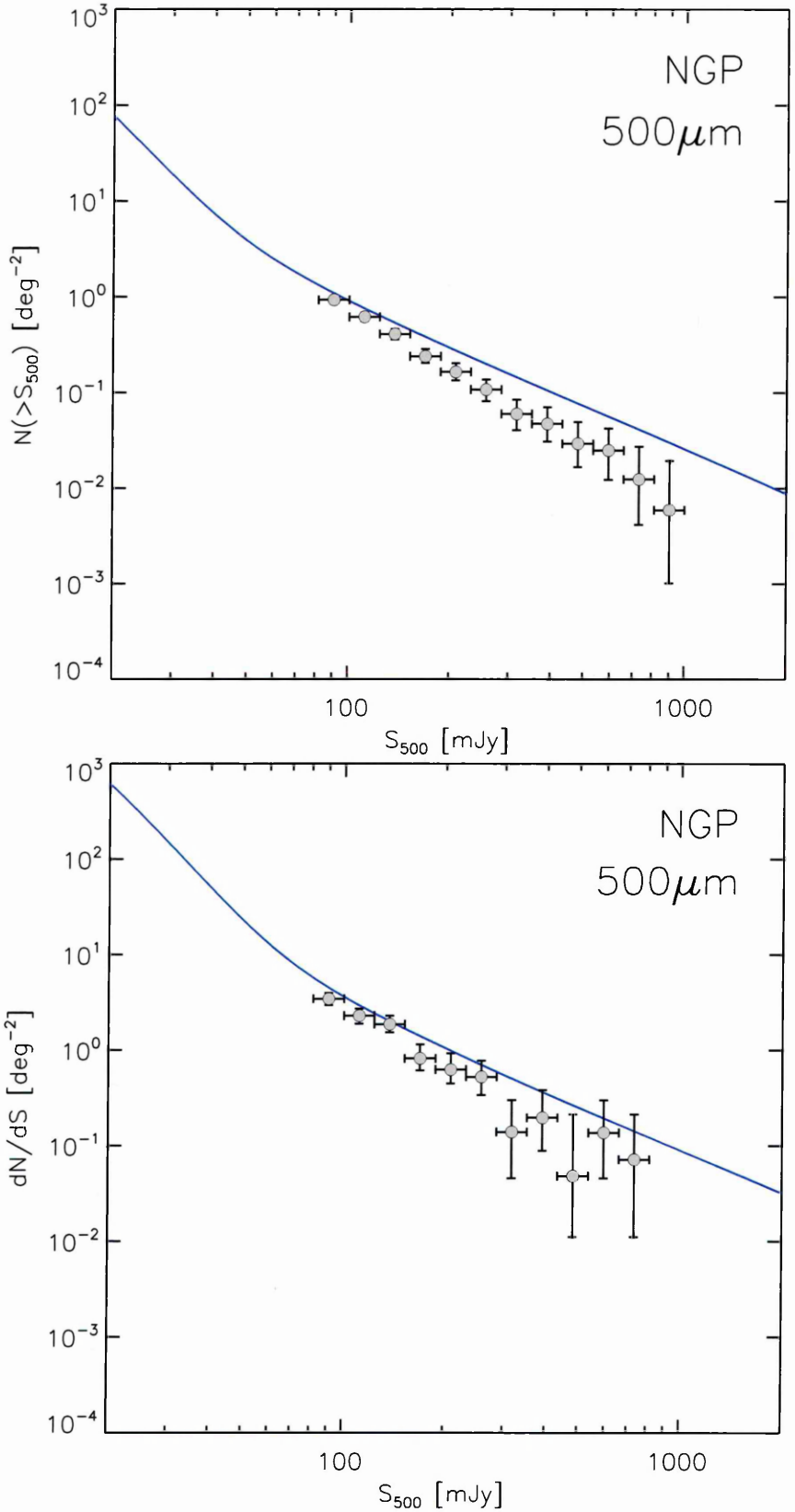

Figure 3.11: Local number counts in the NGP field. Upper panel: Integral number counts. Lower panel: Differential number counts. The solid blue line represents the total local population predictions from the models of Cai et al. (2013)

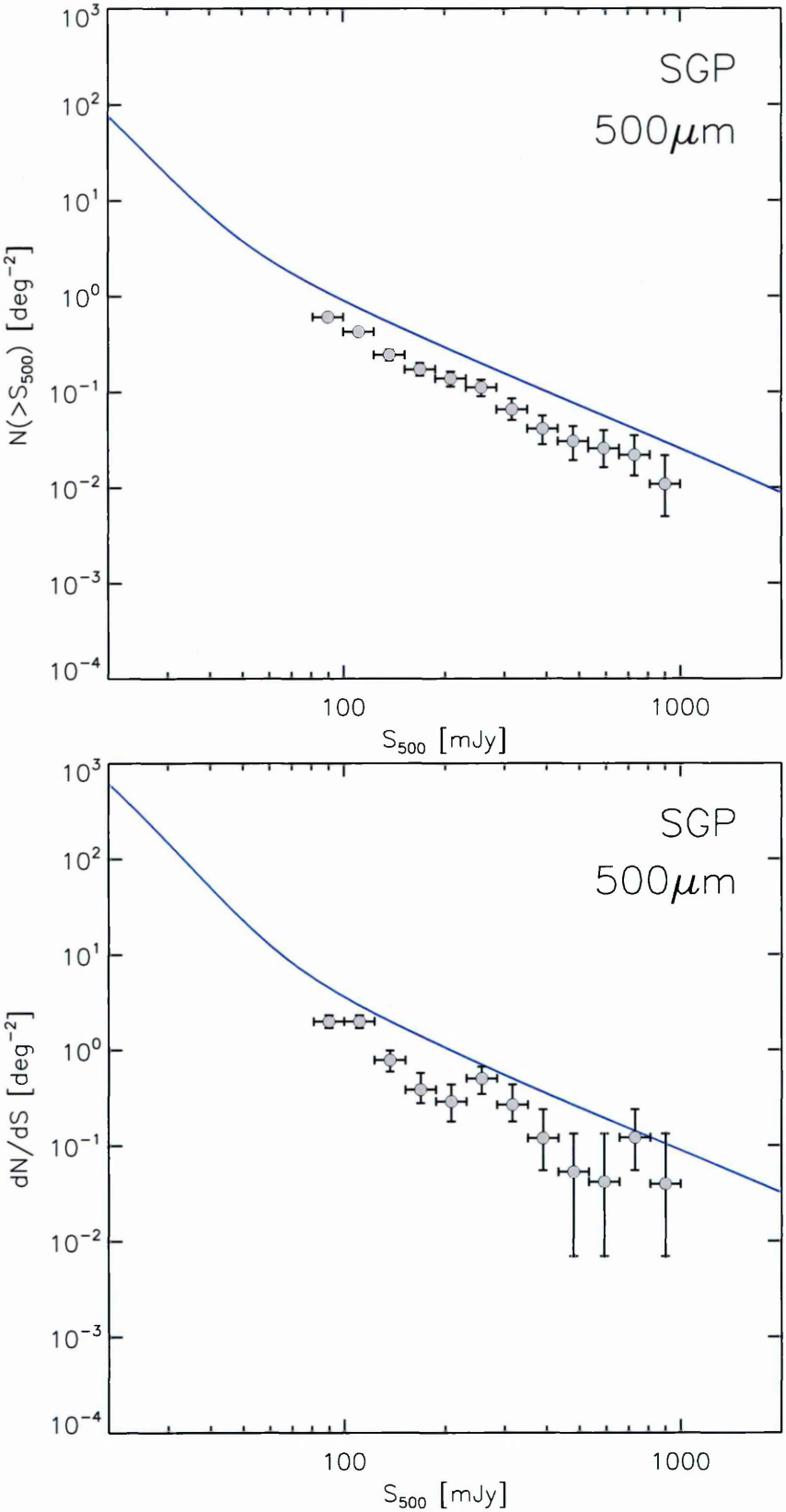

Figure 3.12: Local number counts in the SGP field. Upper panel: Integral number counts. Lower panel: Differential number counts. The solid blue line represents the total local population predictions from the models of Cai et al. (2013)

which lie within this critical region. As source size increases a smaller region of the source is magnified and thus the overall amplification is decreased, a given source size dictates the maximum magnification it can experience for a given lensing model. Lapi et al. (2012) demonstrate that the SISSA and SIS models are in agreement with the H-ATLAS SDP lensed number counts, with a maximum magnification of $\mu_{max} \sim 20 - 30$ for the SISSA lens model, consistent with source sizes of a few kpc.

The most recent SISSA models which are used in comparison to the lens candidate number counts of the full H-ATLAS follow the same calculation as in Lapi et al. (2012) and use the models and corresponding luminosity functions of Cai et al. (2013).

3.4.2 Model Comparison

Figures 3.7, 3.8 and 3.9 for the lens candidates include the predictions for SISSA and NFW models with $\mu_{max} = 10$, 20, 30 and 100. Figures 3.10, 3.11 and 3.12 for the local sources include the predictions of Cai et al. (2013) for local star-forming galaxies.

The SGP number counts are inconsistent with the GAMA and NGP counts (see discussion in §3.5). As a result of this discrepancy the data is compared to the models in five samples: individually, all three in combination and finally the GAMA and NGP fields in combination. Table 3.7 details the reduced χ^2 statistic (3.7) for the five field combinations in comparison to the local and SISSA models.

$$\chi^2_{red} = \frac{\chi^2}{N} \qquad where \qquad N = N_{data} - N_{par} - 1 \tag{3.7}$$

On inspection it is clear that the NFW models cannot reproduce the number counts even at the most extreme case of $\mu_{max} = 100$, for the SGP, where the distinction between data and models is less apparent, the approximate gradient implied by the data favours the SISSA model, as such no statistical comparison for the NFW models is performed.

Taking the best fit model as that with χ^2_{red} closest to unity, representative of a model fit within the errors of the data, the statistics support $\mu_{max} = 30$ for the GAMA and NGP fields (individually and combined), $\mu_{max} = 10$ for the SGP and $\mu_{max} = 20$ for all combined fields. Local number counts are compared to a single model, for which the GAMA data is in best agreement with the model. This work supports the findings of Lapi

Model	GAMA	NGP	SGP	GAMA & NGP	All
$\mu_{max} = 10$	8.895	3.040	3.673	11.737	13.617
$\mu_{max} = 20$	2.386	0.247	7.601	1.841	2.643
$\mu_{max} = 30$	1.091	1.102	17.635	1.365	8.698
$\mu_{max} = 100$	2.228	6.663	50.850	9.062	43.222
local	1.836	6.993	36.229	7.171	35.442

Table 3.7: Reduced χ^2 statistic for integral number counts by H-ATLAS fields and combinations compared to the models of Cai et al. (2013).

et al. (2012) that find a broad agreement of the H-ATLAS data to the SISSA models of $\mu_{max} \sim 20 - 30$.

3.5 Summary and Conclusions

This chapter presents the first classifications of all brights sources ($S_{500} > 80$mJy) from the internally released 'phase 1' catalogs for the H-ATLAS NGP and SGP. The classifications of brights sources was performed using publicly available, shallow, optical and radio survey data.

Photometric redshift estimates are calculated for a sample of confirmed lens candidates with robust CO-based spectroscopic redshifts for three starburst/ULIRG templates. The template for SMM J2135 results in the smallest dispersion between photometric and spectroscopic redshifts and is subsequently used to estimate photometric redshifts for the entire bright samples of the NGP and SGP as classified in this work. The GAMA bright source sample lists of Negrello et al. (in prep.) are included to provide the first photometric redshift analysis of the entire H-ATLAS lens candidate sample. The mean redshift of the lens candidate samples for each field lie within the combined standard errors at $z \sim 2.6$. Postage stamps and data tables for the bright source populations are presented in appendix A.

The NGP and SGP bright source samples of this work are combined with the GAMA bright source sample lists of Negrello et al. (in prep.) to calculate the first discrete number counts of the entire H-ATLAS area. The discrete counts are re-sampled using a bootstrap method and the resulting integral and differential counts of both the lens candidate and

local sources are presented and compared to the models of Lapi et al. (2012) and Cai et al. (2013). Calculation of the reduced-χ^2 for all H-ATLAS lens candidates support the original findings of Lapi et al. (2012) that a purely NFW lens mass model is unsuitable and that the two-component SISSA model reproduce the data with $\mu_{max} \sim 20-30$. These maximum magnification estimates correspond to source sizes of a few kpc corroborated by high resolution source reconstructions performed for, e.g. SMM J2135, Swinbank et al. (2010), the H-ATLAS/HerMES lens sample of Bussmann et al. (2013) and the ALMA reconstructed imaging of H-ATLAS SDP.81 by Rybak et al. (2015).

The number counts of local galaxies are compared to a single model population of the local warm and cold star-forming galaxies of Cai et al. (2013). Where the GAMA number counts are in good agreement with this model the NGP and SGP counts are both too low, a result of the acknowledged flux underestimates of extended sources in the 'phase 1' catalogs.

Comparison of the lens candidate number counts clearly demonstrates that the SGP counts are distinctly lower than the those of the GAMA and NGP fields. This discrepancy is all the more surprising as both the NGP and SGP catalogs were compiled following the same method, Valiante et al. (in prep.). Initial concerns that the SGP catalog had been subject to an incorrect flux calibration have been overshadowed with the intriguing possibility that the lower counts in the SGP are real. The lower SGP number counts, if real, are indicative of a lower density of lensed sources over a vast area, $> 200\text{deg}^2$ in contrast to the other regions of H-ATLAS.

Future Work

The primary motivation for the bright source classifications is to compile the largest lens candidate sample list from a single survey. Such a list will form the basis for large, multi-semester, observing proposals to first validate and then investigate the largest sample of gravitational lens candidates selected from a single survey. Future catalog releases for the NGP and SGP will likely improve on the source extraction and flux calibrations methods used in the 'phase 1' catalogs. As a result it will be necessary to cross-match the bright source samples against future catalog releases to ensure the data is up-to-date.

Photometric redshift estimates will benefit from additional observations; longer wave-

length data for the sample would improve the accuracy of the estimates and CO-based spectroscopic observations, which confirm redshifts for individual sources, would be used to improve the template selection. Improvements to the flux estimates of the samples from future H-ATLAS catalogs would necessitate re-estimating the photometric redshifts with such data.

Both the GAMA and NGP number counts have a slightly raised count of sources at $S_{500} \sim 200$mJy in comparison to the SISSA models. Where the SISSA models have been restricted to single galaxy occupancy in their halos high resolution data HST observations (§5) show that a number of lens candidates are lensed by foreground groups. The slight discrepancy of the SISSA model may be better matched to this data if extended to include halo multiple-occupancy/lensing by multiple sources.

Future catalog releases and the cross-matching of the lens candidate sample will address the interesting discrepancy of the apparently low SGP lens candidate number counts. Future observations with a variety of facilities, both on individual and larger scales, will be invaluable for validating and investigating the full H-ATLAS lens candidate sample first presented here.

Chapter 4

Constraints on Lens Redshifts

An extension to the flux-limited selection method of lens candidates is the Herschel-ATLAS Lensed Object Selection (HALOS) method, González-Nuevo et al. (2012). The inclusion of source redshifts and optical/NIR counterparts in the selection method predicts an identification of $\sim$ 1000 lens candidates over the full H-ATLAS area. The work undertaken in this chapter is the proposal, execution and investigation of the pilot study of spectroscopic observations, targeting the foreground lens, with the objective of proving the HALOS method and the first steps towards a H-ATLAS $\sim$ 1000 lens survey.

The chapter is presented as follows: Section 4.1 presents an overview of the HALOS method of González-Nuevo et al. (2012). Section 4.2 describes the pilot study observations performed at the European Southern Observatory (ESO) as two separate proposals: 091.A-0674 (PI: Serjeant) and 093.A-0320 (PI: Amber). Section 4.3 describes the data reduction performed in this work and presents the reduced spectra. Section 4.4 describes the redshift estimation performed using a minimum-χ^2 grid-based template fitting (using the published SED models of Tremonti (2003) and Bruzual & Charlot (2003)). Section 4.5 presents an overview of the statistical models of Eales (2015) and describes the reduced-χ^2 comparison to the redshift estimates of this work. Section 4.6 concludes with a summary of the chapter; the conclusions and future work.

4.1 Extending the Lens Selection

The flux-limited selection of strongly lensed SMGs is possible due to the distinct number counts of lensed and un-lensed sources at the brightest fluxes, this proven method is providing samples of hundreds of lens candidates (Negrello et al., 2010; Wardlow et al., 2013; Vieira et al., 2013). By including additional source and lens information González-Nuevo et al. (2012) propose the HALOS method which aims to select lens candidates below the distinct flux-limit. By probing below the bright flux limit a HALOS sample of fainter lensed SMGs will be more representative of the typical SMG population and is predicted to yield $\sim 10\times$ more strong ($\mu > 2$) lenses.

Both the flux-limited and the HALOS selection methods rely on the magnification of lensing resulting in a distinction between the lensed and un-lensed populations. Where the flux-limited method relies on the bright end of number counts the HALOS method relies on the magnification effect that manifests at the bright end of the sub-mm luminosity function. The need to estimate the source luminosity, necessarily, requires more information beyond a single sub-mm photometric data point, ideally the source redshifts and multiple photometric points to construct a spectral energy distribution. Using data from the H-ATLAS SDP González-Nuevo et al. (2012) show that a critera of SPIRE colors can be a good estimate of photometric redshift (see also the template based estimates of §3.2). Based solely on SPIRE photometry the HALOS sample from the SDP results in a density of $1.5 - 2\text{deg}^2$ at $\sim 50\%$ efficiency. This moderate efficiency is due to the selection including intrinsically luminous sources. However by including the NIR counterpart analysis of Fleuren et al. (2012), using the VIKING survey data, this efficiency is demonstrated in the SDP to be $\sim 72\%$ at the lower density of ~ 1.5 deg^2, which for the complete H-ATLAS corresponds to ~ 1000 lens candidates.

An early justification for the validity of the HALOS method was the inclusion of the five flux-limited lensed sources of Negrello et al. (2010) in the SDP sample of 31 sources. However follow-up observations are required to investigate the nature of the remaining HALOS candidates to determine the efficiency of this extended lens selection method.

4.2 The NTT Pilot Study

Prior to the completion of the final catalogs of H-ATLAS, and the compilation of the $\sim$ 1000 lens candidates, a pilot study to obtain lens redshifts was proposed for the then-observed fields, primarily, to confirm the efficiency of the HALOS method before embarking on ambitious multi-cycle observations programs.

The the second ESO Faint Object Spectrograph and Camera, EFOSC2 Buzzoni et al. (1984), on the New Technology Telescope (NTT) at the European Southern Observatory (ESO), La Silla, was well suited to the requirements of the pilot study. The active optics of the 3.58m NTT, while not correcting for atmospheric turbulence instead correcting any deformation of the telescope optics, provides an observational platform limited only by atmospheric seeing. In operation for over 20 years, albeit with various improvements over this time, the simple design of EFOSC2 offers exceptional efficiency for low resolution spectroscopy.

Two proposals in cycles 91 and 93 were successful in obtaining observing time on NTT/EFOSC2 with the aim of obtaining 100 absorption line redshifts for the brighter ($I_{AB} < 20$) HALOS lens candidates.

4.2.1 Science Objectives

The initial objective of the pilot study was to assess the feasibility of obtaining absorption line redshifts for the optical/NIR counterparts of lens candidates on a 4m class telescope. The science objectives that the proposed sample of 100 lenses would achieve are: (1) Assess the 72% proposed success rate of the HALOS method by, (2) obtaining spectroscopic redshifts for the lens candidate incompatible with the SMG source redshift thus confirming those candidates as genuine lensing systems and guiding future observing proposals. (3) distinguish between models (NFW/SIS) for the lensing mass distributions. (4) use the redshifts of the lenses (pilot study) and corresponding source redshifts (requiring future observations for spectroscopic estimates) to independently constrain Ω_Λ to an accuracy of ± 0.01. (5) Compare the lens redshift distribution to model predictions based solely on the source redshifts.

4.2.2 Target Selection

Target selection was performed independently for the two periods of observation. Low dispersion spectroscopy using grisms #1 and #2, covering wavelength ranges 3185 – 10940Å and 5100 – 11000Å respectively, was proposed. Requiring a SNR of > 10 for absorption-line identification the EFOSC2 exposure time calculator was used to estimate the necessary exposure time. The calculators early-type galaxy SED normalized to $I_{AB} = 20$ at a redshift $z = 1$ required $\sim$ 1000s exposures to achieve the desired signal to noise. Budgetting for acquisition overheads an assumption of three targets per hour was proposed, the actual hit rate of sources over the two observing runs was under two per hour. Targets from both observing runs are listed in table 4.1.

Cycle 91

Observations in cycle 91 were proposed for optimum observations of GAMA targets, however the allocated time resulted in a later period of observations. The GAMA9 field was visible for only a few hours and during the final hour of the night only observations of the SGP were feasible. Targets were selected from the then-current GAMA catalogs and the preliminary SA region (RA$\sim$ 22hr) from the partially completed SGP field. HALOS source lists for the GAMA fields were circulated (González-Nuevo and Ivison priv. comm.) within the consortium following the criteria of González-Nuevo et al. (2012) and using the optical SDSS counterparts as matched by the likelihood ratio method of Smith et al. (2011). Requiring a photometric redshift for the sub-mm source > 1.5 and a probable lens counterpart within 3.5" these HALOS samples were restricted to the brighter ($I_{AB} <$ 20) lens candidates which lacked SDSS spectroscopic redshifts. Targets of reliable lens counterparts for flux-limited sources were also compiled with the same counterpart and brightness criteria to provide ample target lists while on site.

Without a complete optical survey nor a likelihood analysis of optical counterparts a preliminary target selection was made for HALOS in the SGP and combined with the flux-limited sample (Negrello, priv. comm.). Beginning with photometric redshift estimates of the sub-mm sources (as per §3.2) those with $z_{phot} > 1.5$ were then cross matched to the available VIKING DR3 survey data. A linear interpolation from the VIKING bands to

the optical provided an estimate of the i-band brightness and allowed a final selection of SGP targets with the counterpart proximity and brightness criteria. GAMA targets were prioritised by visibility and brightness and flux-limited targets were given priority in the SGP.

Cycle 93

Cycle 93 observations were proposed for the same optimal coverage of the GAMA fields, however allocated time was one month later rendering observations of the GAMA9 field inappropriate (declination $< 30°$ at the start of the night) and necessarily required more targets from the SGP. The same target lists from cycle 91 for the GAMA12 and GAMA15 fields were used, removing sources with reasonable redshift estimates. The phase 1 SGP catalog was used to produce both flux-limited and HALOS candidates, requiring $z_{phot} > 1.5$ and subject to the same counterpart proximity and brightness criteria of cycle 91 target selection. Additional (unpublished) VIKING data was provided at the location of ~ 30 targets, A. Edge (priv. comm.), to produce the SGP target list. The same target priority was followed as in cycle 91.

Table 4.1: Summary of targets observed during cycles 91 and 93.

		SPIRE Source					Optical Counterpart					
IAU ID	Alt. ID	S_{250} [mJy]	S_{350} [mJy]	S_{500} [mJy]	z_{phot}	Sep. ["]	Identifier[2]	RA [deg]	Dec [deg]	Mag.	z_{phot}	Cycle
J083434+011601	G09.v10.1475	87.1 ± 7.0	83.5 ± 8.2	41.0 ± 8.9	1.81 ± 0.58	0.3	587727943487718153	128.6430	1.26708	19.84	0.33 ± 0.09	91
J084117+020637	G09.v10.1558	84.6 ± 7.0	89.4 ± 8.2	50.1 ± 9.1	2.08 ± 0.64	2.9	587727944562246191	130.3189	2.11070	19.97	–	91
J084347+003332	G09.v10.892	91.3 ± 6.4	80.2 ± 7.7	48.4 ± 8.5	1.81 ± 0.58	1.7	587725075525337770	130.9473	0.55859	20.24	0.47 ± 0.09	91
J090022+001937	G09.v10.2303	66.7 ± 6.2	67.9 ± 7.4	44.4 ± 8.1	2.14 ± 0.65	2.3	588848900429906486	135.0920	0.32635	19.37	0.43 ± 0.11	91
J090139-010855	G09.v10.1183	91.3 ± 6.8	90.0 ± 8.1	51.8 ± 9.0	1.99 ± 0.62	2.1	588010931370394169	135.4113	−1.14840	19.68	0.22 ± 0.05	91
J091350+014543	G09.v10.1251	89.3 ± 7.0	90.8 ± 8.2	52.4 ± 9.1	2.05 ± 0.63	1.4	587726032767222397	138.4588	1.76221	19.56	0.29 ± 0.06	91
J091735+001203	G09.v10.1729	81.5 ± 6.9	82.5 ± 8.1	37.0 ± 8.9	1.87 ± 0.60	0.7	587725074992136947	139.3963	0.20098	19.89	0.29 ± 0.10	91
J092144+003909	G09.v10.825	102.3 ± 6.9	82.4 ± 8.2	39.0 ± 9.1	1.51 ± 0.52	2.0	588848900969071213	140.4338	0.65297	19.16	0.42 ± 0.04	91
J092409-005018[1]	G09.v10.1667	77.3 ± 6.9	104.3 ± 8.2	97.0 ± 8.9	3.01 ± 0.83	1.0	587725073919116045	141.0373	−0.83825	19.51	0.17 ± 0.03	91
J113855+001534	G12.v10.13040	45.5 ± 6.9	89.1 ± 8.1	77.6 ± 8.9	3.42 ± 0.92	1.5	1237648721765270259	174.7291	0.25918	20.20	0.58 ± 0.05	91
J114153-014342	G12.v10.3600	64.3 ± 6.8	70.4 ± 8.1	36.4 ± 8.8	2.08 ± 0.64	1.0	587724650328817904	175.4698	−1.72830	19.64	0.07 ± 0.03	91
J114231+003344	G12.v10.1387	82.8 ± 6.4	69.7 ± 7.7	36.7 ± 8.4	1.63 ± 0.55	1.6	1237674651000504601	175.6271	0.56190	19.35	0.34 ± 0.05	93
J114608+002646	G12.v10.3501	59.4 ± 6.1	65.6 ± 7.4	31.3 ± 8.1	2.05 ± 0.63	2.8	1237671128589074865	176.5353	0.44532	19.65	0.54 ± 0.11	91
J115112-012639[1]	G12.v10.305	153.4 ± 6.8	164.8 ± 8.1	114.6 ± 9.0	2.29 ± 0.68	1.2	587725041701552522	177.8011	−1.44380	19.56	0.34 ± 0.10	91
J120203-004333	G12.v10.1557	88.6 ± 7.0	74.6 ± 8.0	44.0 ± 8.8	1.72 ± 0.57	1.0	1237674649392054860	180.5140	−0.72553	19.09	0.34 ± 0.02	93
J120422-012737	G12.v10.530	124.3 ± 6.8	106.9 ± 8.0	60.1 ± 8.9	1.72 ± 0.57	1.8	587725041702994117	181.0914	−1.46002	19.76	0.23 ± 0.07	91
J120553-015117	G12.v10.3906	61.7 ± 6.9	80.7 ± 8.3	53.8 ± 9.0	2.56 ± 0.74	0.8	1237650371556344244	181.4724	−1.85502	19.74	0.31 ± 0.07	91
J120700-011303	G12.v10.4505	61.9 ± 7.0	65.3 ± 8.2	60.9 ± 9.0	2.59 ± 0.75	0.5	1237674648855708266	181.7510	−1.21758	19.69	0.27 ± 0.05	91
J120729+001557	G12.v10.1649	84.0 ± 6.8	79.3 ± 8.1	58.4 ± 9.0	2.11 ± 0.65	3.2	1237648721768415477	181.8688	0.26657	18.61	0.20 ± 0.02	93
J121335-020323	G12.v10.116	209.5 ± 6.1	204.6 ± 7.5	132.4 ± 8.1	2.05 ± 0.63	0.4	587725041167106237	183.3956	−2.05637	18.20	0.21 ± 0.03	91
J121409-004011	G12.v10.6803	48.5 ± 6.1	72.8 ± 7.4	48.7 ± 8.1	2.77 ± 0.78	2.1	1237648703503401501	183.5387	−0.66917	19.46	0.25 ± 0.03	91
J121417+003305	G12.v10.846	103.7 ± 7.0	100.0 ± 8.1	52.3 ± 9.0	1.87 ± 0.60	1.9	1237648705114013957	183.5722	0.55150	19.97	0.22 ± 0.07	91
J121542+011739	G12.v10.2011	76.3 ± 6.9	68.7 ± 8.1	35.6 ± 8.7	1.75 ± 0.57	2.8	1237651752401437019	183.9270	1.29481	19.71	0.34 ± 0.03	91
J121906-000952	G12.v10.2665	71.8 ± 6.9	76.4 ± 8.0	59.2 ± 9.2	2.38 ± 0.70	1.4	1237648721232855418	184.7773	−0.16450	19.38	0.36 ± 0.07	91
J140828+014209[1]	G15.v10.432	147.4 ± 7.0	128.0 ± 8.0	82.1 ± 8.8	1.84 ± 0.59	2.3	1237651735771021646	212.1169	1.70276	20.33	–	91
J140946+004608	G15.v10.1239	88.7 ± 6.8	75.6 ± 8.0	36.2 ± 9.0	1.60 ± 0.54	3.3	1237648722318655747	212.4413	0.76965	18.20	0.29 ± 0.05	93
J141025-004041	G15.v10.16879	36.8 ± 6.8	62.4 ± 8.3	41.5 ± 8.9	2.92 ± 0.81	1.3	1237648703516115704	212.6023	−0.67826	19.63	0.38 ± 0.08	91
J141150-005633	G15.v10.730	114.5 ± 6.8	100.3 ± 8.1	58.7 ± 9.1	1.78 ± 0.58	2.5	1237648720171434555	212.9572	−0.94302	19.51	0.09 ± 0.02	91
J141350+023956	G15.v10.2042	82.2 ± 6.8	65.9 ± 7.9	41.1 ± 8.7	1.66 ± 0.55	1.5	1237651754561831513	213.4581	2.66560	20.02	0.31 ± 0.04	91
J141915-012352	G15.v10.1648	84.9 ± 6.9	74.5 ± 8.1	59.2 ± 9.1	2.05 ± 0.63	3.4	1237655499743101331	214.8115	−1.39868	19.21	0.35 ± 0.07	93
J142004+014045[1]	G15.v10.592	124.6 ± 6.9	125.2 ± 8.0	87.4 ± 9.0	2.17 ± 0.66	1.2	587726014547361899	215.0160	1.67886	19.67	–	91
J142034+000238	G15.v10.3509	60.0 ± 6.3	68.5 ± 7.6	51.1 ± 8.3	2.47 ± 0.72	2.1	1237648704590971367	215.1434	0.04318	18.09	0.06 ± 0.02	93
J142301-003817	G15.v10.1103	97.4 ± 6.8	84.4 ± 8.0	45.4 ± 8.8	1.72 ± 0.57	1.2	1237648703517491256	215.7545	−0.63787	18.81	0.59 ± 0.04	91
J142605-011110	G15.v10.4002	67.6 ± 7.0	64.4 ± 8.0	41.2 ± 8.9	2.02 ± 0.63	2.6	1237655693548389050	216.5214	−1.18688	18.89	0.40 ± 0.07	91
J142849+004942	G15.v10.3466	60.8 ± 6.1	61.5 ± 7.4	36.3 ± 8.1	2.05 ± 0.63	1.8	1237648722320752937	217.2051	0.82785	19.78	–	91
J143339+001121	G15.v10.2663	74.1 ± 6.8	74.8 ± 8.0	38.6 ± 8.7	1.93 ± 0.61	1.4	1237648704592413448	218.4113	0.18897	19.40	0.23 ± 0.04	91

[1] Flux-limited target.

[2] Identifiers correspond to SDSS DR7 (18 digit), SDSS DR8 (19 digit), VIKING DR3 (12 digit).

Continued on next page...

4.1 – Continued

SPIRE Source							Optical Counterpart					
IAU ID	Alt. ID	S_{250} [mJy]	S_{350} [mJy]	S_{500} [mJy]	z_{phot}	Sep. ["]	Identifier[2]	RA [deg]	Dec [deg]	Mag.	z_{phot}	Cycle
J143354-010112	G15.v10.2405	73.7 ± 6.7	66.4 ± 8.0	44.6 ± 8.9	1.93 ± 0.61	3.3	1237648720173858958	218.4760	−1.02037	18.75	0.18 ± 0.03	93
J143355+003256	G15.v10.1138	97.6 ± 6.9	82.1 ± 8.0	48.8 ± 8.9	1.72 ± 0.57	3.1	1237648705129284662	218.4812	0.54940	18.92	0.28 ± 0.08	93
J143458+005012	G15.v10.4365	63.3 ± 6.8	60.5 ± 8.0	45.4 ± 8.8	2.17 ± 0.66	0.6	1237648722321408860	218.7406	0.83660	19.70	0.34 ± 0.09	91
J143520+012231	G15.v10.2984	69.9 ± 6.8	67.1 ± 8.0	48.9 ± 8.7	2.14 ± 0.65	2.7	1237651752953577975	218.8325	1.37550	19.01	0.36 ± 0.07	93
J144046+000433	G15.v10.2150	69.7 ± 6.2	82.6 ± 7.5	51.2 ± 8.2	2.35 ± 0.70	1.9	1237648704593199772	220.1909	0.07639	19.52	0.12 ± 0.03	91
J144502+004131[1]	G15.v10.606	119.3 ± 6.7	108.5 ± 8.0	85.6 ± 9.1	2.11 ± 0.65	2.1	1237648722322522932	221.2569	0.69255	20.02	0.41 ± 0.09	91
J144539-013649	G15.v10.5549	59.6 ± 6.9	61.0 ± 8.1	38.3 ± 8.9	2.11 ± 0.65	2.2	1237655499209113630	221.4122	−1.61405	19.87	0.36 ± 0.06	91
J144627+004506	G15.v10.7663	52.2 ± 6.8	81.2 ± 8.1	59.6 ± 8.9	2.92 ± 0.81	1.2	1237648722322718891	221.6148	0.75157	18.65	0.27 ± 0.03	93
J144646+013211	G15.v10.1257	93.9 ± 6.8	74.5 ± 8.1	49.2 ± 9.0	1.69 ± 0.56	0.8	1237651735775216255	221.6920	1.53604	19.44	0.43 ± 0.09	91
J144832+022523	G15.v10.2350	73.5 ± 6.8	65.4 ± 8.0	36.8 ± 8.9	1.78 ± 0.58	1.2	1237651754565632205	222.1317	2.42278	18.35	0.18 ± 0.02	93
J222536-295646[1]	SA.v1.53	194.0 ± 8.1	199.5 ± 9.6	119.1 ± 11.0	2.08 ± 0.64	5.3	J222536.67-295649.9[5]	336.4028	−29.94719	19.30[3]	–	91
J223225-284715[1]	SA.v1.151	134.5 ± 8.3	172.3 ± 9.3	148.9 ± 10.0	2.83 ± 0.80	3.6	J223225.46-284717.3[5]	338.1061	−28.78814	17.80[3]	–	91
J223317-292256	SGP.p1.51962	65.7 ± 7.7	72.4 ± 7.9	57.6 ± 9.8	2.47 ± 0.72	1.8	601310166344	338.3222	−29.38270	17.74[34]	–	93
J223829-304149[1]	SA.v1.44	259.7 ± 5.0	210.7 ± 6.1	103.7 ± 7.3	1.54 ± 0.53	4.4	–	339.6198	−30.69700	< 20.8[36]	–	91
J223833-343813	SGP.p1.5369	101.6 ± 5.8	73.4 ± 6.7	51.6 ± 7.8	1.54 ± 0.53	2.2	601325730315	339.6378	−34.63764	17.33[34]	–	93
J225014-325634	SGP.p1.8989	85.5 ± 5.8	69.6 ± 6.9	46.0 ± 7.8	1.72 ± 0.57	3.2	601323109754	342.5589	−32.94249	17.97[34]	–	93
J225018-302300	SGP.p1.4838	114.1 ± 6.3	118.8 ± 6.7	70.9 ± 8.0	2.11 ± 0.65	1.4	601312797505	342.5734	−30.38334	18.27[34]	–	93
J225615-305243	SGP.p1.21715	62.4 ± 5.6	62.3 ± 6.5	41.0 ± 7.9	2.11 ± 0.65	2.8	601311820260	344.0624	−30.87787	17.48[34]	–	93
J000226-302748	SGP.p1.16403	66.1 ± 5.4	69.8 ± 6.5	35.1 ± 7.6	2.02 ± 0.63	3.0	601313082222	0.6079	−30.46362	18.29[34]	–	93
J000411-295935	SGP.p1.8498	86.0 ± 5.6	62.1 ± 6.4	42.7 ± 7.7	1.51 ± 0.52	1.4	601313101750	1.0459	−29.99278	18.10[34]	–	93
J000913-300807[1]	SGP.p1.290	356.3 ± 5.7	273.9 ± 6.6	154.3 ± 7.6	1.51 ± 0.52	1.9	601310696475	2.3023	−30.13526	18.02[34]	–	93

[1] Flux-limited target.

[2] Identifiers correspond to SDSS DR7 (18 digit), SDSS DR8 (19 digit), VIKING DR3 (12 digit).

[3] r band magnitude.

[4] Estimate based on VIKING Z band photometry.

[5] Source identified from NASA Extragalactic Database (NED).

[6] Limiting magnitude from POSS-II r band image.

4.2.3 Observations

Observations for the pilot study were performed in visitor mode with EFOSC2 on the NTT at ESO, La Silla, under proposals: 091.A-0674 (PI: Serjeant) and 093.A-0320 (PI: Amber). Target observations are listed in table 4.2.

Cycle 91

Run 091.A-0674 took place from 30/04/13 to 03/05/13. Poor conditions, high windspeed and cloud cover, affected the first two nights. The majority of observations were performed on the third and fourth nights with seeing ranging from 1"-2". Standard calibration dome flats and arc exposures were taken at the beginning and end of each night, twilight sky flats and a spectrophotometric standard were taken on the final night. Targets were typically observed with two exposures of either 500 or 1000s with either grism #1 or #2 with slit widths of 1.0", 1.5" or 2.0" following an r-band $\sim$ 20s acquisition image.

Cycle 93

Run 093.A-0320 took place from 31/05/14 to 05/06/14. Optimal conditions on the first night deteriorated by the third night which was heavily affected by high windspeeds, snowfall and ice on the dome prevented observations on the fourth and fifth nights, seeing ranged from $< 1'' - 1.5''$. Standard calibration dome flats and arc exposures were taken at the start and end of each night with twlight sky flats were taken on the third night and three spectrophotometric standards were observed at lowest airmass during the three operational nights. Targets were were observed with various exposures of either 600 or 900s with grism #1 and slit width 1.0" following an r-band acquisition of varying length. Active optics focus was verified by inspection of bright point sources in the acquisition image and re-calibrated where necessary.

IAU ID	Exposure [s]	Grism	Slit ["]	Cycle	IAU ID	Exposure [s]	Grism	Slit ["]	Cycle
J083434+011601	1000 × 2	2	1	91	J142004+014045	500 × 2	1	1	91
J084117+020637	1000 × 2	2	1.5	91	J142034+000238	600 × 5	1	1	93
J084347+003332	1000 × 2	2	1.5	91	J142301-003817	500 × 2	2	1.5	91
J090022+001937	500 × 2	2	1	91	J142605-011110	1000 × 2	1	1	91
J090139-010855	500 × 2	2	1	91	J142849+004942	750 × 2	1	1	91
J091350+014543	500 × 3	1	1	91	J143339+001121	750 × 2	1	1	91
J091735+001203	1000 × 2	1	1.5	91	J143354-010112	900 × 4	1	1	93
J092144+003909	500 × 2	2	1	91	J143355+003256	900 × 4	1	1	93
J092409-005018	500 × 2	1	1	91	J143458+005012	750 × 2	1	1	91
J113855+001534	500 × 2	2	1	91	J143520+012231	900 × 4	1	1	93
J114153-014342	500 × 2	1	1	91	J144046+000433	1000 × 3	1	1.5	91
J114231+003344	600 × 5	1	1	93	J144502+004131	600 × 5	1	1	93
J114608+002646	500 × 2	2	1	91	J144539-013649	750 × 1	1	1.5	91
J115112-012639	1000 × 2	1	1	91	J144627+004506	900 × 4	1	1	93
J120203-004333	600 × 5	1	1	93	J144646+013211	750 × 2	2	1	91
J120422-012737	500 × 2	1	1.5	91	J144832+022523	900 × 4	1	1	93
J120553-015117	1000 × 2	1	1	91	J222536-295646	600 × 4	1	1	91
J120700-011303	900 × 4	1	1	93	J223225-284715	800 × 2	1	1.5	91
J120729+001557	600 × 5	1	1	93	J223317-292256	600 × 3	1	1	93
J121335-020323	500 × 2	1	1	91	J223829-304149	1000 × 4	1	1.5	91
J121409-004011	500 × 2	1	1.5	91	J223833-343813	600 × 4	1	1	93
J121417+003305	1000 × 2	1	1.5	91	J225014-325634	600 × 4	1	1	93
J121542+011739	1000 × 1	1	1	91	J225018-302300	900 × 4	1	1	93
J121906-000952	1000 × 2	1	1.5	91	J225615-305243	900 × 5	1	1	93
J140828+014209	1000 × 2	2	1.5	91	J000226-302748	600 × 3	1	1	93
J140946+004608	900 × 3	1	1	93	J000411-295935	600 × 3	1	1	93
J141025-004041	750 × 2	1	1	91	J000913-300807	900 × 5	1	1	93
J141150-005633	1000 × 2	1	1.5	91					
J141350+023956	750 × 2	1	1	91					
J141915-012352	900 × 4	1	1	93					

Table 4.2: Summary of observations during cycles 91 and 93.

4.3 Data Reduction

All spectra were reduced using standard packages in the Image Reduction and Analysis Facility, IRAF, Tody (1986), using the PyRAF[1] environment. Where the built-in packages/tasks of IRAF (denoted by `typewriter` font) were found to be unsuitable for a particular stage in the reduction IDL was used instead (described where appropriate throughout this section). The method was performed in a manner that allowed for batch reductions where possible but ultimately each target was inspected individually in the final stages for optimal reduction. The following subsections describe the general reduction method followed for both cycle 91 and 93 observations providing example images for the case of cycle 93 target J120729+001557. The method remains the same regardless of configuration (grism/slit) where the appropriate calibration files are used for their equivalent science frames.

[1]PyRAF is a product of the Space Telescope Science Institute, which is operated by AURA for NASA.

Throughout the method the IRAF task `imcombine` was used for the median/mean, exposure time weighted combination of individual calibration and science exposures. The `CRREJECT` algorithm was used to reject any cosmic rays, identified as pixels $> 5\sigma$ above the predicted noise level:

$$\sigma = \sqrt{(rn/g)^2 + I/g + g^2} \tag{4.1}$$

where rn is read noise, g is gain and I is the average (median for calibration frames, mean for science frames) pixel count from the individual images.

4.3.1 Standard Reduction

Cycle 91 targets were positioned at the slit center and cycle 93 targets were sequentially positioned between central and $\pm$40pixel offsets. All science and calibration frames were trimmed to the central 201 spatial pixels and to 601 dispersion pixels to truncate the zeroth order (direct) slit exposure whilst preserving the actual dispersion of the grisms.

A bad pixel mask was produced in IDL by comparing dome flats of different exposure lengths and identifying pixels that did not alter significantly between various exposures. The pixel mask was then used to linearly interpolate across the spatial direction to remove bad pixels in all science and calibration exposures.

The bias/pedestal level of all exposures was estimated by median combination of 11 zero length, dark exposures and subsequently subtracted using the IRAF tasks `imcombine` and `imarith`.

During early reduction for cycle 91 it was discovered that the slit illumination varied slightly between exposures, the illumination variations shifting spatially by up to two pixels. The was attributed to the removal and replacement of the slit for the acquisition exposures. The creation of two flat field normalization calibrators were produced to account for the spatial and pixel-to-pixel variations, where the spatial normalization could be shifted where the slit illumination was found to be different between the science and calibration frames. Figure 4.1 shows (a) the median dome flat (b) the pixel-to-pixel normalization (c) the slit normalization and (d) the normalization applied to original dome flat. The IRAF task `imcombine` was used to median combine individual dome flat expo-

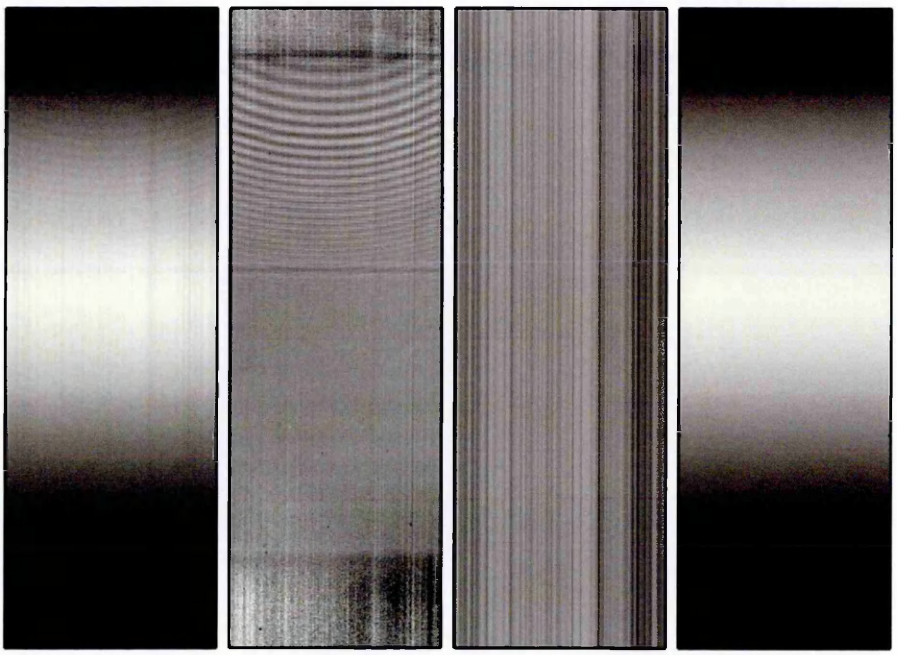

Figure 4.1: Flat normalization demonstration. (a) Median combined dome flat corrected for bad pixels. (b) Pixel-to-pixel normalization. (c) Slit illumnation normalization (d) Normalized dome flat, free from flat-field features.

sures with cosmic ray rejection. IDL was then used to normalize each row (spatial) of the combined dome flat to its mean value and the median of each column (dispersion) was taken as the slit normalization frame. The pixel-to-pixel variation was then calculated as the normalization of each row divided by the slit normalization.

All science frames and arc lamp exposures were flat-fielded by dividing by the pixel and slit normalizations. Any residual artefact arising from a slit illumination variation was not clearly apparent on visual inspection at this stage. Reduction was continued until the background subtraction, if artefacts were found to be present the slit illumination offset was estimated and the flat-fielding was performed by dividing by the pixel and appropriately shifted slit normalizations.

4.3.2 Wavelength Calibration

Wavelength calibration was performed using He/Ar arc lamp exposures. Following standard calibration individual arc exposures were median combined with `imcombine`. The task `identify` was used to inspect the median of the 10 central pixels in the im-

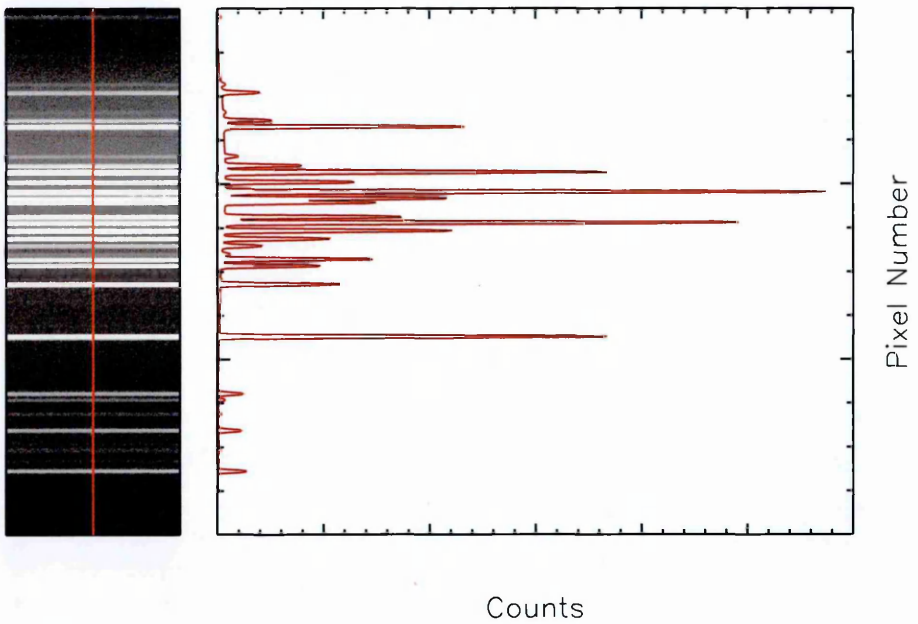

Figure 4.2: Wavelength calibration demonstration. Left: Median combined, bad pixel corrected and bias corrected arc lamp exposure. Right: Counts per dispersion pixel of the median central ten pixels (red line in arc exposure image).

age, figure 4.2, to identify known emission lines with reference to an emission line atlas, figure 4.3.

The task `reidentify` was then used to automatically locate the same emission peaks for the median of 10 pixels at 20 pixel intervals across the spatial axis. The task `fitcoords` was used to fit polynomials to both axes to correct for any distortion of the dispersion across the spatial direction and to transform the pixel positions to wavelengths, best fit polynomials ranged from order $6 - 10$ resulted in residuals of < 1.5Å/pixel. The task `transform` was used to apply the two-dimensional polynomial transformation to all appropriate science frames.

4.3.3 Spectrum Extraction

The task `background` was used to fit and subtract the background sky emission for every science frame. The spectrum position was automatically identified and manually adjusted to be masked in the fitting. Various slices across the wavelength axis were inspected to ensure best fit polynomials, with parameters selected for the same $> 5\sigma$ clipping of possible cosmic ray pixels.

At this stage individual exposures were inspected to check for any illumination residuals

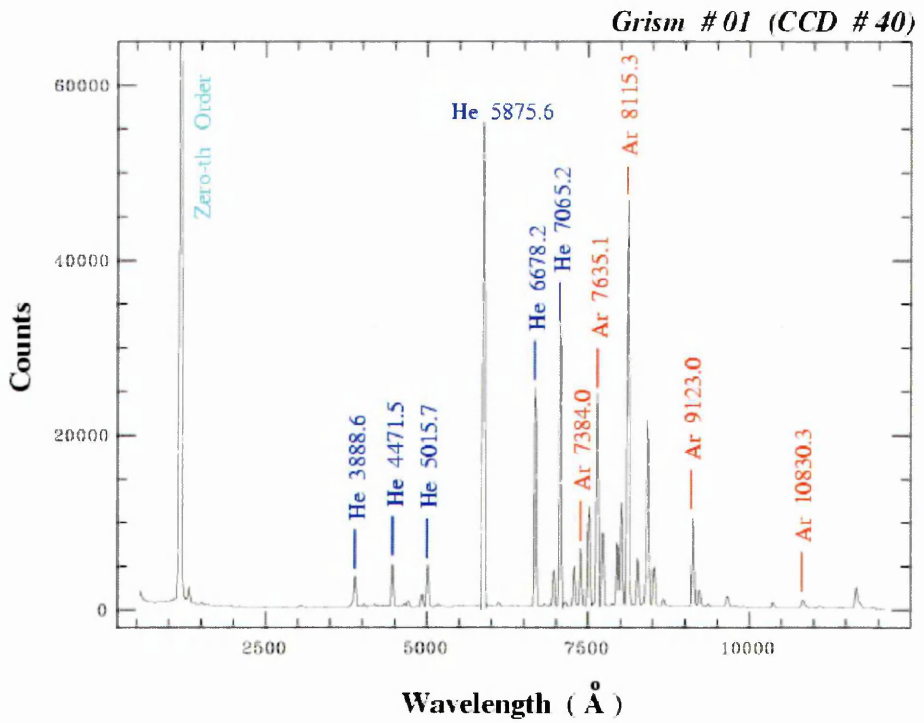

Figure 4.3: EFOSC2 HeAr atlas for grism#1.

caused by the slit positioning (§4.3.1) and if present the reduction method starting again from the shifted slit normalization.

Following successful background subtraction the individual science exposures were mean combined using `imcombine` weighted by exposure time (in the cases of different exposure times) to reject cosmic rays.

The task `apsum` was used to manually specify the aperture position and size and `aptrace` automatically traced the aperture along the wavelength axis. The best fit low order ($n \sim 3$) polynomial was used to trace the spectra and summed along this trace to produce the one-dimensional spectrum. The parameters for `aptrace` were also used to define the background region used to estimate the noise per wavelength pixel. The background regions were defined such that they were offset by an aperture width to the left and right of the aperture limits and extended to cover a total of 120 pixels (60, 60 for centrally positioned targets and 20, 100 for offset targets).

Figure 4.4 shows the stages of reduction on example target J120729+001557, subfigure (a) is the original individual exposure, (b) the exposure following standard reduction and wavelength calibration (note the change in position of the bright sky lines due to the

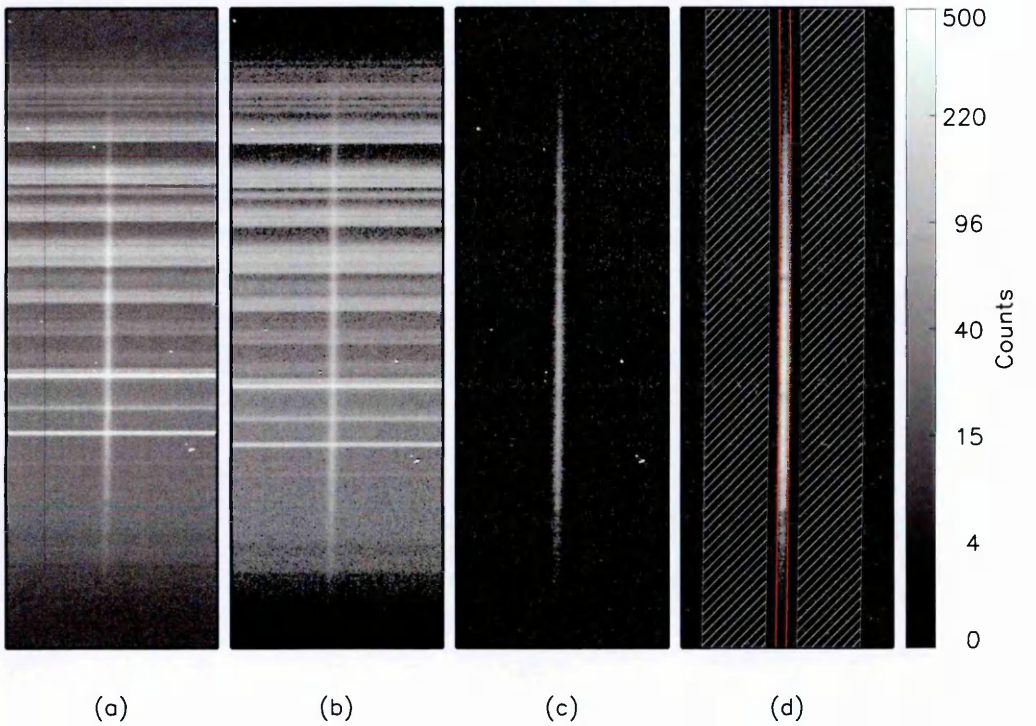

Figure 4.4: Step-by-step reduction images for target J120729+001557. (a) Raw single exposure. (b) Bias corrected, bad-pixel interpolated and wavelength calibrated exposure. (c) Background subtracted exposure (d) Combined image of all individual calibrated exposures. Red highlights the traced aperture limits for the spectra extraction. White denotes the regions used in the noise estimates.

pixel-to-wavelength transformation, there is minimal spatial distortion due to the straight dispersion achieved by the grism). Subfigure (c) shows the image following background subtraction, (d) shows the combined frames with the aperture trace limits in red and the noise estimation windows in white.

4.3.4 Flux Calibration

Following the standard and wavelength calibration and spectrum extraction the observed standards (Feige110, NGC7293, LTT7379 and HD49798) were compared to the ESO library standards of Oke (1990) to calculate the flux calibration to be applied to the target spectra.

Initially flux calibration was attempted using the IRAF tasks `standard`, and `sensfunc` however the library standard spectra were too finely binned in comparison to the 13Å resolution of the observations and these tasks failed to provide an accurate calibration. Instead IDL was used to determine a more accurate sensitivity function to apply to the

target spectra. The observed standard was extinction corrected:

$$m_{em}(\lambda) = m_{obs}(\lambda) - X(\lambda)sec(z) \tag{4.2}$$

using the IRAF included Kitt Peak Observatory extinction coefficients ($X(\lambda)$) to the same airmass ($sec(z)$, where z is the zenith angle) as the observation. It was then re-binned to the coarser resolution of the observation calculating the magnitude per wavelength bin (observation pixel size) by convolving with a top hat function:

$$m_{lib,rebin}(\lambda_{bin}) = \frac{\int T(\lambda) m_{lib}(\lambda)\, d\lambda}{\int T(\lambda)\, d\lambda} \qquad where \qquad T(\lambda) = \begin{cases} 1, & \lambda = \lambda_{bin} \\ 0, & \lambda \neq \lambda_{bin} \end{cases} \tag{4.3}$$

A sensitivity ($S_{func}(\lambda)$) function was produced as the difference in magnitude per wavelength bin of the observed to the rebinned standard:

$$S_{func}(\lambda) = (m_{obs}(\lambda) - X(\lambda)sec(z)) - m_{lib,rebin}(\lambda) \tag{4.4}$$

This sensitivity function for NGC7293 is applied to the observed spectrum and compared to the original, finely sampled, library standard in figure 4.5, the calibration results in an overall fit to $\sim 3\%$. The atmospheric absorption at ~ 7700Å is poorly accounted for by all flux calibrations and is subsequently masked in the use of all the calibrated target spectra.

IDL was used to perform the complete flux calibration and extinction correction for target spectra in an identical manner to the IRAF `calibrate` task:

$$F_{\lambda} = \frac{F_{\lambda,obs} 10^{-0.4 S_{func}}}{\tau_{exp} \lambda_{bin}} \tag{4.5}$$

Corresponding noise estimates were obtained calculating the variance (σ^2) in the background region (subfigure (d) in figure 4.4) as a function of wavelength and applying the flux and extinction correction including a factor of $\sqrt{n_{aper}}$:

$$\sigma^2(\lambda) = \frac{\sigma^2_{obs}(\lambda) 10^{-0.4 S_{func}}}{\tau_{exp} \lambda_{bin}} \sqrt{n_{aper}} \tag{4.6}$$

where τ_{exp} is the exposure time and λ_{bin} is the wavelength resolution. The final spectra

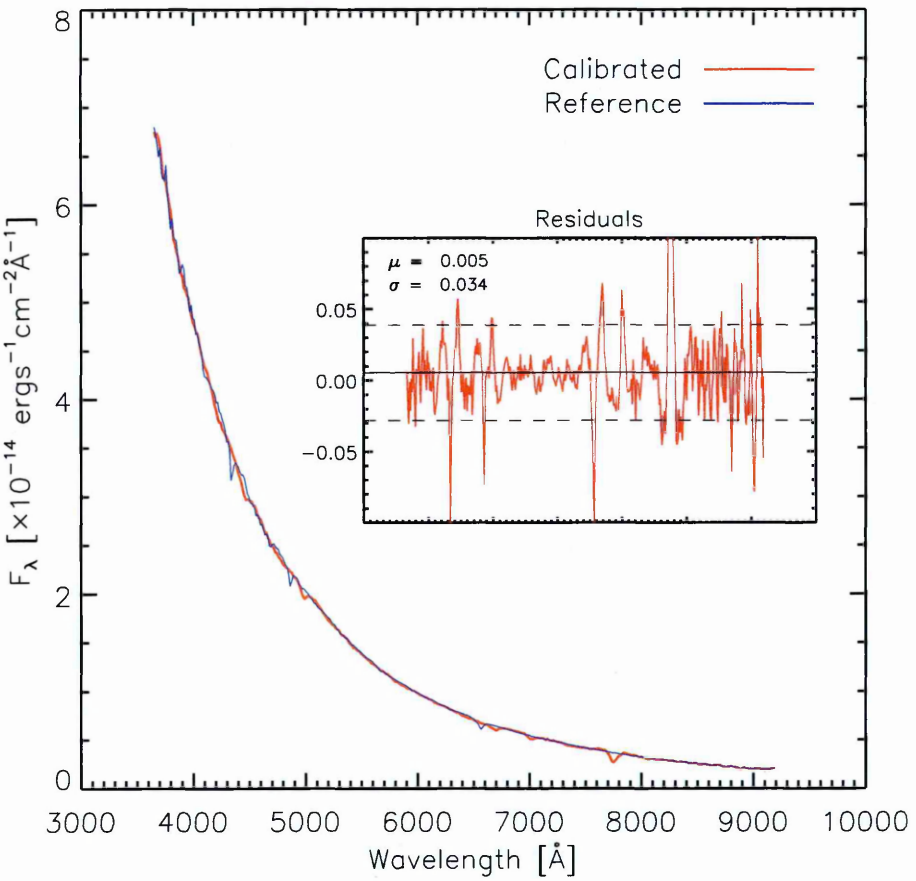

Figure 4.5: Flux calibration example. Red denotes the flux-calibrated standard observation for night 1 of NGC7293. Blue denotes the library standard flux as obtained from the ESO observers repository. Inlay: Residuals, ($F_{library}$ - $F_{observation}$)/$F_{library}$, and statistics, mean and standard deviation.

for all 57 targets are presented in figure 4.6.

4.4 Redshift Estimates

The extracted spectra varied in quality with only a few spectra containing readily identifiable features, e.g. 4000Å break or absorption lines. To estimate the target redshifts a minimum-χ^2 fitting was performed using a SED library.

4.4.1 Models

The SED fitting was performed using the templates of Tremonti (2003), which are included in the release of the population synthesis code of Bruzual & Charlot (2003). The library of 39 SEDs were originally selected to cover the range of galaxies present in SDSS DR1 having been used in the fitting of continuum and emission lines, e.g. Kauffmann et al. (2003); Tremonti et al. (2004).

The library comprises of 13 templates for a range of metallicities ($Z = 0.004, 0.02, 0.05$) over a range of ages ($\tau = 5Myr - 11Gyr$) for three types of star formation: ten instantaneous, two exponentially declining and one constant.

4.4.2 Fitting Method

A minimum χ^2 fitting was performed in a similar manner to that described in §3.2.1, but instead of using three data points and the model inferred broadband photometry the fitting was performed for a varied range of the spectra.

Each spectrum was individually inspected and the regions identified for masking in the fitting. Particular regions of noise were the residuals of bright sky lines at $\sim$ 5500Å and $\sim$ 6300Å for cycle 91 data and the telluric absorption at $\sim$ 7700Å for spectra from both cycles. The masking was performed by setting the noise within these regions to artificially high levels so their contribution to the χ^2 was essentially zero. Each spectrum was also trimmed at the low and high wavelengths where the grism throughput decreased and signal to noise dropped significantly, these regions varied and are presented in table 4.7.

The fitting was performed for each of the spectra to a grid of the 39 template SEDs which were reddened to account for the presence of dust using the two-component curve of

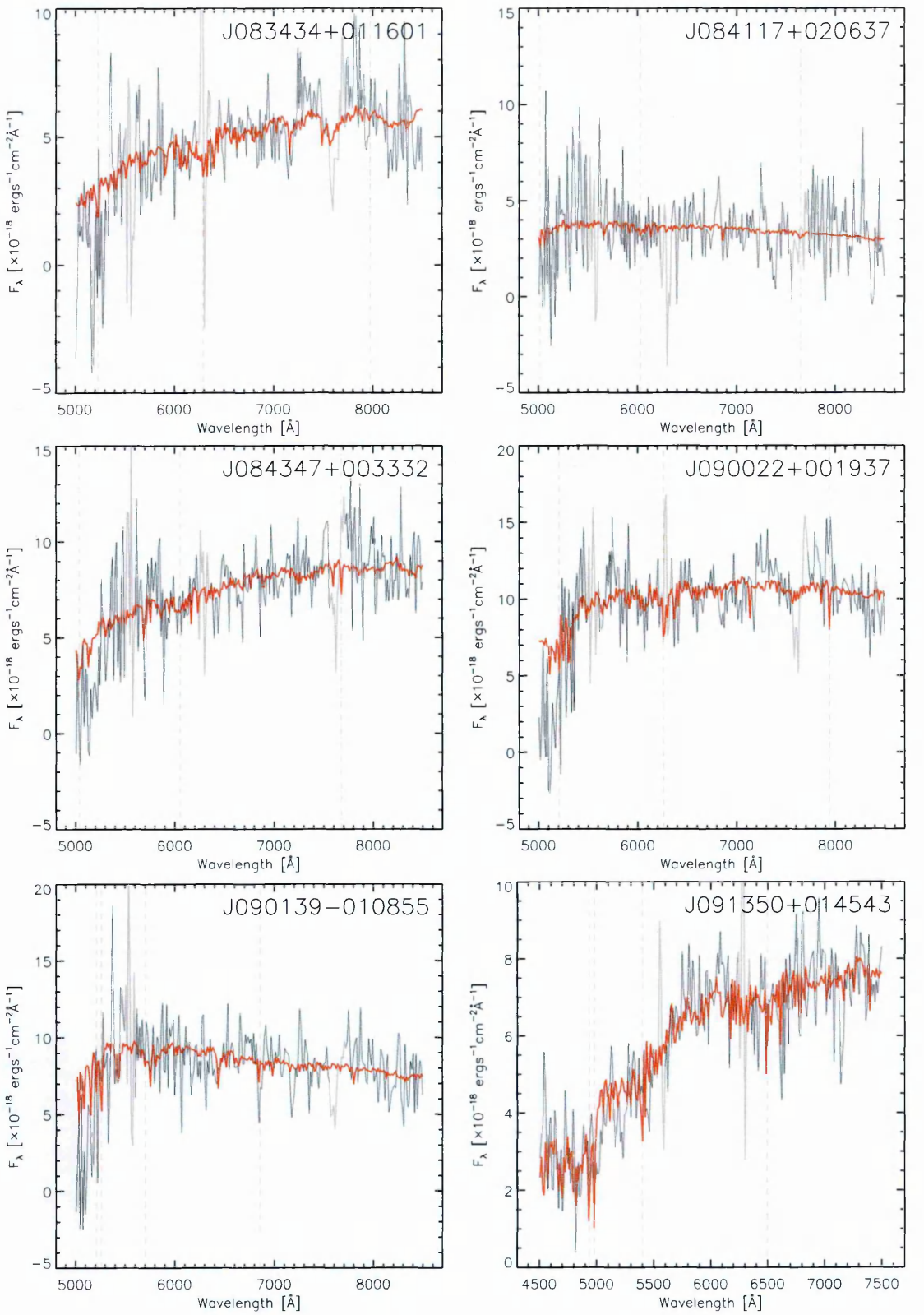

Figure 4.6: NTT spectra stamps. Reduced spectra shown in black and the best-fit template model plotted in solid red. Absorption (dashed) and emission (dot-dashed) line positions are plotted for the best-fit implied redshift (in order of increasing wavelength: Ca H+K, G-band, H_β, Mg and H_α).

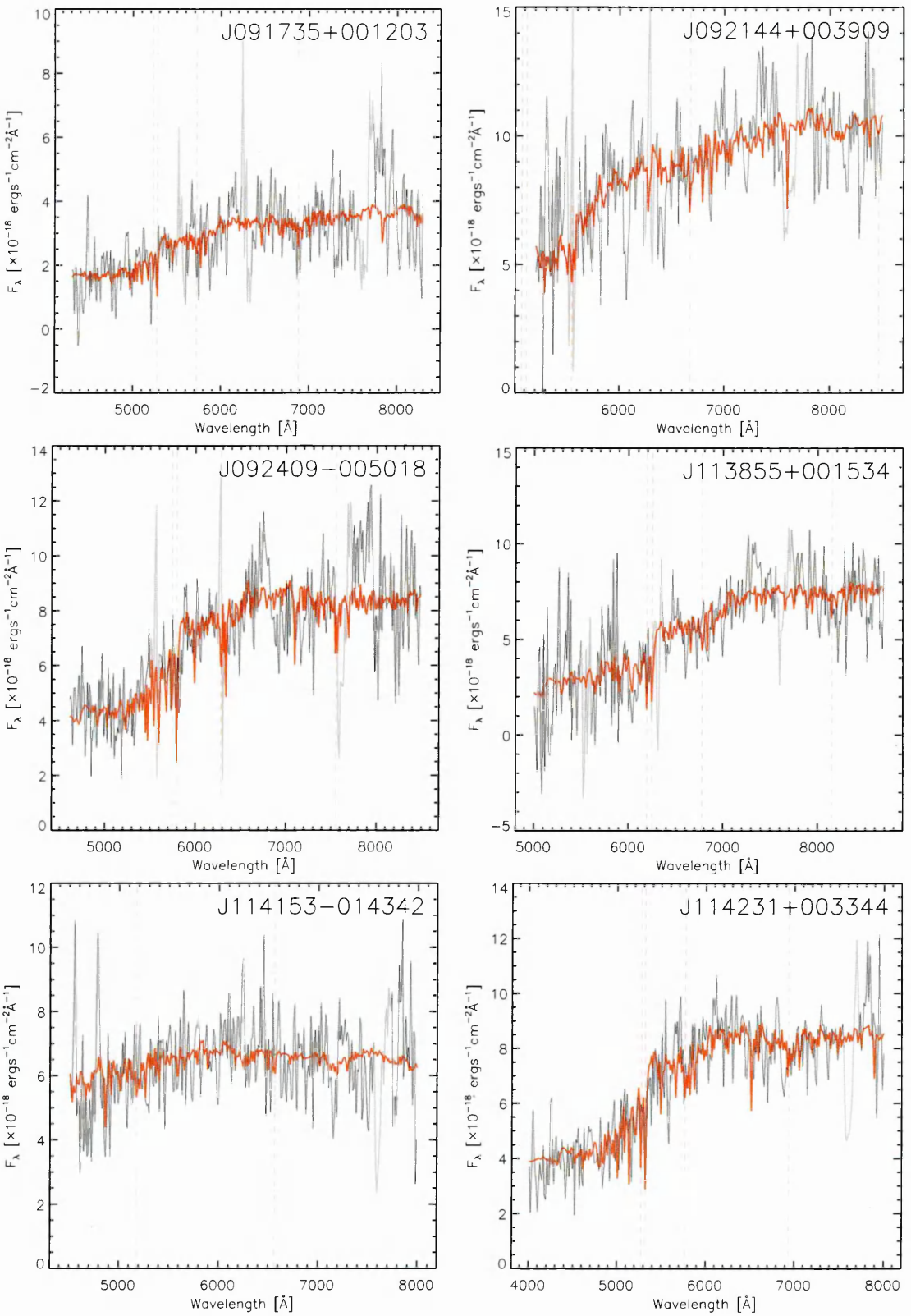

Figure 4.6 (Continued): NTT spectra stamps. Reduced spectra shown in black and the best-fit template model plotted in solid red. Absorption (dashed) and emission (dot-dashed) line positions are plotted for the best-fit implied redshift (in order of increasing wavelength: Ca H+K, G-band, H_β, Mg and H_α).

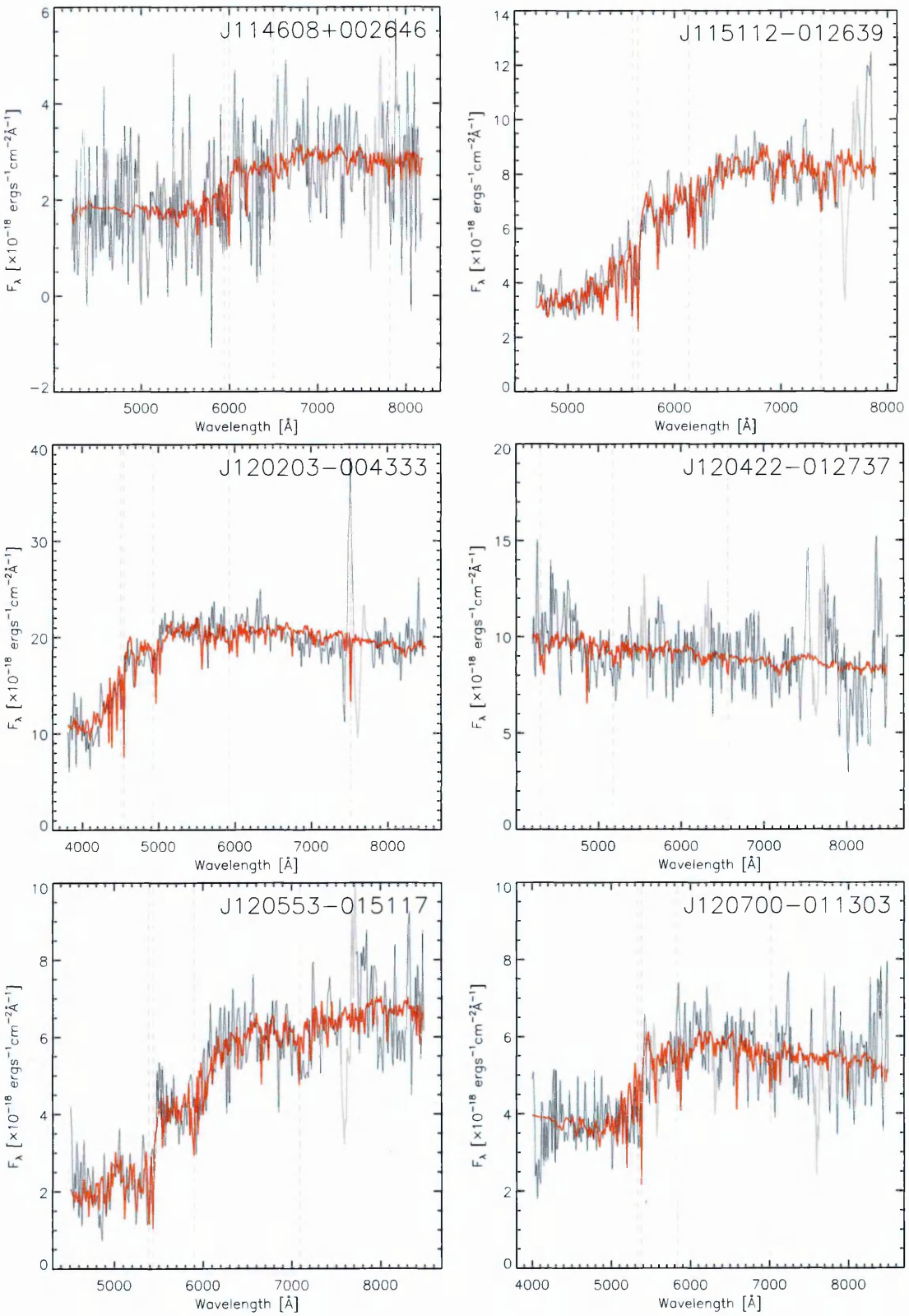

Figure 4.6 (Continued): NTT spectra stamps. Reduced spectra shown in black and the best-fit template model plotted in solid red. Absorption (dashed) and emission (dot-dashed) line positions are plotted for the best-fit implied redshift (in order of increasing wavelength: Ca H+K, G-band, H_β, Mg and H_α).

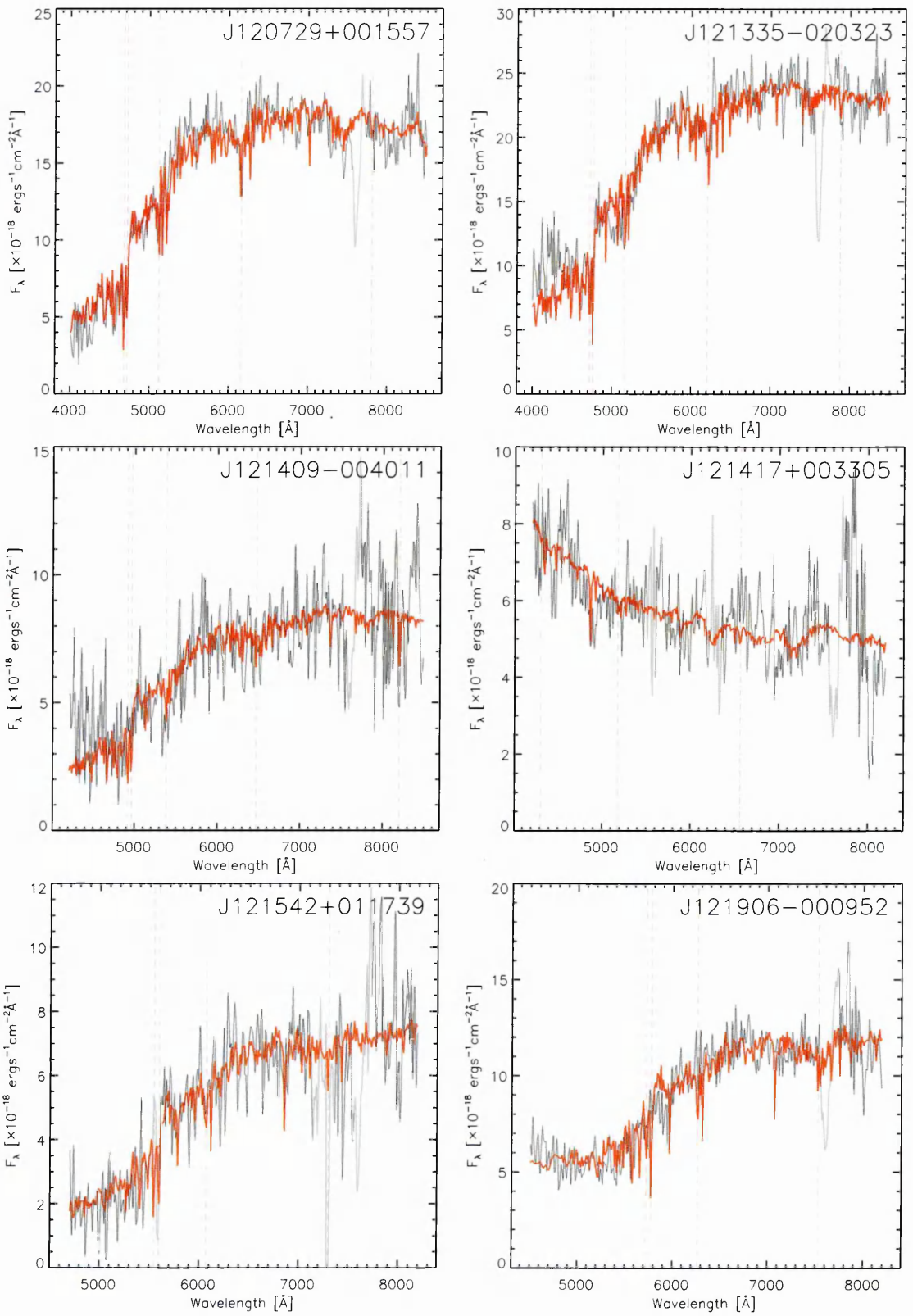

Figure 4.6 (Continued): NTT spectra stamps. Reduced spectra shown in black and the best-fit template model plotted in solid red. Absorption (dashed) and emission (dot-dashed) line positions are plotted for the best-fit implied redshift (in order of increasing wavelength: Ca H+K, G-band, H_β, Mg and H_α).

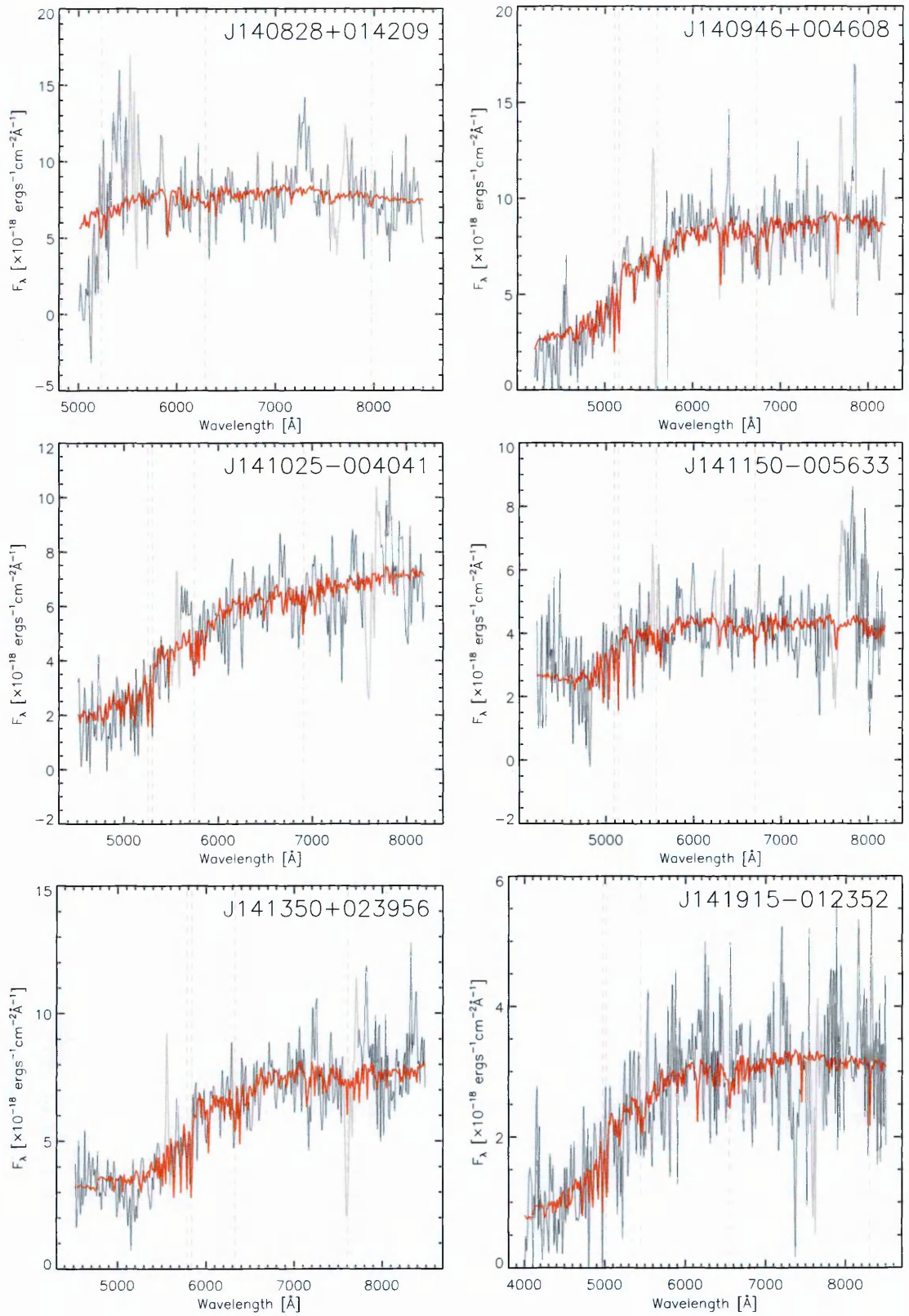

Figure 4.6 (Continued): NTT spectra stamps. Reduced spectra shown in black and the best-fit template model plotted in solid red. Absorption (dashed) and emission (dot-dashed) line positions are plotted for the best-fit implied redshift (in order of increasing wavelength: Ca H+K, G-band, H_β, Mg and H_α).

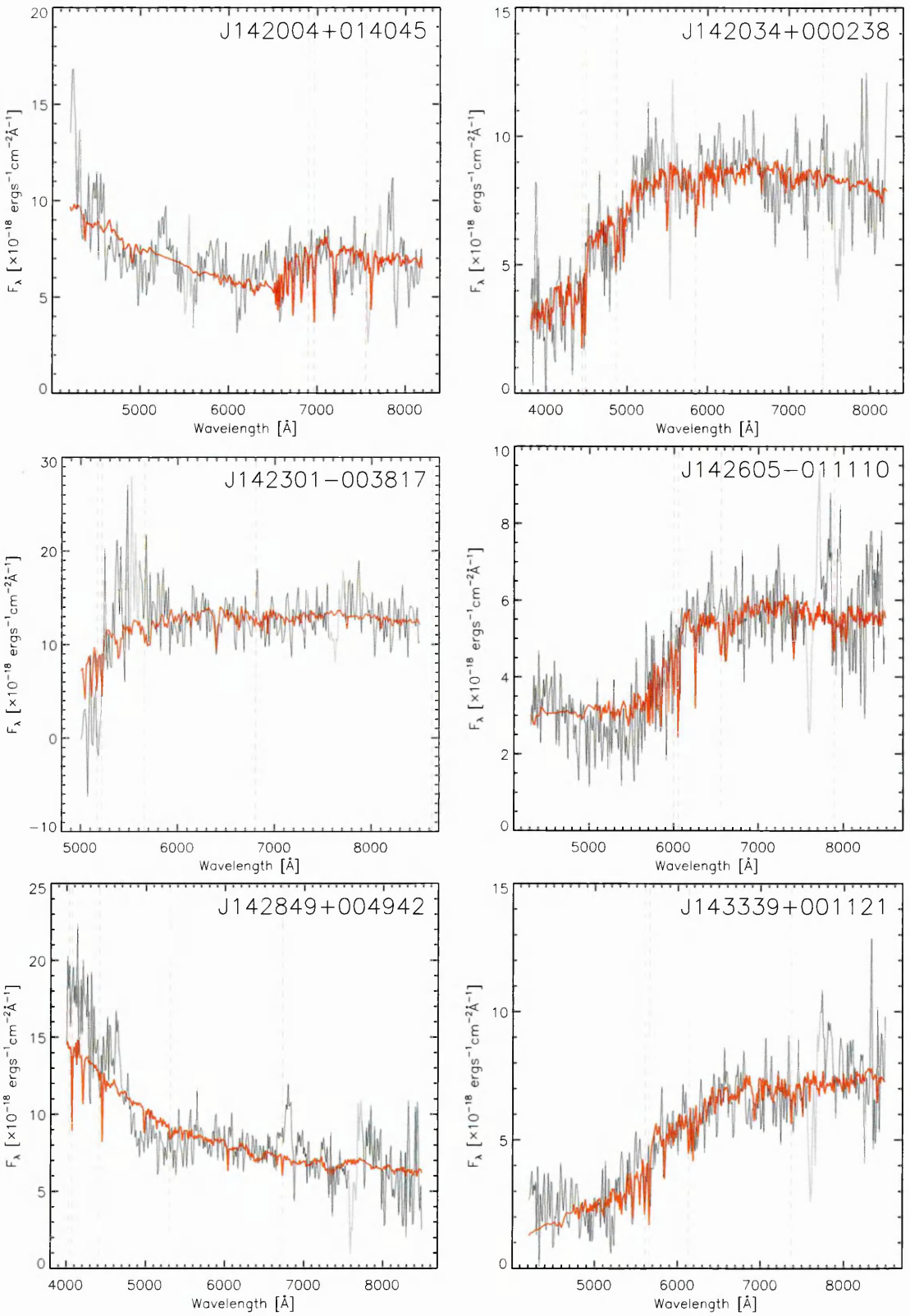

Figure 4.6 (Continued): NTT spectra stamps. Reduced spectra shown in black and the best-fit template model plotted in solid red. Absorption (dashed) and emission (dot-dashed) line positions are plotted for the best-fit implied redshift (in order of increasing wavelength: Ca H+K, G-band, H_β, Mg and H_α).

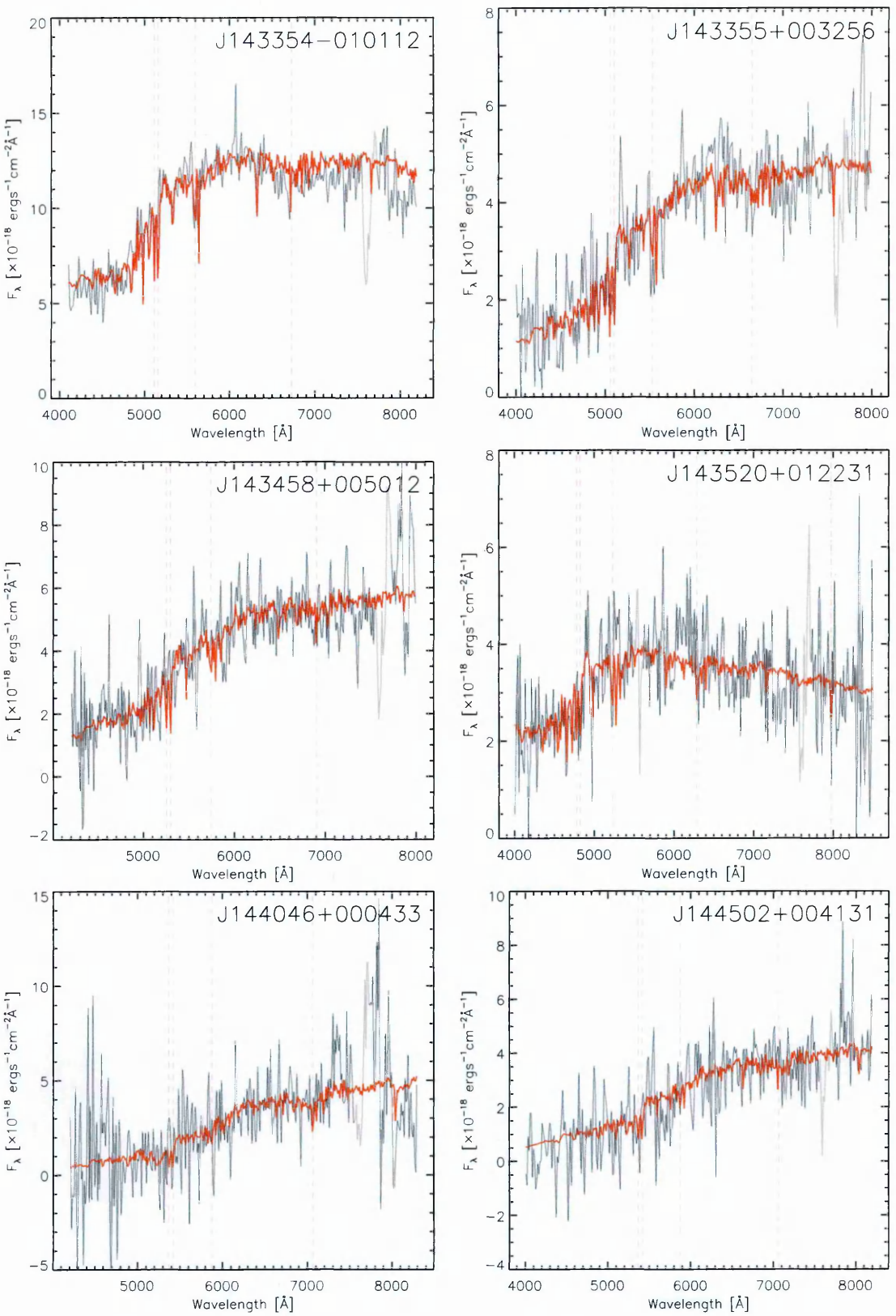

Figure 4.6 (Continued): NTT spectra stamps. Reduced spectra shown in black and the best-fit template model plotted in solid red. Absorption (dashed) and emission (dot-dashed) line positions are plotted for the best-fit implied redshift (in order of increasing wavelength: Ca H+K, G-band, H_β, Mg and H_α).

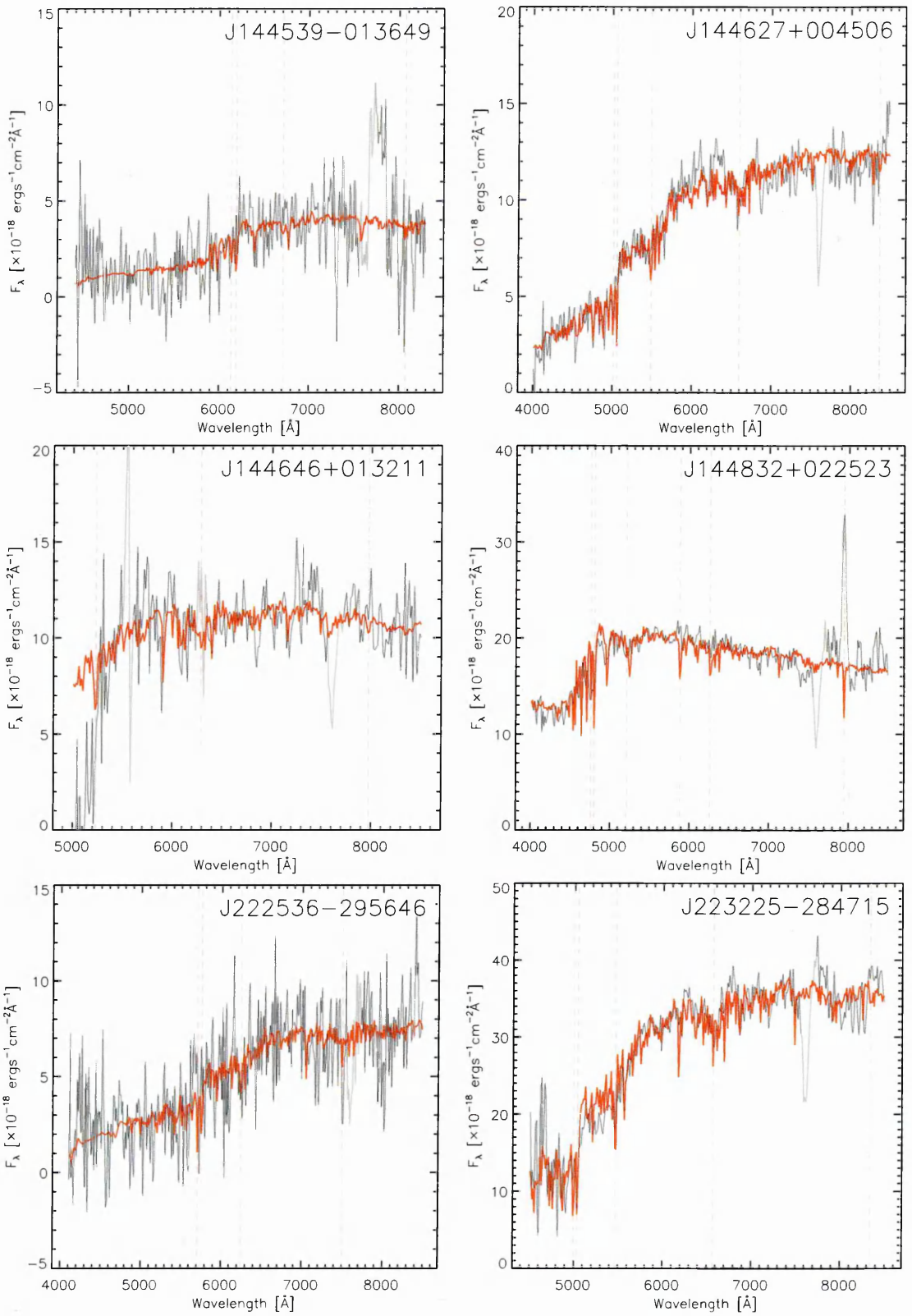

Figure 4.6 (Continued): NTT spectra stamps. Reduced spectra shown in black and the best-fit template model plotted in solid red. Absorption (dashed) and emission (dot-dashed) line positions are plotted for the best-fit implied redshift (in order of increasing wavelength: Ca H+K, G-band, H_β, Mg and H_α).

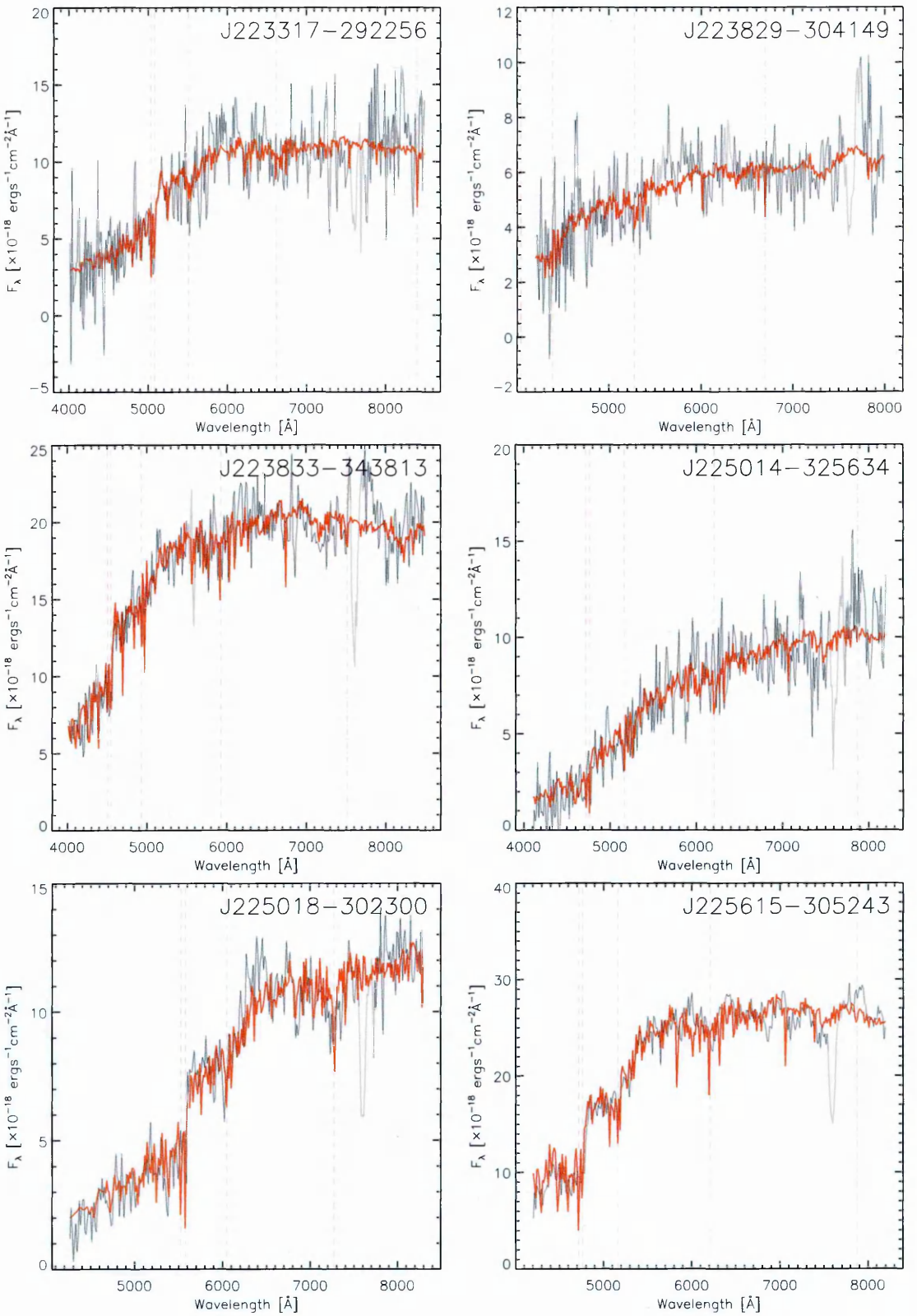

Figure 4.6 (Continued): NTT spectra stamps. Reduced spectra shown in black and the best-fit template model plotted in solid red. Absorption (dashed) and emission (dot-dashed) line positions are plotted for the best-fit implied redshift (in order of increasing wavelength: Ca H+K, G-band, H_β, Mg and H_α).

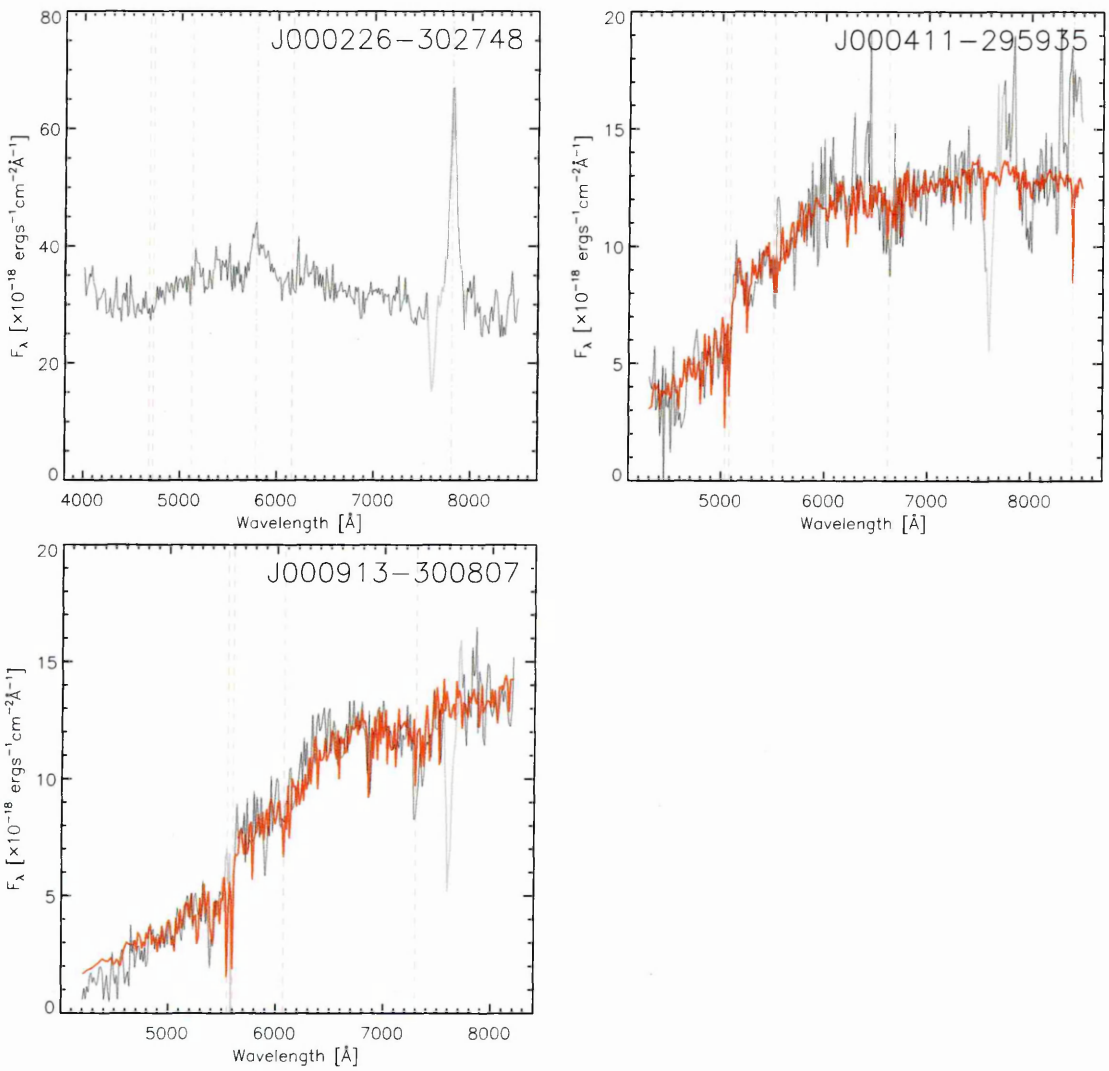

Figure 4.6 (Continued): NTT spectra stamps. Reduced spectra shown in black and the best-fit template model plotted in solid red. Absorption (dashed) and emission (dot-dashed) line positions are plotted for the best-fit implied redshift (in order of increasing wavelength: Ca H+K, G-band, H_β, Mg and H_α).

Calzetti et al. (2000) for the range $A_v = 0-1$ and redshifted over the range $z = 0-1$ (3.1). For each grid variation the template was normalized to the data and errors (3.3), the χ^2 was calculated (3.4) and the minimum taken as the best fit template with corresponding reddening and associated redshift.

Redshift Error Estimates

The low dispersion of the spectra sets a lower limit on the accuracy of any spectroscopic redshifts obtained where the pixels are of the order $\sim$ 13Å. Any uncertainty in the wavelength calibration increases this lower limit, the residuals of the best fit polynomial used for the wavelength transformation was ≤ 1.5 pixels. Taking this error on the observed wavelength into account imposes an redshift uncertainty of

$$\Delta z = \frac{\Delta \lambda_{obs}}{\lambda_{em}}, \tag{4.7}$$

which for identifications of the 4000Å break equate to $\Delta z = 0.0049$. Ultimately, however, the majority of redshift estimates are provided from the best fit template rather than exact absorption/emission line identifications and so all redshifts are quoted to within an accuracy of the fitting redshift bin size of $z_{bin} = 0.005$.

Redshift Quality

The calibrated spectra varied in quality and the best fit templates were used to aid in the identification of distinct absorption features, specifically the rest-frame 4000Å break, 4300Å G-band, 5175Å Mg and H_α absorption/emission at 6563Å (denoted by the vertical red lines in figure 4.6). Quality flags were assigned following visual inspection of the spectra and best fit template: *(a)* denoting multiple identifiable features (three sources with distinctly bright H_α emission the redshifts were directly measured using the peak of this emission line), *(b)* denoting broad agreement with the continuum of the spectra with a good agreement of a 4000Å break but no additional features, *(c)* grade was assigned to spectra where the best fit template did not assist in the identification of spectral features. All best fit template parameters, minimum χ^2 and quality flags are given in table 4.7. A total of 25 out of 57 spectra were classified as grades *(a)* or *(b)*.

IAU ID	Wavelengths [Å]	Masked Regions [Å]	Template	A_V	Min(χ^2)	Redshift[2]	Quality
J083434+011601	5000 – 8500	5550, 6300	ssp_5Gyr_z05	0.4	460.1	0.215	*c*
J084117+020637	5000 – 8500	5550, 6300	ssp_1.4Gyr_z008	0.2	597.0	0.165	*c*
J084347+003332	5000 – 8500	5550, 6300	ssp_11Gyr_z008	1.0	693.4	0.170	*c*
J090022+001937	5000 – 8500	5550, 6300	ssp_11Gyr_z008	0.0	421.1	0.210	*c*
J090139-010855	5000 – 8500	5550	cst_6Gyr_z008	1.0	393.5	0.325	*c*
J091350+014543	4500 – 7500	5550, 6300	ssp_11Gyr_z008	0.2	328.6	0.255	*b*
J091735+001203	4300 – 8300	5550, 6300	t5e9_12Gyr_z05	0.8	518.7	0.330	*c*
J092144+003909	5200 – 8500	5550, 6300	ssp_5Gyr_z02	0.8	429.7	0.290	*c*
J092409-005018	4600 – 8500	5550, 6300	t5e9_12Gyr_z008	0.6	513.3	0.460	*b*
J113855+001534	5000 – 8700	5550, 6300	ssp_5Gyr_z008	0.2	378.6	0.575	*c*
J114153-014342	4500 – 8000		ssp_1.4Gyr_z02	0.8	432.6	0.000	*c*
J114231+003344	4000 – 8000		t5e9_12Gyr_z008	0.6	778.3	0.340	*b*
J114608+002646	5200 – 8500	5550, 6300	t9e9_12Gyr_z05	0.0	306.8	0.620	*c*
J115112-012639	4700 – 7900		ssp_1.4Gyr_z02	0.4	624.7	0.425	*a*
J120203-004333[1]	3800 – 8500		t9e9_12Gyr_z008	0.8	4536.8	0.145	*a*
J120422-012737	4200 – 8500	5550, 6300	cst_6Gyr_z02	1.0	637.0	0.000	*c*
J120553-015117	4500 – 8500		ssp_11Gyr_z008	0.2	603.2	0.370	*a*
J120700-011303	4000 – 8500	5550, 6300	t9e9_12Gyr_z02	0.4	694.2	0.355	*b*
J120729+001557	4000 – 8500		ssp_1.4Gyr_z05	0.4	1622.2	0.190	*a*
J121335-020323	4000 – 8500		ssp_5Gyr_z008	0.6	1119.3	0.200	*a*
J121409-004011	4200 – 8500		ssp_5Gyr_z008	0.6	637.4	0.250	*c*
J121417+003305	4200 – 8200	5550, 6300	ssp_25Myr_z02	1.0	614.8	0.000	*c*
J121542+011739	4700 – 8200	5550, 7200	ssp_900Myr_z05	1.0	478.1	0.410	*b*
J121906-000952	4500 – 8200		t5e9_12Gyr_z02	0.8	968.9	0.455	*c*
J140828+014209	5000 – 8500	5550	ssp_900Myr_z05	0.6	1127.9	0.215	*c*
J140946+004608	4200 – 8200		ssp_1.4Gyr_z008	1.0	917.0	0.300	*b*
J141025-004041	4500 – 8200	5550	ssp_2.5Gyr_z008	1.0	522.5	0.335	*c*
J141150-005633	4200 – 8200	5550, 6300	t9e9_12Gyr_z05	0.8	536.4	0.295	*c*
J141350+023956	4500 – 8500	5550	t5e9_12Gyr_z008	1.0	579.7	0.470	*b*
J141915-012352	4000 – 8500		ssp_1.4Gyr_z008	1.0	618.3	0.265	*c*
J142004+014045	4200 – 8200	5550	cst_6Gyr_z05	0.4	671.2	0.755	*c*
J142034+000238	3800 – 8200	5550	ssp_5Gyr_z008	0.2	1190.8	0.130	*b*
J142301-003817	5000 – 8500	5550	ssp_900Myr_z05	1.0	714.6	0.315	*c*
J142605-011110	4300 – 8500		t9e9_12Gyr_z008	1.0	709.1	0.525	*c*
J142849+004942	4000 – 8500		ssp_25Myr_z02	0.6	1189.4	0.025	*c*
J143339+001121	4200 – 8500		ssp_1.4Gyr_z02	1.0	692.7	0.425	*c*
J143354-010112	4100 – 8200		t9e9_12Gyr_z008	1.0	544.7	0.300	*b*
J143355+003256	4000 – 8000		ssp_1.4Gyr_z008	1.0	676.7	0.285	*b*
J143458+005012	4200 – 8000		ssp_1.4Gyr_z02	1.0	463.0	0.335	*c*
J143520+012231	4000 – 8500	5550	t5e9_12Gyr_z008	0.0	706.2	0.215	*c*
J144046+000433	4200 – 8300		ssp_11Gyr_z05	0.0	904.5	0.365	*c*
J144502+004131	4000 – 8200		ssp_2.5Gyr_z02	1.0	882.0	0.365	*c*
J144539-013649	4400 – 8300		ssp_640Myr_z05	0.6	486.9	0.560	*c*
J144627+004506	4000 – 8500		ssp_2.5Gyr_z008	1.0	215.7	0.275	*a*
J144646+013211	5000 – 8500	5550, 6300	ssp_2.5Gyr_z02	0.2	539.2	0.215	*c*
J144832+022523[1]	4000 – 8500		cst_6Gyr_z02	1.0	4579.0	0.210	*a*
J222536-295646	4100 – 8500		ssp_2.5Gyr_z02	0.2	494.6	0.450	*c*
J223225-284715	4500 – 8500		ssp_11Gyr_z008	0.2	1507.3	0.270	*a*
J223317-292256	4000 – 8500		ssp_1.4Gyr_z008	0.8	479.7	0.280	*b*
J223829-304149	4200 – 8000	5550, 6300	ssp_5Gyr_z02	0.8	412.2	0.020	*c*
J223833-343813	4000 – 8500	5550	ssp_1.4Gyr_z02	0.8	1467.1	0.145	*b*
J225014-325634	4100 – 8200		ssp_2.5Gyr_z05	1.0	1143.1	0.200	*c*
J225018-302300	4250 – 8300		ssp_1.4Gyr_z05	0.6	1253.4	0.405	*a*
J225615-305243	4200 – 8200		ssp_11Gyr_z008	0.0	5477.0	0.200	*a*
J000226-302748[1]	4000 – 8500		–	–	–	0.192	*a*
J000411-295935	4300 – 8500		ssp_1.4Gyr_z02	1.0	1112.2	0.280	*a*
J000913-300807	4200 – 8200	5550	ssp_1.4Gyr_z05	1.0	1634.0	0.410	*b*

[1] H_α emission redshift estimate.

[2] Estimated error ± 0.005

Figure 4.7: Summary of parameters from minimum χ^2 template fitting.

4.5 Model Comparison

Under the assumption that the redshift distribution of the grade *(a)* and *(b)* sources are a representative sample of the true HALOS redshift distribution a comparison to the models of Eales (2015) is performed.

4.5.1 Model Summary

Eales (2015) present a model to predict the redshift distribution of lenses given a fixed source redshift under the assumption that the lensing mass distribution is described by a singular isothermal sphere (as supported by the H-ATLAS number counts). Using the H-ATLAS distribution of HALOS sources Eales (priv. comm.) provide a custom program to predict a lens probability for one of three halo mass functions (Press & Schechter, 1974; Tinker et al., 2008; Sheth & Tormen, 1999) for a source redshift. Relating the halo distribution to apparent magnitude a magnitude limit can be set to produce a prediction of the lens redshifts of HALOS sources for the NTT magnitude limit of $I_{AB} < 20$. Apparent magnitude as a function of halo mass and redshift was estimated using the relation between halo mass, redshift and stellar mass of Behroozi et al. (2010) and the best fit variables as estimated by Leauthaud et al. (2012) from the COSMOS survey data. Interpolation over a range of halo mass and redshifts provided a coarse grid of stellar masses. The stellar mass and redshift grid was then applied to the K-band magnitude, stellar mass redshift relation as modelled by Longhetti & Saracco (2009) for early-type SEDs using the population synthesis of Bruzual & Charlot (2003). The resultant K-band magnitude as a function of redshift and halo mass were converted to I-band magnitudes by calculating the apparent magnitude difference between the filters for an appropriately redshifted template of an early type SED.

4.5.2 Model Comparison

An immediate concern with using the grade *(a)* and *(b)* samples are the possible biases introduced by the instrument configuration in obtaining quality redshifts. All of the cycle 91 targets observed with grism#2 are classified as grade *(c)* these targets were those with $z_{phot} > 0.3$ in that proposal. Cycle 93 observations, firstly lacked the GAMA9 field to

	Press &Schechter	Tinker	Sheth & Tormen
χ^2_{red} (Uncorrected)	3.765	3.789	3.876
χ^2_{red} (Corrected)	2.313	2.329	2.383

Table 4.3: χ^2_{red} of the uncorrected and corrected samples in comparison to the Eales models for the three halo mass functions considered.

re-observe this subset and the photometric redshifts were not considered when prioritising observations.

To account for the incompleteness of the grade *(a)* and *(b)* sample completion factors were estimated as the ratio of the z_{phot} and magnitude histograms for the grade *(a)* and *(b)* sample and the total sample:

$$fr_{bin} = \frac{N_{bin,ab}}{N_{bin,total}} \tag{4.8}$$

where the completion factor (fr_{bin}) for a target equates to that of its histogram bin. Completeness corrected histograms are produced where sources contribute ($1/fr_{bin}$) to the binning. Photometric redshifts only exist for 74% of the targets so magnitude completeness factors were used in place of those sources without photometric redshifts to estimate the z_{phot} corrected sample. Sources without photometric redshifts are those targets from the SGP which were primarily selected based on their photometry whereas targets from the GAMA field were preferentially selected for observations in cycle 91 based on their redshift estimates.

The uncorrected and corrected spectroscopic redshift histograms of the grade *(a)* and *(b)* sample is presented alongside the lens probability for the three halo mass functions for a limiting magnitude of $I_{AB} < 20$ for a source at $z_{source} = 2.1$ (the average source photometric redshift for the grade *(a)* and *(b)* sample) in figure 4.3.

The χ^2_{red} (3.7) was calculated by first interpolating the the lens redshift probabilities to the bin centers and normalising to a sample size equal to the comparison sample (uncorrected or corrected). Histogram errors were taken as $\sqrt{N_{bin}}$ for the original sample and $\sqrt{(\sum(1/fr_{bin}))}$ for the corrected samples. The χ^2_{red} values are presented in table 4.3.

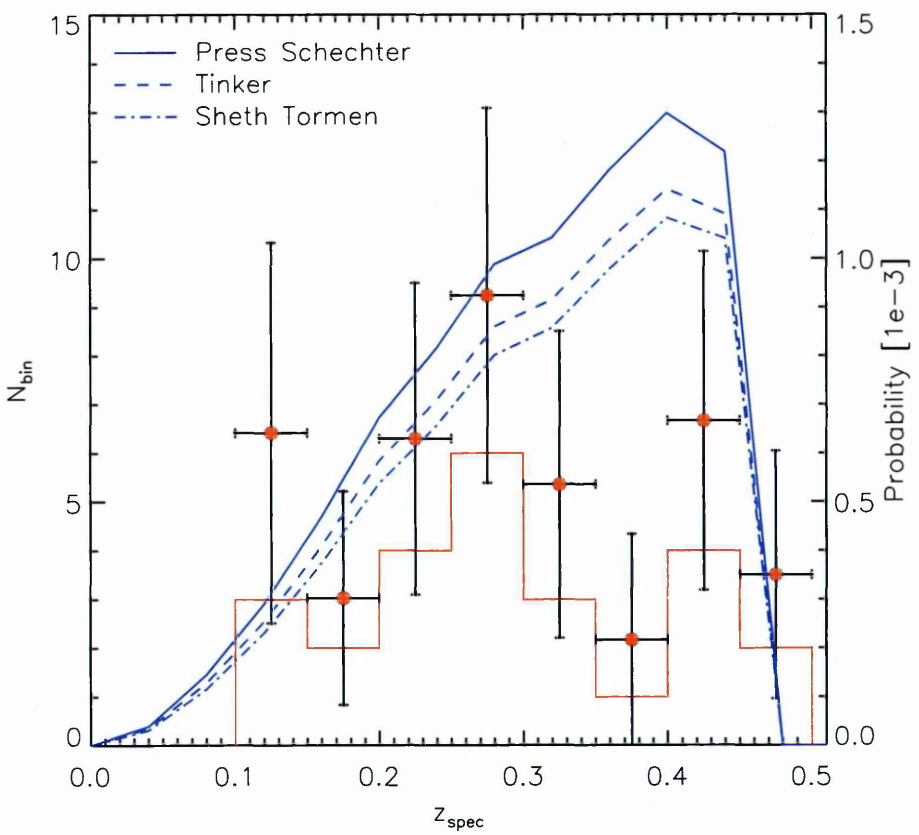

Figure 4.8: NTT redshift histogram for targets graded *a* and *b* quality. Data points represent the corrected sample with associated uncertainties. Also plotted are the probabilities of the lens redshifts as per the model of Eales (2015) for the three halo mass functions and $z_{source} = 2.1$ and $I_{AB} < 20$.

4.6 Summary and Conclusions

This chapter presents the first spectroscopic observations targeting the foreground lenses of the extended HALOS lens candidate sample from the GAMA and SGP fields. A total of 57 out of 100 proposed targets were observed over the course of two observing cycles using the NTT at the European Southern Observatory. Reduction of the spectra was performed using the academic standard IRAF software supplemented with reduction steps performed in IDL as described in this work. The quality of the reduced and extracted spectra varied and a library of SED templates were fitted to the data to assist with redshift estimation. A total of 25 sources are in good agreement with the absorption/emission features (grade *(a)*) or the continuum (grade *(b)*) of the best-fit template.

This partial sample of 25 targets is compared to model predictions of HALOS lens probabilities for the mean source redshift of $z_{source} = 2.1$ for three halo mass functions using the collaborative program of Eales (priv. comm.). This incomplete pilot study sample does not appear to be in agreement with predictions of the model ($\chi^2_{red} \sim 3$). By using the magnitudes and available z_{phot} for all observed targets the partial sample is completeness corrected and both corrected samples are then compared and yield lower χ^2_{red}. The model predictions were subject to a number of assumptions: photometric redshifts were used for the background sources and in particular the estimate of the apparent magnitude as a function of halo mass and redshift, relied on two separate studies and interpolated between the few data bins available.

This work concludes that the observation of the brightest ($I_{AB} < 20$) HALOS lens sample pushes the capabilities of low resolution spectroscopy on a 4m active-optics telescope to the practical limit where observing times were highly inefficient (< 2 per hour). The earnest 25% success rate of the observations are unable to address the original statistical science objectives which were dependant on a redshift distribution of 100 lenses.

Future Work

The identification of robust foreground lens redshifts for HALOS lens candidates has been shown to be impractical with a 4m-class telescope. The long exposure times, despite less than optimal conditions warrant future proposals to observe the increasingly faint

lens candidates of H-ATLAS to be performed on 8m class telescopes for the best time efficiency and signal-to-noise. At the time of writing a proposal to use the Very Large Telescope (VLT) during cycle 96 at ESO has been submitted (PI: Marchetti) to continue the pilot study and improve on the quality and number of spectra obtained so far. The identification of the current 25 foreground lens redshifts would be complemented by CO-based spectroscopic redshifts being obtained for the corresponding background sources and robustly confirm the nature of these lens candidates. An optimistic direction for this work would be to extend the suite of observations performed for flux-limited lens candidates by proposing for the HALOS sample. Such observations (high-resolution imaging, CO-based and optical spectroscopy) would provide the means to identify the nature of HALOS candidates and determine the efficiency of the method.

Comparison to the predicted redshift distribution of the HALOS sample warrant further work to investigate the discrepancy at $z \geq 0.3$. The aforementioned assumptions performed to produce the model distribution could be addressed by obtaining accurate redshift estimates for the corresponding background sources to the 25 foreground lens candidates in this work and to further investigate the relation between apparent magnitude, halo mass and redshift by extending the work of Behroozi et al. (2010) and Leauthaud et al. (2012).

Chapter 5

HST Snapshot Survey of Lens Candidates

Observations with the Hubble Space Telescope (HST) provided striking confirmation of the flux-limited selection method with NIR imaging of the five H-ATLAS SDP targets, Negrello et al. (2010). This chapter details the reduction of the HST snapshots for a sample of 85 lens candidates from the H-ATLAS GAMA and NGP fields. Galaxy profile fitting is performed for the sample of single lens candidates and redshift estimates are compared to optically selected gravitational lenses.

The chapter is organised as follows: Section 5.1 describes the Snapshot program, the H-ATLAS proposal (PI: Negrello) and science objectives. Section 5.2 describes the reduction of the 85 lens candidate snapshots performed in this work using the standard PyRAF software. Section 5.3 describes the galaxy profile fitting method and subsequent analysis performed for the sample of single lens candidates. Section 5.4 concludes with a summary of the chapter; the conclusions and future work.

5.1 Lens Candidate Snapshot Program

Confirmation of the efficient flux-limited selection method arose, initially, from multiple follow-up observations revealing the distinct redshifts of the sub-mm source and optical/ NIR counterpart for the five H-ATLAS SDP sources of Negrello et al. (2010). Imaging obtained with the Hubble Space Telescope (HST), PI: Negrello, proposal ID: 12194, aided

in the identification of lensing. Observations were taken in two filters, J (1.1μm) and H (1.6μm), selected to be sensitive to the emission from the lens and the source respectively. Negrello et al. (2014) and Dye et al. (2014) perform the lens modelling and subsequent source reconstruction for the five lensed sources. Prior to lens subtraction two sources clearly show Einstein rings at longer wavelengths, following lens subtraction a further two reveal lensed images. The high resolution imaging does not reveal obvious lensed structure in the fifth source.

The scheduling of HST observations is performed as efficiently as possible, despite this there are periods where planned observations cannot take place. The Snapshot program is designed to make use of this downtime between regular observations by providing a large number of shorter observations distributed evenly over the sky. As such any snapshot proposal is not guaranteed and chances of success are improved by providing numerous targets across as large an area as possible.

The successful demonstration of the flux-limited selection resulted in the collaboration of H-ATLAS and HerMES consortia to propose a HST snapshot campaign targeting 200 lens candidates to address a number of science objectives.

5.1.1 Science Objectives

Observations were performed using the wide J filter which samples the peak emission of early-type galaxies (the most common lens), thereby capturing as much light as possible for efficient exposure times and allowing the morphology of the lensing object(s) to be identified. The flux-limited selection is based solely on sub-mm flux and produces a sample of lens candidates that is unbiased towards the nature of the lensing mass; as such the lenses are the focus of the science objectives. The aims of which are to: (1) Determine the type/morphology of the lens, investigating the fraction of sources lensed by multiple objects and by late-type galaxies. (2) Model and subtract the light profile of the lens which, for the cases of low obscuration, result in the detection the background source. Regardless of detection of the background source the imaging can (3) constrain the rest frame optical emission. (4) Perform source-image reconstruction in the manner demonstrated by Dye et al. (2014) thus estimating the magnification. Finally (5) confirm lensing directly where the background source is clearly detected in the cases of group/cluster lensing.

5.1.2 Target Selection

A total of 200 flux-limited lens candidates were selected from the H-ATLAS and HerMES consortia, 137 and 63 respectively. All sources with flux density $S_{500} > 80$mJy and further requiring no extended optical emission and no radio emission. The lower flux density was selected due to the increased uncertainties in the source extraction at the time of the snapshot proposal. Table B.1 details the H-ATLAS targets; the HerMES sample is described by Calanog et al. (2014).

5.1.3 Observations

All targets were observed between December 2012 and August 2013 as part of cycle 19 proposal ID: 12488 (PI: Negrello). Observations were made with the Wide Field Camera 3 (WFC3/IR) using the F110W wide-J filter (peak wavelength 1.1μm) and a four point sub-pixel offset of equal exposure times. Total exposure times varied from 252 to 712s according to the brightness of the sub-mm sources, the brighter the source the more likely to be lensed being assigned shorter exposure times and therefore more likely to be selected for snapshot observations. A total of 89 H-ATLAS sources were observed representing a remarkable 75% completion rate compared to the average 33%. Four snapshots failed the guide star acquisition and the resulting telescope drift produced blurred exposures, these snapshots were discarded and excluded from the reduction.

5.2 Data Reduction

Data was reduced using the PyRAF software and the drizzlepac package. Image calibration was performed using the automatic PyRAF drizzlepac pipeline with the appropriate calibration files obtained from the Mikulski Archive for Space Telescopes (MAST), the long duration of the snapshot campaign resulted in updated calibration files for the later snapshots. Cutouts of all reduced snapshots are displayed in figure B.1.

5.2.1 Drizzling

The point spread function (PSF) of the HST is undersampled by the pixel scale of the WFC3, by offsetting different exposures by sub-pixel amounts (dithering) it is possible to

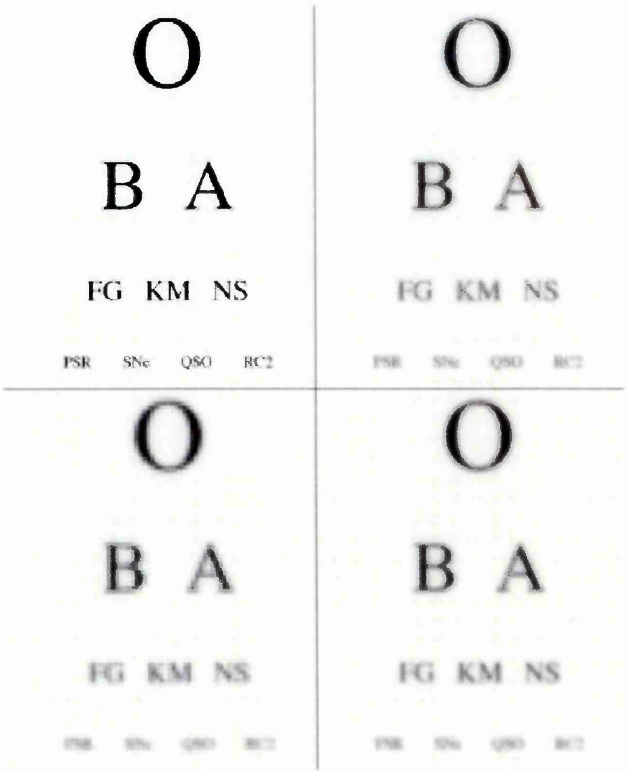

Figure 5.1: The drizzle 'eye chart' reproduced from fig. 1 of Fruchter & Hook (2002). Top left: true image. Top right: image following convolution with the HST/WFC3/IR PSF. Bottom left: image following sampling with the HST/WFC3/IR CCD. Bottom right: reconstruction from dithered CCD images.

recover much of the information lost in the undersampling.

The effect of an undersampled PSF is shown in figure 5.1, a true image will always be subject to convolution with a PSF when observed with a real (finite aperture) telescope. The observed image is then subject to convolution with the pixel size of the detector, which, if the pixel size is large in comparison to the PSF, will result in further degradation of the image quality.

The drizzle algorithm, described by Fruchter & Hook (2002), is used in the reconstruction of HST images from dithered exposures which preserves photometry and astrometry with minimal impact on signal-to-noise. The PyRAF drizzlepac/astrodrizzle routine (Gonzaga & et al., 2012) was used to combine the dithered exposures and produce the final drizzled outputs. Figure 5.2 shows a schematic representation of the drizzling of an input exposure to the output image. An output image grid, of smaller pixel scale, is specified and the individual exposures, following geometric correction, have their pixels reduced in

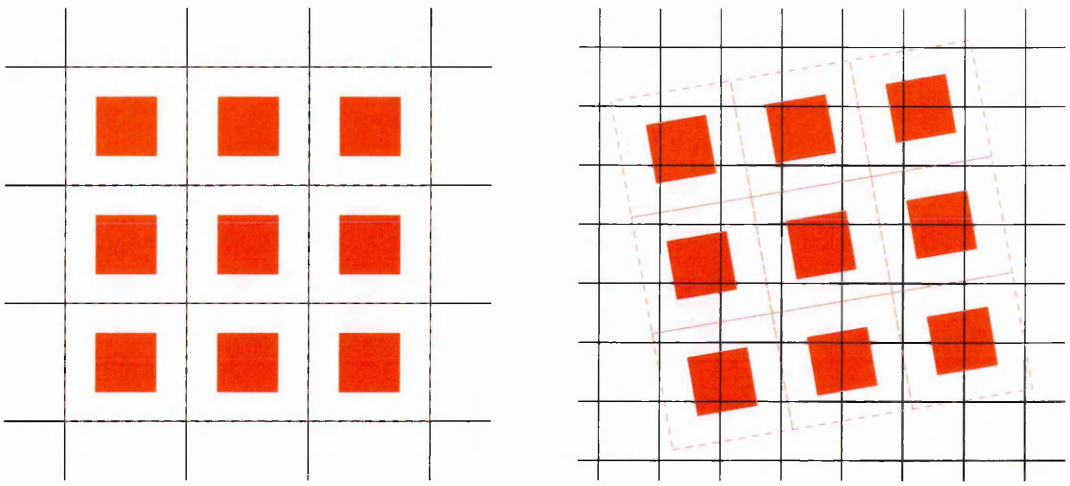

Figure 5.2: Left: Original, coarse pixels of a single exposure are reduced in size to the drops. Right: Following a geometric correction/alignment of all input exposures, these smaller drops are drizzled onto a finer output pixel grid weighted by area.

size and 'dropped' onto the output grid, this is then repeated for each of the dithered exposures. The area of overlap between the input 'drop' and output pixel defines the value of the contribution for input drops that overlap multiple pixels. The single drizzling depicted in figure 5.2 shows that the central output pixel has no contribution from this specific exposure, a particular pattern for the sub-pixel offset of exposures ensure that subsequent drizzlings contribute to this pixel in the final drizzled image, figure 5.3 shows the drizzling schematic specific to the snapshot observations.

The two parameters that define the drizzling of a specific dither pattern are the drop size and output grid size. The reduction of the snapshots used a drop size and output grid scale of 0.7 and 0.5× the original pixel size resulting in output images of 0.064"/pixel. Figure 5.4 shows the improvement in quality for an example snapshot using drizzlepac with the aforementioned parameters.

5.3 Galaxy Profile Fitting

Following data reduction a subsample of targets were selected as the pilot sample for lens modelling, consisting of nine isolated lens candidates. Targets from the GAMA field benefit from the likelihood ratio analysis of Smith et al. (2011), optical counterparts

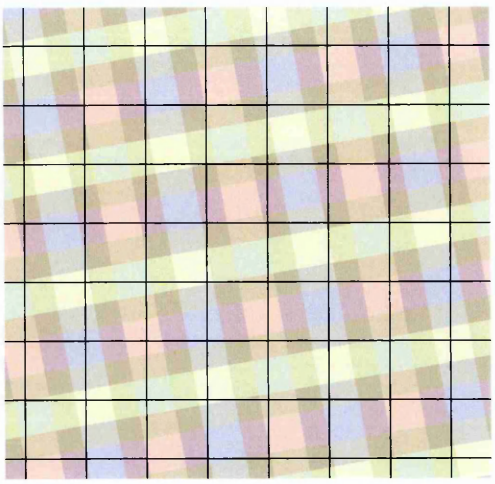

Figure 5.3: Complete schematic of the snapshot reduction. Four exposures (red, blue, green, yellow) representing the box shaped dither pattern are superimposed on the output pixel grid (black). Multiple pixels from the individual exposures contribute to the final, smaller, drizzled pixels.

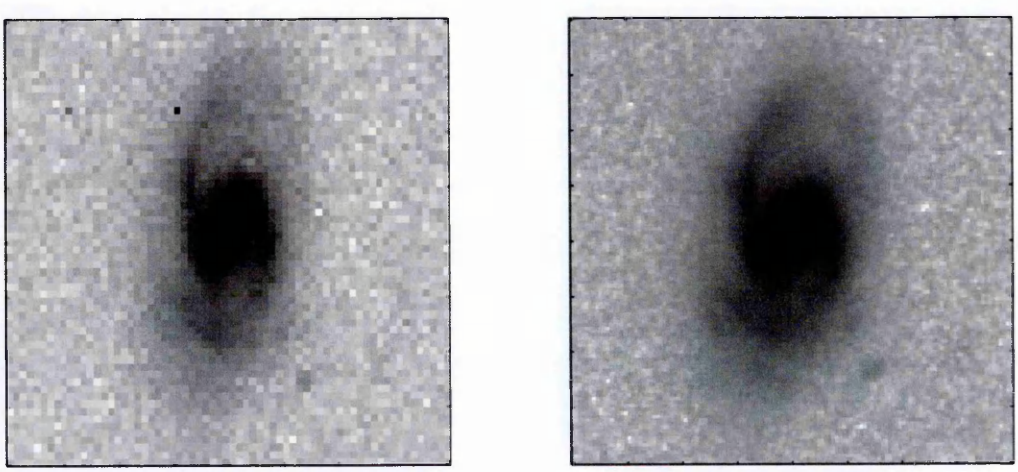

Figure 5.4: Left: Original single HST exposure of snapshot target J090953-010811 (note the cosmic ray still present as the dark pixel approximately top middle of the image). Right: Final drizzled output combining the four dithered exposures with drizzle parameters, drop size= 0.7 and final pixel scale= 0.5.

with reliability, $R > 0.8$, were selected. Targets from the NGP field do not yet have a counterpart analysis, Bourne et al. (in prep.), as such candidates were selected based on the presence of a lensed signature (e.g. J133846+255057) or if the SPIRE emission centroid (red cross in figure 5.7) was within 3.5" of an isolated source.

5.3.1 Galfit

Profile fitting was performed using `Galfit`, Peng et al. (2010), a 2D parametric image fitting program capable of fitting multiple profiles to objects in an image where each profile is characterised by key parameters (e.g. position, effective radius, ellipticity, flux density). The user provides an initial estimate of parameters which the fitting algorithm varies to achieve a minimum χ^2 fit to the data. The user is able to provide a constraint file to restrict or couple parameters for the model(s) and an image mask can be provided to omit regions in the fitting, the later being useful in densely populated fields where the fitting algorithm has a tendency to 'wander' to other sources.

5.3.2 Fitting Method

The profile fitting method was performed individually for the subsample of drizzled snapshots. `SExtractor`, Bertin & Arnouts (1996), was used in its standard configuration to identify and measure all sources within the images, in conjunction with a custom IDL program an image cutout (typically 24" on a side centered on the 500μm source position) and mask file was produced. Neighbouring sources were masked by defining a mask region that encompassed 2.5$\times$ the extracted Kron radius, r_k (Kron, 1980) which, on average, accounts for $> 90\%$ of the source flux (Bertin & Arnouts, 1996). Any masked pixels within $2.5r_k$ of the target were removed from the final mask file. The source extraction and masking is shown in figure 5.5 for the case of J091331-003644.

In order to fit profiles `galfit` requires a point spread function (PSF) and an estimate of the background level in the image. A median PSF was produced by first extracting the brightest stellar sources within the central 1' of all snapshots. After removal of sources with a neighbouring object < 3" a custom IDL program performed a two-dimensional interpolation shifting the peak of the PSF to a central pixel position. Finally the extracted PSFs were then normalised and median-combined to use in the fitting. An estimate of

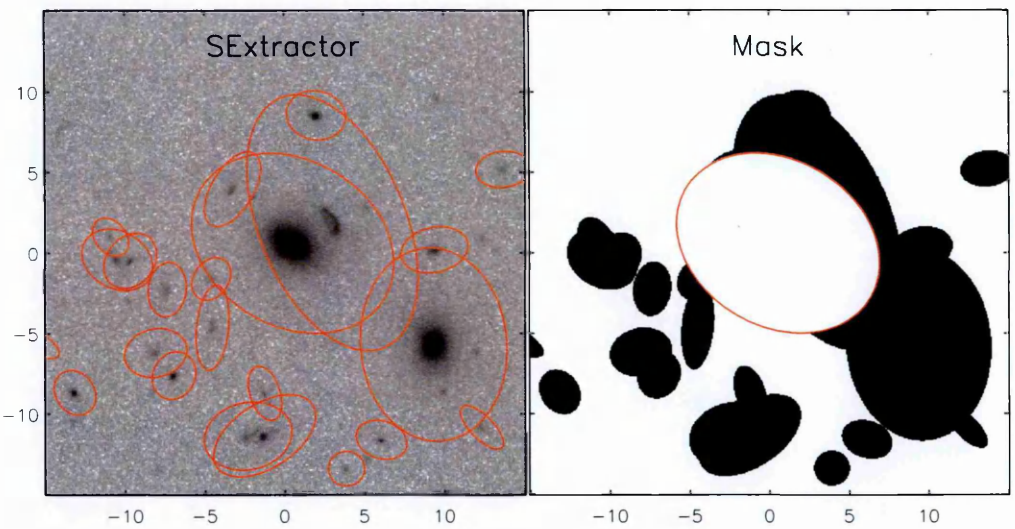

Figure 5.5: Source extraction and masking. Left: `SExtractor` source boundaries, defined by $2.5r_k$. Right: Resulting mask for the profile fitting of the central lens candidate.

the sky background for each image was obtained from the best fit gaussian to the pixel value histogram using the IDL program `sky_stats`. For each lens candidate a single Sérsic profile was fit, using as an initial guess the `SExtractor` parameters for the target position, ellipticity and magnitude. Each target was then iteratively looped through subsequent model fitting following inspection, addition of a model component and/or altering the fitting parameters. Profiles were restricted to a combination of sérsic, exponential and PSF models, the best fit parameters for the component(s) of the models are provided in table 5.1, the original, model and residual images are shown in figure 5.7.

Due to the presence of multiple components in some models the effective radii and surface brightnesses were calculated by summing the flux within increasing apertures, defined by the parameters of the brightest component in the model. The effective/half-light radius was interpolated at the half-light sum of the model image less the sky background value, figure 5.6 shows the example case of J091331-003644. The conversion from counts/s to AB magnitudes was performed using the F110W zero point, $Z(F_\nu) = 6.76 \times 10^{-8}$ Jys/counts.

5.3.3 Kormendy Relation Redshift Estimates

An estimate of the redshift of the sources is performed by comparison to the samples presented by Longhetti et al. (2007). The Kormendy Relation, Kormendy (1977) is the

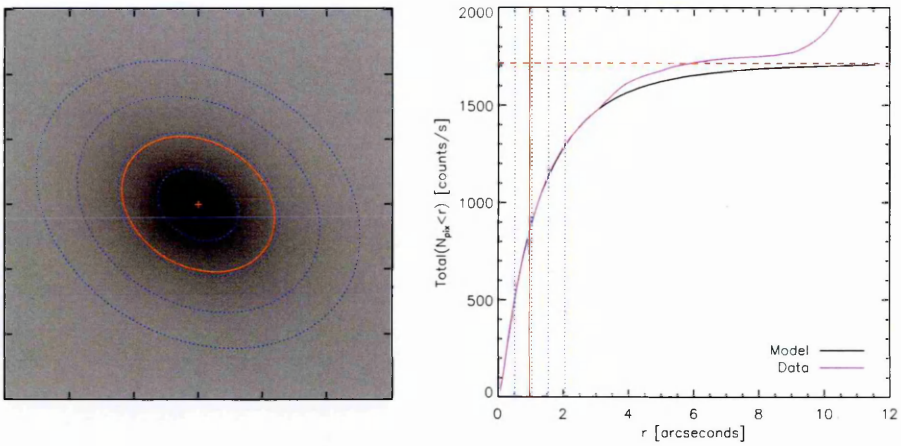

Figure 5.6: Effective radius and surface brightness estimate. Left: `galfit` model, the effective radius (red) and profile ellipses (dashed blue) at 0.5" major axis intervals. Right: Surface brightness, the sum of $N_{pix}(< r)$ in counts/s, as a function of major axis, r. Measured for the model (black) and data (magenta), the effective/half-light radius is the interpolation at half the maximum flux of the model (dashed red line). Note the additional surface brightness in the data is due to the presence of additional sources at increasing r.

H-ATLAS ID	χ^2_{red}	r_e ["]	SB^1 ($< r_e$)	J_{AB}	Profile	J_{AB}	r_s[2] [pix]	n[3]	e	θ[4] [deg]
J091331-003644	1.226	0.97	20.94	18.74	sérsic	18.79	15.1	2.7	0.70	58
					psf	21.82	–	–	–	–
J092409-005018	1.140	0.74	21.63	19.83	sérsic	21.22	5.1	0.6	0.62	76
					exp	20.45	11.9	–	0.57	−63
					psf	21.79	–	–	–	–
J115112-012638	1.117	0.71	21.41	19.77	sérsic	19.97	12.2	3.1	0.65	−87
					psf	21.70	–	–	–	–
J125126+254928	1.138	1.03	22.75	20.25	sérsic	20.25	17.0	7.3	0.52	8
J125760+224558	1.151	0.82	21.63	19.95	sérsic	21.02	18.0	3.5	0.5	48
					sérsic	20.56	10.7	1.9	0.95	−56
					psf	23.04	–	–	–	–
J132630+334410	1.150	1.51	23.36	19.99	sérsic	19.99	23.4	4.7	0.64	−47
J133008+245860	1.136	0.63	21.11	20.09	sérsic	20.24	10.4	2.4	0.85	34
					psf	22.28	–	–	–	–
J133846+255057	1.379	1.98	23.97	20.17	sérsic	20.17	50.7	8.4	1.0	–
J134159+292833	1.059	0.98	20.53	18.50	sérsic	18.62	16.2	3.1	0.94	−68
					sérsic	20.85	1.0	6.7	0.72	−65

[1] Surface brightness, J_{AB} magnitudes.

[2] Profile model scale radius.

[3] Sérsic index.

[4] Degrees left of vertical.

Table 5.1: `galfit` parameters.

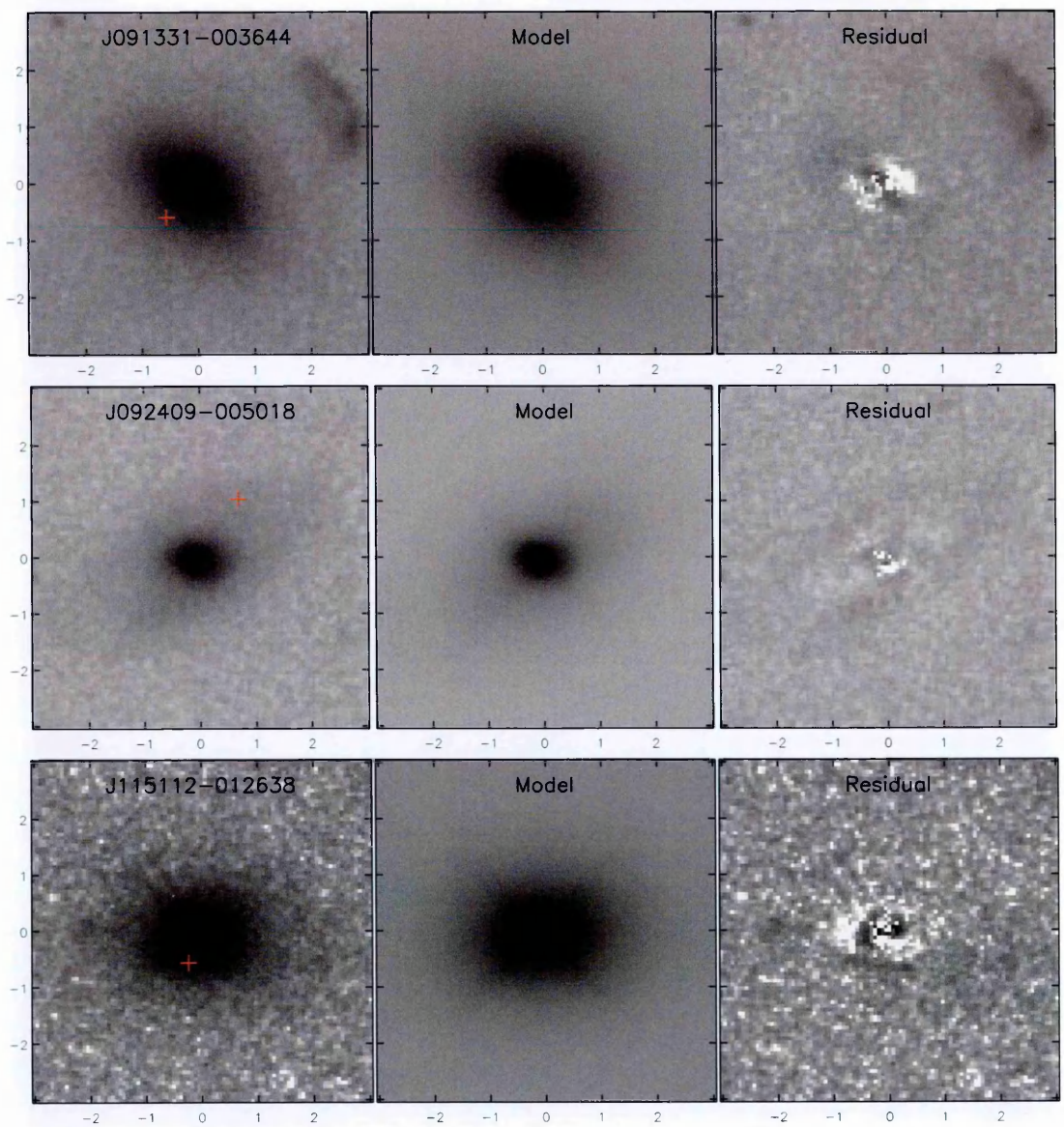

Figure 5.7: `galfit` models for the isolated lens candidate sample. Drizzled, model and residual images as shown in the left, center and right columns respectively. The SPIRE 500μm emission is denoted by the red cross.

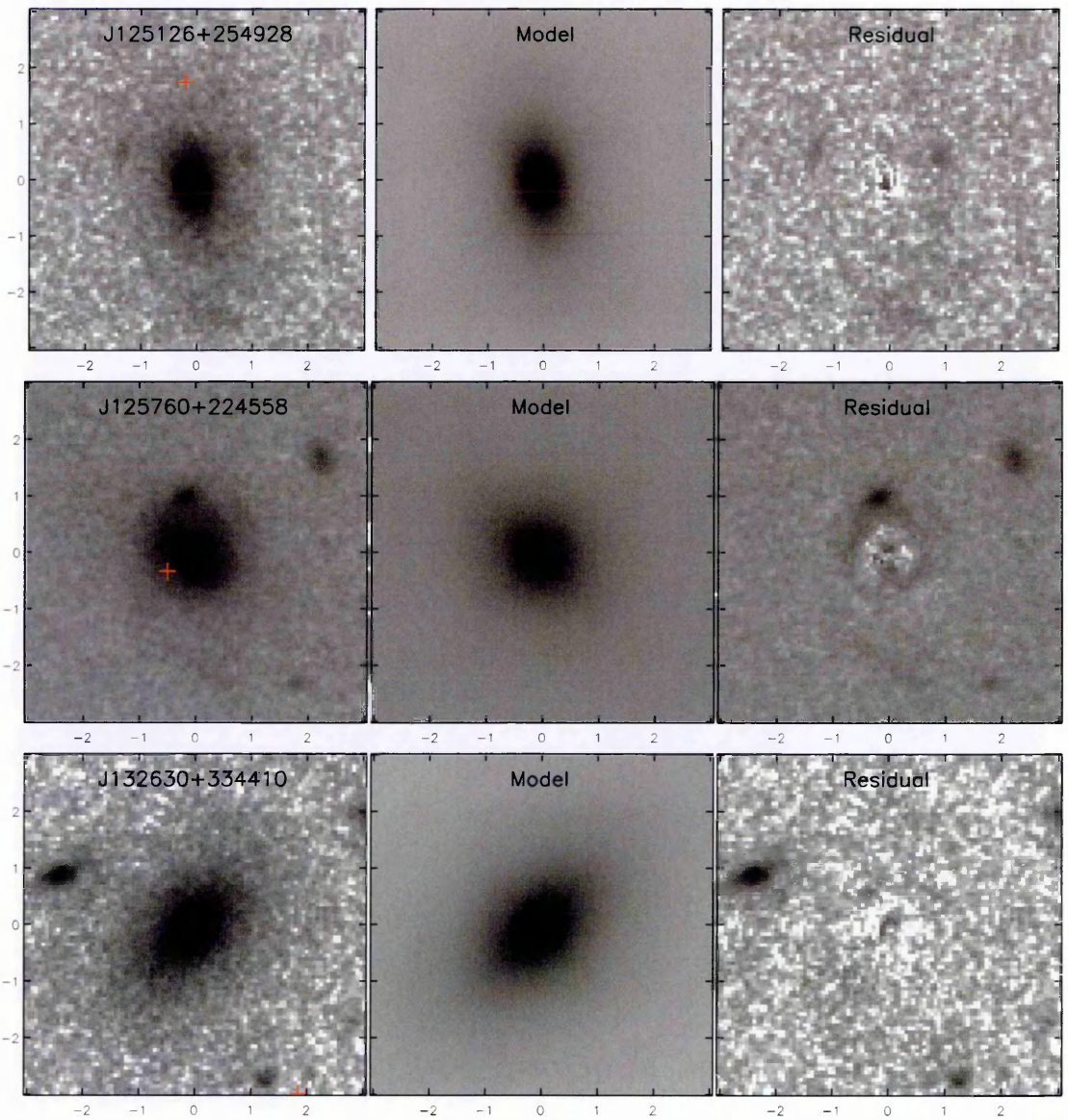

Figure 5.7 (Continued): `galfit` models for the isolated lens candidate sample. Drizzled, model and residual images as shown in the left, center and right columns respectively. The SPIRE 500μm emission is denoted by the red cross.

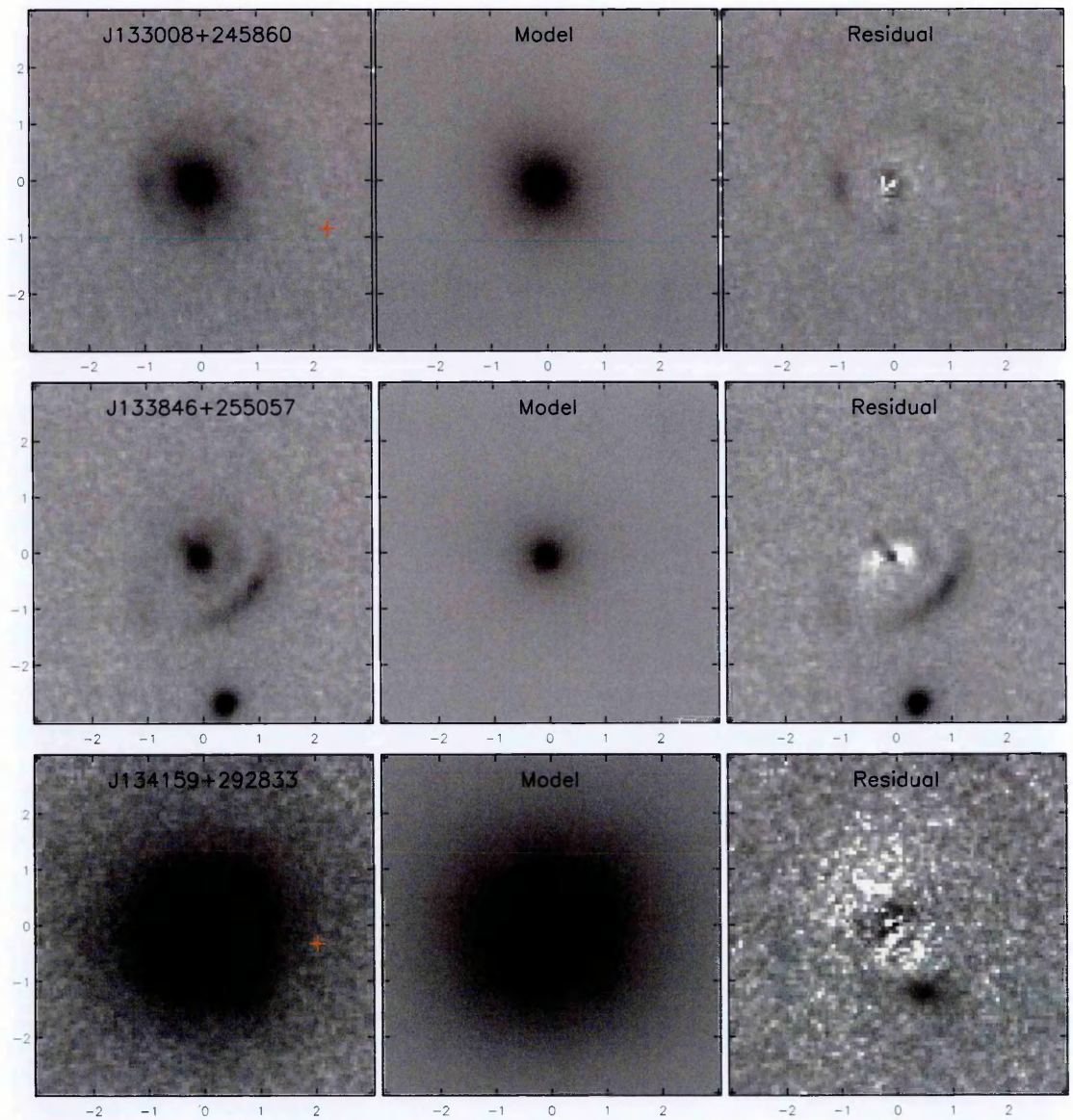

Figure 5.7 (Continued): `galfit` models for the isolated lens candidate sample. Drizzled, model and residual images as shown in the left, center and right columns respectively. The SPIRE 500μm emission is denoted by the red cross (which for J133846+255057 lies outside the cutout region).

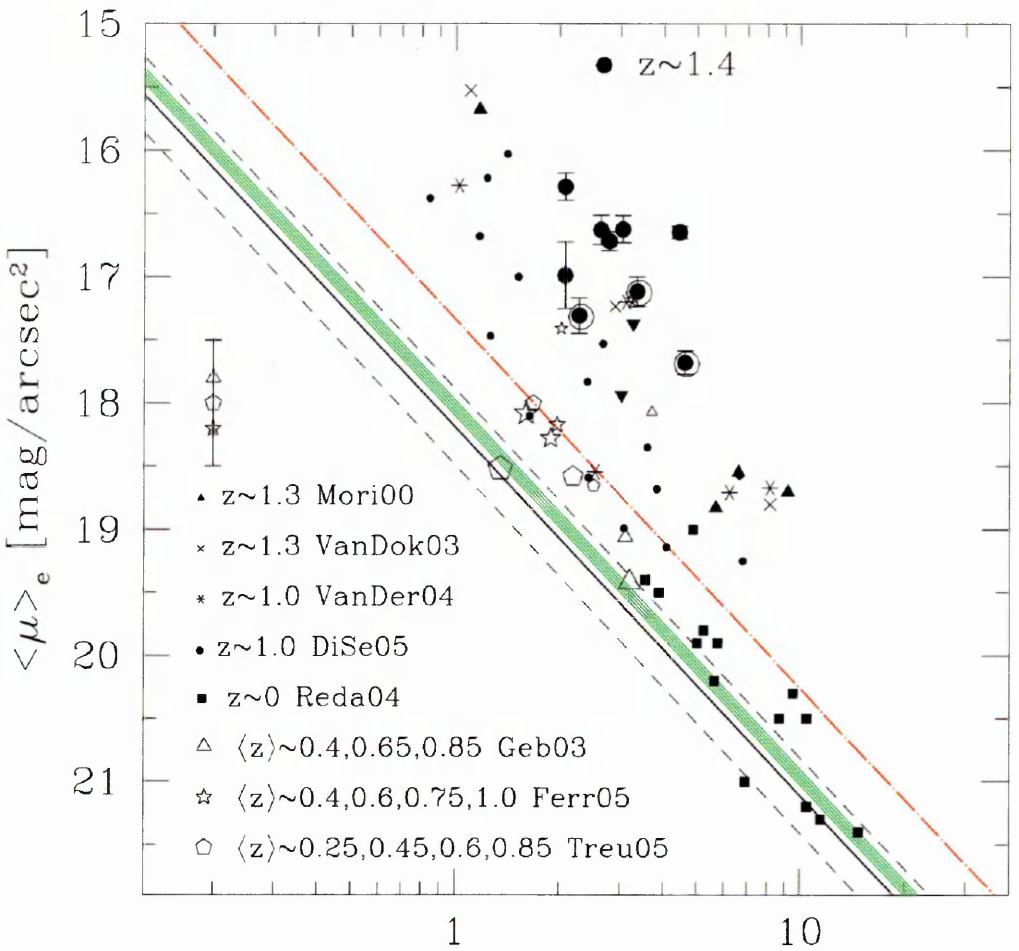

Figure 5.8: Kormendy Relation as presented in Longhetti et al. (2007). The data symbols represent the different data sets annotated in the figure. The green line and solid line (with dashed error estimates) represent different estimates of the Kormendy Relation at $z = 0$ and the dashed red line represents the relation at $z \sim 0.64$ (see Longhetti et al. (2007) and references therein).

observed linear scaling between the surface brightness, $SB(< r_e)$, and the effective radius, r_e, of early-type galaxies:

$$SB(< r_e) = \alpha + \beta log_{10}(r_e) \tag{5.1}$$

The slope of this linear relation is observed to be constant out to a redshift of $z \sim 1$, e.g. di Serego Alighieri et al. (2005), but the intercept is observed to increase with redshift, see e.g. Longhetti et al. (2007) and the sample references therein. Figure 5.8 is the Kormendy Relation presented in Longhetti et al. (2007) for number of samples of early-type galaxies which have been calibrated to the r-band and corrected for the cosmological dimming, $(1 + z)^4$.

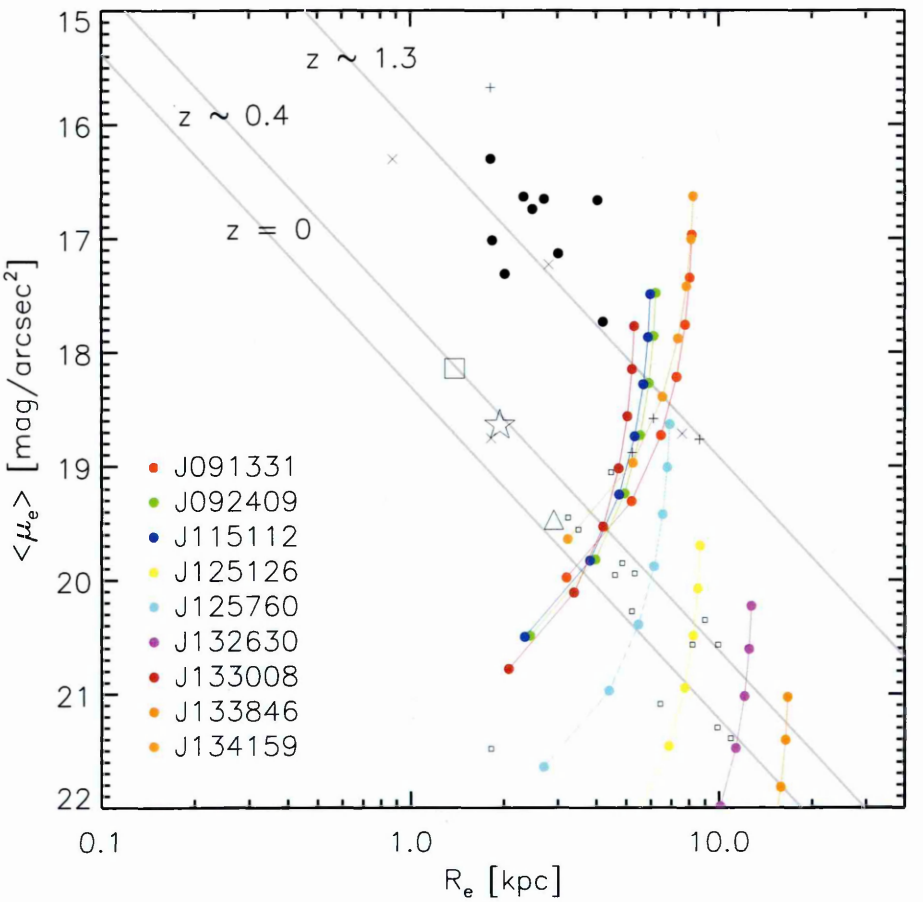

Figure 5.9: Reproduction of figure 5.8 with the addition of the HST snapshot sample as plotted in redshift tracks at points increasing vertically for $z = 0.2, 0.4, 0.6, 0.8, 1.0, 1.2, 1.4$. Kormendy Relations as determined from the linear best fits are represented as annotated grey lines for $z = 0, 0.4$ and 1.3.

Using the r-band model magnitudes and the effective radii as measured from the F110W models, under the assumption that this radius is approximately consistent at the r-band, the r-band surface brightness ($SB(< r_e)$) of the sample was calculated. For a range of redshifts, $z = 0.2 - 1.4$ with $z_{bin} = 0.2$ the effective radius is converted to the projected radius at that redshift using the angular diameter distance for each redshift bin. The resulting tracks are overplotted in figure 5.9. The best fit Kormendy Relation for the redshifts $z \sim 0.4$ is defined by the best fit lines with a slope $\beta = 2.92$ for the data points of Geb03, Ferr05 and Treu05 (square, star and triangle) and the $z \sim 1.3$ by the best fit to the data points of Mori00, VanDer04 and the Longhetti points (crosses and black points). An estimate of the redshift for each snapshot candidate is where the redshift track corresponds to the Kormendy Relation slopes.

The redshift tracks for sources *J125760* and *J133008* are in close proximity to the $z \sim 1.3$ slope for redshifts of $z = 1.2$ and $z = 1.4$ respectively, in addition the two sources *J092409* and *J115112* cross this track at a similar redshift of $z \sim 1$. Under the assumption that these sources are early-type galaxies, as supported by the best fit lens models, and that their effective radii as measured in the F110W image is an approximation to the r-band effective radii, this supports these sources lying at $z \sim 1$. The redshift tracks of sources *J091331* and *J133846* imply a convergence with a slope of much higher redshift but cannot be determined from the samples included in the work of Longhetti et al. (2007). The remaining three tracks fail to converge at plausible intercepts to support any redshift estimate.

5.3.4 Einstein Radius Redshift Estimates

Under the assumptions that the lens mass is well described by a SIS model the Einstein radius may be approximated by

$$\theta_E \sim \left(\frac{\sigma_v[km/s]}{186}\right)^2 \frac{D_{LS}}{D_S} \; [arcsec] \tag{5.2}$$

where for the majority of lens systems $D_{LS}/D_S \sim 1$ see, e.g. Serjeant (2012). The Faber-Jackson relation, Faber & Jackson (1976), correlates the luminosity of early-type galaxies

ID	θ_E [arcsec]	I_{AB}	z_{est}
J115112-012638	0.7	19.56	0.50
J125126+254928	1.2	20.20	0.91
J125760+224558	0.9	20.07	0.72
J133008+245860	0.8	20.00	0.65
J133846+255057	1.1	21.51	1.34

Table 5.2: Estimated lens redshifts based on Einstein radius, θ_E and magnitude, under the general assumption $D_{LS}/D_S \sim 1$.

with velocity dispersion,

$$f(L) \propto \sigma_v^4 \propto \theta_E^2 \tag{5.3}$$

Conversion from luminosity to magnitude incorporates the k-correction and cosmological dimming of the source defining a function of redshift dependent on magnitude and Einstein radius,

$$g(z) \propto m + 5log_{10}(\theta_E) \tag{5.4}$$

Application of the above equation to existing lens samples is shown in figure 5.10 for I_{AB} magnitudes. The SLACS sample, Bolton et al. (2008) and the high redshift lens of HDF850.1, Dunlop et al. (2004); Serjeant & Marchetti (2014), are plotted and the best fit second order polynomial determines a relation from which redshifts are estimated for the snapshot sample. Estimating θ_E as the distance of the lensed image (see discussion for individual sources) from the center of the model in the residual images and taking the SDSS I_{AB} magnitudes for the lenses the estimates of lens redshift are presented in table 5.2. The five lensed sources that display source images are estimated to be $z_{lens} > 0.5$.

5.4 Discussion and Summary

5.4.1 Model Discussion

A discussion of the targets and best fit models for the isolated sample are presented, following inspection of the best fit single sérsic profile all components and parameters were iteratively altered. Where a single sérsic profile failed to produce an adequate fit two sérsic profiles were then attempted, followed by the addition of extra components and

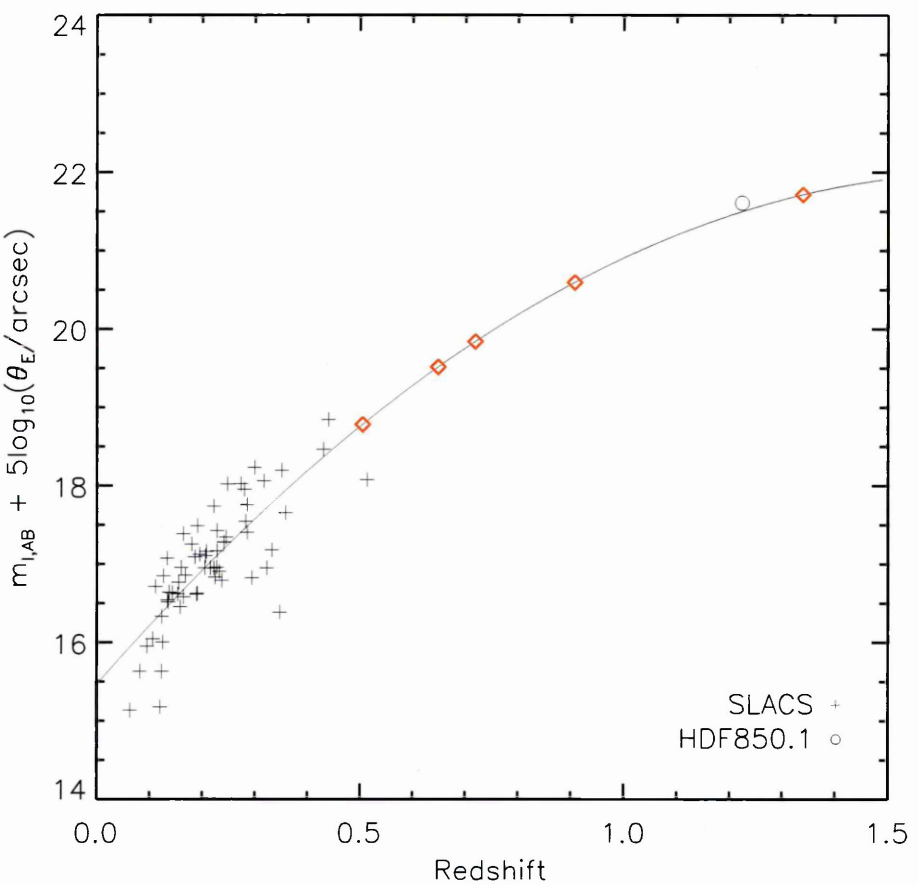

Figure 5.10: Lens redshifts as a function of magnitude and Einstein radius, derived under the general assumption of an SIS lensing mass, the Faber-Jackson relation and for $D_{LS}/D_S \sim 1$.

constrained parameters.

J091331-003644: A single sérsic profile fit revealed a bright core, prompting the addition of a psf. The residual of the resulting model indicated a bar-like component oriented diagonally. The nature of the irregular object at $\sim$ 3" is unclear and at such a distance, for an isolated galaxy lens, is unlikely to be a distorted source image.

J092409-005018: Subject to multiple fitting iterations the best fit was achieved with an exponential profile alongside a very low order sérsic and psf models. The components used in the best fit are indicative of a late-type galaxy?

J115112-012638: The initial sérsic profile revealed a bright core which with the addition of a psf component still failed to produce a smooth residual at the core. Faintly apparent is the horizontal feature $\sim$ 1.5" in length 0".5 below the center of the cutout coincident with the SPIRE centroid, this is proposed to be a direct detection of the source image. The nature of residual at the core is unclear.

J125126+254928: The best fit is produced by a single sérsic profile of index $n = 7.3$. Prior to fitting the faint images about the lens are suggestive of lensing with a discernable curvature in the tangential direction of the lens of the image on the left of center.

J125760+224558: A multiple component model fit was achieved by also fitting to the small source above the lens, which was ignored in the final model. The residual leaves a faint ring coincident with the small source and the SPIRE centroid.

J132630+334410: The best fit is produced by a single sérsic profile of index $n = 4.7$. A reasonably smooth residual does not reveal any evidence of lensing but the nature of the three sources surrounding the lens at a radius of $\sim$ 3" is unclear.

J133008+245860: A sérsic profile in combination with a psf for the core provide an adequate fit. The arc (left) and counterimages (bottom and top-right) are apparent without the model subtraction.

J133846+255057: Selected as the only isolated source in the NGP located $>$ 3.5" from the SPIRE centroid due to the obvious tangential arc about the lens candidate. The residual from the single sérsic profile may be indicative of the radial counter-image to the tangential arc.

J134159+292833: Two sérsic profiles produce the best fit which despite the noise at the core reveals the faint source $\sim$ 1" from the lens center, no tangential distortion is

apparent as such the nature of this source is unclear.

The quality of the fitting varies for this isolated sample, all of which are approximated by elliptical profiles (one indicating the presence of a bar) suggesting these early-type galaxies are not the source of bright sub-mm emission. Distinct lensing signatures are detected in three images prior to lens model subtraction and there is evidence that two more display lensed features in their residuals and a single faint source is revealed within the brightest of this sample. The remaining three have no detection of faint components which sets an upper limit (as derived from the zero point of the instrument/filter) $J_{AB} < 26.8$, which corresponds to rest-frame optical emission for $z_{source} \sim 2$.

5.4.2 Discussion and Conclusions

This chapter presents the H-ATLAS HST snapshot observations and their reduction and the first profile fitting to the isolated, robust counterpart lenses. The best fit models are indicative of early-type galaxies and five of the images alone provide compelling evidence for lensing with the presence of faint arcs and a partial ring. The lens candidates presented in this work are selected based solely on the magnification of the background source, the morphology of the lens does not affect the selection. The dominant lens sampled by SLACS, Bolton et al. (2008) were early-type galaxies due to selection effects, that the models of the lenses from this magnification based subsample are all indicative of elliptical galaxies implies that early-type galaxies are indeed a dominant lensing population.

Estimates of the redshifts of the sources by means of the Kormendy Relation and the data sets of Longhetti et al. (2007) tentatively suggest that two sources lie at $z \sim 1$ and an additional two lie at $z > 1$.

Further estimates which follow from the assumptions of an SIS lensing mass constrain the lens redshifts of those targets with observed source images in the model subtracted residuals and are found to be at $z > 0.5$.

This is in stark contrast to the lens redshifts of e.g. SLACS ($z \sim 0.3$), demonstrating that a magnification based selection reveals lenses to much higher redshifts than previous optically based selections.

Future Work

The isolated, robust counterpart, lens sample investigated in this work represent only $\sim$ 11% of the total H-ATLAS HST Snapshots. Although other targets lack the robust single counterpart identifications a similar profile fitting can be performed for all potential lens counterparts. For all profiles fitted similar analyses to estimate lens redshifts can be performed and the larger sample distribution compared to other samples (e.g. SLACS) with different selection methods.

Foreground model subtraction for the entire sample has the potential to directly reveal the signatures of the lensed background source where this is not apparent upon visual inspection of the un-subtracted images. Such cases will allow estimates of the rest-frame optical emission which will complement existing photometry and background source SED models. Where no background emission is detected the upper limits to the rest-frame optical emission can be estimated. For sources that have been observed with high-resolution ground-based instruments (e.g. Keck imaging in Calanog et al. (2014)) the HST Snapshots benefit from lower background noise and have the potential to reveal the source emission that may be overlooked with ground-based observations.

This magnification based selection of lens candidates, un-biased towards the nature of the lens, has the potential to reveal the true fraction of lensing by multiple objects/ groups/clusters. Investigations to confirm the nature of each of the 85 H-ATLAS HST Snapshots will allow this ground-breaking estimate to be made.

Chapter 6

Conclusions and Future Work

This work has investigated the large gravitational lens candidate samples of the Herschel-ATLAS by: §3: producing the first lens candidates lists for the phase 1 H-ATLAS catalogs of the NGP and SGP fields. §4: proposing, executing and reducing two cycles of visitor mode observations as the first part of a pilot study seeking lens redshifts with low resolution spectra. §5: the reduction and modelling of the H-ATLAS HST snapshot observations. A summary of these three areas and a discussion of future work is presented in this chapter.

6.1 Source Classifications and Number Counts

The inspection of $\sim$ 700 bright, $S_{500} > 80$mJy, sources from the phase 1 NGP and SGP has resulted in the classifications of local, blazar and flux-limited lens candidate target lists and postage stamps. Although compiled using an early, internal, release of the NGP and SGP source lists the lower flux limit of 80mJy ensures that any (minor) changes to source extraction and flux calibration of subsequent catalogs will not change the final sample of highly efficient ($S_{500} > 100$mJy) flux-limited candidates is present in this sample.

The bootstrap re-sampling of the local galaxies shows that, acknowledging the under-estimates of flux for extended sources present in the phase 1 catalogs, the number counts are in agreement with the models of Cai et al. (2013). This comparison was a by-product of the classification of bright sources and the local source lists and postage stamps may complement the analysis being undertaken within the local universe working group and their in-depth publications, H-ATLAS consortium (in prep.).

Comparison of the lens candidate number counts shows a good agreement with the SISSA model predictions of Lapi et al. (2012); Cai et al. (2013) and support maximum magnifications $\mu_{max} \sim 20 - 30$ in the GAMA and NGP fields. A surprise outcome of this work is the low density of lens candidates in the SGP, particularly at brighter fluxes, where the number counts are indicative of a maximum magnification $\mu_{max} \sim 10$. Two scenarios are considered: (1) the reduction of the SGP includes an underestimate in the flux calibration and (2) the number counts represent an under-density of lensed candidates over a field of 300deg^2. It has been suggested (Valiante priv. comm.) that a flux calibration error is unlikely since both the NGP and SGP were subject to exactly the same reduction pipeline. At this early stage of data reduction no conclusions will be made pending the release of future reductions and improved catalogs. Naturally, the investigation of this apparent under-density over such a large region is the immediate focus for the future work of the SGP flux-limited lens candidates. Should a flux calibration error be the cause then additional sources from future catalogs would require classification. The completion (and pending publication) of the VIKING survey would provide an improvement on the depth and the partial coverage used in the classification of this initial sample. Should the apparent under-density be confirmed with future catalogs then an investigation into the distribution of lenses and sources would be a primary focus to determine the differences in optical depth between the H-ATLAS fields.

Proposals to observe lens candidates will continue, with a particular interest to exploit the efficiency offered by ALMA, e.g. Hezaveh et al. (2013). The SGP is ideal for ALMA observations, further emphasising the importance of the future work in ensuring the sanity of the SGP lens candidate sample.

6.2 Lens Candidate Spectroscopy at the NTT

The observations of the H-ATLAS pilot study was subject to varied conditions over the course of both, cycle 91 and 93, runs. This has resulted in 25 out of a total of 57 targets being classified as *(a)* or *(b)* grade redshift estimates, robust and tentative respectively. The low success rate of observations on a 4m-class telescope has prompted future proposals to seek 8m-class observations. At the time of writing the consortium has

submitted a proposal to complete the pilot study using service mode time in moderate conditions on the VLT. The target lists generated as part of the planning for cycles 91 and 93 have provided a large number of potential targets spread over the GAMA and SGP fields which are observable throughout cycle 96.

The lens redshift distribution of the pilot sample, after a completeness correction, do not support the predictions (priv. comm.) of Eales (2015) for a range of lens mass distributions. Whilst the redshifts of the grade *(a)* lenses are robust with multiple spectral features identified it is possible that some of the *(b)* classifications are incorrect. This would have a large impact on the redshift bins presented in figure 4.8 and the corresponding completeness correction may provide a better agreement. A successful proposal that completes the remaining sample and provides $\sim$ 100 lens redshifts is the immediate objective, of which a proposal for the upcoming cycle has been submitted (PI: Marchetti). This work has demonstrated that a H-ATLAS large program to chase the redshifts of the full $\sim$ 1000 HALOS candidates is unsuitable for 4m class observations.

6.3 Lens Candidate Snapshot Observations with the HST

The reduction of the H-ATLAS HST snapshots has resulted in four co-authorships where this work has been instrumental in providing high-resolution NIR data for the investigations of the lenses of strongly lensed SMGs. Alongside simple galaxy-galaxy lenses the snapshots indicate examples of lensing by a group/cluster and cases of no distinct lenses, indicative of sources that must be highly luminous to appear in the sample of $S_{500} > 80$mJy. An initial subsample of clearly identified, isolated, lenses are subject to profile fitting with `galfit` highlighting the characteristic signatures of lensing.

Profile fitting on the remaining sources may reveal the presence of lensed signatures that are confused with the emission of the lens (e.g. J115112-012638). Measurements of the surface brightness and effective radii used in conjunction with the Kormendy Relation provide tentative estimates for the lens redshifts. Under the assumptions of a SIS lensing mass distribution estimates of redshift are obtained which place five sources at $z > 0.5$. These redshift estimates are much higher than the redshift distribution of optically selected lens sameples (SLACS) and demonstrates that a flux-limited lens selection, based purely

on the magnification of the background source, reveals lenses to much higher redshifts than optically selected samples. Further investigation into the more complex lens configurations suggested by the snapshots will further probe the lens morphology and group/cluster lensing fraction in an unbiased manner.

6.4 Concluding Remarks

This thesis has presented three data chapters: the first complete bright source classification of H-ATLAS released catalogs $\sim$ 700 sources, the first HALOS lens redshift campaign of 57 spectra and the HST snapshot campaign of 85 sources. These now form the first of rich datasets from which future proposals and additional observations will be based. The modest analyses that have been performed are but the first steps towards investigating the groundbreaking H-ATLAS gravitational lens sample.

Appendix A

Bright Source Classifications

Table A.1: Summary of NGP sources classified as lens candidates.

IAU ID	Alt. ID	S_{250} [mJy]	S_{350} [mJy]	S_{500} [mJy]	z_{phot}	z_{spec}
J134429+303034	NGP.p1.151	465.4 ± 5.7	474.1 ± 6.7	341.6 ± 7.7	2.23 ± 0.67	2.301
J132630+334408	NGP.p1.691	198.7 ± 5.6	293.0 ± 6.4	289.8 ± 7.8	3.24 ± 0.88	2.951
J132859+292327	NGP.p1.292	276.7 ± 4.7	311.9 ± 5.7	260.4 ± 6.8	2.56 ± 0.74	2.778
J125632+233627	NGP.p1.643	209.6 ± 5.6	285.7 ± 6.5	254.7 ± 7.6	2.98 ± 0.83	3.565
J132427+284450	NGP.p1.258	348.0 ± 5.6	378.3 ± 6.4	251.6 ± 7.6	2.26 ± 0.68	1.676
J125135+261458	NGP.p1.1177	156.9 ± 5.7	207.3 ± 6.4	215.2 ± 7.5	3.15 ± 0.86	3.675
J133009+245900	NGP.p1.413	269.3 ± 5.4	284.5 ± 6.4	204.2 ± 7.5	2.29 ± 0.68	3.111
J133650+291800	NGP.p1.277	294.6 ± 4.9	282.8 ± 5.9	193.6 ± 7.2	2.08 ± 0.64	2.202
J132504+311534	NGP.p1.478	245.4 ± 5.5	237.6 ± 6.5	178.2 ± 7.7	2.17 ± 0.66	1.836
J125800+224559	NGP.p1.383	291.7 ± 5.6	237.0 ± 6.4	144.9 ± 7.7	1.66 ± 0.55	–
J133414+260458	NGP.p1.1114	149.1 ± 5.4	175.6 ± 6.1	141.8 ± 7.4	2.59 ± 0.75	–
J132302+341649	NGP.p1.1528	133.3 ± 5.6	152.2 ± 6.4	140.3 ± 7.7	2.71 ± 0.77	2.194
J133847+255055	NGP.p1.1091	158.4 ± 5.7	181.1 ± 6.4	137.8 ± 7.9	2.47 ± 0.72	2.341
J125652+275900	NGP.p1.1507	139.4 ± 5.7	168.1 ± 6.5	133.8 ± 7.8	2.62 ± 0.75	2.792
J133543+300402	NGP.p1.1113	150.1 ± 5.5	158.5 ± 6.3	129.3 ± 7.5	2.41 ± 0.71	2.685
J133256+342208	NGP.p1.964	169.8 ± 5.7	189.1 ± 6.3	123.3 ± 7.7	2.29 ± 0.68	–
J133256+265528	NGP.p1.759	194.1 ± 5.7	167.7 ± 6.3	120.2 ± 7.6	1.90 ± 0.60	–
J131541+262323	NGP.p1.3837	95.7 ± 5.6	127.2 ± 6.5	118.5 ± 7.6	2.98 ± 0.83	–
J132419+320752	NGP.p1.2623	96.2 ± 5.0	121.0 ± 5.9	115.3 ± 7.1	2.92 ± 0.82	–
J134423+231952	NGP.p1.3227	113.7 ± 6.2	111.6 ± 7.2	113.4 ± 8.2	2.56 ± 0.74	–
J134159+292833	NGP.p1.684	174.4 ± 4.9	175.3 ± 6.0	110.1 ± 7.2	2.08 ± 0.64	–
J125126+254929	NGP.p1.13080	64.8 ± 5.7	103.4 ± 6.4	109.1 ± 7.7	3.48 ± 0.93	–
J134342+263919	NGP.p1.9081	70.3 ± 5.6	113.0 ± 6.3	108.1 ± 7.9	3.33 ± 0.90	–
J125441+333753	NGP.p1.536	236.7 ± 5.7	186.3 ± 6.5	107.0 ± 7.7	1.57 ± 0.53	–
J125810+263710	NGP.p1.812	190.5 ± 5.7	153.2 ± 6.4	107.0 ± 7.9	1.72 ± 0.57	–
J124753+322449	NGP.p1.13999	64.7 ± 5.7	95.1 ± 6.3	106.9 ± 7.9	3.45 ± 0.93	–
J133038+255129	NGP.p1.878	179.7 ± 5.6	163.7 ± 6.5	106.7 ± 7.8	1.93 ± 0.61	–
J130140+292918	NGP.p1.1748	127.8 ± 5.7	145.9 ± 6.4	106.6 ± 7.7	2.44 ± 0.72	–
J132900+281914	NGP.p1.1452	132.8 ± 5.5	151.2 ± 6.4	106.2 ± 7.9	2.41 ± 0.71	–
J130118+253708	NGP.p1.8965	63.3 ± 5.0	110.3 ± 6.0	106.1 ± 7.1	3.45 ± 0.93	–
J133809+255154	NGP.p1.22190	55.1 ± 5.7	90.6 ± 6.5	104.6 ± 7.6	3.69 ± 0.98	–
J130333+244643	NGP.p1.3348	98.5 ± 5.5	122.0 ± 6.4	104.3 ± 7.7	2.74 ± 0.78	–
J134856+240745	NGP.p1.4682	91.1 ± 5.7	102.9 ± 6.4	104.0 ± 7.5	2.83 ± 0.80	–
J134442+240345	NGP.p1.2045	118.5 ± 5.6	131.8 ± 6.5	103.6 ± 7.7	2.47 ± 0.72	–
J132330+311528	NGP.p1.8594	72.4 ± 5.5	92.4 ± 6.5	103.2 ± 7.7	3.21 ± 0.88	–
J132020+231500	NGP.p1.6727	65.1 ± 4.7	106.4 ± 5.8	100.8 ± 7.0	3.33 ± 0.90	–
J132411+250856	NGP.p1.2739	104.6 ± 5.5	119.7 ± 6.3	100.1 ± 7.6	2.59 ± 0.75	–
J133538+265742	NGP.p1.1702	128.3 ± 5.5	147.1 ± 6.4	99.6 ± 7.5	2.38 ± 0.70	–
J132258+325050	NGP.p1.6848	79.3 ± 5.6	88.6 ± 6.4	98.9 ± 7.6	2.95 ± 0.82	–
J130054+260304	NGP.p1.16295	62.3 ± 5.7	97.1 ± 6.4	98.3 ± 7.6	3.36 ± 0.91	–
J125526+304930	NGP.p1.857	174.5 ± 5.5	161.7 ± 6.4	98.0 ± 7.5	1.90 ± 0.60	–
J131539+292220	NGP.p1.3552	94.8 ± 5.5	115.1 ± 6.3	97.9 ± 7.6	2.71 ± 0.77	–

Continued on next page...

A.1 – Continued

IAU ID	Alt. ID	S_{250} [mJy]	S_{350} [mJy]	S_{500} [mJy]	z_{phot}	z_{spec}
J133905+340819	NGP.p1.1343	154.1 ± 5.9	158.8 ± 6.6	97.9 ± 7.8	2.11 ± 0.65	2.390
J132521+330610	NGP.p1.19275	54.3 ± 5.6	73.4 ± 6.3	97.0 ± 7.8	3.63 ± 0.96	–
J131434+335218	NGP.p1.2176	116.8 ± 5.6	132.6 ± 6.4	96.7 ± 7.8	2.44 ± 0.72	–
J131919+235439	NGP.p1.1931	120.6 ± 5.5	120.0 ± 6.5	96.5 ± 7.7	2.29 ± 0.68	–
J132227+300721	NGP.p1.1298	141.9 ± 5.4	133.1 ± 6.4	96.0 ± 7.6	2.08 ± 0.64	–
J130415+303539	NGP.p1.2353	115.9 ± 5.6	119.9 ± 6.4	95.9 ± 7.7	2.38 ± 0.70	–
J133147+285531	NGP.p1.694	192.5 ± 5.4	149.2 ± 6.4	95.7 ± 7.7	1.60 ± 0.54	–
J132314+285039	NGP.p1.911	175.1 ± 5.6	144.4 ± 6.4	95.4 ± 7.7	1.75 ± 0.57	–
J130432+295338	NGP.p1.7770	79.8 ± 5.7	108.2 ± 6.3	95.1 ± 7.6	2.95 ± 0.82	–
J131211+323837	NGP.p1.7855	78.4 ± 5.8	101.3 ± 6.5	95.0 ± 7.6	2.95 ± 0.82	–
J134903+284636	NGP.p1.32851	49.4 ± 5.6	89.3 ± 6.4	94.7 ± 7.7	3.66 ± 0.97	–
J133440+353141	NGP.p1.6171	83.5 ± 5.8	111.1 ± 6.5	94.4 ± 7.8	2.86 ± 0.80	–
J132909+300957	NGP.p1.6642	76.6 ± 5.5	115.0 ± 6.5	94.3 ± 7.6	3.01 ± 0.83	–
J133534+341836	NGP.p1.3065	107.8 ± 5.8	120.2 ± 6.4	94.2 ± 7.6	2.47 ± 0.72	–
J133700+321758	NGP.p1.2445	104.7 ± 5.2	107.2 ± 6.1	93.2 ± 7.3	2.44 ± 0.72	–
J133702+320847	NGP.p1.7450	75.9 ± 5.6	97.5 ± 6.3	93.1 ± 7.7	2.98 ± 0.83	–
J134403+242627	NGP.p1.4114	93.3 ± 5.6	108.1 ± 6.6	92.9 ± 7.7	2.65 ± 0.76	–
J131612+281219	NGP.p1.9536	71.7 ± 5.7	103.0 ± 6.3	92.7 ± 7.6	3.06 ± 0.84	–
J133057+311740	NGP.p1.12013	65.2 ± 5.6	72.0 ± 6.4	92.8 ± 7.6	3.21 ± 0.88	–
J132129+282020	NGP.p1.1944	119.4 ± 5.5	132.9 ± 6.5	92.6 ± 7.5	2.35 ± 0.70	–
J131222+270219	NGP.p1.5793	82.2 ± 5.5	105.7 ± 6.3	92.2 ± 7.5	2.83 ± 0.80	–
J134124+354007	NGP.p1.3886	93.2 ± 5.6	104.8 ± 6.5	92.1 ± 7.7	2.62 ± 0.75	–
J125911+293843	NGP.p1.1128	155.7 ± 5.6	135.6 ± 6.6	90.8 ± 7.8	1.87 ± 0.60	–
J130712+263931	NGP.p1.7818	75.3 ± 5.7	101.4 ± 6.4	90.5 ± 7.6	2.95 ± 0.82	–
J131805+325016	NGP.p1.4707	86.7 ± 5.6	110.2 ± 6.5	90.2 ± 7.7	2.74 ± 0.78	–
J125354+271746	NGP.p1.5697	86.5 ± 5.8	92.8 ± 6.4	89.1 ± 7.8	2.65 ± 0.76	–
J131247+320723	NGP.p1.5727	82.6 ± 5.6	103.4 ± 6.5	87.8 ± 8.0	2.77 ± 0.78	–
J133705+291137	NGP.p1.2273	107.4 ± 5.1	108.9 ± 6.0	87.8 ± 7.4	2.32 ± 0.69	–
J131157+301320	NGP.p1.3750	97.6 ± 5.7	131.4 ± 6.4	87.6 ± 7.5	2.62 ± 0.75	–
J131741+350325	NGP.p1.5184	89.8 ± 5.9	108.5 ± 6.7	87.4 ± 8.0	2.65 ± 0.76	–
J131915+330824	NGP.p1.10893	69.0 ± 5.6	81.1 ± 6.3	86.9 ± 7.5	2.98 ± 0.83	–
J134140+322833	NGP.p1.8960	64.8 ± 5.0	91.8 ± 5.9	86.7 ± 7.2	3.12 ± 0.86	–
J125905+314727	NGP.p1.330	283.0 ± 4.9	217.3 ± 5.9	86.0 ± 7.1	1.36 ± 0.49	–
J131020+253732	NGP.p1.8953	74.2 ± 5.6	101.1 ± 6.4	86.0 ± 7.8	2.92 ± 0.82	–
J131811+335707	NGP.p1.7764	70.3 ± 5.7	84.9 ± 6.5	85.7 ± 7.7	2.95 ± 0.82	–
J131642+251159	NGP.p1.793	185.7 ± 5.5	142.5 ± 6.5	85.6 ± 7.8	1.54 ± 0.53	–
J131718+305505	NGP.p1.7263	67.6 ± 4.9	90.8 ± 5.8	84.6 ± 7.0	3.01 ± 0.83	–
J131435+301803	NGP.p1.4004	90.2 ± 5.5	102.7 ± 6.4	84.2 ± 7.6	2.56 ± 0.74	–
J131059+323329	NGP.p1.51946	42.3 ± 5.7	67.8 ± 6.4	84.0 ± 7.5	3.78 ± 0.99	–
J133518+311118	NGP.p1.3624	99.0 ± 5.7	116.9 ± 6.4	83.8 ± 7.6	2.47 ± 0.72	–
J134624+341607	NGP.p1.20835	56.9 ± 5.8	85.8 ± 6.4	83.8 ± 7.6	3.27 ± 0.89	–
J133828+313955	NGP.p1.3257	100.2 ± 5.5	100.0 ± 6.4	83.6 ± 7.6	2.35 ± 0.70	–
J131149+302211	NGP.p1.8588	71.8 ± 5.7	85.9 ± 6.5	83.5 ± 7.6	2.86 ± 0.80	–
J134654+295659	NGP.p1.1017	163.9 ± 5.7	130.8 ± 6.5	83.3 ± 7.8	1.66 ± 0.55	–
J133250+272945	NGP.p1.3555	100.7 ± 5.7	99.3 ± 6.5	82.8 ± 7.7	2.32 ± 0.69	–
J131002+264759	NGP.p1.18492	53.2 ± 5.5	85.4 ± 6.4	82.7 ± 7.9	3.33 ± 0.90	–
J125504+283817	NGP.p1.9544	57.7 ± 5.0	50.6 ± 5.9	82.6 ± 7.1	3.18 ± 0.87	–
J133715+352055	NGP.p1.11930	66.5 ± 5.6	92.3 ± 6.4	82.5 ± 7.8	3.01 ± 0.83	–
J124954+330737	NGP.p1.9414	72.1 ± 5.6	96.5 ± 6.4	82.3 ± 7.6	2.89 ± 0.81	–
J130525+342852	NGP.p1.1595	132.0 ± 5.6	134.4 ± 6.5	82.2 ± 7.6	2.08 ± 0.64	–
J132736+253228	NGP.p1.5320	84.5 ± 5.6	99.2 ± 6.5	82.0 ± 7.7	2.62 ± 0.75	–
J124903+342520	NGP.p1.16997	59.1 ± 5.6	83.3 ± 6.3	81.5 ± 7.6	3.15 ± 0.86	–
J125105+261653	NGP.p1.2070	116.5 ± 5.5	125.3 ± 6.5	81.3 ± 7.7	2.23 ± 0.67	–
J131322+285832	NGP.p1.16137	52.7 ± 5.1	84.0 ± 5.9	81.2 ± 7.1	3.33 ± 0.90	–
J131302+305942	NGP.p1.1133	155.3 ± 5.6	127.8 ± 6.4	81.0 ± 7.8	1.72 ± 0.57	–
J132048+330956	NGP.p1.11250	67.4 ± 5.6	95.3 ± 6.4	81.0 ± 7.7	2.98 ± 0.83	–
J133345+263815	NGP.p1.18439	57.4 ± 5.5	82.7 ± 6.4	81.0 ± 7.6	3.18 ± 0.87	–
J131645+321223	NGP.p1.5092	68.7 ± 4.5	87.1 ± 5.6	80.5 ± 6.9	2.89 ± 0.81	–
J130505+305558	NGP.p1.5391	85.9 ± 5.6	100.8 ± 6.5	80.3 ± 7.7	2.59 ± 0.75	–
J132818+300137	NGP.p1.7299	76.2 ± 5.6	97.6 ± 6.4	80.4 ± 7.8	2.77 ± 0.78	–
J133232+350843	NGP.p1.1801	129.5 ± 5.8	114.4 ± 6.4	80.3 ± 7.7	1.93 ± 0.61	–
J125452+271930	NGP.p1.3597	96.2 ± 5.6	90.6 ± 6.4	80.2 ± 7.5	2.32 ± 0.69	–

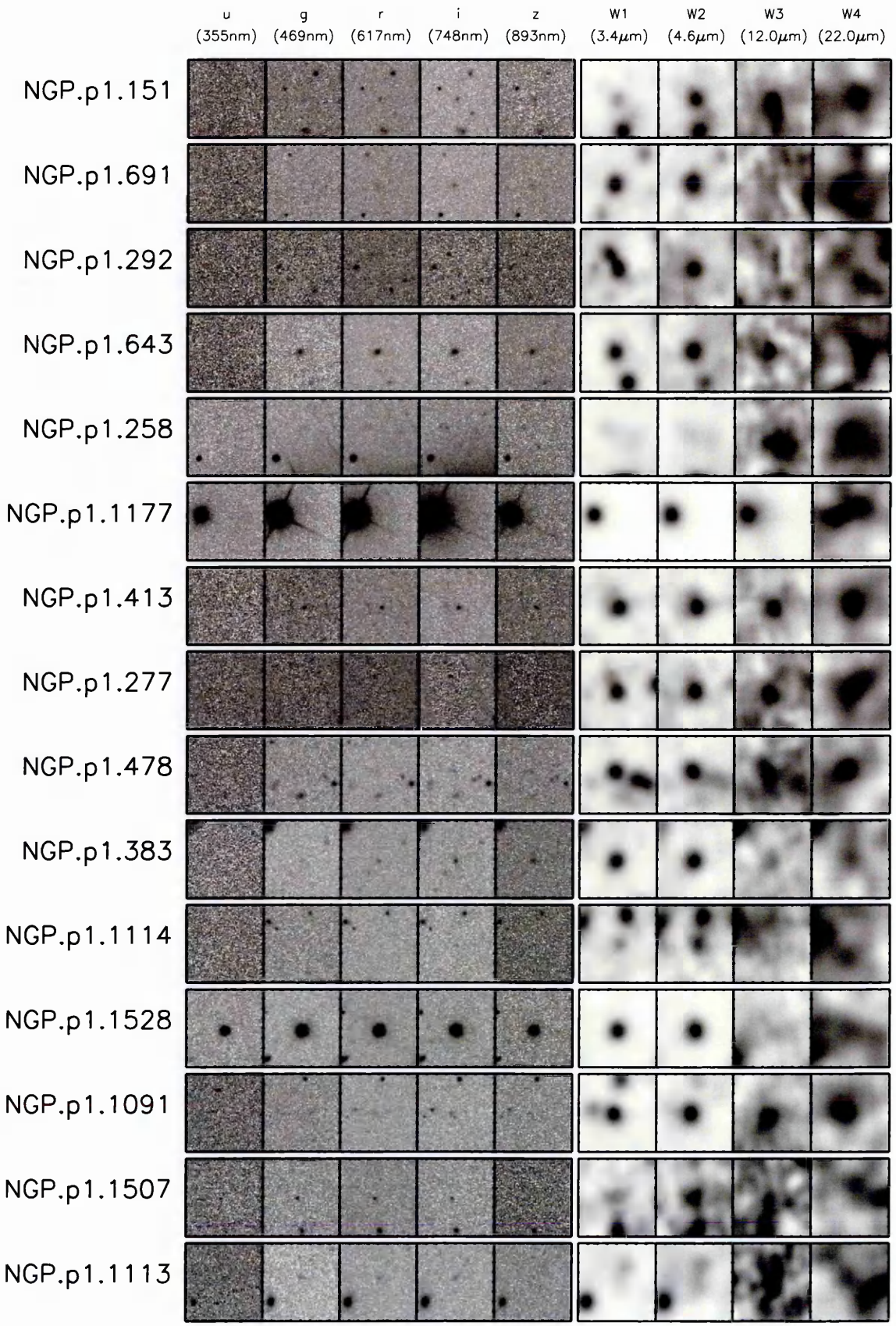

Figure A.1: NGP $S_{500} \geq 100$mJy lens candidate postage stamps.

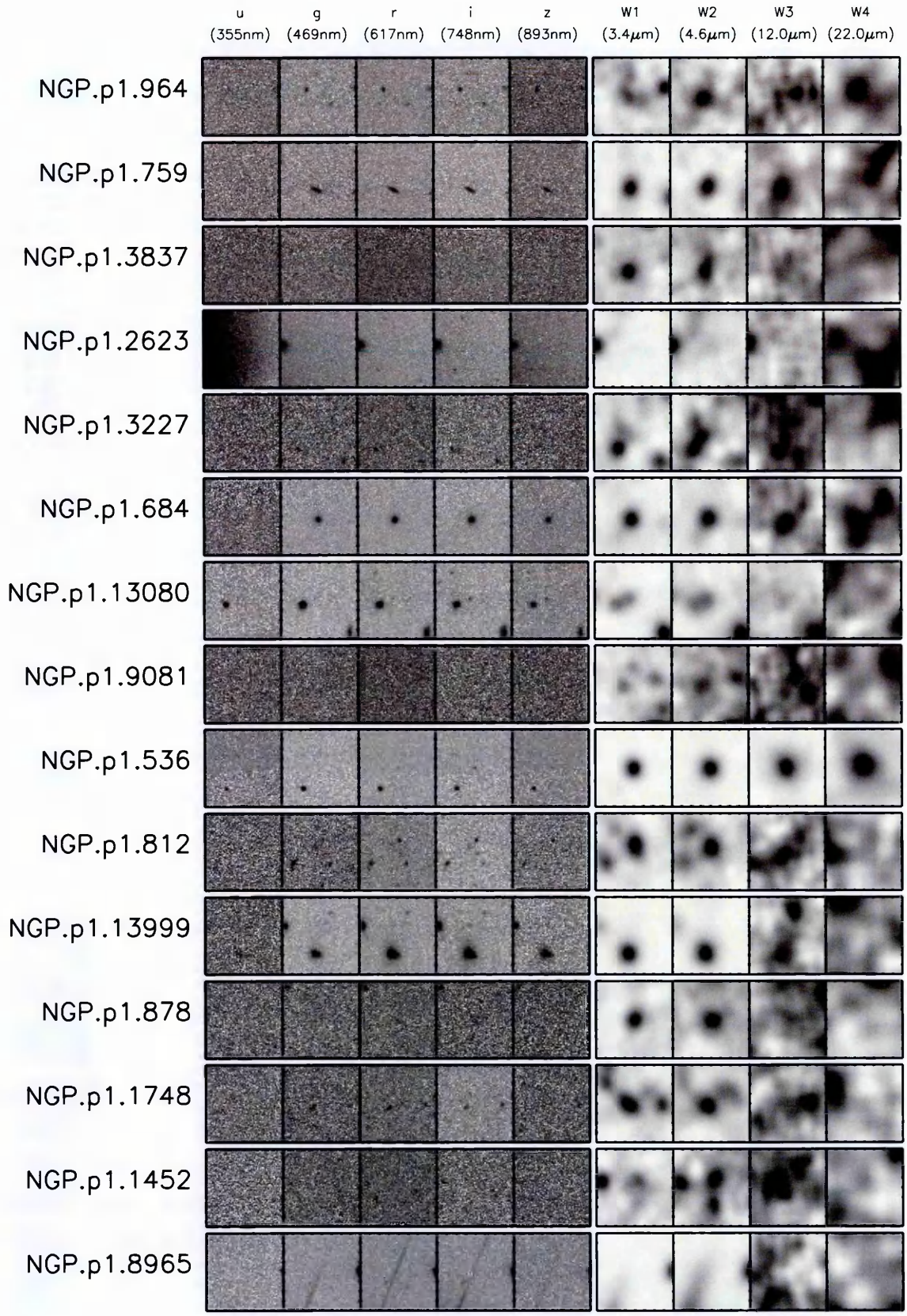

Figure A.1 (Continued): NGP $S_{500} \geq 100$mJy lens candidate postage stamps.

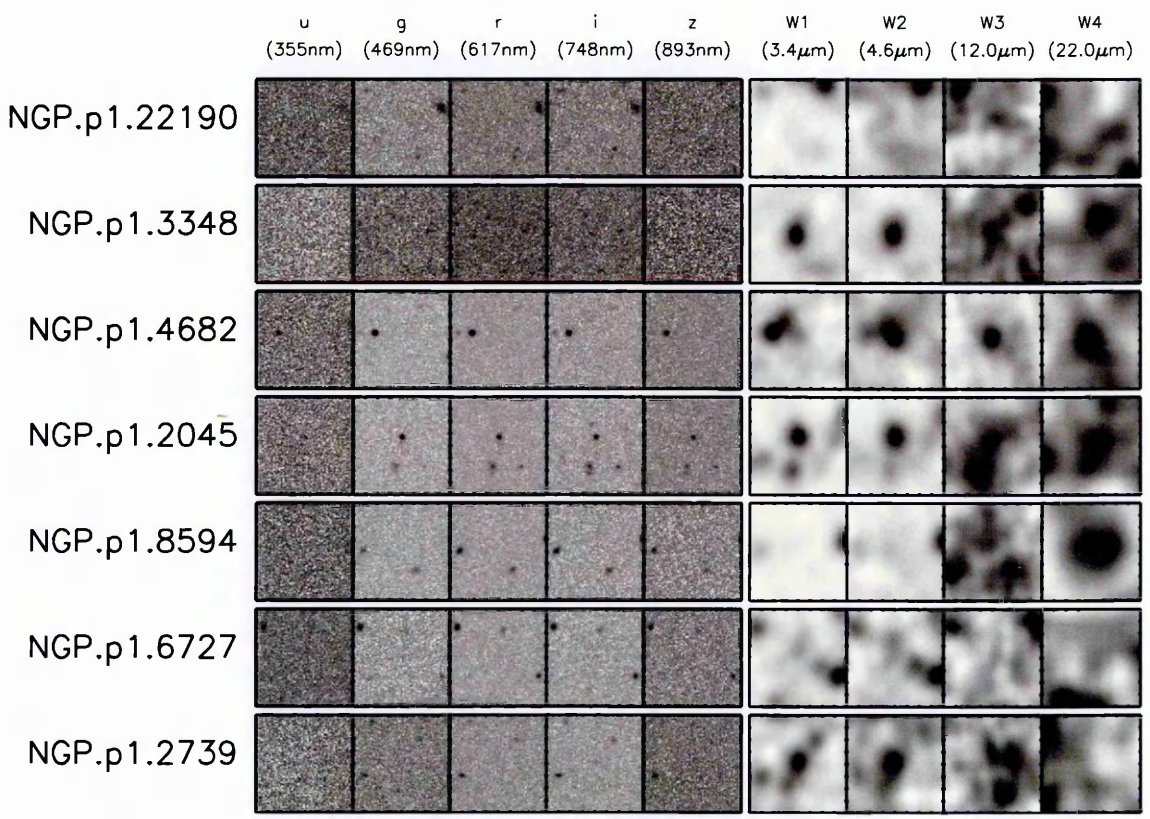

Figure A.1 (Continued): NGP $S_{500} \geq 100$mJy lens candidate postage stamps.

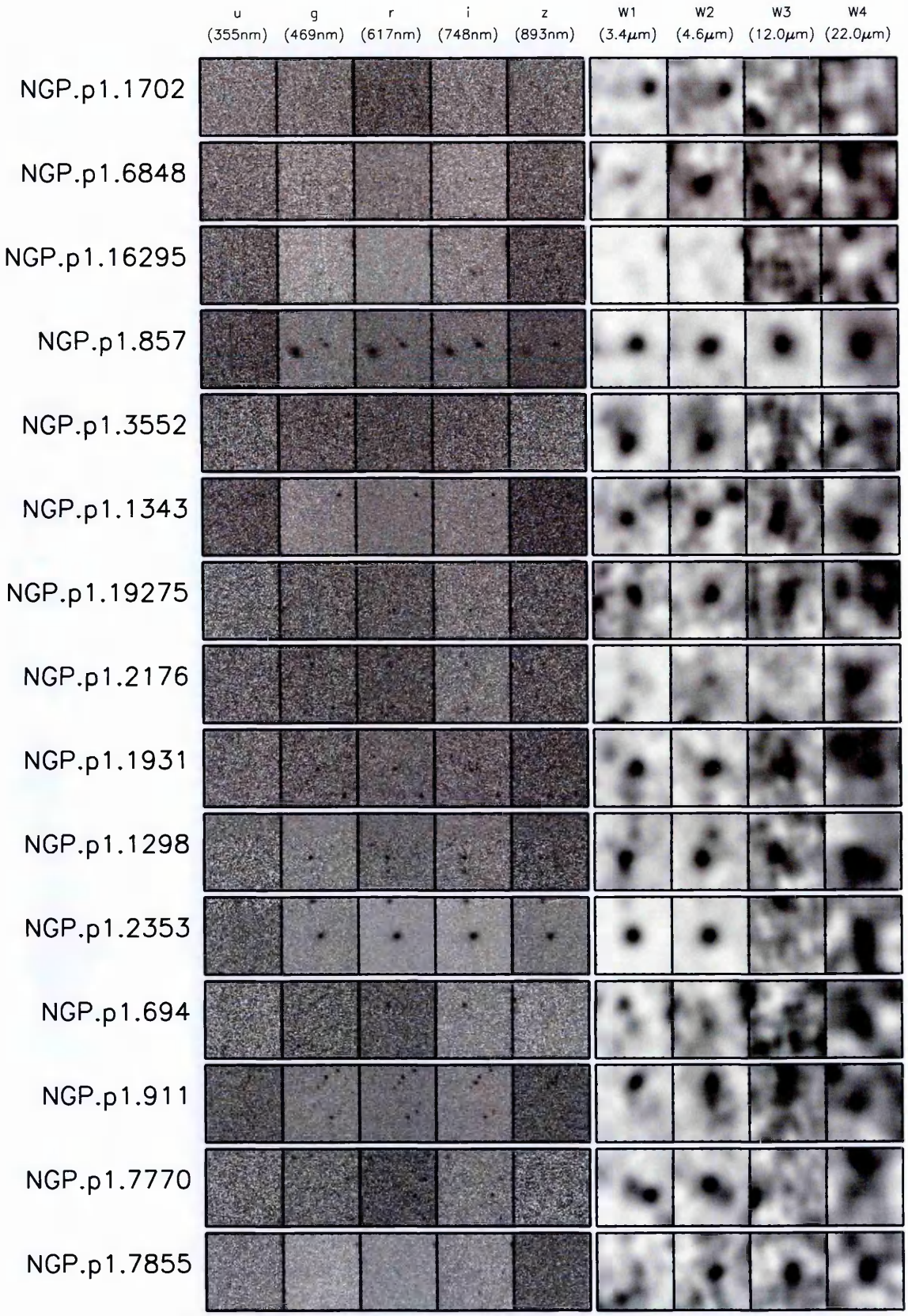

Figure A.2: NGP $90 \leq S_{500} < 100$mJy lens candidate postage stamps.

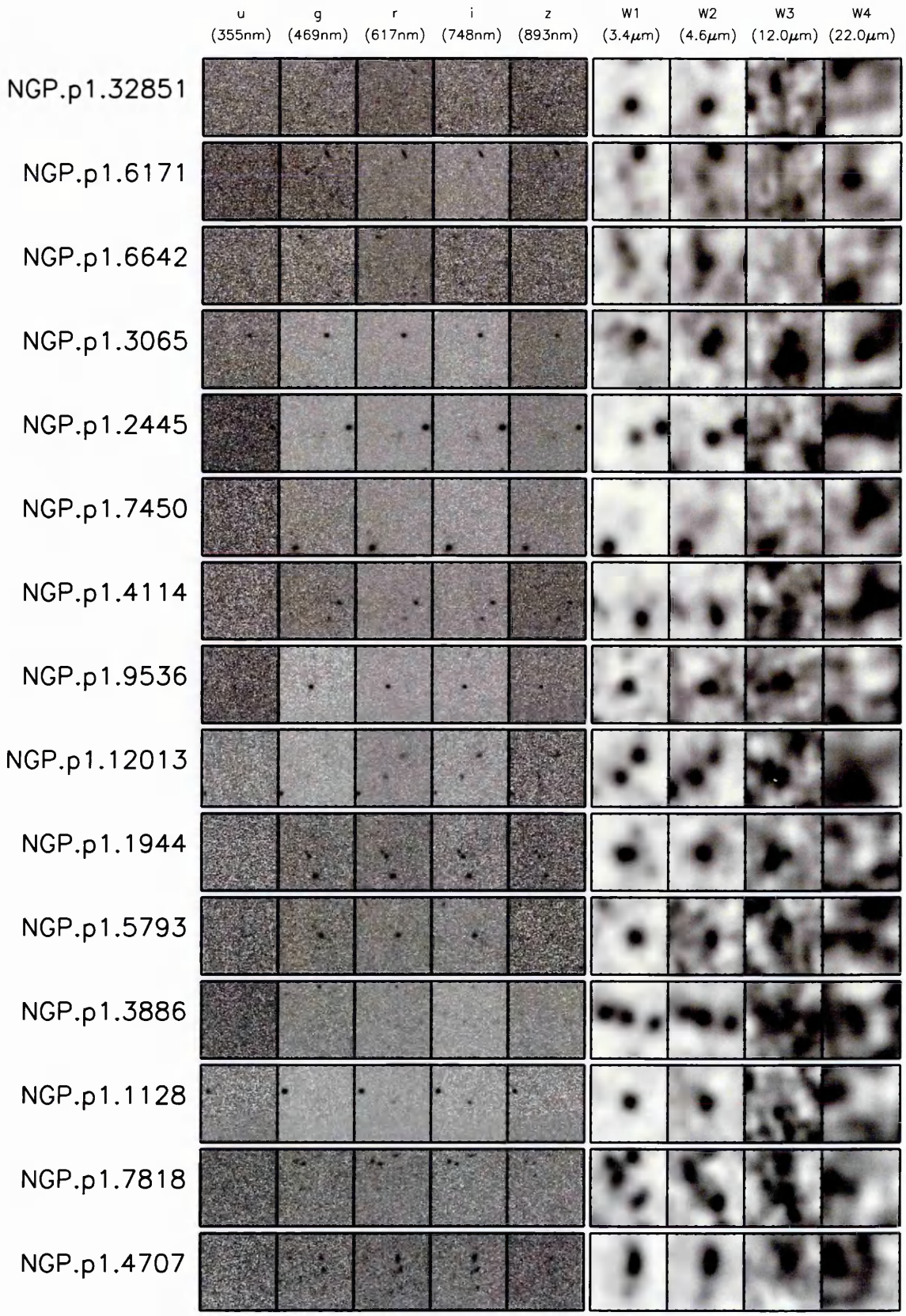

Figure A.2 (Continued): NGP $90 \leq S_{500} < 100$mJy lens candidate postage stamps.

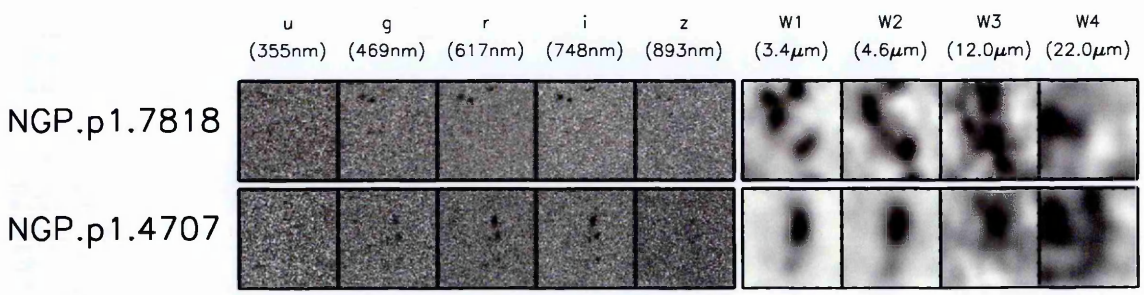

Figure A.2 (Continued): NGP $90 \leq S_{500} < 100$mJy lens candidate postage stamps.

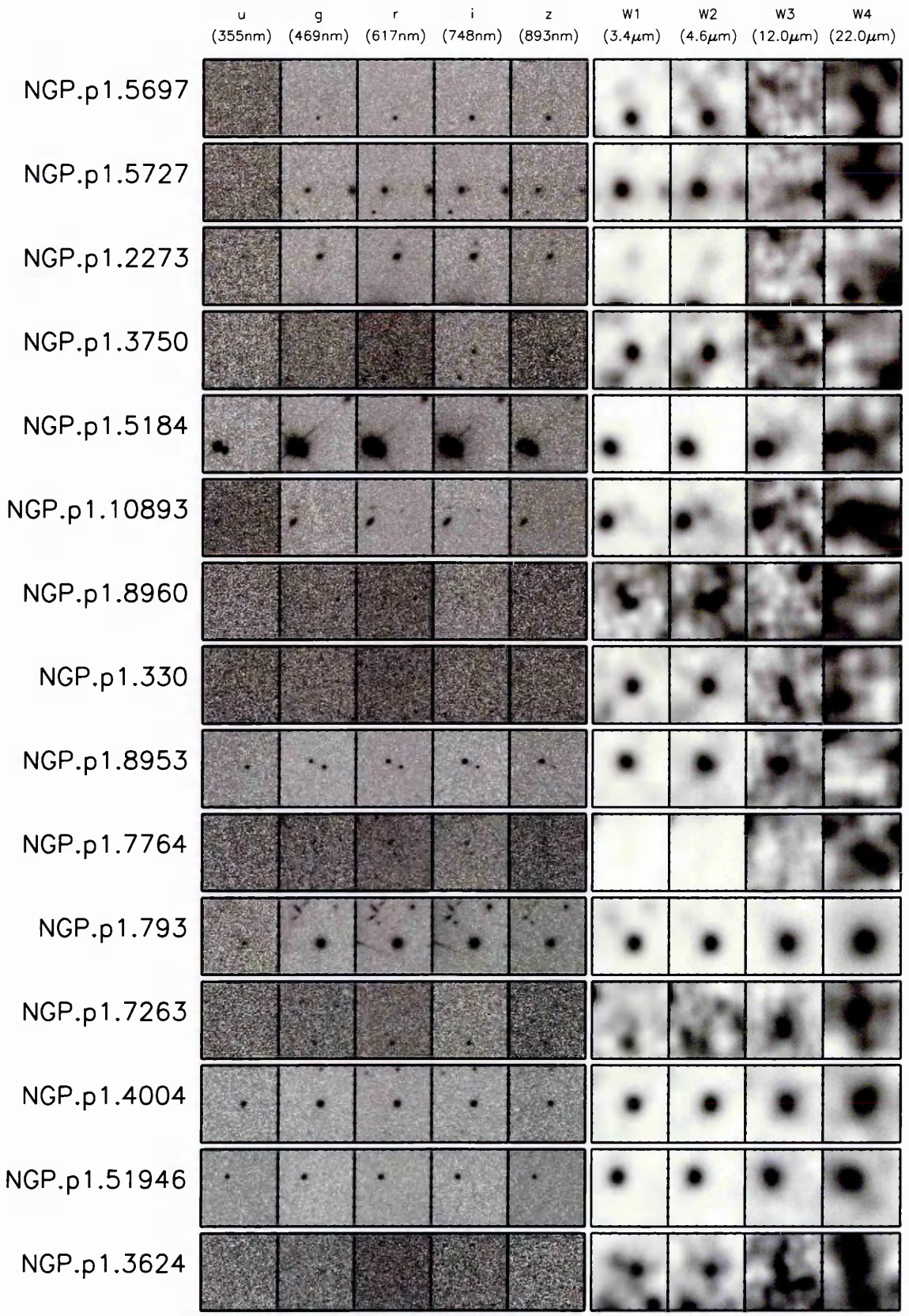

Figure A.3: NGP $80 \leq S_{500} < 90$mJy lens candidate postage stamps.

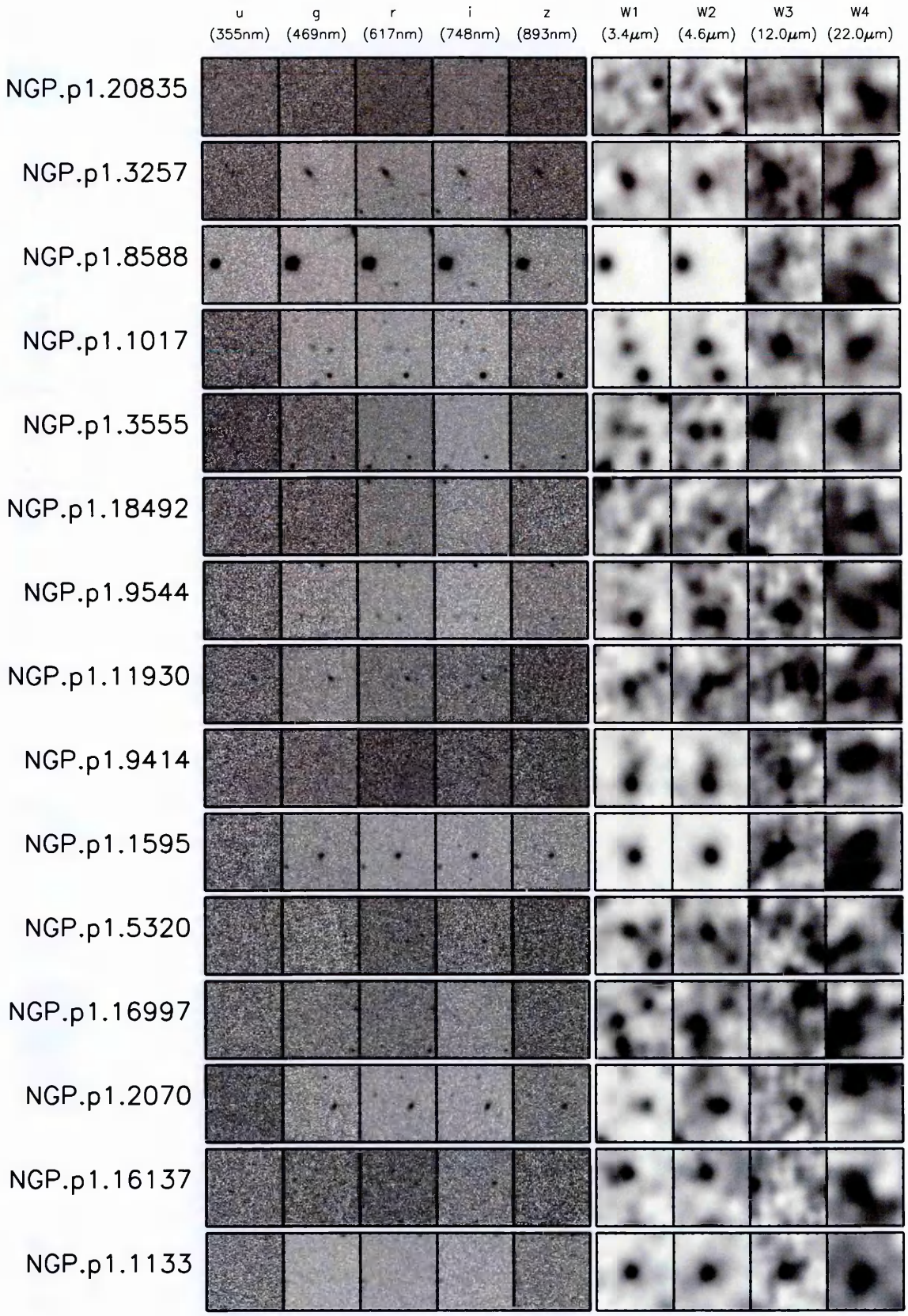

Figure A.3 (Continued): NGP $80 \leq S_{500} < 90$mJy lens candidate postage stamps.

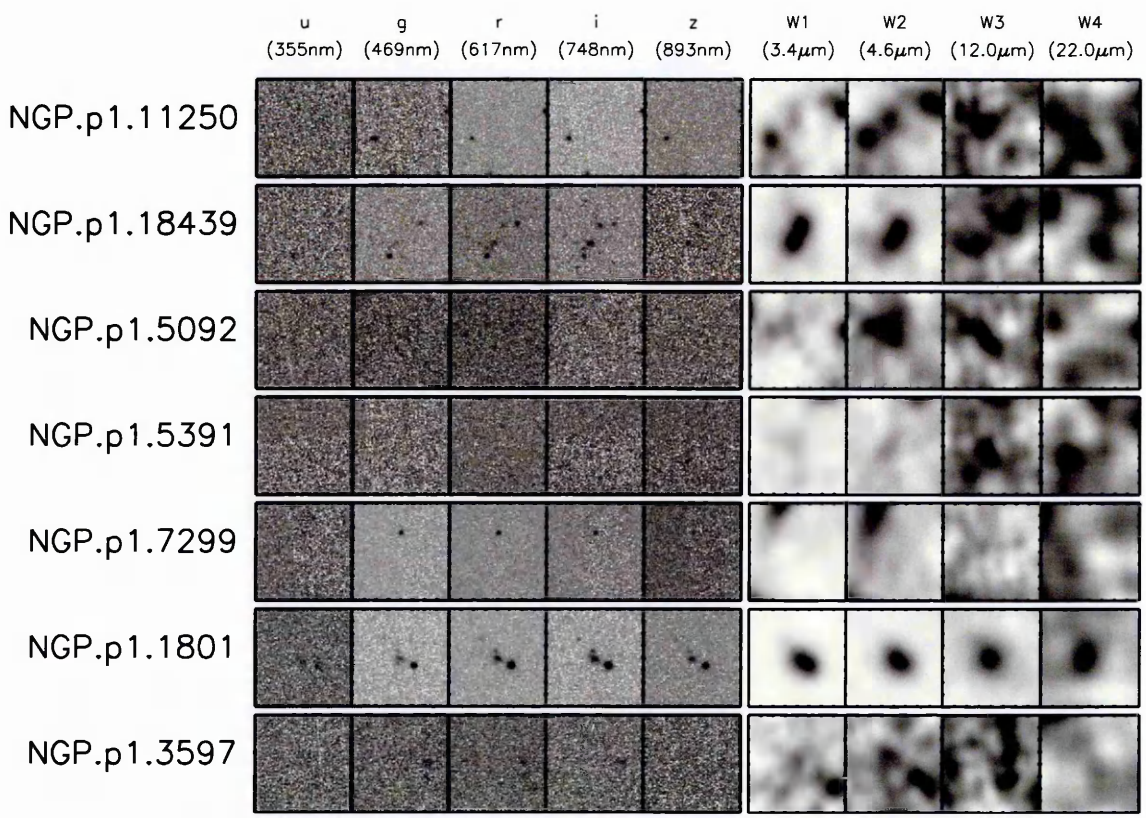

Figure A.3 (Continued): NGP $80 \leq S_{500} < 90$mJy lens candidate postage stamps.

Table A.2: Summary of SGP sources classified as lens candidates.

IAU ID	Alt. ID	S_{250} [mJy]	S_{350} [mJy]	S_{500} [mJy]	z_{phot}	z_{spec}
J012407-281435	SGP.p1.631	262.4 ± 6.1	276.9 ± 6.6	208.2 ± 7.7	2.35 ± 0.70	–
J013841-281855	SGP.p1.3411	120.0 ± 5.9	184.2 ± 6.6	185.6 ± 7.9	3.33 ± 0.90	–
J010251-311723	SGP.p1.410	282.6 ± 5.5	272.7 ± 6.4	182.2 ± 7.8	2.05 ± 0.63	–
J232531-302236	SGP.p1.772	181.4 ± 4.9	233.0 ± 5.8	178.3 ± 7.0	2.68 ± 0.77	–
J232420-323926	SGP.p1.545	219.0 ± 4.9	248.5 ± 5.8	175.0 ± 7.0	2.41 ± 0.71	–
J234358-351724	SGP.p1.463	270.4 ± 5.6	230.2 ± 6.4	155.9 ± 7.7	1.84 ± 0.59	–
J000913-300807	SGP.p1.290	356.3 ± 5.7	273.9 ± 6.6	154.3 ± 7.6	1.51 ± 0.52	–
J002625-341738	SGP.p1.2022	139.8 ± 5.6	189.4 ± 6.5	148.3 ± 7.7	2.80 ± 0.79	–
J012046-282403	SGP.p1.4775	107.3 ± 5.9	158.9 ± 6.5	147.9 ± 8.0	3.15 ± 0.86	–
J230816-343758	SGP.p1.9838	82.5 ± 5.7	133.2 ± 6.4	146.7 ± 7.8	3.57 ± 0.95	–
J234418-303936	SGP.p1.2590	124.5 ± 5.5	182.6 ± 6.4	146.4 ± 7.8	2.95 ± 0.82	–
J235828-323244	SGP.p1.2691	113.4 ± 5.1	145.5 ± 6.0	141.2 ± 7.1	2.98 ± 0.83	–
J225845-295125	SGP.p1.1064	183.4 ± 5.6	193.8 ± 6.6	138.3 ± 8.1	2.29 ± 0.68	–
J224805-335820	SGP.p1.2601	132.0 ± 5.9	150.5 ± 6.8	137.7 ± 7.9	2.71 ± 0.77	–
J232623-342642	SGP.p1.936	169.3 ± 5.0	194.9 ± 6.0	132.0 ± 7.2	2.38 ± 0.70	–
J013240-330906	SGP.p1.2941	122.4 ± 5.7	164.0 ± 6.7	127.3 ± 7.8	2.77 ± 0.78	–
J000008-334100	SGP.p1.1956	137.2 ± 5.6	173.5 ± 6.5	125.2 ± 7.5	2.59 ± 0.75	–
J003208-303724	SGP.p1.3428	108.1 ± 5.3	128.2 ± 6.1	120.0 ± 7.3	2.80 ± 0.79	–
J225251-313658	SGP.p1.1527	136.2 ± 4.8	150.0 ± 5.9	119.5 ± 7.0	2.47 ± 0.72	–
J013952-321447	SGP.p1.2304	124.7 ± 5.3	136.8 ± 6.1	117.5 ± 7.3	2.53 ± 0.73	–
J224435-324203	SGP.p1.839	217.6 ± 6.0	180.5 ± 6.7	116.7 ± 8.1	1.75 ± 0.57	–
J014520-313835	SGP.p1.3697	117.7 ± 5.9	126.6 ± 6.7	116.3 ± 8.1	2.59 ± 0.75	–
J001030-330615	SGP.p1.4722	90.6 ± 5.0	112.2 ± 5.9	114.5 ± 7.2	2.98 ± 0.83	–
J011824-274405	SGP.p1.2002	142.9 ± 5.7	148.8 ± 6.4	114.3 ± 8.0	2.32 ± 0.69	–
J005630-311206	SGP.p1.3584	113.7 ± 5.7	152.2 ± 6.4	113.8 ± 8.0	2.74 ± 0.78	–
J224207-324200	SGP.p1.17359	70.2 ± 5.8	100.2 ± 6.7	113.8 ± 8.2	3.42 ± 0.92	–
J222629-321111	SGP.p1.6229	129.2 ± 7.8	142.0 ± 8.0	113.6 ± 10.5	2.47 ± 0.72	–
J230546-331039	SGP.p1.9847	83.6 ± 5.8	117.1 ± 6.5	113.6 ± 7.7	3.15 ± 0.86	–
J232901-321744	SGP.p1.2390	120.2 ± 5.1	144.2 ± 6.1	113.4 ± 7.3	2.59 ± 0.75	–
J223754-305828	SGP.p1.1798	142.5 ± 5.3	154.4 ± 6.1	111.6 ± 7.3	2.35 ± 0.70	–
J224401-340031	SGP.p1.3237	121.5 ± 5.8	141.6 ± 6.7	111.4 ± 7.9	2.56 ± 0.74	–
J004853-303109	SGP.p1.2266	121.6 ± 5.0	154.4 ± 5.9	110.7 ± 7.1	2.59 ± 0.75	–
J002534-333825	SGP.p1.2624	118.0 ± 5.3	138.7 ± 6.5	110.5 ± 7.7	2.59 ± 0.75	–
J012416-310500	SGP.p1.1893	146.6 ± 5.7	157.8 ± 6.5	110.1 ± 7.8	2.29 ± 0.68	–
J005133-301848	SGP.p1.1427	164.5 ± 5.7	158.0 ± 6.5	109.1 ± 7.9	2.08 ± 0.64	–
J000018-333738	SGP.p1.28606	60.4 ± 5.8	84.4 ± 6.3	107.3 ± 7.8	3.63 ± 0.96	–
J005132-302012	SGP.p1.1849	139.4 ± 5.4	140.8 ± 6.4	106.4 ± 7.5	2.26 ± 0.68	–
J005659-295040	SGP.p1.16972	70.7 ± 5.8	116.2 ± 6.5	106.4 ± 7.8	3.30 ± 0.89	–
J003729-284124	SGP.p1.3915	108.6 ± 5.6	106.4 ± 6.4	105.0 ± 7.8	2.50 ± 0.73	–
J224028-343135	SGP.p1.3020	124.7 ± 5.9	129.7 ± 6.6	104.5 ± 8.0	2.38 ± 0.70	–
J013004-305514	SGP.p1.897	170.7 ± 4.9	158.5 ± 6.0	104.0 ± 7.0	1.99 ± 0.62	–
J223829-304149	SGP.p1.415	259.7 ± 5.0	210.7 ± 6.1	103.7 ± 7.3	1.54 ± 0.53	–
J234921-331514	SGP.p1.1048	185.9 ± 5.7	152.8 ± 6.3	102.8 ± 7.8	1.75 ± 0.57	–
J014313-332633	SGP.p1.3507	119.7 ± 5.9	130.4 ± 6.5	102.3 ± 7.9	2.44 ± 0.72	–
J000722-352014	SGP.p1.567	245.7 ± 5.6	192.6 ± 6.4	101.9 ± 7.5	1.51 ± 0.52	–
J002145-295217	SGP.p1.2982	119.6 ± 5.6	111.8 ± 6.5	101.6 ± 7.5	2.32 ± 0.69	–
J230003-315006	SGP.p1.2100	137.5 ± 5.7	131.5 ± 6.6	101.0 ± 7.9	2.17 ± 0.66	–
J235325-331110	SGP.p1.11153	78.9 ± 5.6	96.0 ± 6.3	100.6 ± 7.7	3.01 ± 0.83	–
J222353-323512	SGP.p1.7806	119.1 ± 7.7	102.2 ± 8.0	99.8 ± 9.9	2.23 ± 0.67	–
J223031-290653	SGP.p1.3224	167.1 ± 8.1	148.1 ± 7.8	99.1 ± 9.7	1.90 ± 0.60	–
J012222-274456	SGP.p1.20418	66.5 ± 5.8	109.6 ± 6.7	99.0 ± 7.9	3.27 ± 0.89	–
J223925-332627	SGP.p1.1000	206.5 ± 6.0	189.4 ± 6.5	98.8 ± 7.8	1.78 ± 0.58	–
J223943-333303	SGP.p1.4066	118.9 ± 6.2	126.7 ± 6.6	98.8 ± 7.8	2.41 ± 0.71	–
J001725-295152	SGP.p1.1370	163.2 ± 5.4	159.3 ± 6.3	98.6 ± 7.6	2.02 ± 0.63	–
J012853-332719	SGP.p1.3384	121.4 ± 5.9	133.7 ± 6.5	97.8 ± 7.8	2.38 ± 0.70	–
J224027-315155	SGP.p1.1850	135.2 ± 5.2	140.6 ± 6.1	97.7 ± 7.3	2.23 ± 0.67	–
J001802-313505	SGP.p1.2479	131.2 ± 5.7	132.0 ± 6.4	97.6 ± 7.8	2.23 ± 0.67	–
J233024-325032	SGP.p1.11579	76.0 ± 5.6	104.0 ± 6.5	97.6 ± 7.8	3.03 ± 0.84	–
J232551-333826	SGP.p1.1244	157.0 ± 5.1	152.8 ± 6.0	97.5 ± 7.2	2.05 ± 0.63	–
J002055-312753	SGP.p1.5775	93.6 ± 5.5	120.5 ± 6.4	97.3 ± 7.6	2.74 ± 0.78	–
J232211-333749	SGP.p1.1593	143.5 ± 5.2	154.4 ± 6.1	97.2 ± 7.4	2.20 ± 0.67	–
J003455-283537	SGP.p1.1675	148.5 ± 5.5	155.5 ± 6.4	96.1 ± 7.6	2.14 ± 0.65	–
J234750-352931	SGP.p1.8171	85.5 ± 5.5	91.5 ± 6.2	96.1 ± 7.5	2.77 ± 0.78	–
J011754-280457	SGP.p1.13075	75.8 ± 5.8	96.0 ± 6.5	95.5 ± 7.7	3.01 ± 0.83	–
J011014-314815	SGP.p1.25432	59.1 ± 5.6	97.0 ± 6.5	95.5 ± 7.6	3.39 ± 0.91	–
J225339-325550	SGP.p1.4440	98.1 ± 5.2	112.3 ± 6.1	94.9 ± 7.5	2.59 ± 0.75	–

Continued on next page...

A.2 – Continued

IAU ID	Alt. ID	S_{250} [mJy]	S_{350} [mJy]	S_{500} [mJy]	z_{phot}	z_{spec}
J235122-332901	SGP.p1.4166	109.0 ± 5.7	117.6 ± 6.4	94.8 ± 7.6	2.44 ± 0.72	–
J011246-330611	SGP.p1.2906	126.0 ± 5.7	123.9 ± 6.6	93.6 ± 7.9	2.20 ± 0.67	–
J225324-323505	SGP.p1.1952	133.3 ± 5.3	141.2 ± 6.2	93.4 ± 7.5	2.23 ± 0.67	–
J231357-340555	SGP.p1.4354	103.2 ± 5.5	105.9 ± 6.4	93.0 ± 7.6	2.44 ± 0.72	–
J011730-320719	SGP.p1.2485	130.9 ± 5.7	125.1 ± 6.7	92.7 ± 8.0	2.14 ± 0.65	–
J002241-320544	SGP.p1.6250	94.6 ± 5.7	109.5 ± 6.3	92.7 ± 7.6	2.62 ± 0.75	–
J003717-323307	SGP.p1.6289	93.7 ± 5.7	115.0 ± 6.4	92.5 ± 7.9	2.65 ± 0.76	–
J012530-302507	SGP.p1.7195	88.8 ± 5.7	35.7 ± 6.3	92.5 ± 7.5	1.84 ± 0.59	–
J225601-313232	SGP.p1.2782	126.2 ± 5.8	140.9 ± 6.6	92.3 ± 7.9	2.32 ± 0.69	–
J222504-304848	SGP.p1.198305	35.0 ± 6.9	59.9 ± 8.2	92.3 ± 9.9	4.38 ± 1.12	–
J012131-300431	SGP.p1.9817	84.8 ± 5.9	97.2 ± 6.6	91.8 ± 7.9	2.74 ± 0.78	–
J012335-314618	SGP.p1.11328	79.8 ± 5.8	82.3 ± 6.6	91.7 ± 8.0	2.80 ± 0.79	–
J224800-310136	SGP.p1.2438	136.4 ± 5.9	134.0 ± 6.7	91.5 ± 7.9	2.11 ± 0.65	–
J000807-351205	SGP.p1.10821	79.8 ± 5.6	114.7 ± 6.4	91.5 ± 7.5	2.92 ± 0.82	–
J233750-351804	SGP.p1.7519	77.0 ± 5.0	90.5 ± 6.0	91.3 ± 7.3	2.89 ± 0.81	–
J225046-304719	SGP.p1.30645	60.6 ± 5.9	89.7 ± 6.5	91.2 ± 7.9	3.30 ± 0.89	–
J013941-290452	SGP.p1.18274	60.0 ± 5.1	90.4 ± 6.1	91.1 ± 7.5	3.30 ± 0.89	–
J225707-294315	SGP.p1.1494	166.2 ± 5.7	149.3 ± 6.5	91.0 ± 7.6	1.87 ± 0.60	–
J000455-330812	SGP.p1.13489	70.6 ± 5.5	86.2 ± 6.4	90.9 ± 7.6	3.03 ± 0.84	–
J014506-284454	SGP.p1.6126	98.0 ± 5.9	105.4 ± 6.8	90.7 ± 7.9	2.53 ± 0.73	–
J005517-285711	SGP.p1.33950	54.5 ± 5.6	77.0 ± 6.5	90.6 ± 8.0	3.48 ± 0.93	–
J223005-322623	SGP.p1.48099	69.6 ± 7.9	97.4 ± 8.3	90.2 ± 9.5	3.06 ± 0.84	–
J224351-334447	SGP.p1.4084	111.5 ± 5.9	120.1 ± 6.7	90.0 ± 7.9	2.38 ± 0.70	–
J000331-321137	SGP.p1.25288	62.0 ± 5.7	98.1 ± 6.3	90.0 ± 7.6	3.24 ± 0.88	–
J003606-290025	SGP.p1.766	206.8 ± 5.6	167.0 ± 6.4	89.9 ± 7.8	1.57 ± 0.53	–
J223615-343301	SGP.p1.8755	89.9 ± 5.9	107.2 ± 6.6	89.8 ± 7.7	2.65 ± 0.76	–
J225201-322055	SGP.p1.682	185.5 ± 4.6	153.3 ± 5.7	89.5 ± 6.8	1.66 ± 0.55	–
J223702-331934	SGP.p1.2526	118.5 ± 5.2	103.6 ± 6.1	89.5 ± 7.4	2.11 ± 0.65	–
J235654-320234	SGP.p1.4843	81.8 ± 4.6	103.0 ± 5.7	89.4 ± 6.8	2.80 ± 0.79	–
J005747-311054	SGP.p1.16131	72.3 ± 5.8	96.4 ± 6.4	89.2 ± 7.5	2.98 ± 0.83	–
J000421-350900	SGP.p1.3233	119.0 ± 5.7	107.7 ± 6.4	89.1 ± 8.0	2.14 ± 0.65	–
J011557-322918	SGP.p1.5959	94.1 ± 5.8	105.4 ± 6.4	89.1 ± 7.7	2.56 ± 0.74	–
J003721-333058	SGP.p1.37871	46.4 ± 5.6	75.7 ± 6.5	88.4 ± 7.9	3.69 ± 0.98	–
J011925-330231	SGP.p1.18056	67.5 ± 5.7	86.8 ± 6.4	88.0 ± 7.8	3.06 ± 0.84	–
J013028-304206	SGP.p1.4754	80.4 ± 4.5	97.6 ± 5.6	87.7 ± 6.8	2.77 ± 0.78	–
J223923-344710	SGP.p1.4288	110.4 ± 5.8	111.4 ± 6.5	87.5 ± 8.0	2.29 ± 0.68	–
J013303-315544	SGP.p1.8009	88.4 ± 5.8	96.2 ± 6.5	87.2 ± 7.8	2.59 ± 0.75	–
J014502-282652	SGP.p1.4340	113.2 ± 6.0	106.4 ± 6.7	87.1 ± 8.2	2.20 ± 0.67	–
J225708-315258	SGP.p1.1977	143.2 ± 5.7	112.4 ± 6.7	87.0 ± 8.2	1.78 ± 0.58	–
J234704-315224	SGP.p1.1308	171.8 ± 5.8	134.3 ± 6.5	86.8 ± 7.8	1.63 ± 0.55	–
J013217-320954	SGP.p1.17532	65.9 ± 5.5	85.8 ± 6.3	86.8 ± 7.5	3.06 ± 0.84	–
J012208-311541	SGP.p1.4813	103.4 ± 5.8	104.5 ± 6.6	86.2 ± 7.7	2.35 ± 0.70	–
J005506-300028	SGP.p1.4874	103.4 ± 5.7	128.0 ± 6.5	86.2 ± 7.8	2.50 ± 0.73	–
J000812-341256	SGP.p1.7414	86.1 ± 5.5	103.4 ± 6.3	86.2 ± 7.6	2.68 ± 0.77	–
J010751-301741	SGP.p1.12685	74.8 ± 5.6	78.9 ± 6.4	86.2 ± 7.5	2.83 ± 0.80	–
J224844-320520	SGP.p1.23411	59.3 ± 5.4	94.4 ± 6.4	86.1 ± 7.5	3.24 ± 0.88	–
J234050-353126	SGP.p1.13587	68.9 ± 5.6	82.7 ± 6.5	85.8 ± 7.7	2.98 ± 0.83	–
J225745-324231	SGP.p1.11062	71.7 ± 5.2	96.2 ± 6.1	85.6 ± 7.2	2.95 ± 0.82	–
J223940-330421	SGP.p1.13434	79.4 ± 6.1	88.0 ± 6.7	85.6 ± 8.2	2.74 ± 0.78	–
J232627-323134	SGP.p1.10136	69.3 ± 5.1	92.1 ± 6.1	85.4 ± 7.2	2.98 ± 0.83	–
J233037-331217	SGP.p1.4186	108.0 ± 5.7	105.9 ± 6.4	85.2 ± 7.8	2.26 ± 0.68	–
J012228-300842	SGP.p1.21397	64.1 ± 5.7	95.7 ± 6.5	85.0 ± 7.8	3.09 ± 0.85	–
J013543-330637	SGP.p1.1674	161.0 ± 6.0	127.0 ± 6.4	84.9 ± 7.9	1.66 ± 0.55	–
J003934-294937	SGP.p1.17152	64.6 ± 5.4	102.8 ± 6.3	84.8 ± 7.7	3.09 ± 0.85	–
J224559-343249	SGP.p1.8226	90.0 ± 5.9	88.2 ± 6.5	84.7 ± 7.9	2.47 ± 0.72	–
J235512-343233	SGP.p1.3968	97.5 ± 5.1	96.2 ± 6.0	84.6 ± 7.1	2.38 ± 0.70	–
J013649-273316	SGP.p1.5108	104.4 ± 5.8	105.3 ± 6.7	84.6 ± 7.9	2.32 ± 0.69	–
J013450-280624	SGP.p1.22421	67.2 ± 6.1	87.6 ± 6.6	84.5 ± 8.0	3.01 ± 0.83	–
J230538-312203	SGP.p1.5577	98.9 ± 5.7	116.5 ± 6.6	84.3 ± 8.1	2.50 ± 0.73	–
J230604-313248	SGP.p1.14274	74.0 ± 5.8	93.5 ± 6.5	84.2 ± 7.5	2.86 ± 0.80	–
J000513-294154	SGP.p1.15003	69.9 ± 5.6	79.9 ± 6.5	84.3 ± 7.7	2.89 ± 0.81	–
J013304-303643	SGP.p1.964	177.2 ± 5.2	136.2 ± 6.1	84.1 ± 7.5	1.57 ± 0.53	–
J224203-333452	SGP.p1.641	249.7 ± 6.1	155.7 ± 6.8	84.0 ± 7.7	1.12 ± 0.44	–
J001517-325652	SGP.p1.23501	61.9 ± 5.6	85.2 ± 6.4	84.0 ± 7.5	3.12 ± 0.86	–
J010443-325247	SGP.p1.6033	96.5 ± 5.8	102.8 ± 6.4	83.9 ± 7.9	2.44 ± 0.72	–
J222847-333954	SGP.p1.3220	172.1 ± 8.2	132.3 ± 8.1	83.8 ± 9.2	1.60 ± 0.54	–
J011554-291630	SGP.p1.2219	120.5 ± 5.1	118.4 ± 6.0	83.6 ± 7.3	2.14 ± 0.65	–

Continued on next page...

A.2 – Continued

IAU ID	Alt. ID	S_{250} [mJy]	S_{350} [mJy]	S_{500} [mJy]	z_{phot}	z_{spec}
J001030-321208	SGP.p1.9846	76.6 ± 5.3	91.3 ± 6.2	83.6 ± 7.3	2.77 ± 0.78	–
J234626-332615	SGP.p1.1299	168.2 ± 5.6	150.7 ± 6.4	83.4 ± 7.6	1.78 ± 0.58	–
J000423-303658	SGP.p1.3921	105.8 ± 5.4	124.4 ± 6.6	83.4 ± 7.6	2.41 ± 0.71	–
J225042-295201	SGP.p1.6201	74.1 ± 5.9	60.2 ± 6.6	83.4 ± 7.9	2.65 ± 0.76	–
J224514-312449	SGP.p1.2328	143.6 ± 6.2	121.1 ± 6.5	83.3 ± 8.1	1.81 ± 0.58	–
J225612-325653	SGP.p1.6830	88.2 ± 5.5	100.5 ± 6.5	83.3 ± 7.8	2.56 ± 0.74	–
J223107-291542	SGP.p1.45177	67.4 ± 8.0	99.8 ± 8.7	83.3 ± 10.1	3.01 ± 0.83	–
J235955-312736	SGP.p1.6496	92.2 ± 5.6	98.4 ± 6.3	83.2 ± 7.5	2.47 ± 0.72	–
J222629-304421	SGP.p1.9929	103.9 ± 7.3	108.9 ± 8.1	83.2 ± 9.7	2.35 ± 0.70	–
J232828-294831	SGP.p1.2670	127.0 ± 5.6	126.1 ± 6.6	83.1 ± 7.8	2.11 ± 0.65	–
J222611-295321	SGP.p1.52444	62.8 ± 7.3	73.3 ± 8.0	83.1 ± 10.4	3.06 ± 0.84	–
J234755-300902	SGP.p1.2330	129.6 ± 5.6	131.9 ± 6.3	83.0 ± 7.6	2.11 ± 0.65	–
J223332-304047	SGP.p1.3439	147.6 ± 7.2	117.8 ± 8.5	83.0 ± 10.3	1.72 ± 0.57	–
J234203-345332	SGP.p1.4225	108.0 ± 5.7	124.7 ± 6.4	83.0 ± 7.9	2.38 ± 0.70	–
J005006-274650	SGP.p1.3504	110.8 ± 5.5	119.1 ± 6.4	82.8 ± 7.8	2.29 ± 0.68	–
J002703-324614	SGP.p1.4165	83.6 ± 4.4	107.0 ± 5.6	82.8 ± 6.8	2.68 ± 0.77	–
J005638-321646	SGP.p1.7712	86.7 ± 5.6	108.6 ± 6.6	82.8 ± 7.8	2.65 ± 0.76	–
J225503-330438	SGP.p1.3941	101.7 ± 5.6	98.6 ± 6.6	82.7 ± 8.0	2.29 ± 0.68	–
J224235-294902	SGP.p1.11729	79.9 ± 5.9	104.0 ± 6.6	82.7 ± 8.0	2.74 ± 0.78	–
J223041-334408	SGP.p1.21933	88.6 ± 7.8	89.8 ± 7.9	82.6 ± 9.3	2.50 ± 0.73	–
J014326-293226	SGP.p1.31392	61.0 ± 6.0	76.5 ± 6.5	82.6 ± 8.0	3.12 ± 0.86	–
J002232-311134	SGP.p1.9479	80.4 ± 5.5	96.3 ± 6.5	82.5 ± 7.5	2.71 ± 0.77	–
J000746-342014	SGP.p1.5263	100.9 ± 5.8	99.5 ± 6.4	82.4 ± 7.9	2.32 ± 0.69	–
J013916-312426	SGP.p1.14380	65.2 ± 5.1	92.7 ± 6.0	82.3 ± 7.2	3.03 ± 0.84	–
J013418-295400	SGP.p1.8233	89.4 ± 5.9	106.8 ± 6.7	82.2 ± 8.0	2.56 ± 0.74	–
J233531-332258	SGP.p1.12190	76.8 ± 5.7	93.0 ± 6.4	82.2 ± 7.5	2.77 ± 0.78	–
J232612-332001	SGP.p1.4926	91.1 ± 5.0	106.8 ± 5.9	82.0 ± 7.0	2.53 ± 0.73	–
J011850-283642	SGP.p1.6541	93.3 ± 5.8	114.7 ± 6.5	82.0 ± 7.8	2.53 ± 0.73	–
J234544-353746	SGP.p1.12204	75.4 ± 5.6	87.2 ± 6.4	82.0 ± 7.8	2.77 ± 0.78	–
J012055-305551	SGP.p1.42813	46.3 ± 5.6	74.8 ± 6.5	82.0 ± 7.7	3.57 ± 0.95	–
J005850-290122	SGP.p1.3609	112.3 ± 5.6	124.6 ± 6.4	81.9 ± 7.6	2.29 ± 0.68	–
J001334-324432	SGP.p1.1813	130.8 ± 5.0	125.4 ± 6.0	81.8 ± 7.0	2.02 ± 0.63	–
J230150-295453	SGP.p1.2029	145.0 ± 5.9	116.1 ± 6.6	81.8 ± 7.9	1.75 ± 0.57	–
J013405-304238	SGP.p1.2864	109.9 ± 5.1	108.9 ± 6.1	81.8 ± 7.4	2.23 ± 0.67	–
J013524-330959	SGP.p1.1238	179.8 ± 5.9	142.4 ± 6.6	81.7 ± 8.1	1.57 ± 0.53	–
J225158-314449	SGP.p1.13362	68.5 ± 5.2	89.0 ± 6.2	81.7 ± 7.3	2.92 ± 0.82	–
J232402-325531	SGP.p1.4795	85.4 ± 4.7	100.1 ± 5.7	81.6 ± 6.8	2.59 ± 0.75	–
J232355-325451	SGP.p1.54961	36.1 ± 4.7	65.5 ± 5.7	81.6 ± 6.9	3.93 ± 1.03	–
J222722-290729	SGP.p1.143511	50.7 ± 8.7	21.9 ± 8.6	81.5 ± 10.3	6.00 ± 1.46	–
J231504-303400	SGP.p1.2167	135.2 ± 5.6	122.3 ± 6.5	81.3 ± 7.7	1.93 ± 0.61	–
J004658-290141	SGP.p1.5979	93.1 ± 5.6	122.0 ± 6.6	81.3 ± 7.7	2.56 ± 0.74	–
J233523-344941	SGP.p1.11453	78.3 ± 5.8	84.6 ± 6.4	81.3 ± 7.6	2.68 ± 0.77	–
J223607-334445	SGP.p1.5212	93.9 ± 5.2	105.1 ± 6.2	81.2 ± 7.4	2.47 ± 0.72	–
J012959-290901	SGP.p1.10577	71.0 ± 5.1	77.3 ± 6.0	81.2 ± 7.3	2.80 ± 0.79	–
J011742-281101	SGP.p1.8657	86.5 ± 5.8	109.2 ± 6.6	81.1 ± 8.0	2.62 ± 0.75	–
J230332-323332	SGP.p1.13854	67.2 ± 5.1	77.6 ± 6.0	81.0 ± 7.2	2.89 ± 0.81	–
J014309-332726	SGP.p1.4825	112.4 ± 6.0	108.2 ± 6.6	80.9 ± 8.0	2.17 ± 0.66	–
J235353-332818	SGP.p1.7377	89.6 ± 5.8	101.4 ± 6.5	80.9 ± 7.8	2.53 ± 0.73	–
J001223-333534	SGP.p1.13032	73.2 ± 5.6	93.3 ± 6.5	80.8 ± 7.7	2.83 ± 0.80	–
J225841-312015	SGP.p1.6624	96.7 ± 6.0	96.9 ± 6.5	80.7 ± 7.8	2.35 ± 0.70	–
J004151-312425	SGP.p1.11751	75.2 ± 5.5	95.2 ± 6.3	80.7 ± 7.7	2.77 ± 0.78	–
J014011-332633	SGP.p1.16858	71.5 ± 5.9	72.8 ± 6.5	80.7 ± 7.9	2.77 ± 0.78	–
J003931-273737	SGP.p1.21816	63.6 ± 5.7	79.6 ± 6.4	80.6 ± 7.7	3.01 ± 0.83	–
J222928-291138	SGP.p1.22677	79.2 ± 7.5	61.8 ± 8.0	80.4 ± 9.6	2.47 ± 0.72	–
J225735-344243	SGP.p1.2090	141.9 ± 5.7	133.2 ± 6.5	80.3 ± 7.9	1.93 ± 0.61	–
J005618-303320	SGP.p1.2449	116.0 ± 5.1	108.1 ± 6.0	80.3 ± 7.2	2.08 ± 0.64	–
J010212-310116	SGP.p1.11486	78.2 ± 5.6	93.6 ± 6.4	80.0 ± 7.6	2.71 ± 0.77	–

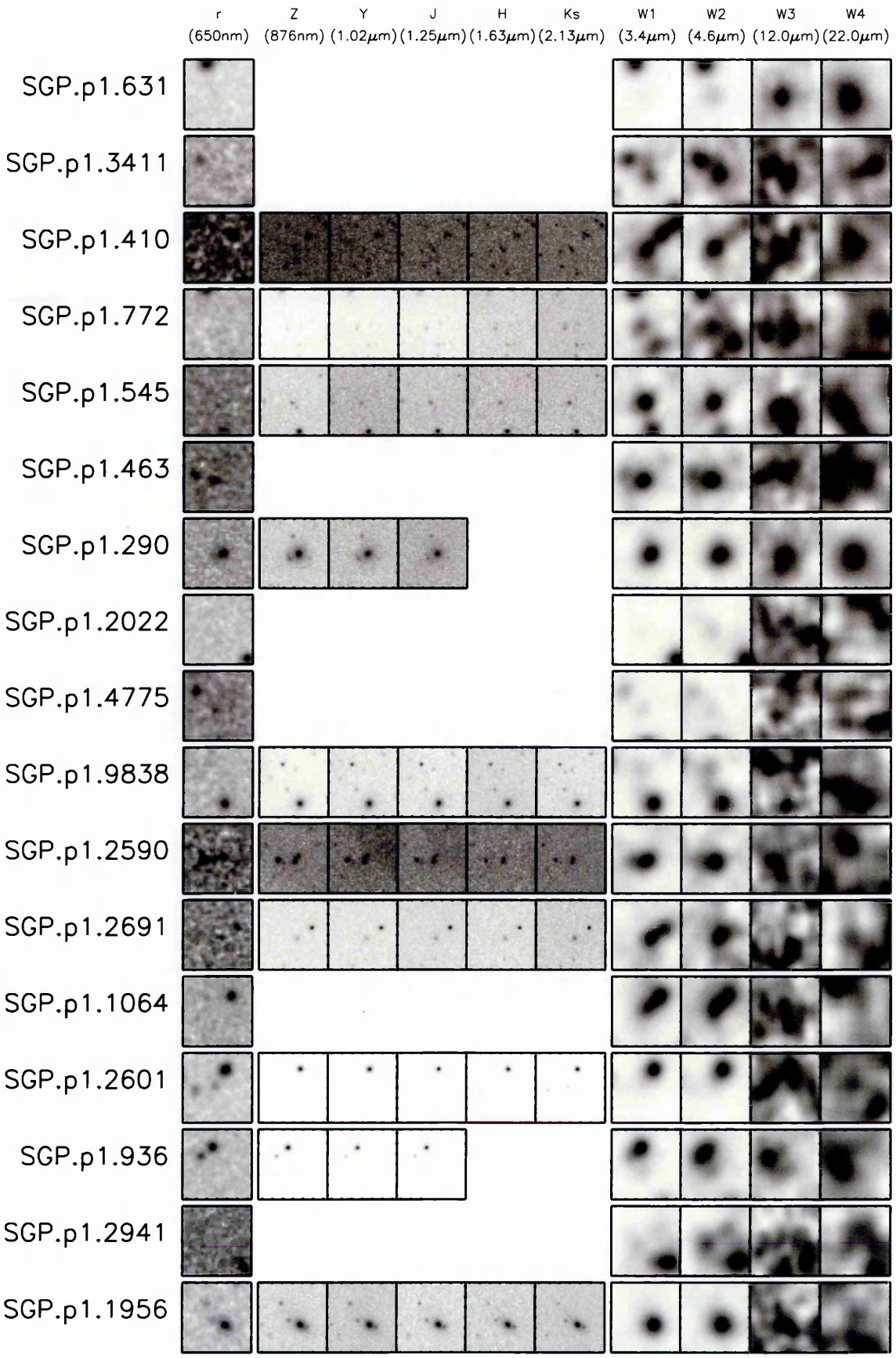

Figure A.4: SGP $S_{500} \geq 100$mJy lens candidate postage stamps.

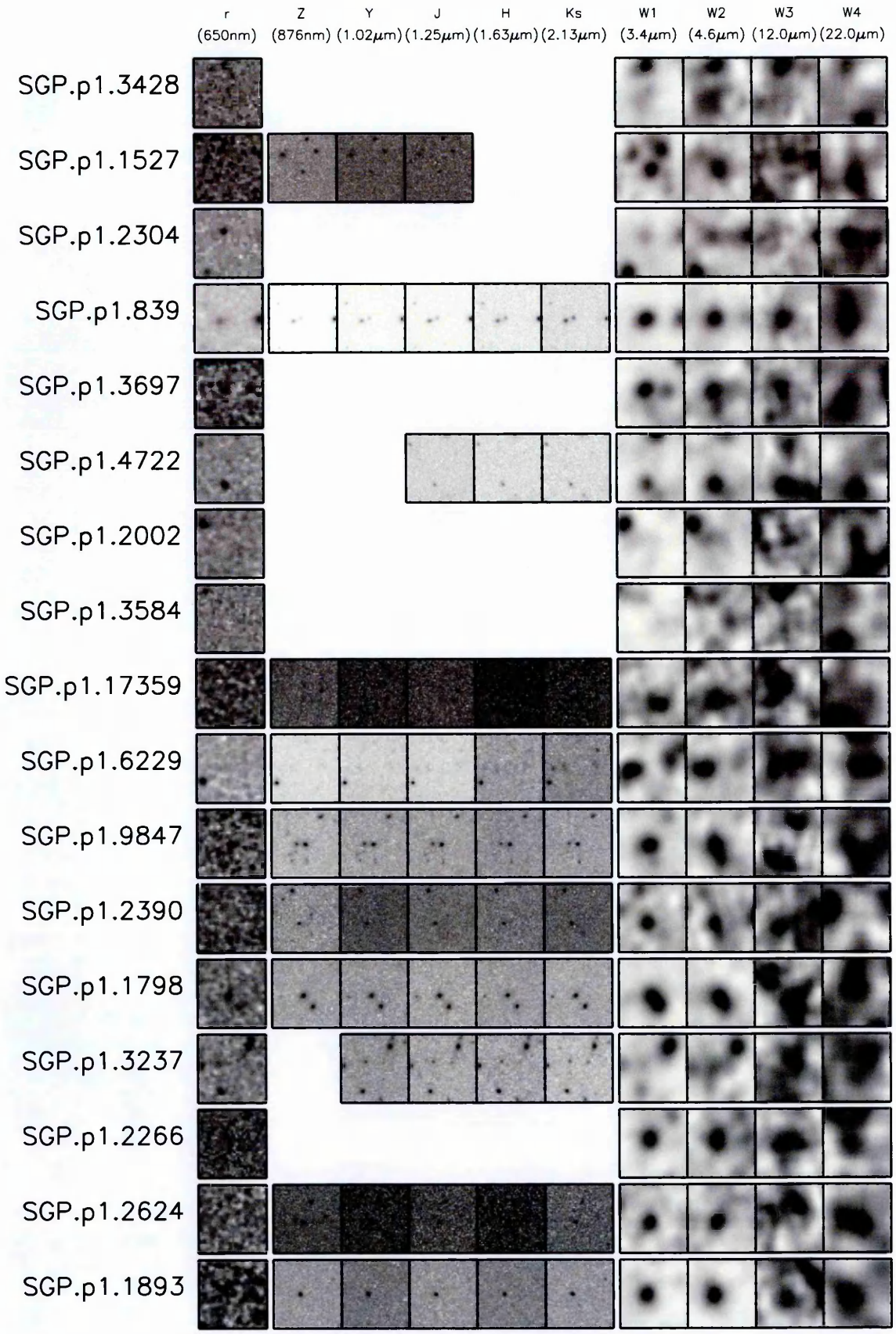

Figure A.4 (Continued): SGP $S_{500} \geq 100$mJy lens candidate postage stamps.

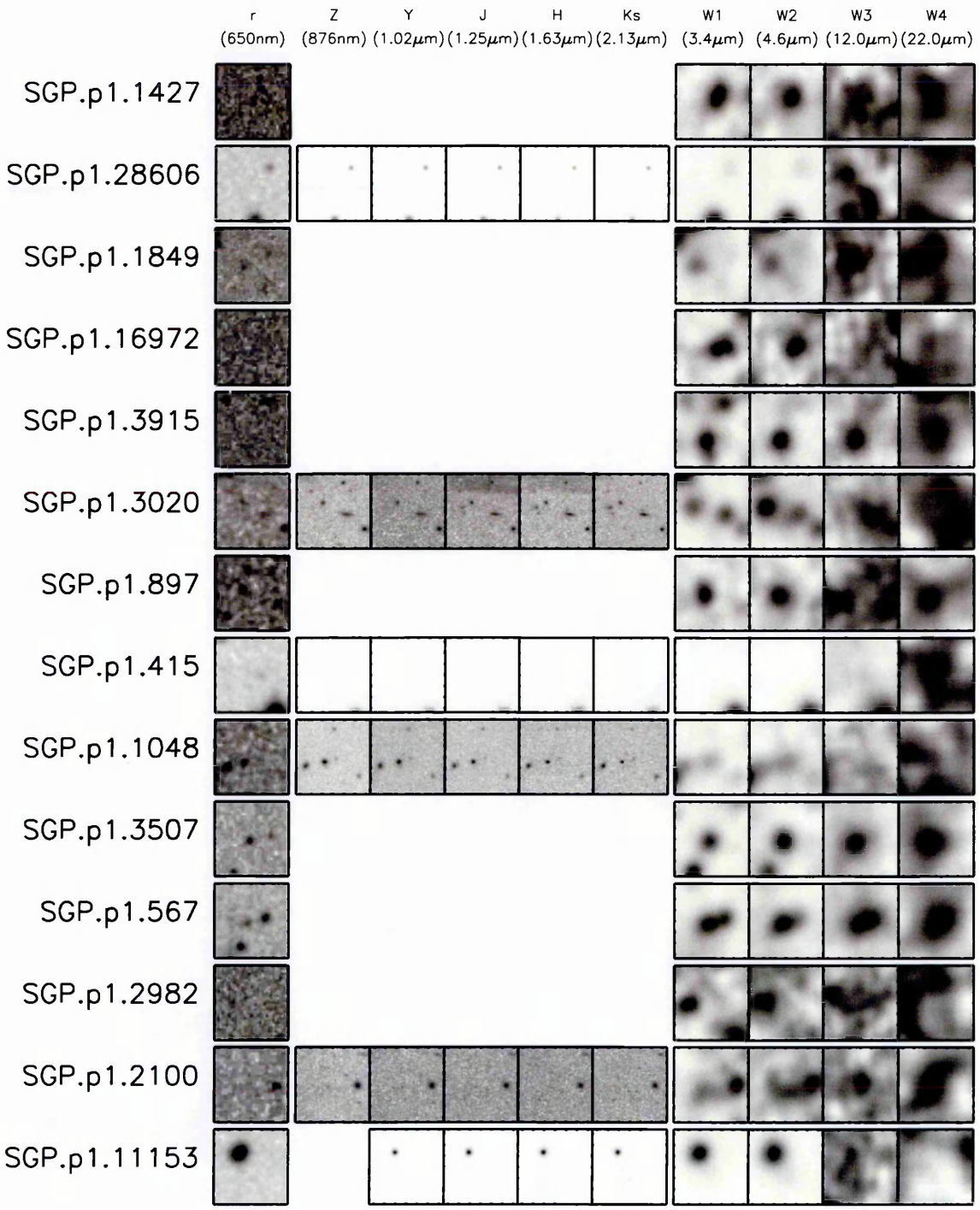

Figure A.4 (Continued): SGP $S_{500} \geq 100$mJy lens candidate postage stamps.

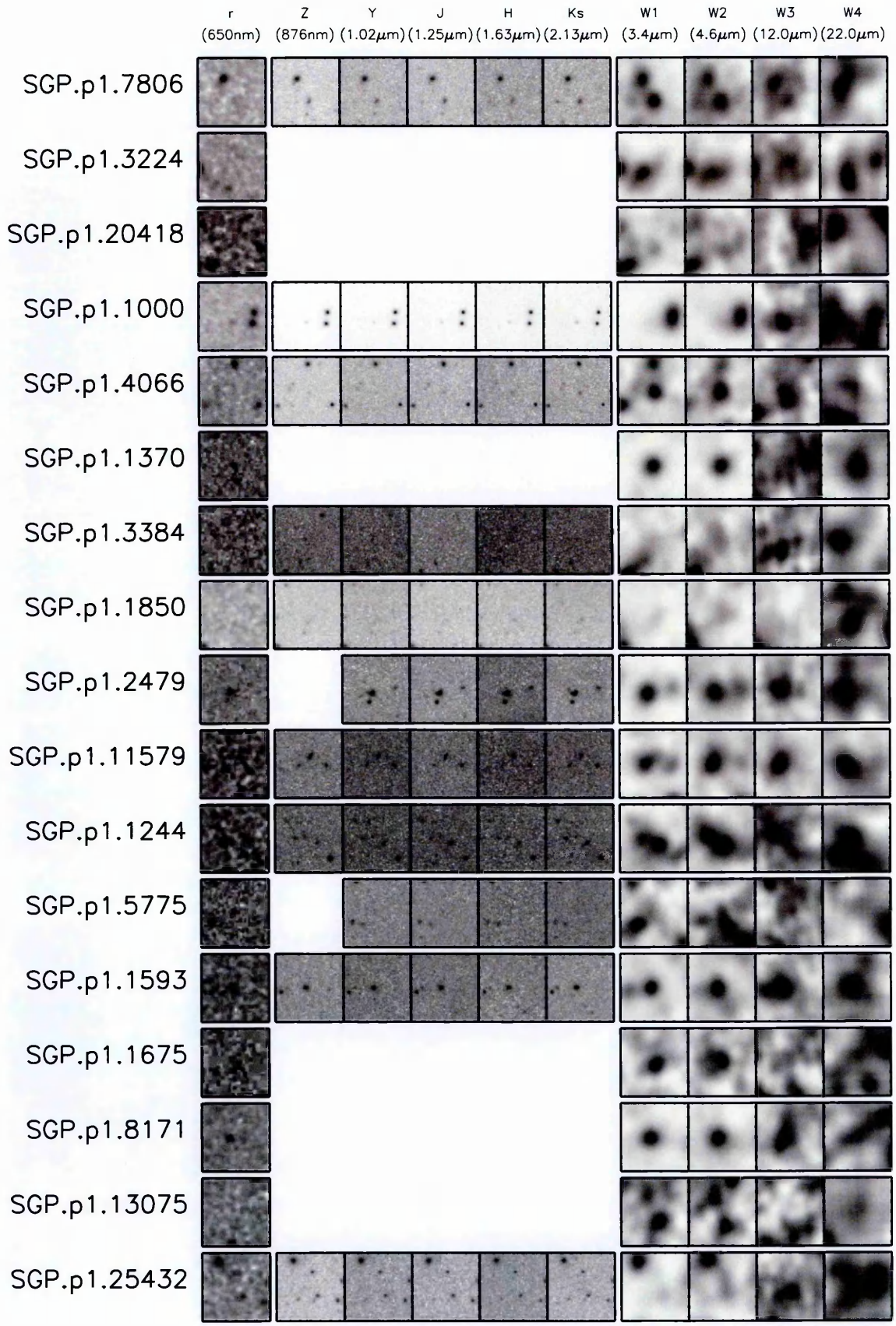

Figure A.5: SGP $90 \leq S_{500} < 100$mJy lens candidate postage stamps.

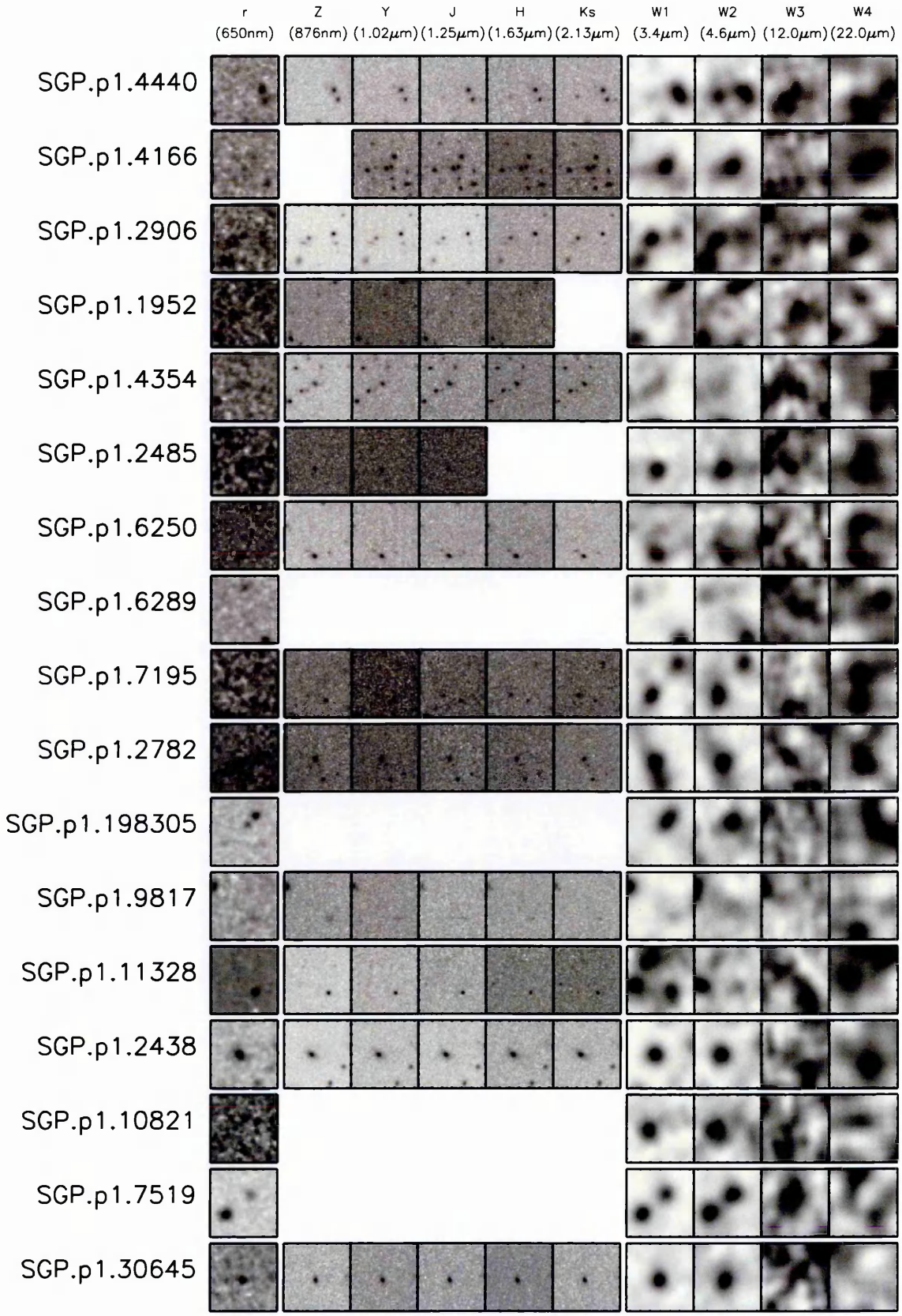

Figure A.5 (Continued): SGP 90 $\leq$ S_{500} < 100mJy lens candidate postage stamps.

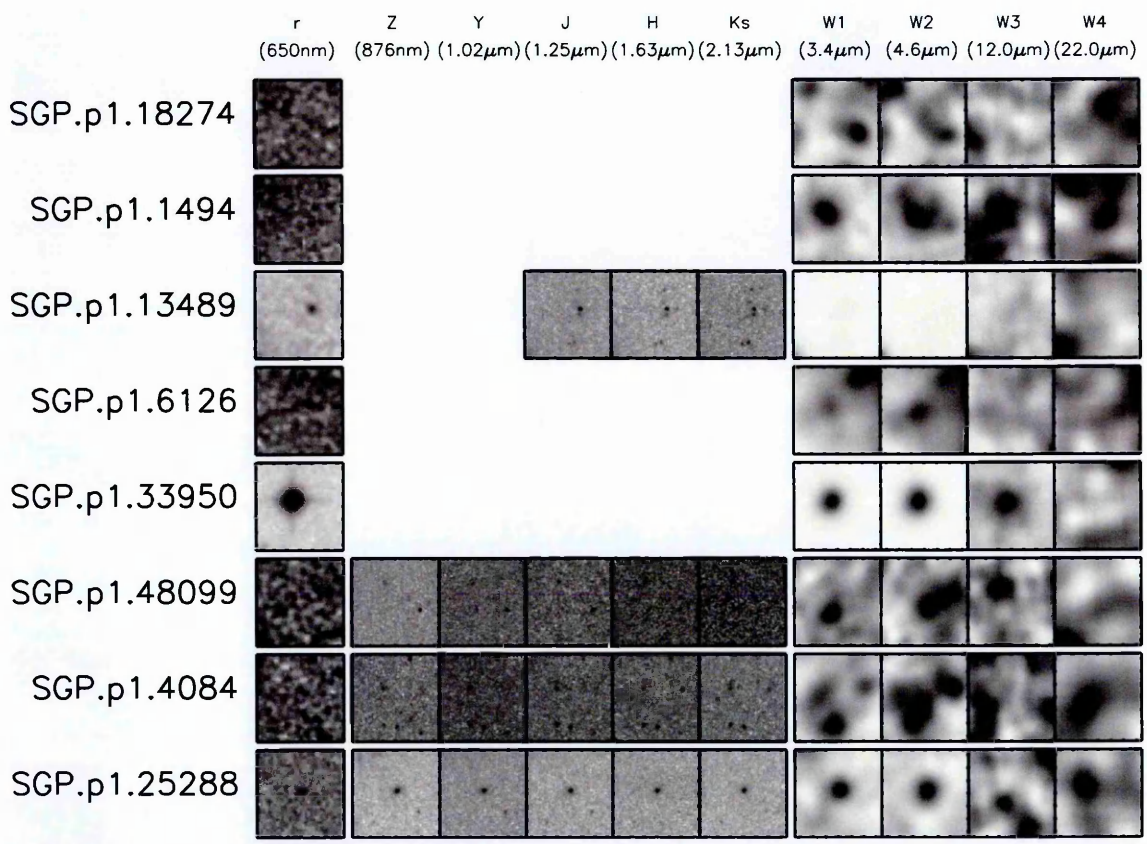

Figure A.5 (Continued): SGP $90 \leq S_{500} < 100$mJy lens candidate postage stamps.

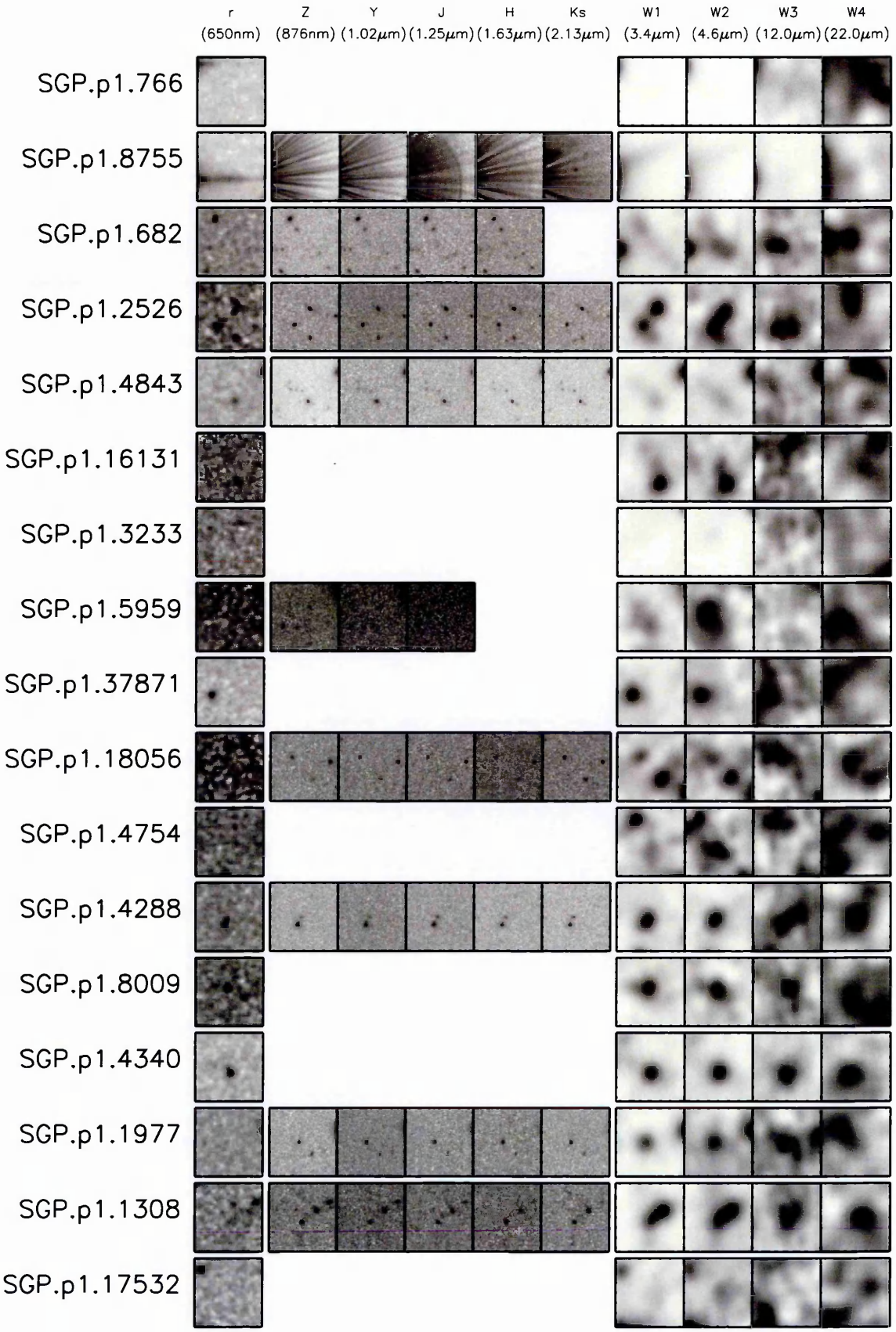

Figure A.6: SGP $80 \leq S_{500} < 90$mJy lens candidate postage stamps.

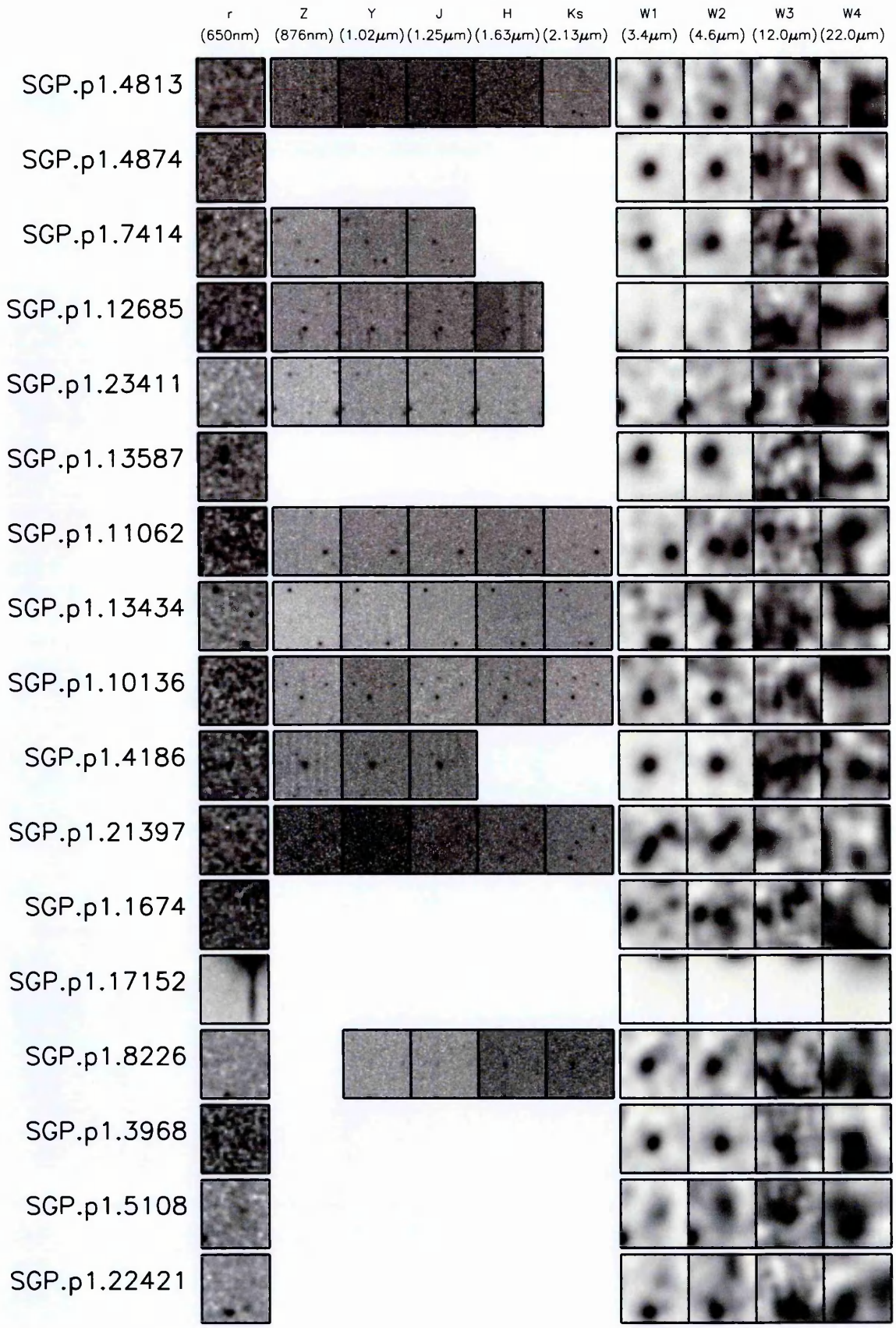

Figure A.6 (Continued): SGP $80 \leq S_{500} < 90$mJy lens candidate postage stamps.

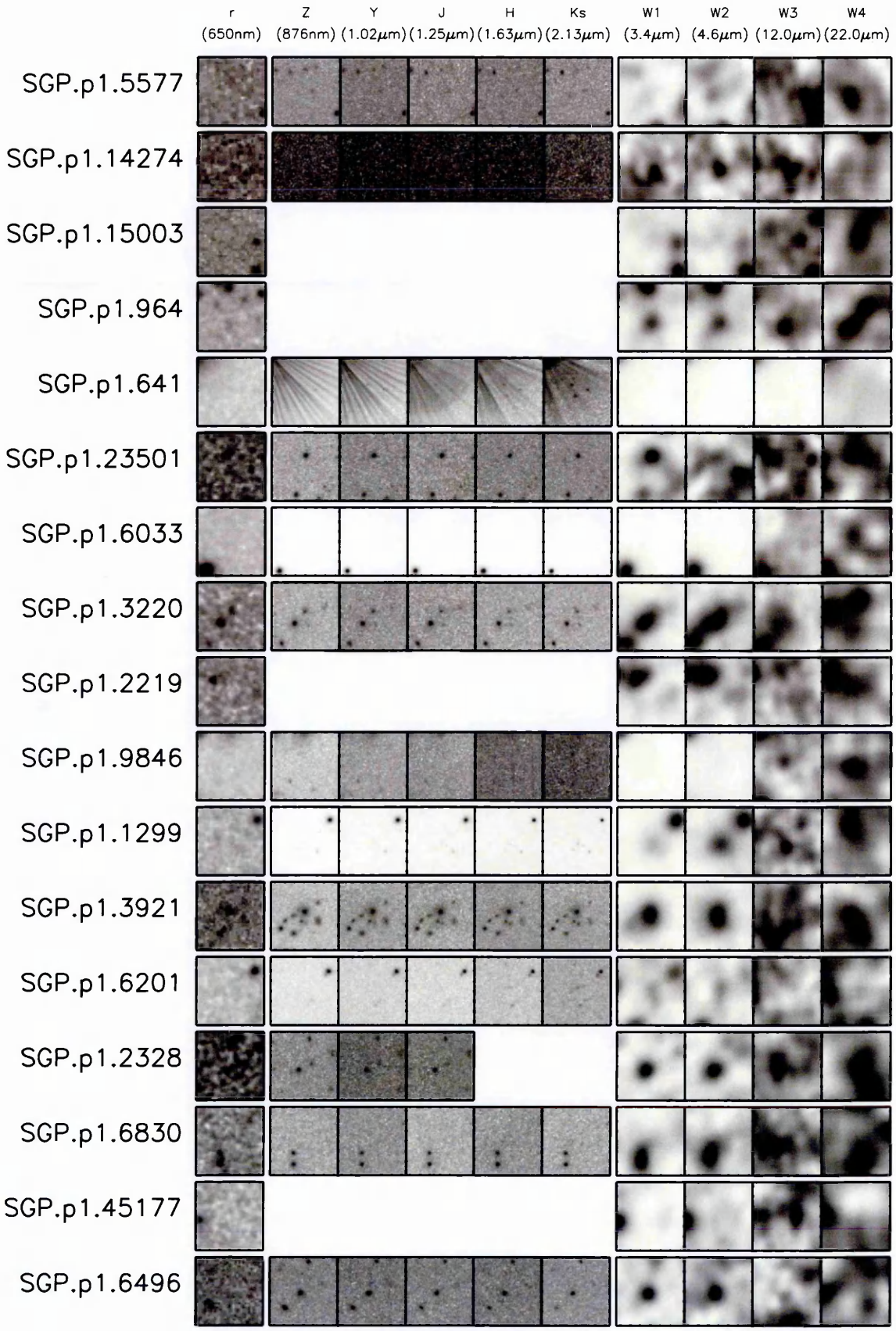

Figure A.6 (Continued): SGP 80 $\leq$ S_{500} < 90mJy lens candidate postage stamps.

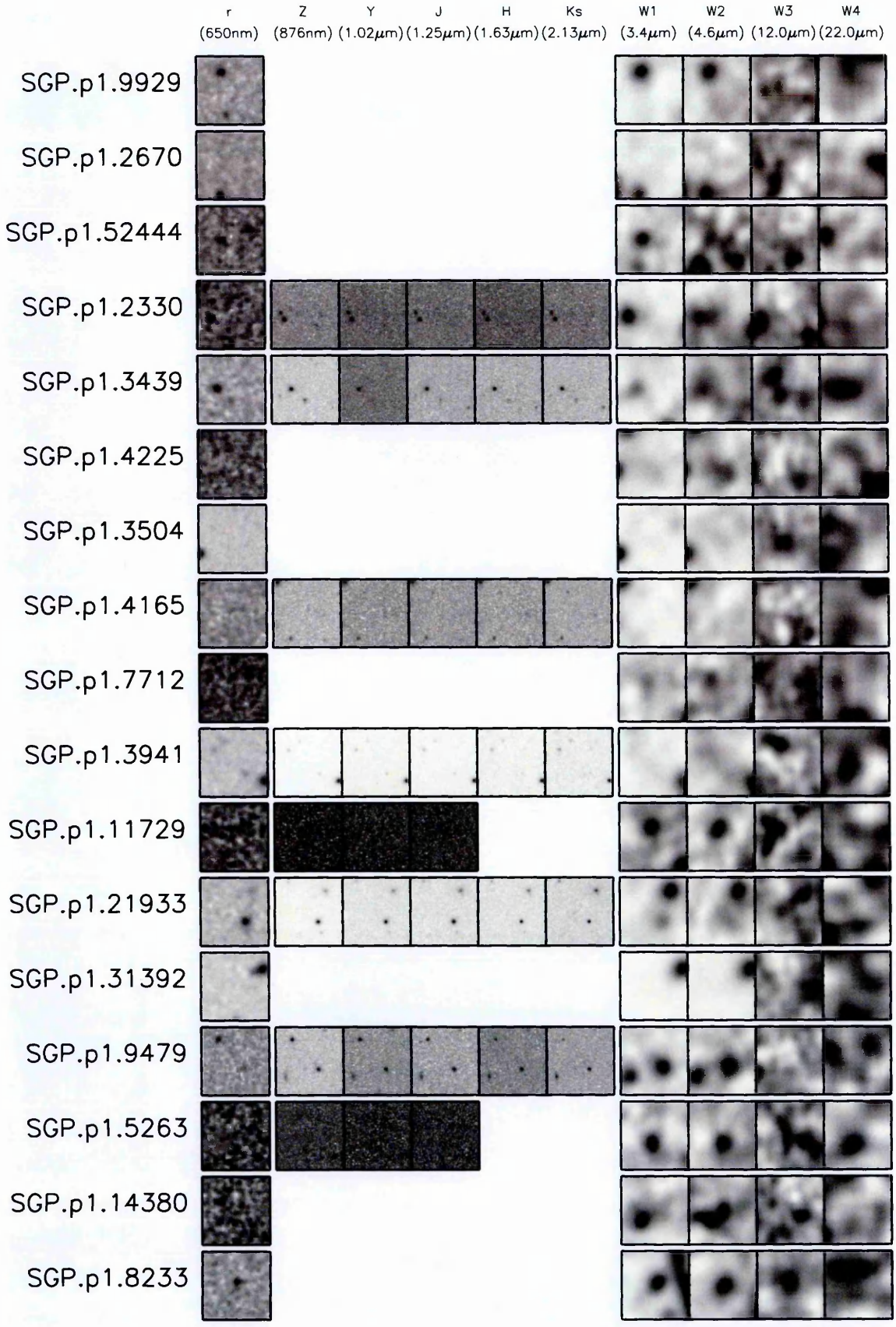

Figure A.6 (Continued): SGP $80 \leq S_{500} < 90$mJy lens candidate postage stamps.

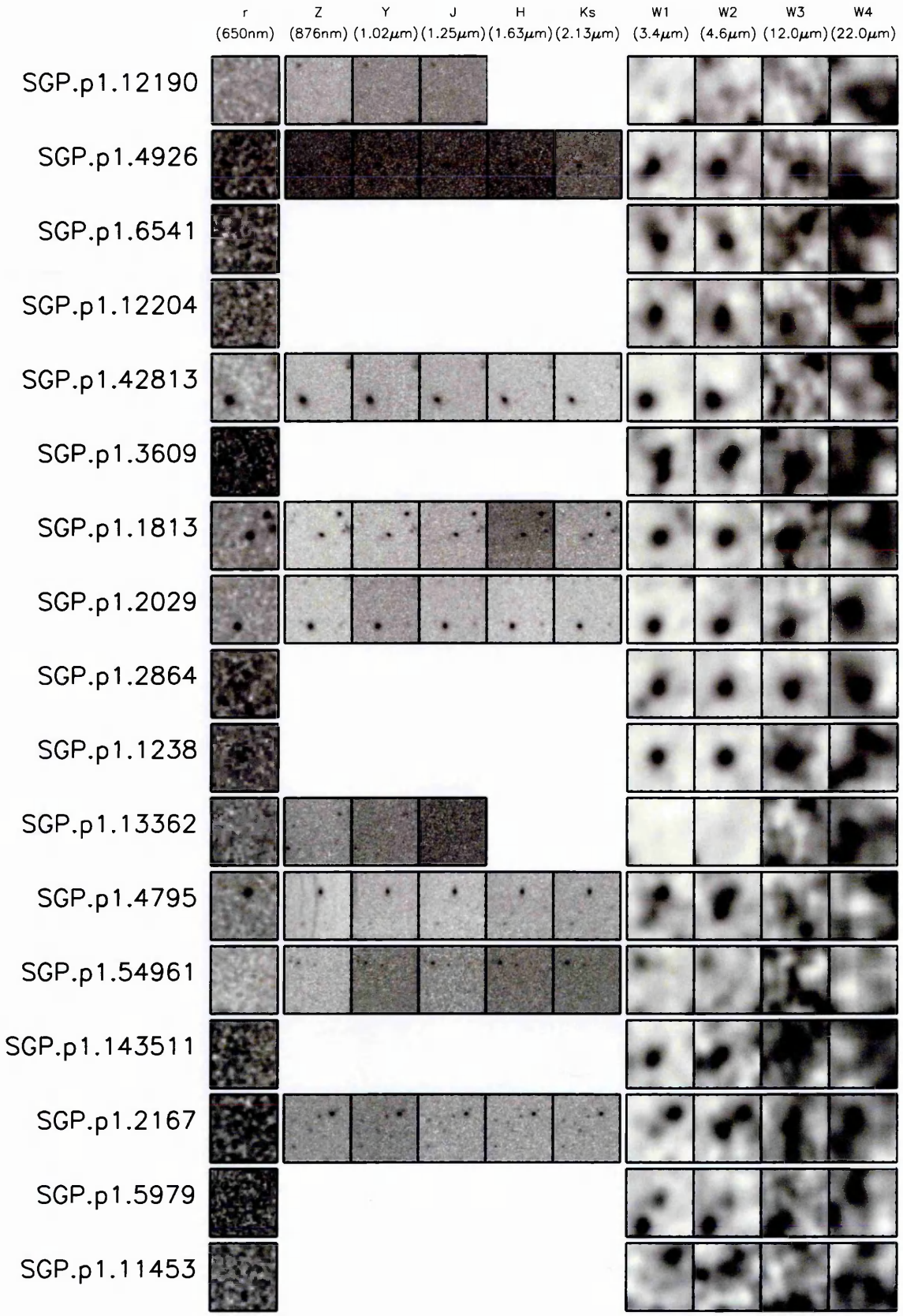

Figure A.6 (Continued): SGP 80 $\leq$ S_{500} < 90mJy lens candidate postage stamps.

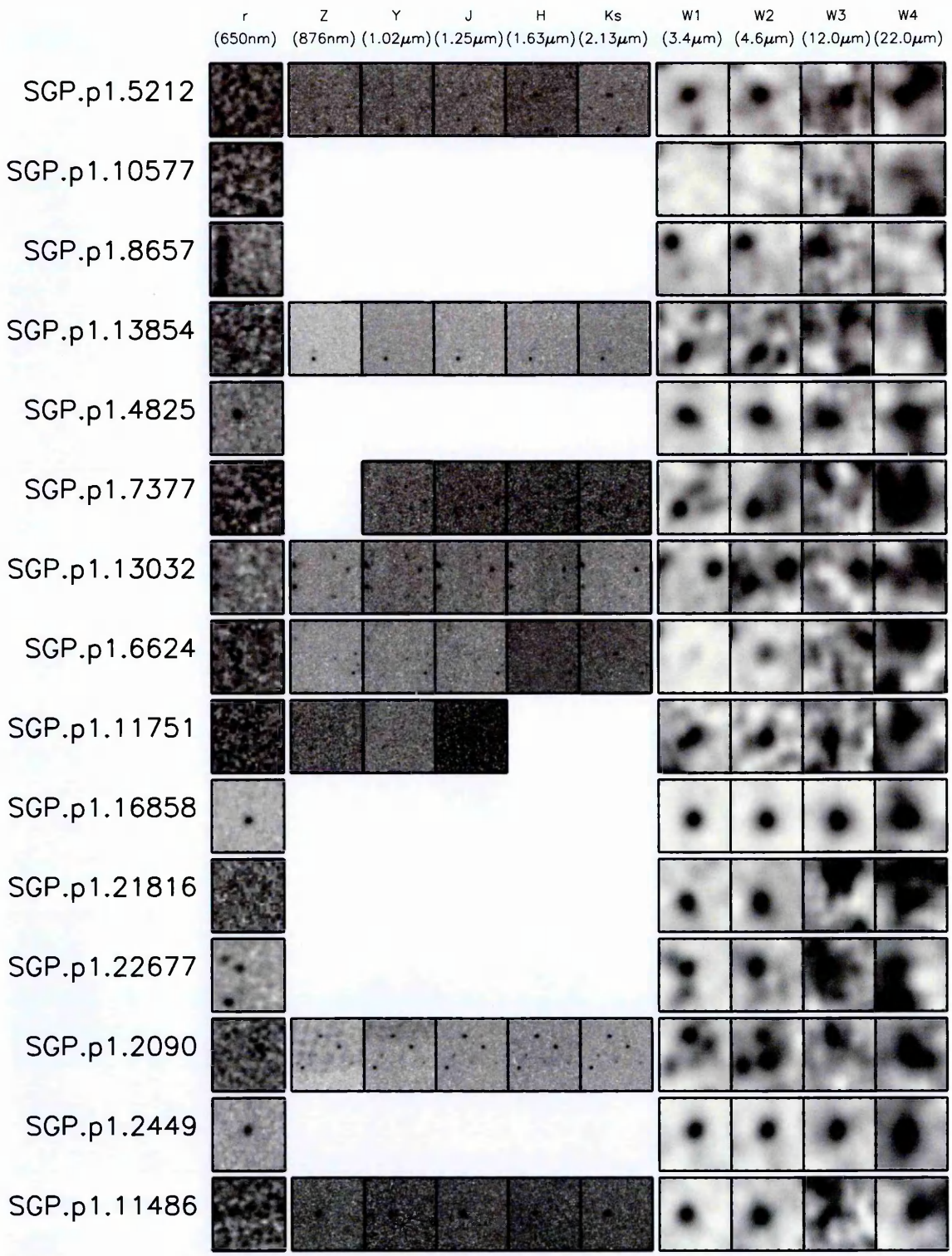

Figure A.6 (Continued): SGP 80 $\leq$ S_{500} < 90mJy lens candidate postage stamps.

Table A.3: Summary of NGP sources classified as local contaminants.

IAU ID	Alt. ID	S_{250} [mJy]	S_{350} [mJy]	S_{500} [mJy]	Source Name	z_{spec}
J125441+285622	NGP.p1.2	5367.3 ± 5.5	2624.8 ± 6.4	1153.3 ± 7.7	NGC 4793	0.0083
J132035+340824	NGP.p1.1	6382.6 ± 6.0	2331.2 ± 6.7	727.9 ± 7.9	IC 0883	0.0233
J131137+225455	NGP.p1.6	2144.3 ± 5.6	1204.6 ± 6.5	649.6 ± 7.6	NGC 5012	0.0087
J131504+243709	NGP.p1.3	4027.6 ± 5.9	1588.2 ± 6.4	543.9 ± 7.9	IC 0860	0.0112
J133956+282402	NGP.p1.4	2750.5 ± 5.6	1283.0 ± 6.5	530.4 ± 7.9	NGC 5263	0.0161
J133457+340238	NGP.p1.7	2029.9 ± 5.5	940.0 ± 6.6	401.3 ± 8.2	UGC 08561	0.0238
J125145+254616	NGP.p1.17	1351.5 ± 5.7	749.4 ± 6.5	395.7 ± 7.5	NGC 4747	0.0040
J125254+282216	NGP.p1.5	2137.9 ± 4.6	993.1 ± 5.8	379.7 ± 6.8	UGC 08017	0.0236
J134309+302016	NGP.p1.8	2038.1 ± 5.7	897.2 ± 6.4	338.7 ± 7.8	UGC 08685	0.0348
J132815+320157	NGP.p1.13	1375.6 ± 5.4	708.5 ± 6.2	312.4 ± 7.7	NGC 5166	0.0155
J130548+274405	NGP.p1.30	930.3 ± 5.6	543.3 ± 6.5	277.9 ± 7.4	NGC 4961	0.0085
J130514+315959	NGP.p1.10	1486.6 ± 5.1	688.0 ± 5.9	268.3 ± 7.0	UGC 08179	0.0518
J131207+240543	NGP.p1.20	1090.0 ± 5.5	565.8 ± 6.4	268.2 ± 7.5	NGC 5016	0.0087
J124610+304355	NGP.p1.12	1553.5 ± 5.6	639.8 ± 6.4	259.1 ± 7.9	Arp242	0.0221
J131612+305702	NGP.p1.19	1012.1 ± 5.0	543.2 ± 5.9	258.8 ± 7.0	NGC 5056	0.0187
J132256+265856	NGP.p1.31	904.5 ± 5.5	535.0 ± 6.4	248.9 ± 7.7	NGC 5116	0.0096
J130056+274727	NGP.p1.18	1260.9 ± 5.5	634.6 ± 6.3	248.3 ± 7.7	NGC 4911	0.0266
J130125+291849	NGP.p1.9	1881.3 ± 5.6	716.6 ± 6.4	240.7 ± 7.7	NGC 4922	0.0232
J131245+314832	NGP.p1.60	706.4 ± 5.6	417.5 ± 6.4	229.3 ± 7.6	NGC 5025	0.0212
J125026+252953	NGP.p1.77	608.2 ± 5.5	354.6 ± 6.4	210.2 ± 7.8	NGC4725	0.0040
J130850+320953	NGP.p1.11	1429.6 ± 5.1	585.5 ± 5.9	204.2 ± 7.0		0.0501
J130617+290348	NGP.p1.33	891.9 ± 5.4	456.1 ± 6.1	202.3 ± 7.4	NGC 4966	0.0235
J133026+313708	NGP.p1.58	737.4 ± 5.7	420.3 ± 6.4	201.1 ± 7.5	UGC 08498	0.0244
J134108+231655	NGP.p1.15	1553.6 ± 6.4	574.7 ± 6.7	199.6 ± 8.3	IC 0910	0.0271
J131700+340607	NGP.p1.34	888.0 ± 5.5	429.6 ± 6.4	197.0 ± 7.8	UGC 08352	0.0314
J131102+293442	NGP.p1.14	1437.8 ± 5.6	564.3 ± 6.4	196.5 ± 7.4	NGC 5004	0.0242
J130832+244204	NGP.p1.61	721.8 ± 5.7	408.3 ± 6.4	188.9 ± 7.5	IC 4202	0.0238
J125109+284710	NGP.p1.100	263.7 ± 5.7	352.1 ± 6.6	188.0 ± 7.7	NGC 4738	0.0159
J133421+335619	NGP.p1.16	1343.5 ± 5.6	548.2 ± 6.7	187.0 ± 7.8		0.0408
J132948+310749	NGP.p1.21	1160.0 ± 5.7	509.6 ± 6.4	185.7 ± 7.5	NGC 5187	0.0239
J131731+310533	NGP.p1.38	713.1 ± 4.7	389.0 ± 5.7	179.9 ± 6.9	NGC 5065	0.0185
J130947+285424	NGP.p1.28	839.3 ± 5.0	417.2 ± 6.0	179.2 ± 7.1	NGC 5000	0.0187
J132800+315216	NGP.p1.23	1082.0 ± 5.5	455.2 ± 6.6	169.3 ± 7.7	CGCG 161-059	0.0387
J133550+345957	NGP.p1.42	838.1 ± 5.5	430.5 ± 6.4	168.4 ± 7.8	UGC 08583	0.0251
J133825+330704	NGP.p1.135	495.7 ± 5.7	317.9 ± 6.5	164.0 ± 7.7	UGC 08630	0.0081
J131745+273411	NGP.p1.48	802.5 ± 5.6	403.3 ± 6.4	160.7 ± 7.5	UGC 08359	0.0233
J133313+330633	NGP.p1.35	802.1 ± 5.0	372.5 ± 6.0	159.9 ± 7.3	KUG 1330+333	0.0247
J134234+350115	NGP.p1.53	761.1 ± 5.5	378.5 ± 6.5	157.1 ± 8.0	UGC 08681	0.0244
J131432+304220	NGP.p1.67	645.7 ± 5.5	342.7 ± 6.6	156.8 ± 7.7	NGC 5041	0.0249
J132857+325244	NGP.p1.22	1146.2 ± 5.9	460.4 ± 6.4	153.0 ± 7.7		0.0256
J125009+330933	NGP.p1.46	812.4 ± 5.7	351.4 ± 6.6	152.0 ± 7.8	NGC 4719	0.0237
J133043+335501	NGP.p1.116	542.2 ± 5.6	316.0 ± 6.4	147.5 ± 7.7	UGC 08505	0.0399
J132257+281859	NGP.p1.287	324.8 ± 5.5	229.2 ± 6.4	147.2 ± 7.7	NGC 5117	0.0079
J130143+290239	NGP.p1.75	628.6 ± 5.6	327.2 ± 6.5	146.4 ± 7.7	IC 4088	0.0237
J131939+301523	NGP.p1.117	540.0 ± 5.6	299.3 ± 6.4	144.3 ± 7.9	NGC 5089	0.0071
J131840+313234	NGP.p1.25	1106.8 ± 5.7	462.3 ± 6.4	140.4 ± 7.5	CGCG 160-187	0.0357
J132015+305400	NGP.p1.43	821.8 ± 5.5	356.9 ± 6.4	139.6 ± 7.5	CGCG 160-200	0.0246
J130950+243439	NGP.p1.45	785.4 ± 5.5	359.8 ± 6.4	138.9 ± 7.7	IC 0854	0.0237
J131259+270830	NGP.p1.36	878.2 ± 5.6	377.3 ± 6.5	138.1 ± 7.9	CGCG 160-163	0.0597
J130854+281102	NGP.p1.103	548.3 ± 5.6	275.5 ± 6.4	137.3 ± 7.5	UGC 08229	0.0200
J131139+343812	NGP.p1.40	859.1 ± 5.7	364.6 ± 6.4	137.0 ± 7.7		0.0374
J125806+281434	NGP.p1.26	1055.8 ± 5.6	466.6 ± 6.3	136.9 ± 7.6	NGC 4848	0.0235
J124937+305044	NGP.p1.127	502.6 ± 5.6	283.4 ± 6.4	136.8 ± 7.6	UGC 07978	0.0269
J131909+283024	NGP.p1.132	401.2 ± 4.6	280.0 ± 5.7	136.3 ± 6.8	NGC 5081	0.0222
J134707+335253	NGP.p1.295	336.1 ± 5.8	216.1 ± 6.5	135.9 ± 8.0	UGC 08715	0.0151
J133316+343214	NGP.p1.24	1093.7 ± 5.5	437.1 ± 6.5	135.2 ± 7.7	UGC 08536	0.0245
J131020+322902	NGP.p1.166	424.5 ± 5.3	257.0 ± 6.3	135.1 ± 7.4	UGC 08250	0.0176
J133329+330235	NGP.p1.74	614.8 ± 5.4	341.7 ± 6.2	134.3 ± 7.5	UGC 08539	0.0245
J134510+351310	NGP.p1.139	493.1 ± 5.8	293.3 ± 6.6	133.9 ± 7.8	UGC 08698	0.0126
J125402+293611	NGP.p1.146	465.0 ± 5.6	279.2 ± 6.3	132.4 ± 7.6	UGC 08025	0.0211
J130329+263303	NGP.p1.80	619.9 ± 5.7	305.1 ± 6.3	131.7 ± 7.7	UGC 08161	0.0223
J130040+290108	NGP.p1.118	544.9 ± 5.7	295.2 ± 6.3	131.5 ± 7.6	IC 0842	0.0243
J132444+323224	NGP.p1.37	835.4 ± 5.4	356.3 ± 6.2	131.5 ± 7.4	KUG 1322+328	0.0398
J132145+311413	NGP.p1.32	923.4 ± 5.5	394.2 ± 6.4	130.9 ± 7.5	UGC 08399	0.0242
J131327+274804	NGP.p1.203	403.9 ± 5.6	235.7 ± 6.3	129.6 ± 7.7	NGC 5032	0.0214
J134701+335339	NGP.p1.185	440.0 ± 5.7	249.6 ± 6.4	126.8 ± 7.7	UGC 08713	0.0165

Continued on next page...

A.3 – Continued

IAU ID	Alt. ID	S_{250} [mJy]	S_{350} [mJy]	S_{500} [mJy]	Source Name	z_{spec}
J133039+311703	NGP.p1.52	784.4 ± 5.7	324.6 ± 6.5	126.6 ± 7.6	UGC 08502	0.0341
J134836+333042	NGP.p1.29	984.0 ± 5.9	379.2 ± 6.5	124.9 ± 7.8		0.0144
J132838+333620	NGP.p1.49	795.7 ± 5.7	354.0 ± 6.4	124.2 ± 7.5	2MFGC 10838	0.0263
J130218+325326	NGP.p1.112	524.5 ± 5.5	305.6 ± 6.5	123.0 ± 7.5	UGC 08145	0.0253
J131424+302901	NGP.p1.170	428.9 ± 5.4	247.4 ± 6.4	122.2 ± 7.8	UGC 08317	0.0201
J131000+300223	NGP.p1.66	655.0 ± 5.5	287.6 ± 6.4	120.1 ± 7.7	CGCG 160-153	0.0348
J132654+321134	NGP.p1.195	368.5 ± 5.0	238.4 ± 5.9	119.9 ± 7.1	UGC 08451	0.0176
J132515+324015	NGP.p1.110	539.9 ± 5.5	270.6 ± 6.4	118.0 ± 7.8		0.0399
J131313+335904	NGP.p1.98	563.9 ± 5.6	289.8 ± 6.3	117.2 ± 7.6	UGC 08299	0.0353
J134018+262056	NGP.p1.87	529.1 ± 5.0	276.3 ± 6.0	116.8 ± 7.1	UGC 08652	0.0280
J134222+353728	NGP.p1.76	636.8 ± 5.7	305.8 ± 6.5	116.5 ± 7.8	NGC 5276	0.0181
J130038+280327	NGP.p1.27	1014.9 ± 5.6	379.9 ± 6.5	116.0 ± 7.8	IC 4040	0.0262
J133725+272509	NGP.p1.86	587.0 ± 5.6	291.8 ± 6.4	114.0 ± 7.6	NGC 5251	0.0367
J125130+314853	NGP.p1.55	756.0 ± 5.6	333.2 ± 6.4	113.4 ± 7.9	2MFGC 10140	0.0246
J130002+332615	NGP.p1.54	666.4 ± 5.0	303.9 ± 6.0	112.3 ± 7.1	Mrk 0235	0.0240
J125809+284231	NGP.p1.51	665.2 ± 4.8	310.8 ± 5.8	110.3 ± 6.9	CGCG 160-058	0.0254
J130615+252740	NGP.p1.56	732.5 ± 5.6	311.8 ± 6.3	110.0 ± 7.5	Ark 401	0.0242
J133947+300725	NGP.p1.187	424.6 ± 5.6	224.4 ± 6.4	109.6 ± 7.6	UGC 08646	0.0338
J134428+351134	NGP.p1.222	385.0 ± 5.7	244.8 ± 6.4	109.6 ± 8.1	UGC 08693	0.0081
J133239+252627	NGP.p1.105	555.9 ± 5.7	259.2 ± 6.5	109.3 ± 8.1	IC 4287	0.0341
J132416+312041	NGP.p1.172	441.6 ± 5.6	241.6 ± 6.4	108.1 ± 7.7	UGC 08426	0.0166
J130519+312631	NGP.p1.101	567.2 ± 5.7	266.3 ± 6.6	107.0 ± 8.0	IC 4166	0.0362
J132240+325323	NGP.p1.83	593.7 ± 5.5	265.1 ± 6.3	106.8 ± 7.5	CGCG 189-059	0.0359
J134404+253948	NGP.p1.99	562.4 ± 5.6	257.6 ± 6.3	106.5 ± 8.0		0.0486
J125625+232054	NGP.p1.41	838.5 ± 5.5	333.2 ± 6.5	106.2 ± 7.6		0.0742
J124726+294714	NGP.p1.216	389.1 ± 5.7	227.6 ± 6.4	105.9 ± 7.8	IC 0821	0.0224
J131048+294236	NGP.p1.165	446.4 ± 5.5	229.4 ± 6.4	105.6 ± 7.8	NGC 5004B	0.0212
J125731+263045	NGP.p1.47	815.1 ± 5.7	350.0 ± 6.4	105.5 ± 7.6	IC 0837	0.0241
J132539+323440	NGP.p1.44	826.1 ± 5.5	330.0 ± 6.2	105.4 ± 7.5		0.0512
J132539+334051	NGP.p1.119	506.2 ± 5.5	266.9 ± 6.5	104.6 ± 7.7	KUG 1323+339	0.0390
J125652+262916	NGP.p1.111	556.9 ± 5.7	266.4 ± 6.4	103.6 ± 7.8	IC 0835	0.0253
J133536+332228	NGP.p1.235	374.0 ± 5.8	207.5 ± 6.5	103.2 ± 7.9	IC 4301	0.0235
J131218+264109	NGP.p1.193	430.9 ± 5.7	229.0 ± 6.3	102.8 ± 7.5	KUG 1309+269	0.0028
J133214+265700	NGP.p1.57	728.1 ± 5.6	299.6 ± 6.4	101.9 ± 7.5	Mrk 0661	0.0354
J125800+311026	NGP.p1.102	576.5 ± 5.8	266.1 ± 6.4	100.6 ± 7.8	CGCG 160-054	0.0523
J134718+340856	NGP.p1.215	404.1 ± 5.8	211.6 ± 6.4	99.6 ± 7.8	UGC 08718	0.0162
J130755+345509	NGP.p1.154	459.7 ± 5.5	224.9 ± 6.4	99.2 ± 7.8	KUG 1305+351	0.0237
J132135+261817	NGP.p1.71	574.8 ± 5.0	256.5 ± 6.1	98.8 ± 7.3		0.0165
J130348+260521	NGP.p1.175	438.6 ± 5.6	212.9 ± 6.4	97.6 ± 7.6	KUG 1301+263	0.0376
J131651+313451	NGP.p1.130	431.5 ± 4.9	212.3 ± 5.8	97.1 ± 6.9	KUG 1314+318B	0.0298
J130926+282457	NGP.p1.88	585.5 ± 5.6	251.0 ± 6.5	96.8 ± 7.7		0.0207
J131345+245857	NGP.p1.95	566.5 ± 5.6	257.1 ± 6.6	96.8 ± 7.8	KUG 1311+252	0.0242
J125656+322651	NGP.p1.131	481.3 ± 5.5	221.5 ± 6.4	96.8 ± 7.6	Mrk 0054	0.0449
J134111+302240	NGP.p1.108	567.3 ± 5.7	247.4 ± 6.3	96.2 ± 7.7	Mrk 0268	0.0399
J125223+305106	NGP.p1.69	640.0 ± 5.5	273.7 ± 6.4	95.8 ± 7.7		0.0523
J134051+242824	NGP.p1.96	565.2 ± 5.6	264.1 ± 6.3	95.5 ± 7.6	IC 0909	0.0270
J130516+255728	NGP.p1.122	468.3 ± 5.0	229.7 ± 6.0	94.9 ± 7.1	KUG 1302+262	0.0218
J130936+345218	NGP.p1.143	494.8 ± 5.7	224.1 ± 6.5	94.6 ± 7.8	CGCG 189-029	0.0353
J133410+344555	NGP.p1.106	571.4 ± 5.8	262.4 ± 6.5	94.6 ± 7.8	UGC 08547	0.0252
J131540+303518	NGP.p1.89	560.4 ± 5.3	253.9 ± 6.3	94.2 ± 7.4		0.0930
J132946+332109	NGP.p1.120	523.7 ± 5.6	256.8 ± 6.4	94.1 ± 7.8	VV 325b	0.0357
J132022+313055	NGP.p1.273	349.8 ± 5.7	207.2 ± 6.4	93.8 ± 8.0	KUG 1318+317	0.0168
J133813+324921	NGP.p1.263	311.3 ± 5.0	182.2 ± 6.0	93.2 ± 7.1	UGC 08627	0.0245
J132218+330544	NGP.p1.107	579.3 ± 5.8	252.7 ± 6.3	93.1 ± 7.6	2MFGC 10705	0.0350
J132936+343608	NGP.p1.94	559.1 ± 5.6	251.9 ± 6.6	93.0 ± 7.9	CGCG 190-014	0.0326
J133451+340319	NGP.p1.81	639.5 ± 5.7	285.0 ± 6.3	92.9 ± 7.8	UGC 08561	0.0242
J131242+224955	NGP.p1.329	291.9 ± 5.6	190.3 ± 6.5	92.7 ± 7.7	NGC 5012A	0.0086
J132703+305834	NGP.p1.188	428.5 ± 5.6	208.5 ± 6.5	92.6 ± 7.7	IC 4256	0.0225
J132805+341843	NGP.p1.221	380.3 ± 5.6	206.9 ± 6.4	92.5 ± 7.8	MCG +06-30-013	0.0360
J133659+333412	NGP.p1.434	262.1 ± 5.5	142.1 ± 6.6	92.3 ± 7.7	UGC 08609	0.0259
J133519+262530	NGP.p1.194	348.7 ± 4.7	189.6 ± 5.7	91.7 ± 6.8	IC 4297	0.0255
J124917+341947	NGP.p1.70	656.5 ± 5.6	282.0 ± 6.4	90.9 ± 7.7		–
J131453+270029	NGP.p1.225	368.3 ± 5.6	189.4 ± 6.5	90.9 ± 7.9	UGC 08325	0.0154
J135045+251121	NGP.p1.234	373.6 ± 5.8	201.2 ± 6.6	90.2 ± 8.0	UGC 08753	0.0308
J130633+344857	NGP.p1.162	450.3 ± 5.6	226.4 ± 6.4	89.3 ± 7.5	2MFGC 10429	0.0371
J133536+332846	NGP.p1.314	338.3 ± 5.9	185.8 ± 6.4	88.9 ± 7.6	IC 4302	0.0249
J125433+273758	NGP.p1.91	576.2 ± 5.6	259.7 ± 6.6	88.6 ± 7.7	2MFGC 10196	0.0246

Continued on next page...

A.3 – Continued

IAU ID	Alt. ID	S_{250} [mJy]	S_{350} [mJy]	S_{500} [mJy]	Source Name	z_{spec}
J131230+340323	NGP.p1.84	602.9 ± 5.6	252.5 ± 6.4	88.6 ± 7.6	KUG 1310+343A	0.0339
J132052+312159	NGP.p1.311	317.6 ± 5.5	160.1 ± 6.3	88.2 ± 7.6	KUG 1318+316	0.0168
J130126+275310	NGP.p1.518	238.3 ± 5.6	171.2 ± 6.3	88.0 ± 7.5	NGC 4921	0.0183
J133431+351433	NGP.p1.400	288.9 ± 5.7	164.3 ± 6.5	87.5 ± 7.8	MCG +06-30-041	0.0258
J131326+274548	NGP.p1.167	472.5 ± 5.8	210.3 ± 6.3	87.5 ± 7.5	NGC 5032B	0.0206
J131508+302413	NGP.p1.68	677.5 ± 5.7	256.2 ± 6.4	87.2 ± 7.5	CGCG 160-170	0.0232
J132140+312102	NGP.p1.357	286.8 ± 5.4	157.5 ± 6.4	87.2 ± 7.6	UGC 08397	0.0161
J132202+311641	NGP.p1.93	566.8 ± 5.6	234.3 ± 6.3	86.7 ± 7.6	CGCG 161-034	0.0249
J131616+301551	NGP.p1.65	609.8 ± 5.0	251.8 ± 5.9	86.4 ± 7.1	Mrk 0785	0.0492
J125945+320241	NGP.p1.190	389.8 ± 5.2	206.8 ± 6.3	85.9 ± 7.6	CGCG 160-080	0.0228
J132814+284010	NGP.p1.64	684.8 ± 5.6	267.2 ± 6.6	85.7 ± 7.6	CGCG 161-061	0.0373
J133911+285733	NGP.p1.332	312.0 ± 5.6	163.5 ± 6.4	85.3 ± 8.0	UGC 08636	0.0325
J130636+275224	NGP.p1.62	694.7 ± 5.5	270.3 ± 6.3	85.1 ± 7.8	KUG 1304+281	0.0208
J133842+321831	NGP.p1.270	334.9 ± 5.5	170.1 ± 6.3	85.1 ± 7.7	MCG +06-30-064	0.0609
J132233+260831	NGP.p1.114	479.7 ± 5.0	216.0 ± 5.9	84.8 ± 7.2		0.0604
J124942+265332	NGP.p1.393	282.8 ± 5.6	134.9 ± 6.4	84.6 ± 8.0	CGCG 159-083	0.0228
J130546+325023	NGP.p1.92	586.5 ± 5.7	233.9 ± 6.4	84.5 ± 7.6	CGCG 189-019	0.0517
J130638+285058	NGP.p1.502	221.4 ± 5.0	150.0 ± 5.9	83.9 ± 7.2	VV 841	0.0158
J125628+265916	NGP.p1.155	469.2 ± 5.6	219.1 ± 6.4	83.9 ± 7.7	NGC 4819	0.0216
J131258+311526	NGP.p1.946	164.4 ± 5.6	116.8 ± 6.5	83.9 ± 7.7	UGC 08284	0.0203
J132826+304857	NGP.p1.305	312.7 ± 5.5	173.9 ± 6.4	83.8 ± 7.6	UGC 08466	0.0245
J134010+232027	NGP.p1.149	465.2 ± 5.6	213.0 ± 6.4	83.8 ± 7.6	IC 0906	0.0319
J125349+293518	NGP.p1.331	309.7 ± 5.5	172.3 ± 6.4	83.3 ± 7.7	CGCG 159-107	0.0463
J132935+262436	NGP.p1.152	411.1 ± 4.9	201.4 ± 5.9	83.2 ± 7.1	UGC 08482	0.0247
J134832+284929	NGP.p1.181	445.7 ± 5.8	213.3 ± 6.5	83.1 ± 7.6		0.0632
J132716+320157	NGP.p1.681	186.0 ± 5.2	136.4 ± 6.2	82.9 ± 7.3	NGC 5157	0.0244
J132113+311318	NGP.p1.752	191.7 ± 5.6	118.2 ± 6.5	82.4 ± 7.7	UGC 08392	0.0170
J133307+330903	NGP.p1.192	374.0 ± 5.0	188.4 ± 5.9	82.4 ± 7.2	CGCG 190-022	0.0250
J132032+331730	NGP.p1.320	316.0 ± 5.6	182.4 ± 6.4	82.3 ± 7.6	CGCG 189-053	0.0355
J132616+333541	NGP.p1.160	458.2 ± 5.6	204.5 ± 6.5	82.3 ± 7.9		0.0354
J130448+225334	NGP.p1.137	499.0 ± 5.7	206.1 ± 6.3	82.3 ± 8.0	IC 4160	0.0614
J130428+264019	NGP.p1.138	439.3 ± 5.0	209.6 ± 5.9	82.2 ± 7.1	CGCG 160-126	0.0361
J133117+292206	NGP.p1.284	287.1 ± 4.8	166.0 ± 5.8	81.9 ± 7.0	UGC 08510	0.0479
J125810+320100	NGP.p1.183	430.5 ± 5.6	221.4 ± 6.5	81.7 ± 7.7	CGCG 160-060	0.0267
J133944+274634	NGP.p1.198	419.8 ± 5.7	190.2 ± 6.3	81.6 ± 7.9	KUG 1337+280	0.0285
J134553+264632	NGP.p1.289	326.4 ± 5.5	179.0 ± 6.3	81.4 ± 7.6	KUG 1343+270	0.0299
J133455+312335	NGP.p1.693	204.3 ± 5.7	142.3 ± 6.4	80.9 ± 7.7	UGC 08560	0.0166
J132400+305555	NGP.p1.129	499.8 ± 5.7	217.5 ± 6.5	80.9 ± 7.5	IC 4238	0.0223
J131940+274222	NGP.p1.97	466.9 ± 4.6	200.0 ± 5.7	80.7 ± 6.9		0.0231
J125856+274959	NGP.p1.121	510.7 ± 5.5	223.5 ± 6.4	80.6 ± 7.7	IC 3949	0.0253
J131547+315047	NGP.p1.254	317.2 ± 5.0	179.0 ± 5.9	80.5 ± 7.1	KUG 1313+321	0.0170
J130016+223320	NGP.p1.140	479.1 ± 5.6	219.2 ± 6.5	80.3 ± 7.6	IC 4017	0.1774

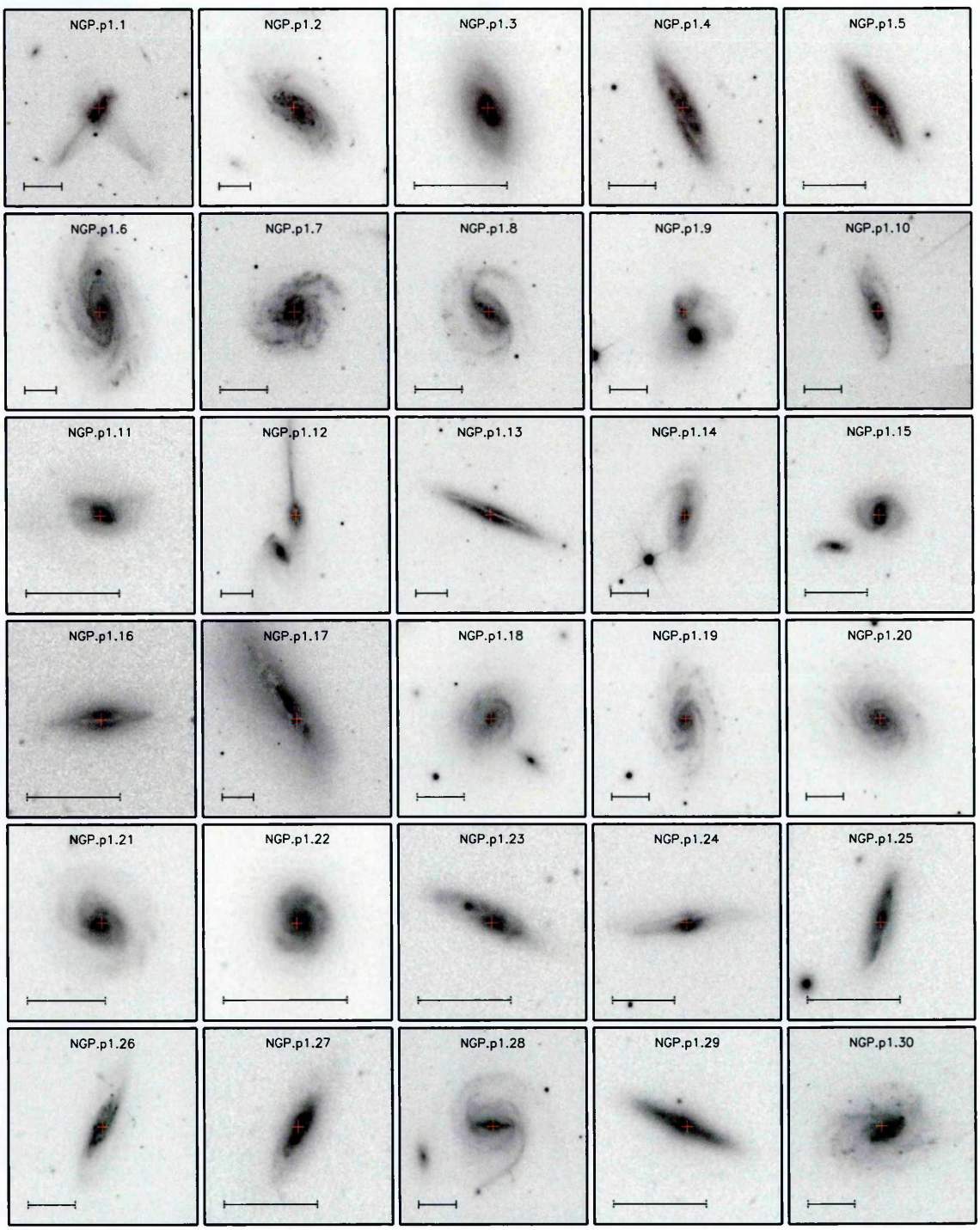

Figure A.7: NGP local postage stamps.

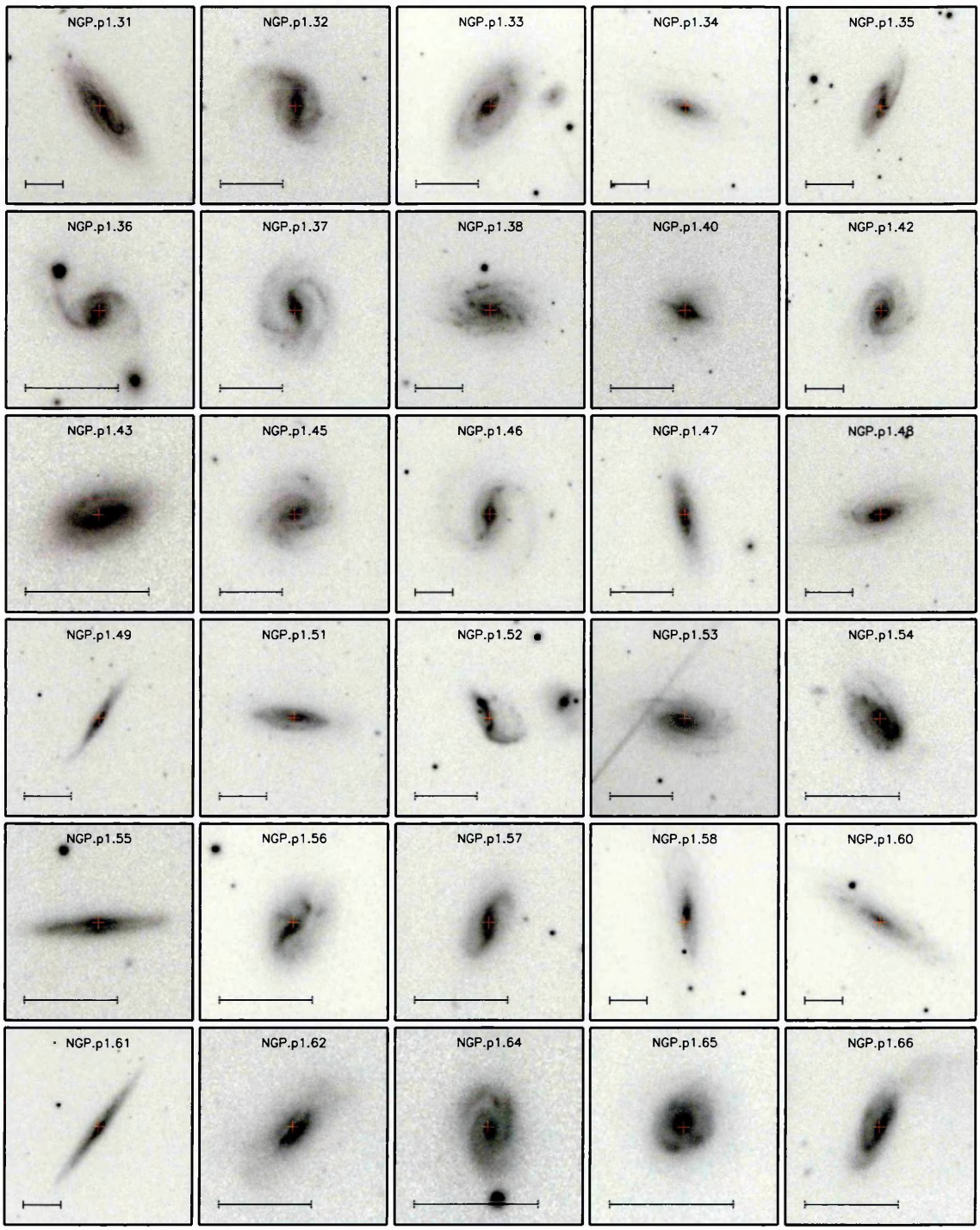

Figure A.7 (Continued): NGP local candidate postage stamps.

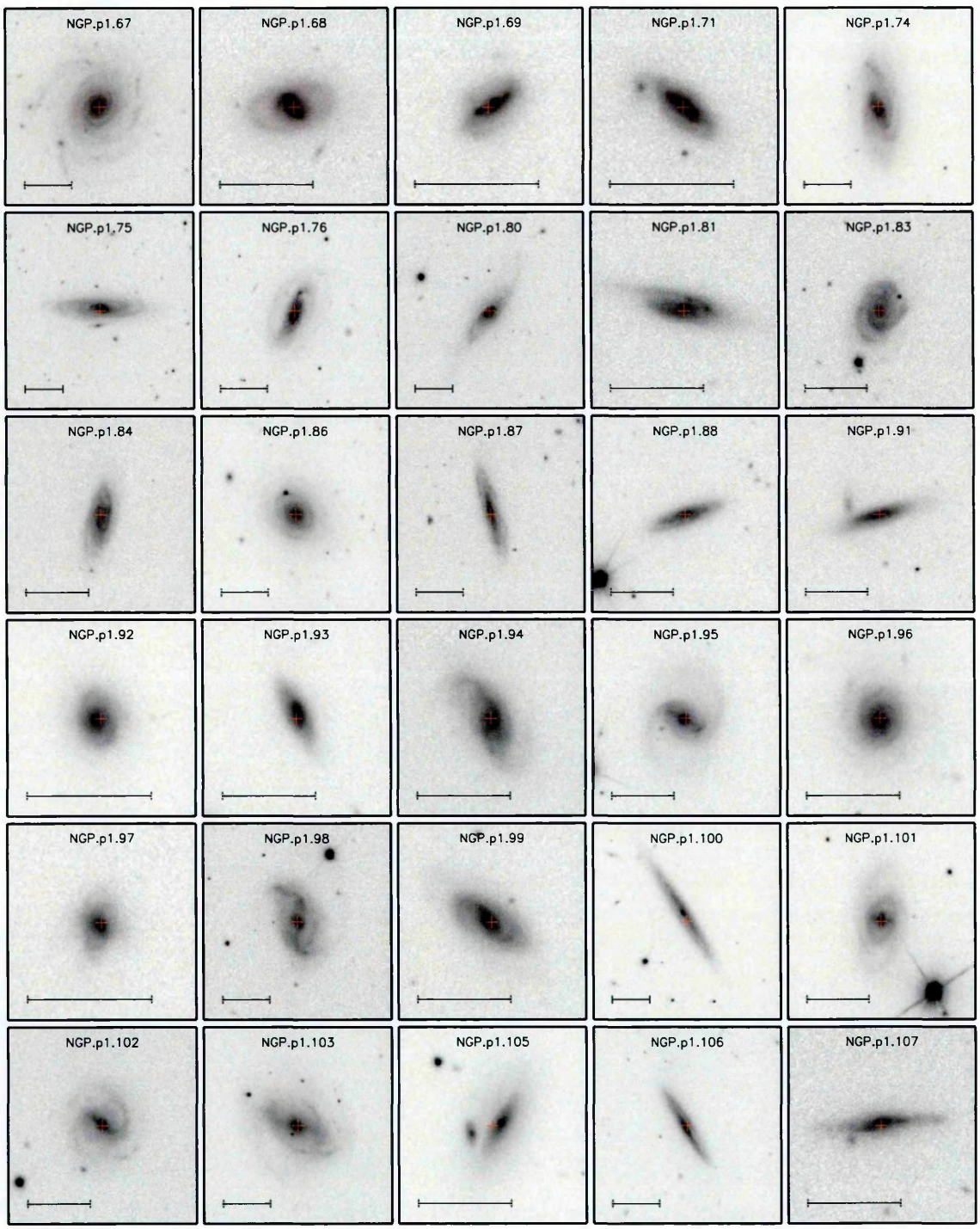

Figure A.7 (Continued): NGP local candidate postage stamps.

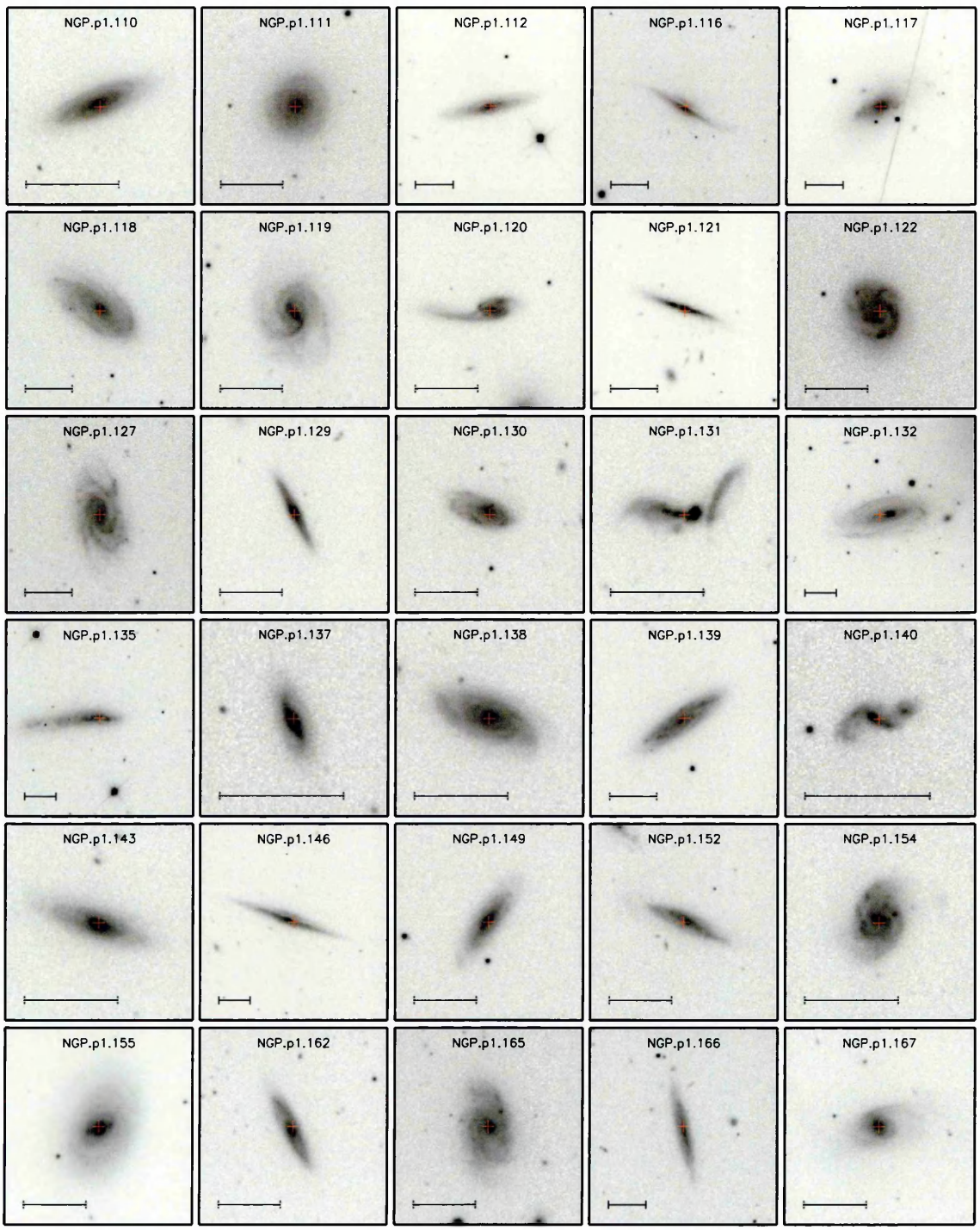

Figure A.7 (Continued): NGP local candidate postage stamps.

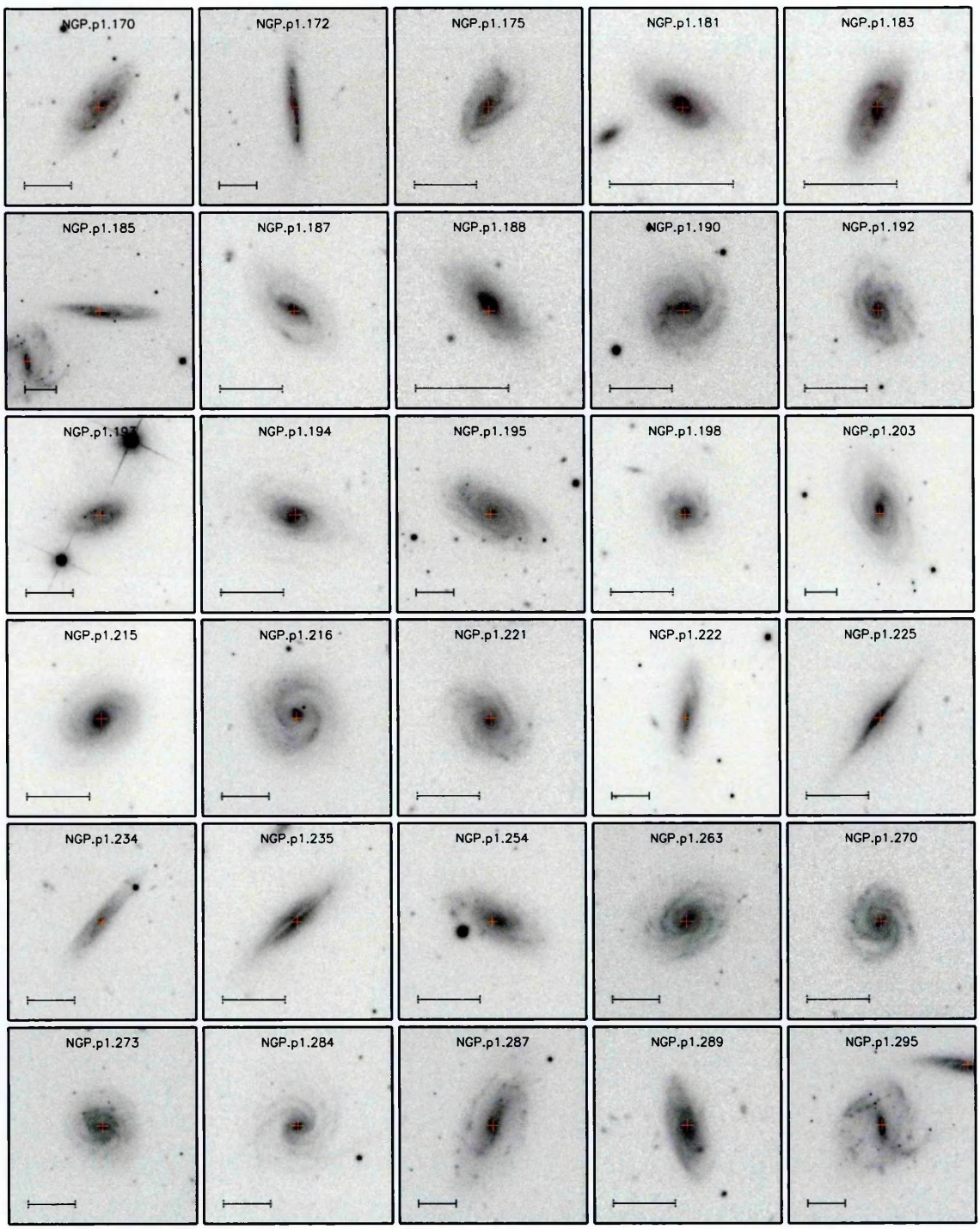

Figure A.7 (Continued): NGP local candidate postage stamps.

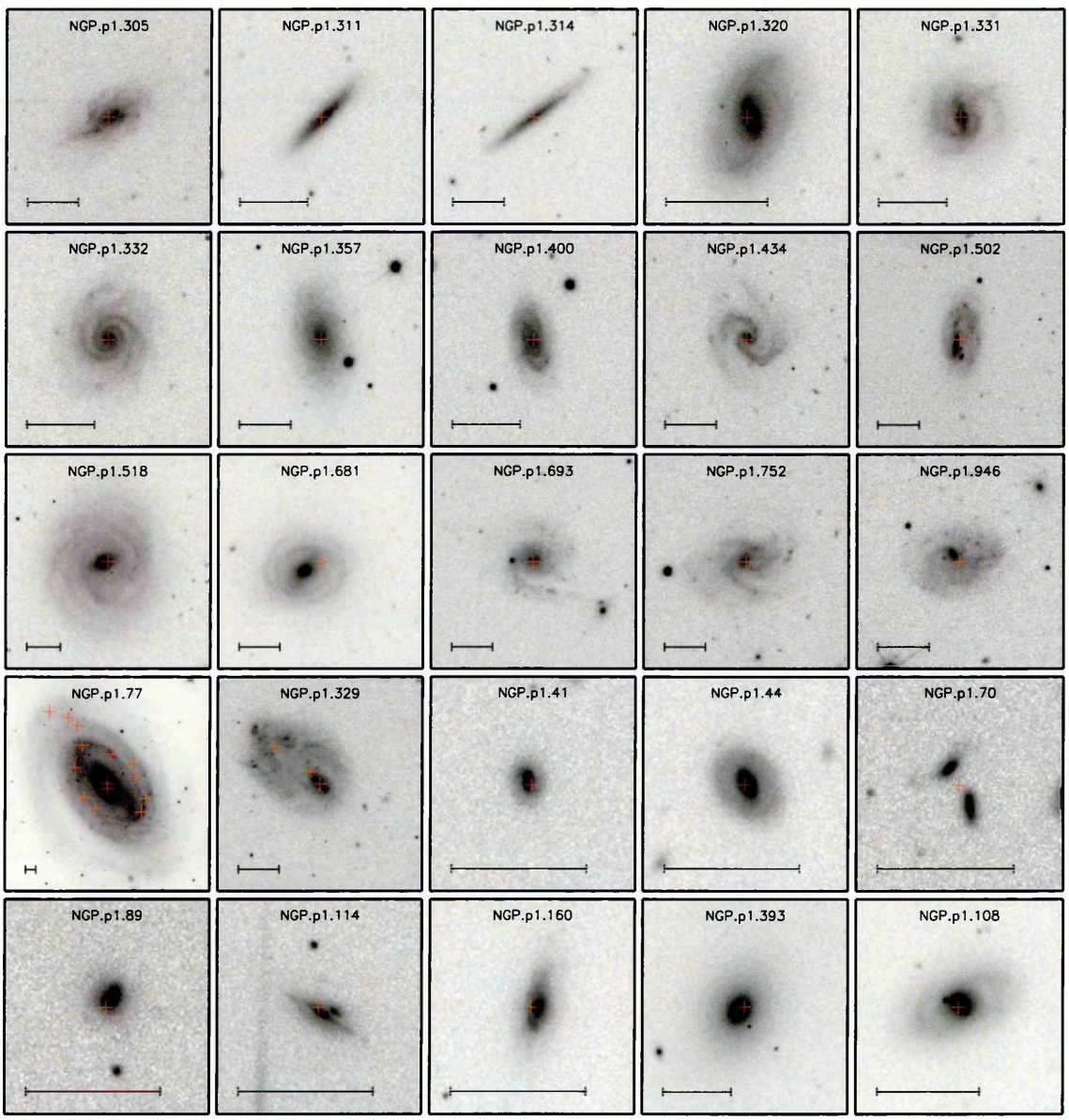

Figure A.7 (Continued): NGP local candidate postage stamps.

Table A.4: Summary of SGP sources classified as local contaminants.

IAU ID	Alt. ID	S_{250} [mJy]	S_{350} [mJy]	S_{500} [mJy]	Source Name	z_{spec}
J003021-331442	SGP.p1.3	5452.7 ± 5.1	3007.5 ± 6.0	1770.1 ± 7.4	NGC 0134	0.0053
J013418-292505	SGP.p1.1	9591.2 ± 6.3	4025.2 ± 7.0	1553.8 ± 8.0	NGC 0613	0.0049
J005242-311221	SGP.p1.6	3416.6 ± 5.7	1800.9 ± 6.7	878.2 ± 8.0	NGC 0289	0.0054
J003415-274811	SGP.p1.5	3421.2 ± 5.8	1608.4 ± 6.4	767.3 ± 7.5	NGC 0150	0.0053
J003659-292839	SGP.p1.4	5882.8 ± 5.6	2324.3 ± 6.7	763.0 ± 7.7	NGC 0174	0.0119
J235750-323527	SGP.p1.16	1361.9 ± 4.7	916.4 ± 5.7	673.0 ± 6.8	NGC 7793	0.0008
J225802-334430	SGP.p1.9	2056.4 ± 5.8	1224.5 ± 6.7	620.2 ± 7.9	IC 5271	0.0057
J234752-303118	SGP.p1.18	1604.0 ± 5.7	844.9 ± 6.5	443.4 ± 7.6	NGC 7755	0.0099
J011407-323908	SGP.p1.12	1616.8 ± 5.1	844.1 ± 5.9	430.9 ± 7.3	IC 1657	0.0120
J222521-312116	SGP.p1.14	2266.7 ± 7.4	957.8 ± 8.0	405.1 ± 9.8	ESO 467-IG055	0.0307
J222422-334138	SGP.p1.33	1668.8 ± 8.1	803.0 ± 8.2	379.3 ± 10.2	NGC 7267	0.0112
J013906-295451	SGP.p1.27	1164.5 ± 5.2	691.9 ± 6.1	346.0 ± 7.2	NGC 0642	0.0196
J225957-341415	SGP.p1.10	2057.7 ± 5.7	902.8 ± 6.6	335.8 ± 7.6	ESO 406-G039	0.0296
J224218-300331	SGP.p1.100	641.6 ± 5.7	495.7 ± 6.6	327.0 ± 8.0	NGC 7361	0.0042
J010612-301041	SGP.p1.17	1632.6 ± 5.8	780.1 ± 6.5	324.0 ± 7.6	NGC 0378	0.0320
J014022-285446	SGP.p1.21	1492.4 ± 5.8	736.6 ± 6.6	323.0 ± 7.7	IC 1720	0.0190
J013150-330710	SGP.p1.13	1704.9 ± 5.4	745.2 ± 6.2	296.6 ± 7.2	ESO 353-G009	0.0165
J003307-321531	SGP.p1.19	1618.3 ± 5.8	704.1 ± 6.5	283.1 ± 7.8	IC 1554	0.0058
J225520-335317	SGP.p1.23	1472.8 ± 6.0	677.6 ± 6.6	278.4 ± 7.8	ESO 406-IG020	0.0290
J011430-311053	SGP.p1.11	1631.0 ± 5.0	712.4 ± 6.0	276.4 ± 7.1	ESO 412-G021	0.0185
J222611-310842	SGP.p1.74	1011.0 ± 7.3	583.4 ± 8.5	271.5 ± 10.1	NGC 7277	0.0133
J000835-335118	SGP.p1.90	614.1 ± 5.5	460.6 ± 6.4	271.0 ± 7.7	NGC 0010	0.0227
J012315-325028	SGP.p1.30	1255.2 ± 5.7	617.3 ± 6.6	265.0 ± 8.0	ESO 352-G063	0.0311
J011036-301316	SGP.p1.51	937.6 ± 5.7	502.4 ± 6.5	261.0 ± 7.6	NGC 0418	0.0190
J005457-320115	SGP.p1.15	1735.8 ± 5.6	745.2 ± 6.4	259.0 ± 7.6	ESO 411-G030	0.0318
J011122-291405	SGP.p1.26	1324.3 ± 5.8	607.5 ± 6.8	253.0 ± 7.7	NGC 0423	0.0053
J013957-284139	SGP.p1.66	554.9 ± 5.2	240.7 ± 6.1	252.9 ± 7.3	ESO 413-G016	0.0197
J011101-302619	SGP.p1.61	750.9 ± 5.0	479.7 ± 6.1	241.4 ± 7.2	IC 1637	0.0202
J225828-321423	SGP.p1.37	1010.0 ± 5.2	518.8 ± 6.0	237.8 ± 7.3	ESO 406-G035	0.0319
J014000-280202	SGP.p1.25	1249.6 ± 5.2	593.2 ± 6.0	233.5 ± 7.3	ESO 413-G018	0.0198
J002938-331535	SGP.p1.59	701.4 ± 4.6	435.2 ± 5.7	231.3 ± 6.8	NGC 0131	0.0047
J231740-344726	SGP.p1.69	805.2 ± 5.6	462.6 ± 6.6	228.6 ± 7.7	ESO 407-G014	0.0092
J235458-343604	SGP.p1.40	945.7 ± 5.1	478.4 ± 5.9	208.8 ± 7.0	2dFGRS S546z007	0.0535
J230549-303642	SGP.p1.22	1454.9 ± 5.6	557.3 ± 6.6	204.8 ± 7.7	ESO 469-G011	0.0284
J014250-275004	SGP.p1.34	1153.5 ± 5.6	534.2 ± 6.6	196.6 ± 8.0	AM 0140-280	0.0567
J235149-345545	SGP.p1.28	1282.2 ± 5.6	547.9 ± 6.5	194.1 ± 7.5		0.0311
J013025-330209	SGP.p1.32	1049.8 ± 4.8	468.1 ± 5.8	189.6 ± 6.9	ESO 353-G007	0.0163
J000254-341407	SGP.p1.46	929.8 ± 5.5	442.8 ± 6.3	188.6 ± 7.7	NGC 7812	0.0227
J012434-331024	SGP.p1.65	863.4 ± 5.8	436.7 ± 6.5	179.8 ± 7.9	ESO 352-G071	0.0309
J225859-302939	SGP.p1.96	689.3 ± 6.0	392.5 ± 6.7	179.5 ± 7.7	ESO 469-G007	0.0289
J002354-323212	SGP.p1.112	535.9 ± 5.1	335.8 ± 6.0	179.2 ± 7.1	NGC 0101	0.0113
J014155-283251	SGP.p1.42	1040.4 ± 5.8	450.7 ± 6.5	170.0 ± 7.8	2MFGC 01281	0.0377
J222606-305203	SGP.p1.93	918.9 ± 7.9	418.4 ± 8.0	167.5 ± 10.2	ESO 467-G058	0.0281
J010723-324943	SGP.p1.38	1136.7 ± 5.8	422.2 ± 6.5	164.5 ± 7.7		0.0358
J013215-332948	SGP.p1.88	661.0 ± 5.5	343.4 ± 6.2	162.2 ± 7.5	2dFGRS S508z128	0.0169
J000903-325449	SGP.p1.76	759.4 ± 5.6	410.1 ± 6.5	159.8 ± 7.5	ESO 349-G033	0.0230
J231117-322715	SGP.p1.49	884.9 ± 5.2	416.4 ± 6.1	157.1 ± 7.3	IC 5289	0.0378
J013859-295526	SGP.p1.39	954.2 ± 5.1	422.0 ± 6.1	144.3 ± 7.3	NGC 0639	0.0193
J003651-282159	SGP.p1.186	450.9 ± 5.7	273.3 ± 6.5	141.8 ± 7.6		–
J011250-311159	SGP.p1.111	621.3 ± 5.7	324.5 ± 6.5	141.1 ± 7.9	ESO 412-G015	0.0186
J011431-321551	SGP.p1.143	457.1 ± 5.1	274.9 ± 5.9	137.6 ± 7.2	ESO 352-G027	0.0178
J002646-334031	SGP.p1.374	303.4 ± 5.7	210.7 ± 6.4	137.2 ± 7.3	NGC 0115	0.0061
J001113-333442	SGP.p1.98	549.6 ± 4.8	313.1 ± 5.8	137.0 ± 7.1	ESO 349-G038	0.0262
J000537-344849	SGP.p1.77	736.3 ± 5.6	324.9 ± 6.3	136.4 ± 7.7	ESO 349-G024	0.0286
J011554-322837	SGP.p1.279	357.0 ± 5.6	236.7 ± 6.6	135.2 ± 8.1	ESO 352-G030	0.0202
J003755-285522	SGP.p1.119	583.3 ± 5.6	305.4 ± 6.4	135.1 ± 7.5	ESO 411-G002	0.0116
J001415-313927	SGP.p1.52	944.2 ± 5.6	379.5 ± 6.4	133.4 ± 7.6		0.0220
J003403-325907	SGP.p1.60	823.3 ± 5.4	360.1 ± 6.3	128.4 ± 7.6	2dFGRS S500z122	0.0150
J010721-331806	SGP.p1.50	933.5 ± 5.5	383.6 ± 6.4	126.9 ± 7.6		0.0357
J233003-310922	SGP.p1.53	923.2 ± 5.6	378.2 ± 6.5	126.7 ± 7.8	ESO 470-G013	0.0372
J223503-313058	SGP.p1.258	386.0 ± 5.9	235.3 ± 6.8	125.4 ± 8.1	ESO 468-G015	0.0566
J224933-331218	SGP.p1.137	556.7 ± 5.9	277.3 ± 6.7	125.3 ± 8.5	DUKST 406-016	0.0289
J230856-305128	SGP.p1.110	594.5 ± 5.6	304.3 ± 6.5	124.6 ± 7.9	ESO 469-G015	0.0055
J222744-300218	SGP.p1.209	598.1 ± 7.9	305.3 ± 8.4	124.2 ± 9.4	ESO 467-G065	0.0282
J235701-344050	SGP.p1.55	813.6 ± 5.0	381.8 ± 5.9	122.8 ± 7.1	ESO 349-G009	0.0421
J004807-284818	SGP.p1.41	1010.8 ± 5.5	406.1 ± 6.4	121.4 ± 7.9		0.1100

Continued on next page...

A.4 – Continued

IAU ID	Alt. ID	S_{250} [mJy]	S_{350} [mJy]	S_{500} [mJy]	Source Name	z_{spec}
J225020-332028	SGP.p1.97	637.7 ± 5.6	294.8 ± 6.3	121.3 ± 7.4	2dFGRS S483z008	0.0412
J235754-314855	SGP.p1.56	831.7 ± 5.1	365.3 ± 6.0	121.0 ± 6.9	MCG -05-01-015	0.0286
J235156-303554	SGP.p1.81	718.0 ± 5.7	322.0 ± 6.5	120.8 ± 7.6	2dFGRS S356z118	0.0505
J002300-343158	SGP.p1.58	842.6 ± 5.5	379.9 ± 6.4	119.1 ± 7.6	ESO 350-IG013	0.0487
J000417-295321	SGP.p1.113	603.3 ± 5.6	305.5 ± 6.5	119.0 ± 7.7	ESO 409-G010	0.0638
J011948-330458	SGP.p1.92	666.9 ± 5.7	314.9 ± 6.5	118.7 ± 7.7	2dFGRS S506z181	0.0312
J003606-323611	SGP.p1.115	583.5 ± 5.5	273.2 ± 6.3	118.5 ± 7.8	ESO 350-G037	0.0148
J224454-341246	SGP.p1.75	800.7 ± 5.9	316.8 ± 6.5	117.8 ± 7.8	2dFGRS S534z238	0.0287
J005019-302910	SGP.p1.133	476.4 ± 5.0	232.3 ± 6.0	117.5 ± 7.1	AM 0047-304	0.0428
J002711-325148	SGP.p1.43	811.3 ± 4.7	321.0 ± 5.7	117.4 ± 6.8		0.0477
J013418-324430	SGP.p1.105	640.9 ± 5.8	298.6 ± 6.6	116.7 ± 7.8	ESO 353-G018	0.0832
J012450-314526	SGP.p1.332	326.7 ± 5.7	220.1 ± 6.6	115.0 ± 7.8	ESO 413-G004	0.0361
J225403-340339	SGP.p1.381	282.7 ± 5.4	192.9 ± 6.3	114.3 ± 7.5	ESO 406-G017	0.0290
J225908-340424	SGP.p1.82	720.1 ± 5.7	312.8 ± 6.5	113.7 ± 7.8	ESO 406-G037	0.0298
J233737-310104	SGP.p1.79	757.5 ± 5.8	310.8 ± 6.3	113.3 ± 7.6		0.0500
J011414-323747	SGP.p1.78	668.8 ± 5.1	272.9 ± 6.0	112.7 ± 7.2		0.0325
J225035-341035	SGP.p1.154	460.6 ± 5.2	214.6 ± 6.0	112.6 ± 7.4		0.0305
J013749-325436	SGP.p1.141	525.7 ± 5.7	267.5 ± 6.7	112.5 ± 7.7	AM 0135-330	0.0348
J234259-334542	SGP.p1.126	552.5 ± 5.5	269.5 ± 6.4	111.3 ± 7.6	2MFGC 17794	0.0516
J012515-332429	SGP.p1.146	524.0 ± 5.7	276.2 ± 6.6	111.3 ± 7.9	ESO 352-G073	0.0233
J224707-292816	SGP.p1.246	414.7 ± 6.1	226.1 ± 6.7	110.6 ± 7.6	ESO 468-G027	0.0228
J233437-321105	SGP.p1.94	641.3 ± 5.6	279.4 ± 6.4	110.4 ± 7.6	FGCE 1830	0.0626
J230441-340327	SGP.p1.103	647.0 ± 5.8	307.5 ± 6.5	109.0 ± 7.9	ESO 407-G002	0.0057
J234142-341214	SGP.p1.178	447.9 ± 5.5	238.0 ± 6.6	108.9 ± 7.8		0.0394
J005852-281812	SGP.p1.91	686.5 ± 5.8	313.8 ± 6.5	108.7 ± 7.6	AM 0056-283	0.0584
J235940-342830	SGP.p1.117	581.5 ± 5.5	293.4 ± 6.3	107.6 ± 7.7	ESO 349-G015	0.0566
J013220-314744	SGP.p1.83	686.0 ± 5.4	283.8 ± 6.2	106.6 ± 7.6		0.0389
J233005-310746	SGP.p1.232	397.3 ± 5.7	192.6 ± 6.4	106.5 ± 7.7		0.0377
J235150-334103	SGP.p1.85	704.7 ± 5.7	291.3 ± 6.3	106.5 ± 7.6		0.0701
J005043-312303	SGP.p1.277	364.5 ± 5.7	202.8 ± 6.4	106.2 ± 7.6		0.0195
J013720-331952	SGP.p1.124	616.8 ± 5.9	295.6 ± 6.6	105.2 ± 8.1	2dFGRS S509z070	0.0446
J004157-325812	SGP.p1.354	311.2 ± 5.6	199.5 ± 6.6	104.6 ± 7.6	ESO 351-G002	0.0319
J232610-303108	SGP.p1.57	730.7 ± 4.7	302.5 ± 5.8	104.0 ± 7.0		0.0641
J005152-303959	SGP.p1.68	730.3 ± 5.0	325.8 ± 6.1	103.7 ± 7.2	2dFGRS S369z084	0.0510
J004450-282323	SGP.p1.72	709.1 ± 5.1	316.1 ± 6.0	103.5 ± 7.0	2dFGRS S287z064	0.0503
J003546-282902	SGP.p1.87	703.7 ± 5.7	288.6 ± 6.3	103.1 ± 7.6	2dFGRS S284z026	0.0236
J003626-281758	SGP.p1.136	534.7 ± 5.6	247.0 ± 6.3	103.0 ± 7.8		0.0741
J235817-300639	SGP.p1.214	377.4 ± 5.1	211.2 ± 6.0	102.9 ± 7.1	ESO 471-G051	0.0301
J230600-324234	SGP.p1.70	737.2 ± 5.1	318.7 ± 6.1	102.7 ± 7.3	2dFGRS S420z025	0.0661
J235713-342819	SGP.p1.123	491.7 ± 4.9	253.6 ± 5.9	102.5 ± 7.1		0.0336
J235657-320757	SGP.p1.139	439.6 ± 4.7	229.3 ± 5.7	102.1 ± 6.8	ESO 471-G048	0.0291
J005104-322525	SGP.p1.273	376.2 ± 5.7	218.6 ± 6.4	101.8 ± 7.5	ESO 351-G011	0.0324
J010013-304836	SGP.p1.125	473.8 ± 4.7	257.4 ± 5.7	101.7 ± 6.8	ESO 412-G001	0.0322
J002727-340433	SGP.p1.212	406.0 ± 5.5	231.1 ± 6.4	101.1 ± 7.8	MCG-06-02-008	0.0306
J003049-332751	SGP.p1.131	520.5 ± 5.4	260.0 ± 6.4	100.8 ± 7.8	2MFGC 00356	0.0322
J231927-343746	SGP.p1.89	689.4 ± 5.7	305.7 ± 6.5	100.5 ± 7.6		0.0555
J000204-332802	SGP.p1.73	799.0 ± 5.6	317.3 ± 6.5	100.3 ± 7.6	ESO 349-G020	0.0292
J004416-283756	SGP.p1.204	432.2 ± 5.6	208.1 ± 6.4	100.0 ± 7.9	ESO 411-G009	0.0432
J222950-303127	SGP.p1.293	469.3 ± 7.5	255.8 ± 7.9	99.9 ± 9.3	ESO 468-G003	0.0540
J001254-311036	SGP.p1.446	244.1 ± 5.0	152.0 ± 5.9	99.7 ± 7.2		0.0593
J000556-310609	SGP.p1.116	576.2 ± 5.5	279.9 ± 6.4	99.4 ± 7.7	ESO 409-G016	0.0261
J223022-311007	SGP.p1.155	686.2 ± 7.8	262.5 ± 8.0	98.9 ± 10.1		0.0585
J223835-305456	SGP.p1.151	477.4 ± 5.3	233.9 ± 6.1	98.8 ± 7.4		0.0493
J223748-322143	SGP.p1.152	476.8 ± 5.4	206.6 ± 6.2	98.7 ± 7.6		0.0484
J003819-285131	SGP.p1.108	601.1 ± 5.5	259.1 ± 6.4	98.7 ± 7.7		0.0525
J002734-341150	SGP.p1.149	487.8 ± 5.4	247.2 ± 6.4	98.3 ± 7.7	ESO 350-G019	0.0303
J223745-320726	SGP.p1.138	466.4 ± 5.0	256.6 ± 6.1	98.3 ± 7.3		0.0276
J222950-335258	SGP.p1.145	701.1 ± 7.6	266.9 ± 8.0	98.3 ± 9.4		0.0596
J224803-344226	SGP.p1.211	415.1 ± 5.7	219.6 ± 6.6	98.3 ± 7.7		0.0283
J232116-324727	SGP.p1.104	545.4 ± 4.9	249.3 ± 6.0	96.8 ± 7.1		0.0574
J010513-284752	SGP.p1.190	435.7 ± 5.5	226.1 ± 6.4	96.4 ± 7.7	MCG -05-03-023	0.0190
J223402-322351	SGP.p1.628	284.4 ± 6.8	174.8 ± 7.6	96.3 ± 9.7	ESO 405-G029	0.0121
J004641-275354	SGP.p1.132	535.0 ± 5.6	268.5 ± 6.3	96.3 ± 7.7	ESO 411-G011	0.0603
J002846-322423	SGP.p1.177	376.5 ± 4.7	223.6 ± 5.7	96.0 ± 6.8	ESO 350-G020	0.0459
J224318-300540	SGP.p1.219	451.6 ± 6.2	186.3 ± 6.6	95.3 ± 8.2	MCG -05-53-029	0.0282
J014149-281449	SGP.p1.342	338.9 ± 6.0	211.8 ± 6.6	94.8 ± 7.8	ESO 413-G023	0.0193
J225644-334658	SGP.p1.169	492.4 ± 5.9	240.7 ± 6.6	94.7 ± 7.7	ESO 406-G028	0.0285

Continued on next page...

A.4 – Continued

IAU ID	Alt. ID	S_{250} [mJy]	S_{350} [mJy]	S_{500} [mJy]	Source Name	z_{spec}
J003245-331014	SGP.p1.172	456.6 ± 5.5	228.9 ± 6.4	94.5 ± 7.6	MCG -06-02-016	0.0494
J005947-332220	SGP.p1.71	695.7 ± 4.9	289.1 ± 5.9	94.3 ± 7.1	2MFGC 00718	0.0196
J235728-302740	SGP.p1.144	428.7 ± 4.7	216.2 ± 5.7	93.8 ± 6.8	AM 2354-304	0.0307
J225318-335559	SGP.p1.114	540.6 ± 5.1	240.9 ± 6.2	93.2 ± 7.2		0.0273
J014043-282122	SGP.p1.917	215.0 ± 6.2	133.1 ± 6.7	92.5 ± 7.8		0.0589
J230327-320123	SGP.p1.286	358.9 ± 5.7	207.3 ± 6.7	92.3 ± 7.6		0.0734
J013847-314916	SGP.p1.285	324.6 ± 5.2	182.7 ± 6.1	91.7 ± 7.4	ESO 413-G012	0.0295
J005856-281930	SGP.p1.156	493.4 ± 5.6	220.2 ± 6.4	91.0 ± 7.5	AM 0056-283	0.0577
J012855-320044	SGP.p1.254	386.0 ± 5.8	199.3 ± 6.4	90.8 ± 8.1	MCG -05-04-040	0.0209
J014031-324205	SGP.p1.167	461.7 ± 5.7	212.8 ± 6.5	90.8 ± 8.0	MCG -06-04-065	0.0166
J001743-332401	SGP.p1.159	488.3 ± 5.7	215.2 ± 6.4	89.9 ± 7.9	2dFGRS S497z230	0.0312
J003601-311154	SGP.p1.157	485.5 ± 5.7	188.3 ± 6.4	89.9 ± 7.7	AM 0033-312	0.0538
J014400-303533	SGP.p1.175	434.9 ± 5.2	191.0 ± 6.0	89.8 ± 7.4	2dFGRS S381z032	0.1661
J223659-321321	SGP.p1.148	454.1 ± 5.0	243.5 ± 6.1	89.0 ± 7.2	ESO 468-G017	0.0270
J233004-325208	SGP.p1.184	462.3 ± 5.8	201.8 ± 6.5	88.9 ± 7.6		0.0552
J235324-314142	SGP.p1.121	571.5 ± 5.6	264.2 ± 6.5	88.8 ± 7.7	ESO 471-G038	0.0498
J230659-325232	SGP.p1.107	546.2 ± 5.0	238.8 ± 6.0	88.7 ± 7.2	PRC C-70	0.0606
J235759-295158	SGP.p1.109	509.0 ± 4.6	244.4 ± 5.6	88.6 ± 6.9	ESO 471-G050	0.0298
J235508-313439	SGP.p1.225	408.4 ± 5.7	214.4 ± 6.3	87.8 ± 7.6	ESO 471-G041	0.0286
J011551-313522	SGP.p1.228	385.4 ± 5.5	210.5 ± 6.3	87.6 ± 7.7	MCG -05-04-026	0.0357
J232514-315306	SGP.p1.45	815.1 ± 4.7	293.4 ± 5.7	87.4 ± 6.9		0.0414
J013900-283419	SGP.p1.185	453.9 ± 5.7	211.2 ± 6.5	87.2 ± 7.7	MCG -05-05-004	0.0433
J000630-315721	SGP.p1.335	315.5 ± 5.5	184.9 ± 6.6	86.9 ± 7.7	ESO 409-G019	0.0261
J012154-323843	SGP.p1.102	686.5 ± 6.0	255.6 ± 6.6	85.6 ± 7.8		0.0307
J232301-312156	SGP.p1.170	474.6 ± 5.8	210.0 ± 6.5	85.5 ± 7.6		0.0777
J223151-305903	SGP.p1.383	412.8 ± 7.7	181.9 ± 8.8	85.4 ± 9.6		–
J011201-300306	SGP.p1.158	491.2 ± 5.7	222.5 ± 6.4	85.1 ± 7.7		0.0902
J225204-342608	SGP.p1.288	356.8 ± 5.7	200.2 ± 6.6	84.6 ± 8.2	MCG-06-50-006	0.0280
J005349-331740	SGP.p1.552	250.0 ± 5.6	163.6 ± 6.5	84.4 ± 7.6		0.0178
J002037-342819	SGP.p1.224	407.3 ± 5.6	193.9 ± 6.4	82.7 ± 8.0	ESO 350-IG010	0.0253
J010305-330651	SGP.p1.135	537.3 ± 5.8	219.9 ± 6.5	82.4 ± 7.6		0.0507
J011941-330622	SGP.p1.595	245.9 ± 5.7	130.6 ± 6.6	82.0 ± 8.0	ESO 352-G044	0.0310
J010904-304040	SGP.p1.2690	114.4 ± 5.2	96.4 ± 6.1	81.9 ± 7.3		0.0806
J001720-313727	SGP.p1.86	717.0 ± 5.8	261.5 ± 6.4	81.5 ± 7.9	2dFGRS S435z205	0.1034
J230454-312905	SGP.p1.412	307.0 ± 5.9	158.9 ± 6.5	81.3 ± 7.9		0.1313
J003637-274719	SGP.p1.334	318.6 ± 5.6	152.6 ± 6.4	81.3 ± 7.7	ESO 410-G025	0.0233
J012116-331315	SGP.p1.2283	136.3 ± 5.8	116.7 ± 6.5	81.2 ± 7.7		0.0192
J000821-295449	SGP.p1.1772	147.4 ± 5.6	132.6 ± 6.5	81.1 ± 7.7	NGC 0007	0.0050
J233233-344725	SGP.p1.343	322.4 ± 5.7	169.0 ± 6.5	81.1 ± 7.9	2dFGRS S542z109	0.0609
J012323-303434	SGP.p1.205	385.0 ± 5.1	183.1 ± 6.1	80.8 ± 7.2		0.0628
J000604-303743	SGP.p1.518	251.7 ± 5.5	140.2 ± 6.5	80.6 ± 7.8	ESO 409-G018	0.0294
J232923-351006	SGP.p1.312	343.5 ± 5.6	167.6 ± 6.6	80.4 ± 7.7		0.0516
J012455-303715	SGP.p1.371	273.3 ± 5.1	150.6 ± 6.0	80.4 ± 7.3	MCG -05-04-037	0.0657
J013639-332156	SGP.p1.3209	115.7 ± 5.5	101.6 ± 6.5	80.3 ± 7.8		0.0692

Table A.5: Summary of NGP sources classified as blazars.

IAU ID	Alt. ID	S_{250} [mJy]	S_{350} [mJy]	S_{500} [mJy]	$S_{1.4}$ [mJy/beam]	z_{spec}
J131029+322044	NGP.p1.373	265.3 ± 4.9	373.0 ± 6.0	453.5 ± 7.1	1459.0	0.9980
J125757+322930	NGP.p1.1255	144.9 ± 5.5	190.1 ± 6.4	217.6 ± 7.6	589.2	0.8059
J133307+272518	NGP.p1.4302	91.0 ± 5.6	107.6 ± 6.3	121.5 ± 7.4	209.5	2.1260
J131736+342518	NGP.p1.7031	77.1 ± 5.5	97.2 ± 6.3	114.7 ± 7.6	421.0	1.0554
J133108+303035	NGP.p1.9434	72.6 ± 5.7	88.4 ± 6.3	92.7 ± 7.5	14774.4	0.8499
J132953+315411	NGP.p1.32217	50.4 ± 5.6	67.8 ± 6.3	81.7 ± 7.9	779.0	–

Table A.6: Summary of SGP sources classified as blazars.

IAU ID	Alt. ID	S_{250} [mJy]	S_{350} [mJy]	S_{500} [mJy]	$S_{1.4}$ [mJy/beam]	z_{spec}
J014503-273333	SGP.p1.2350	139.5 ± 5.9	188.0 ± 6.8	242.2 ± 7.9	837.5	1.1550
J224839-323551	SGP.p1.3100	125.7 ± 5.7	166.2 ± 6.5	204.3 ± 7.6	655.9	2.2680
J014310-320055	SGP.p1.5607	98.3 ± 5.6	123.5 ± 6.6	128.4 ± 7.9	73.7	0.3751
J235347-303744	SGP.p1.8463	82.8 ± 5.5	102.6 ± 6.5	107.2 ± 7.8	339.8	–
J235935-313337	SGP.p1.14228	47.7 ± 5.8	94.2 ± 6.5	99.4 ± 7.9	304.5	–
J235010-293950	SGP.p1.3139	61.0 ± 6.0	76.5 ± 6.5	82.6 ± 8.0	58.5	–

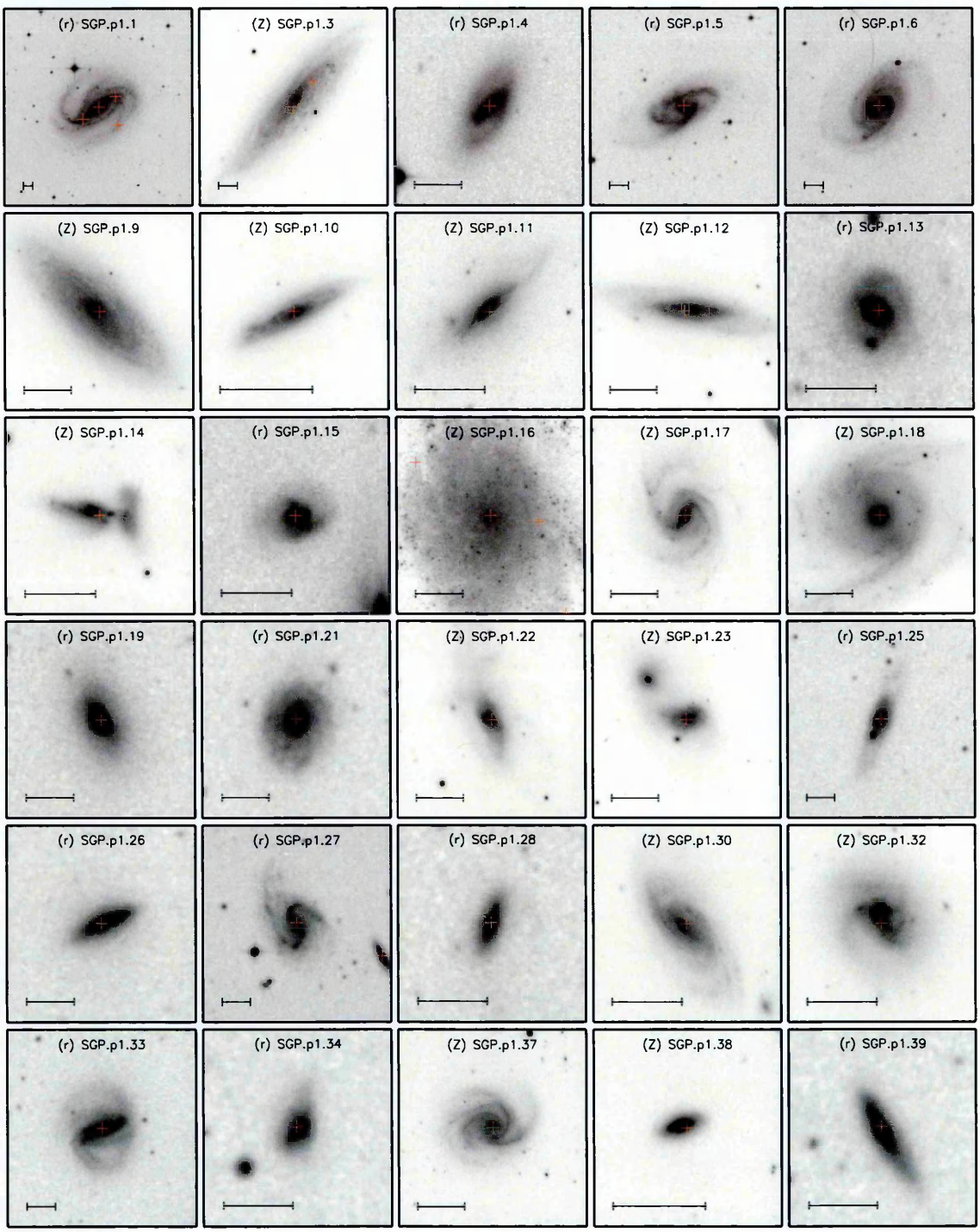

Figure A.8: SGP local postage stamps.

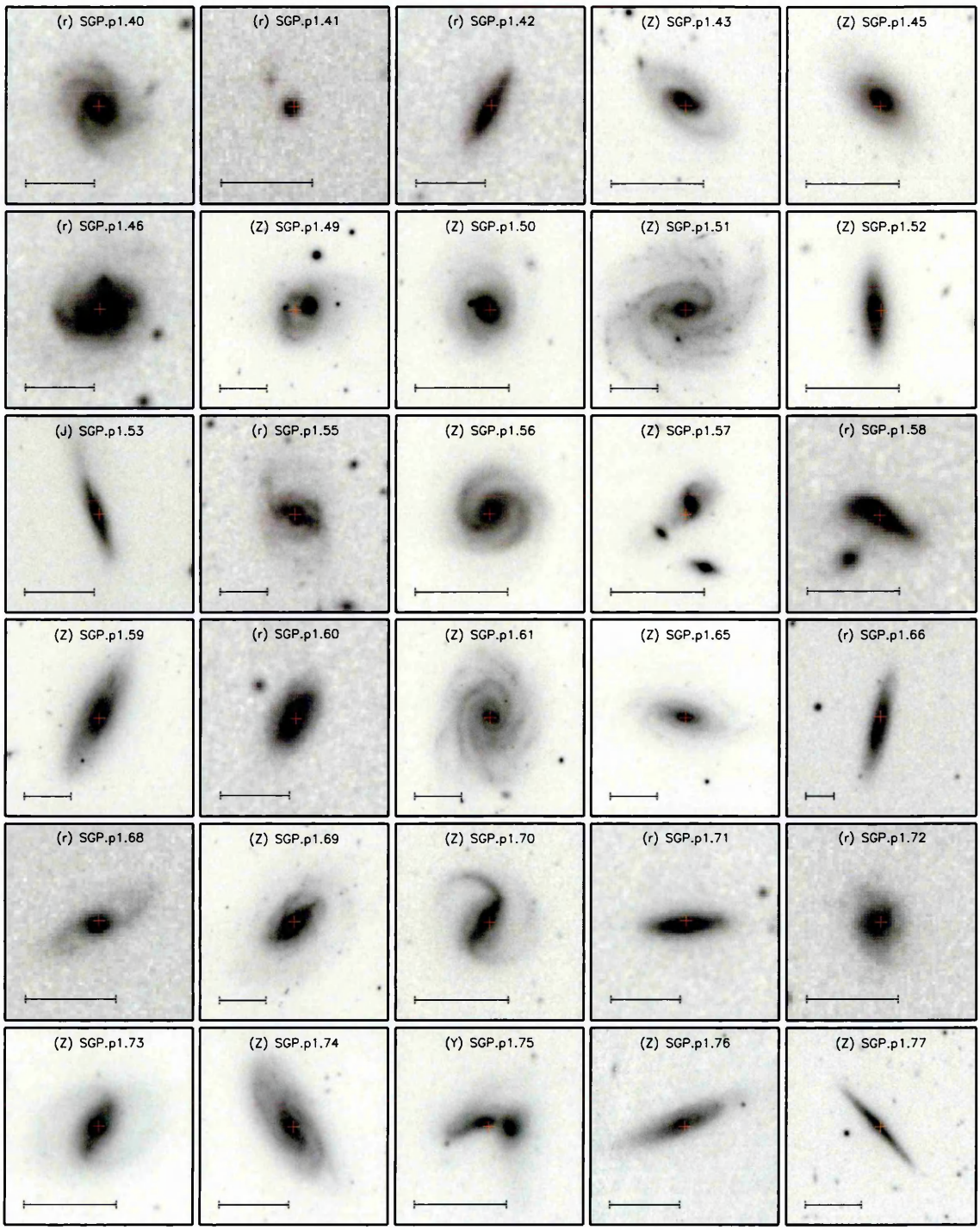

Figure A.8 (Continued): SGP local candidate postage stamps.

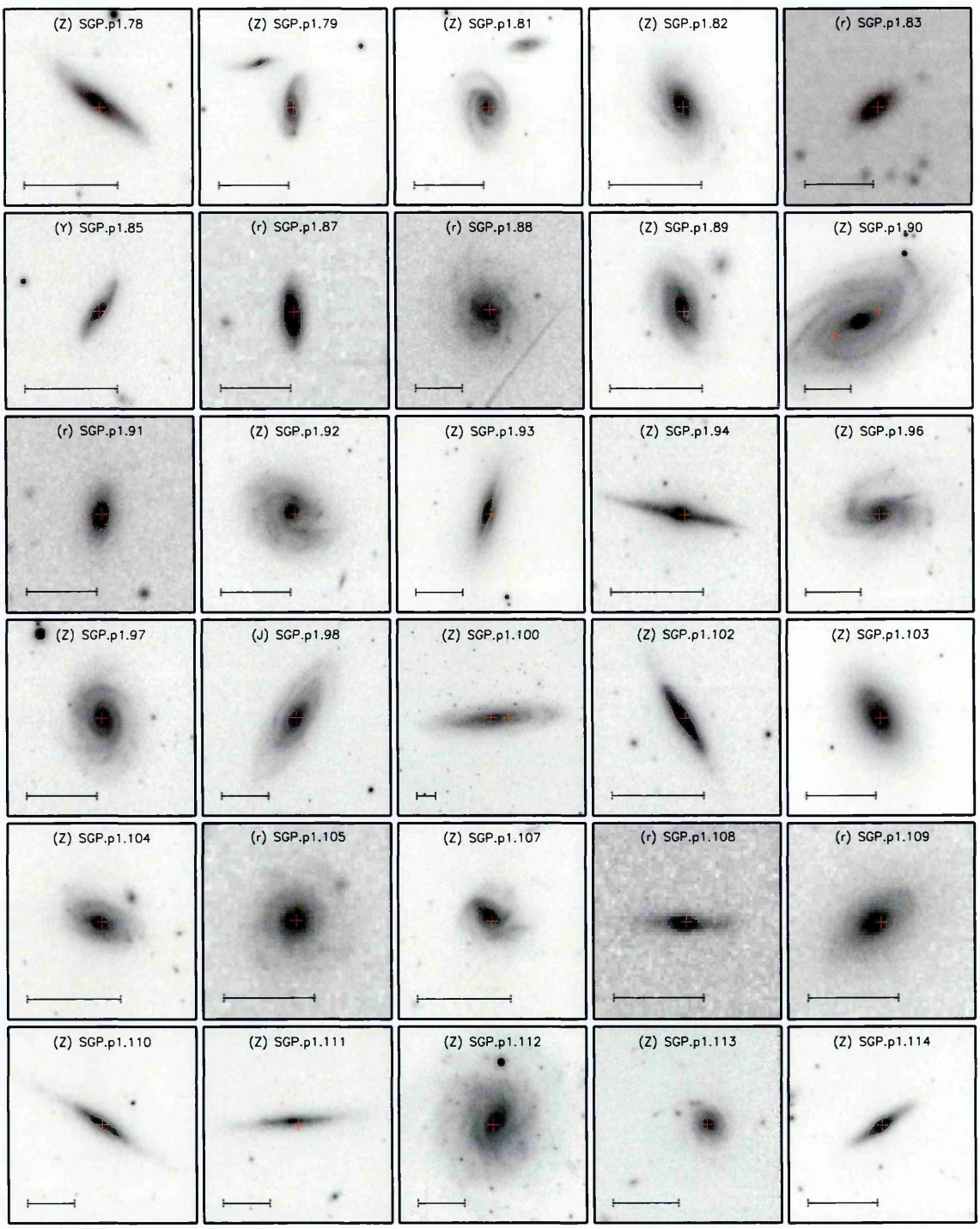

Figure A.8 (Continued): SGP local candidate postage stamps.

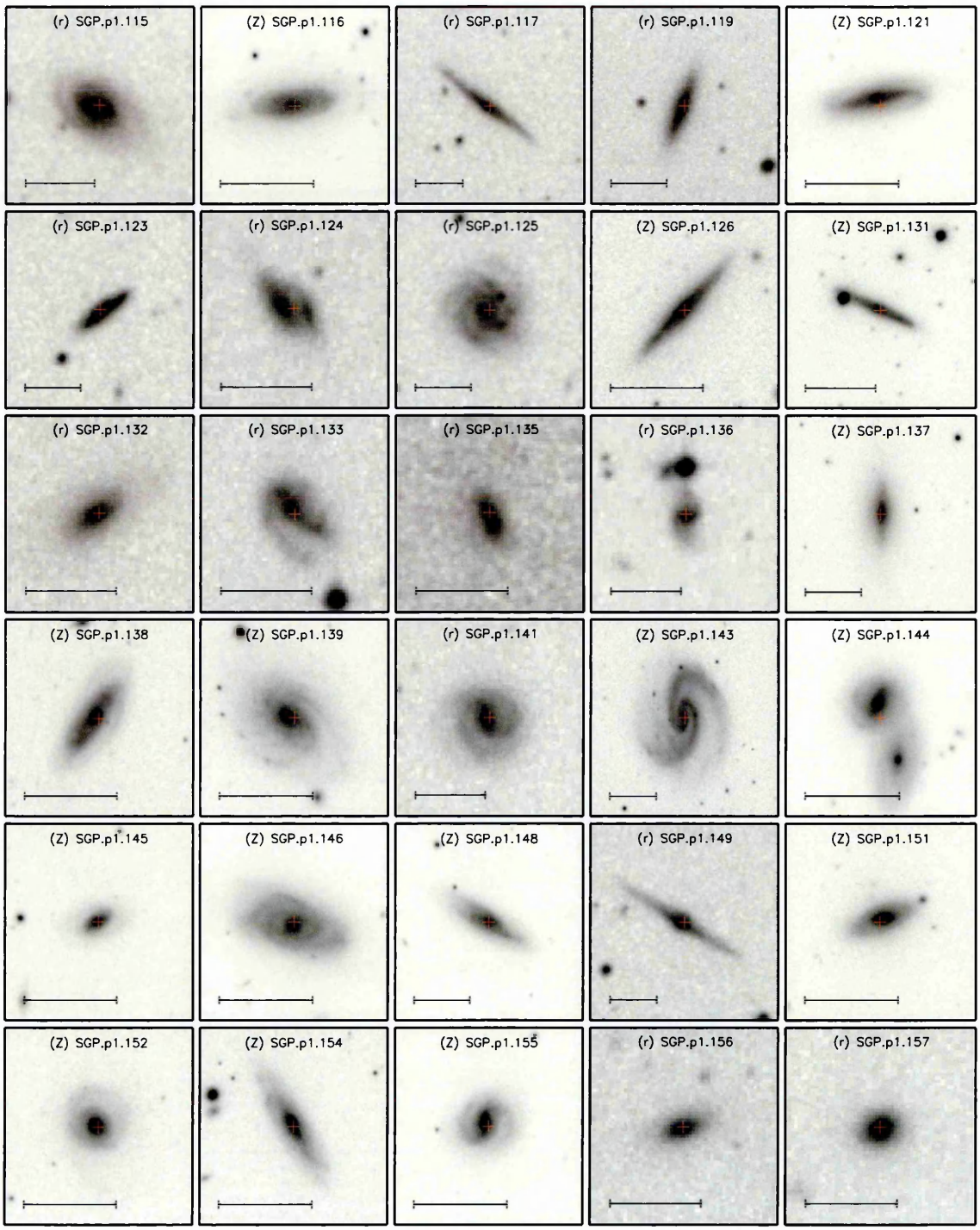

Figure A.8 (Continued): SGP local candidate postage stamps.

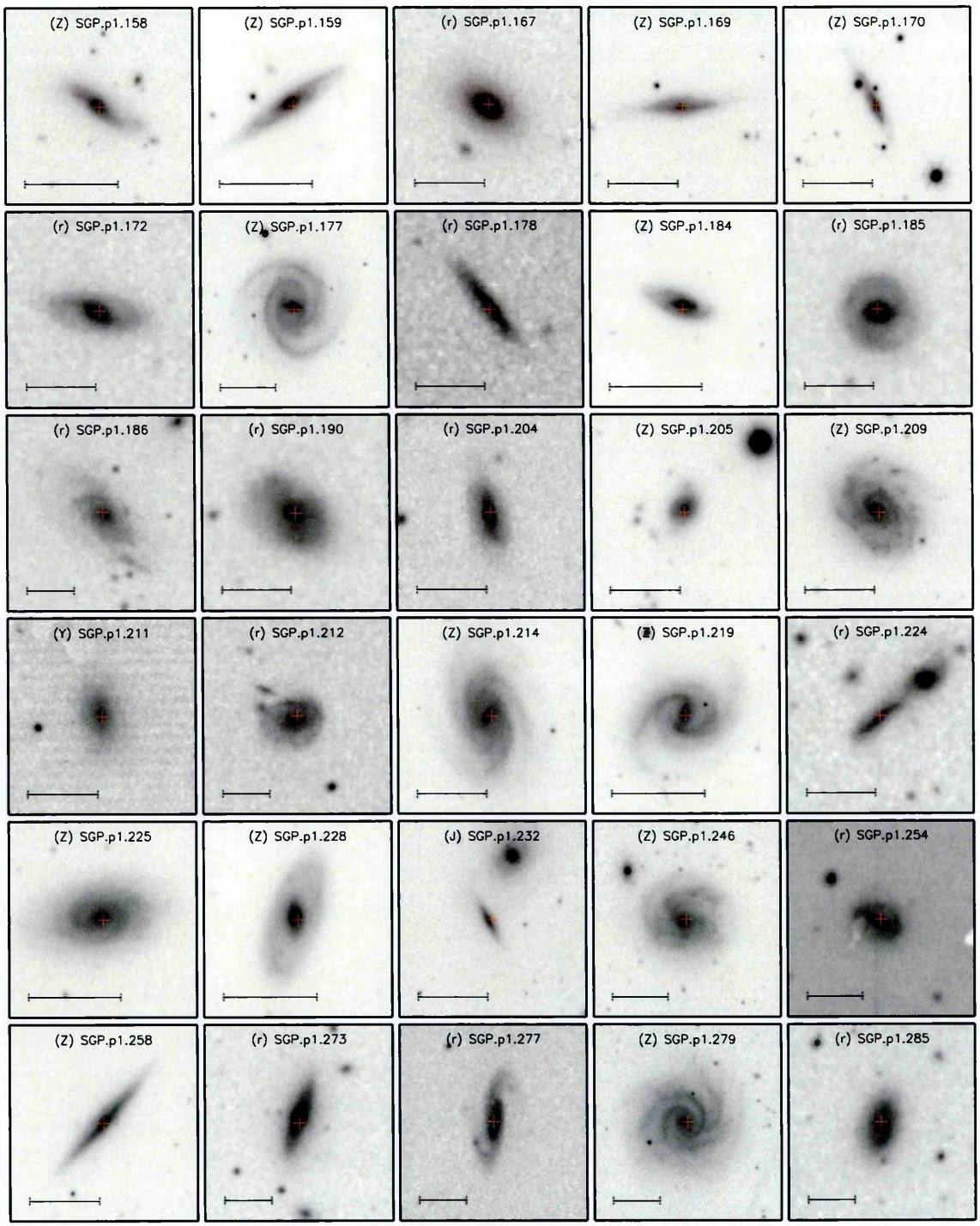

Figure A.8 (Continued): SGP local candidate postage stamps.

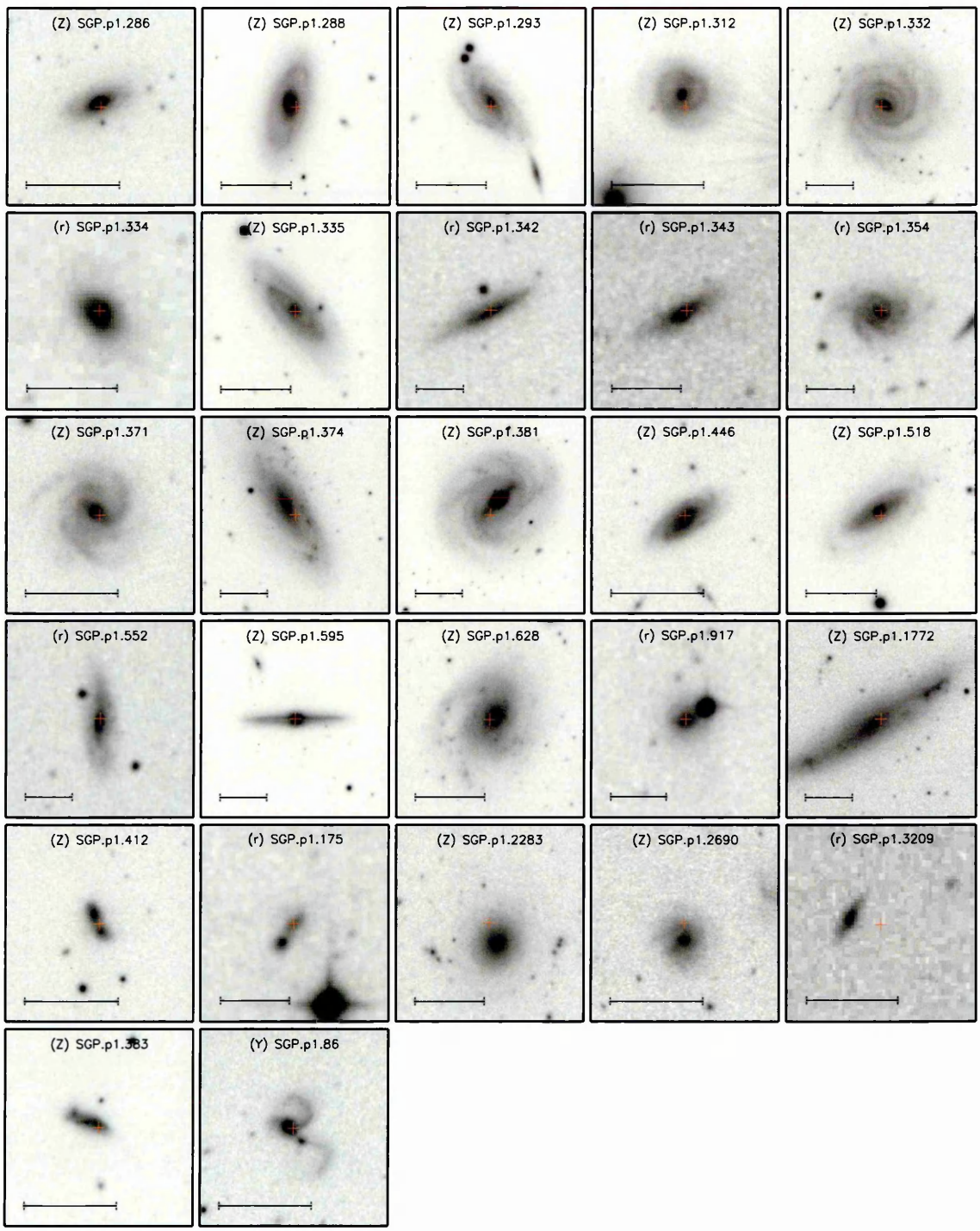

Figure A.8 (Continued): SGP local candidate postage stamps.

Appendix B

HST Snapshots

Table B.1: HST snapshot target data.

IAU ID	S_{100} [mJy]	S_{160} [mJy]	S_{250} [mJy]	S_{350} [mJy]	S_{500} [mJy]	z_{phot}
J083051+013225	21 ± 62	0 ± 90	260 ± 7	321 ± 8	269 ± 9	2.74 ± 0.57
J083153+014014	48 ± 43	114 ± 45	94 ± 7	121 ± 8	98 ± 8	2.74 ± 0.57
J083345+000109	126 ± 50	30 ± 63	91 ± 7	119 ± 8	103 ± 8	2.86 ± 0.59
J083546+002804	10 ± 48	35 ± 44	76 ± 6	100 ± 8	89 ± 8	2.92 ± 0.61
J083817-004134	54 ± 49	137 ± 65	89 ± 6	113 ± 8	98 ± 9	2.80 ± 0.58
J083932-011760	75 ± 45	33 ± 62	79 ± 6	108 ± 8	100 ± 8	3.03 ± 0.63
J083945+021023	31 ± 40	93 ± 63	77 ± 6	108 ± 8	91 ± 8	2.95 ± 0.61
J084933+021443	0 ± 38	168 ± 46	241 ± 6	292 ± 8	231 ± 8	2.62 ± 0.54
J084958+010713	0 ± 46	0 ± 67	90 ± 6	123 ± 8	95 ± 8	2.80 ± 0.58
J085033+012914	22 ± 50	42 ± 67	68 ± 6	103 ± 8	89 ± 8	3.09 ± 0.64
J085112+004934	0 ± 39	109 ± 47	131 ± 6	133 ± 8	95 ± 8	2.23 ± 0.46
J085126+014638	0 ± 50	0 ± 66	71 ± 6	108 ± 8	102 ± 9	3.21 ± 0.67
J085309-005727	2 ± 50	0 ± 65	77 ± 7	119 ± 8	98 ± 8	3.03 ± 0.63
J085359+015537	59 ± 40	196 ± 48	388 ± 6	381 ± 8	240 ± 9	2.05 ± 0.43
J090953-010811	153 ± 46	228 ± 50	156 ± 6	134 ± 8	89 ± 8	1.84 ± 0.38
J091238+020050	26 ± 41	122 ± 69	85 ± 6	97 ± 8	94 ± 8	2.80 ± 0.58
J091331-003644	101 ± 29	180 ± 33	172 ± 6	148 ± 7	101 ± 8	1.87 ± 0.39
J091454-010357	7 ± 44	83 ± 45	71 ± 6	97 ± 8	103 ± 8	3.24 ± 0.67
J091809+001927	26 ± 51	167 ± 69	108 ± 6	136 ± 8	103 ± 8	2.65 ± 0.55
J091841+023048	11 ± 45	118 ± 67	141 ± 6	175 ± 8	138 ± 8	2.65 ± 0.55
J091857-000047	0 ± 46	0 ± 66	72 ± 6	107 ± 8	95 ± 8	3.09 ± 0.64
J091949-005037	86 ± 40	126 ± 45	169 ± 6	164 ± 8	98 ± 8	1.99 ± 0.41
J092136+000132	50 ± 50	101 ± 45	142 ± 6	139 ± 8	96 ± 8	2.14 ± 0.44
J092141+005356	0 ± 47	78 ± 62	64 ± 6	105 ± 8	100 ± 9	3.36 ± 0.70
J092409-005018	0 ± 39	93 ± 67	77 ± 6	104 ± 8	97 ± 8	3.03 ± 0.63
J113243-005109	0 ± 0	0 ± 0	75 ± 6	120 ± 8	107 ± 8	3.21 ± 0.67
J113526-014606	29 ± 44	97 ± 44	289 ± 6	295 ± 8	216 ± 8	2.26 ± 0.47
J113804-011736	62 ± 38	82 ± 46	109 ± 6	133 ± 8	114 ± 8	2.74 ± 0.57
J113834-014657	0 ± 46	0 ± 65	82 ± 6	109 ± 8	114 ± 8	3.18 ± 0.66
J113841-020237	34 ± 49	31 ± 43	84 ± 6	108 ± 8	92 ± 9	2.80 ± 0.58
J114638-001132	91 ± 33	223 ± 34	289 ± 6	356 ± 7	295 ± 8	2.71 ± 0.56
J114753-005832	47 ± 27	78 ± 33	111 ± 6	135 ± 7	117 ± 8	2.74 ± 0.57
J115112-012638	13 ± 48	104 ± 47	153 ± 6	164 ± 8	114 ± 9	2.29 ± 0.48
J115120-003322	87 ± 39	97 ± 48	134 ± 6	124 ± 8	81 ± 8	1.96 ± 0.41
J115521-021332	1 ± 40	0 ± 70	59 ± 6	92 ± 8	94 ± 8	3.39 ± 0.71
J115820-013754	34 ± 31	162 ± 54	130 ± 6	142 ± 7	106 ± 8	2.38 ± 0.49
J125105+261653	– ± –	– ± –	116 ± 5	125 ± 6	81 ± 7	2.23 ± 0.46
J125126+254928	– ± –	– ± –	64 ± 5	103 ± 6	109 ± 7	3.48 ± 0.72
J125653+275903	– ± –	– ± –	139 ± 5	168 ± 6	133 ± 7	2.62 ± 0.54
J125800+224558	– ± –	– ± –	291 ± 5	237 ± 6	144 ± 7	1.66 ± 0.34

Continued on next page...

B.1 – Continued

IAU ID	S_{100} [mJy]	S_{160} [mJy]	S_{250} [mJy]	S_{350} [mJy]	S_{500} [mJy]	z_{phot}
J125810+263710	– ± –	– ± –	190 ± 5	153 ± 6	107 ± 7	1.75 ± 0.36
J130054+260303	– ± –	– ± –	62 ± 5	97 ± 6	98 ± 7	3.36 ± 0.70
J130601+231322	– ± –	– ± –	192 ± 4	143 ± 5	77 ± 7	1.45 ± 0.30
J131001+264759	– ± –	– ± –	53 ± 5	85 ± 6	82 ± 7	3.33 ± 0.69
J131020+253731	– ± –	– ± –	74 ± 5	101 ± 6	86 ± 7	2.92 ± 0.61
J131322+285836	– ± –	– ± –	52 ± 5	84 ± 5	81 ± 7	3.33 ± 0.69
J131609+254931	– ± –	– ± –	140 ± 5	124 ± 6	72 ± 7	1.81 ± 0.38
J131611+281220	– ± –	– ± –	71 ± 5	102 ± 6	92 ± 7	3.06 ± 0.64
J131642+251158	– ± –	– ± –	185 ± 5	142 ± 6	85 ± 7	1.54 ± 0.32
J132128+282023	– ± –	– ± –	119 ± 5	132 ± 6	92 ± 7	2.35 ± 0.49
J132227+300723	– ± –	– ± –	141 ± 5	133 ± 6	96 ± 7	2.08 ± 0.43
J132302+341650	– ± –	– ± –	133 ± 5	152 ± 6	140 ± 7	2.71 ± 0.56
J132419+320754	– ± –	– ± –	96 ± 5	121 ± 5	115 ± 7	2.92 ± 0.61
J132630+334410	– ± –	– ± –	198 ± 5	292 ± 6	289 ± 7	3.24 ± 0.67
J132909+300958	– ± –	– ± –	76 ± 5	114 ± 6	94 ± 7	3.01 ± 0.63
J133008+245860	– ± –	– ± –	269 ± 5	284 ± 6	204 ± 7	2.29 ± 0.48
J133255+265529	– ± –	– ± –	194 ± 5	167 ± 6	120 ± 7	1.90 ± 0.39
J133256+342210	– ± –	– ± –	169 ± 5	189 ± 6	123 ± 7	2.29 ± 0.48
J133440+353140	– ± –	– ± –	83 ± 5	111 ± 6	94 ± 7	2.86 ± 0.59
J133534+341837	– ± –	– ± –	107 ± 5	120 ± 6	94 ± 7	2.47 ± 0.51
J133543+300404	– ± –	– ± –	150 ± 5	158 ± 6	129 ± 7	2.41 ± 0.50
J133623+343806	– ± –	– ± –	196 ± 5	156 ± 6	77 ± 7	1.51 ± 0.31
J133715+352058	– ± –	– ± –	66 ± 5	92 ± 6	82 ± 7	3.01 ± 0.63
J133846+255057	– ± –	– ± –	158 ± 5	181 ± 6	137 ± 7	2.47 ± 0.51
J133905+340820	– ± –	– ± –	154 ± 5	158 ± 6	97 ± 7	2.11 ± 0.44
J134124+354007	– ± –	– ± –	93 ± 5	104 ± 6	92 ± 7	2.62 ± 0.54
J134139+322837	– ± –	– ± –	64 ± 5	91 ± 5	86 ± 7	3.12 ± 0.65
J134159+292833	– ± –	– ± –	174 ± 4	175 ± 5	110 ± 7	2.11 ± 0.44
J134403+242627	– ± –	– ± –	93 ± 5	108 ± 6	92 ± 7	2.65 ± 0.55
J134429+303036	– ± –	– ± –	465 ± 5	474 ± 6	341 ± 7	2.23 ± 0.46
J134442+240346	– ± –	– ± –	118 ± 5	131 ± 6	103 ± 7	2.47 ± 0.51
J134654+295659	– ± –	– ± –	163 ± 5	130 ± 6	83 ± 7	1.66 ± 0.34
J140422-001218	23 ± 43	48 ± 45	85 ± 6	112 ± 8	89 ± 8	2.77 ± 0.58
J141118-010655	0 ± 46	219 ± 65	62 ± 6	87 ± 8	89 ± 8	3.21 ± 0.67
J141352-000027	29 ± 53	105 ± 68	189 ± 6	240 ± 8	200 ± 8	2.77 ± 0.58
J141833+010212	0 ± 49	92 ± 63	77 ± 6	113 ± 7	96 ± 8	3.01 ± 0.63
J142004+014045	68 ± 47	209 ± 45	124 ± 6	125 ± 8	87 ± 9	2.17 ± 0.45
J142140+000448	1 ± 53	122 ± 70	102 ± 6	111 ± 8	92 ± 8	2.50 ± 0.52
J142414+022304	0 ± 50	0 ± 70	115 ± 6	191 ± 8	203 ± 8	3.54 ± 0.74
J142707+002258	31 ± 29	87 ± 31	137 ± 6	136 ± 8	96 ± 8	2.17 ± 0.45
J142935-002837	821 ± 27	1163 ± 32	778 ± 6	466 ± 7	226 ± 8	0.94 ± 0.20
J143203-005219	0 ± 45	2 ± 47	89 ± 6	115 ± 7	93 ± 8	2.77 ± 0.58
J144243+015506	42 ± 52	48 ± 48	121 ± 6	144 ± 8	92 ± 8	2.38 ± 0.49
J144715-012114	17 ± 45	65 ± 46	176 ± 6	156 ± 8	97 ± 8	1.84 ± 0.38
J145754+000017	0 ± 0	0 ± 0	89 ± 6	112 ± 8	96 ± 9	2.77 ± 0.58

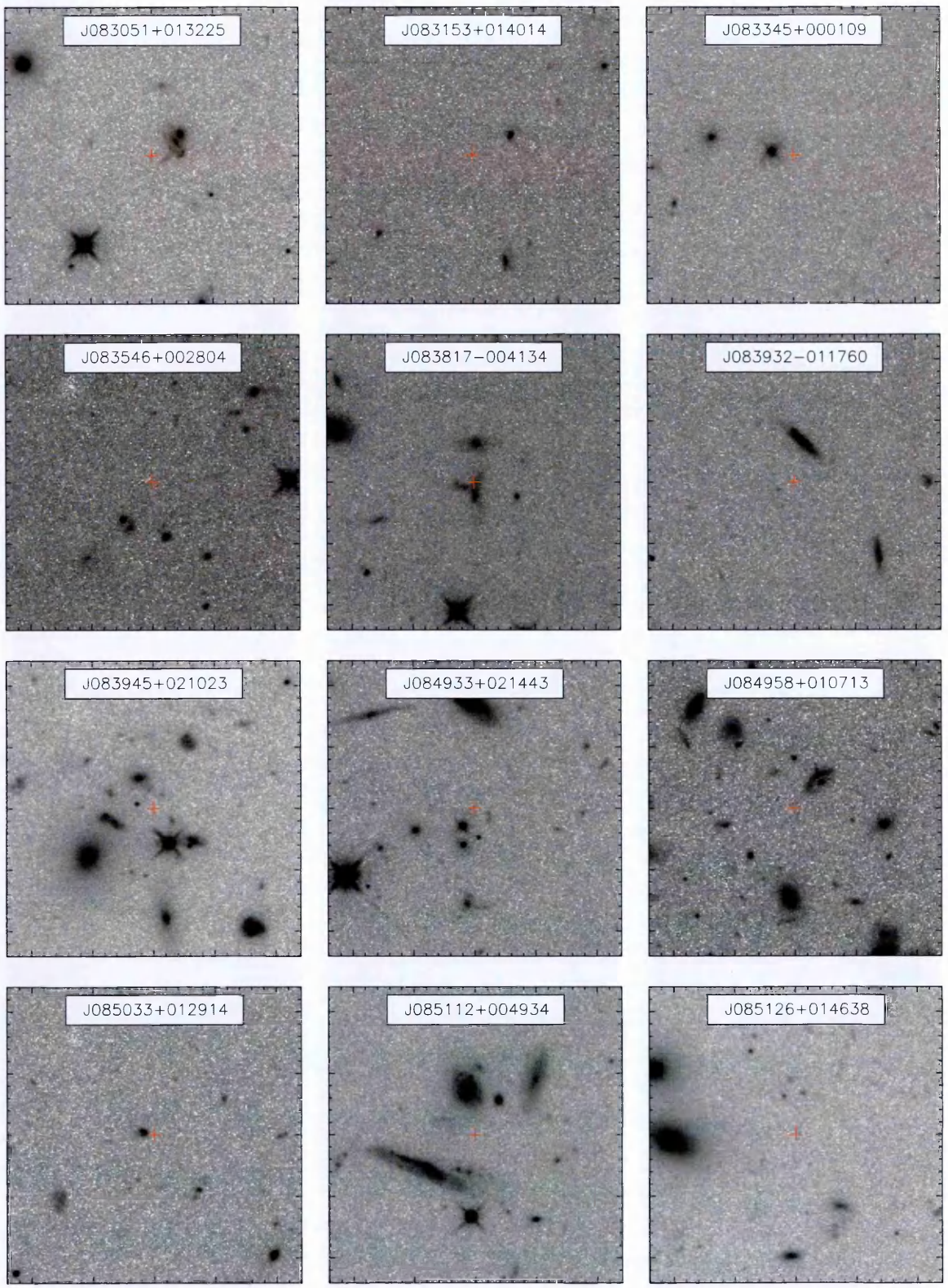

Figure B.1: HST drizzled snapshots, images are 24" on a side centered at the SPIRE emission marked by the red cross.

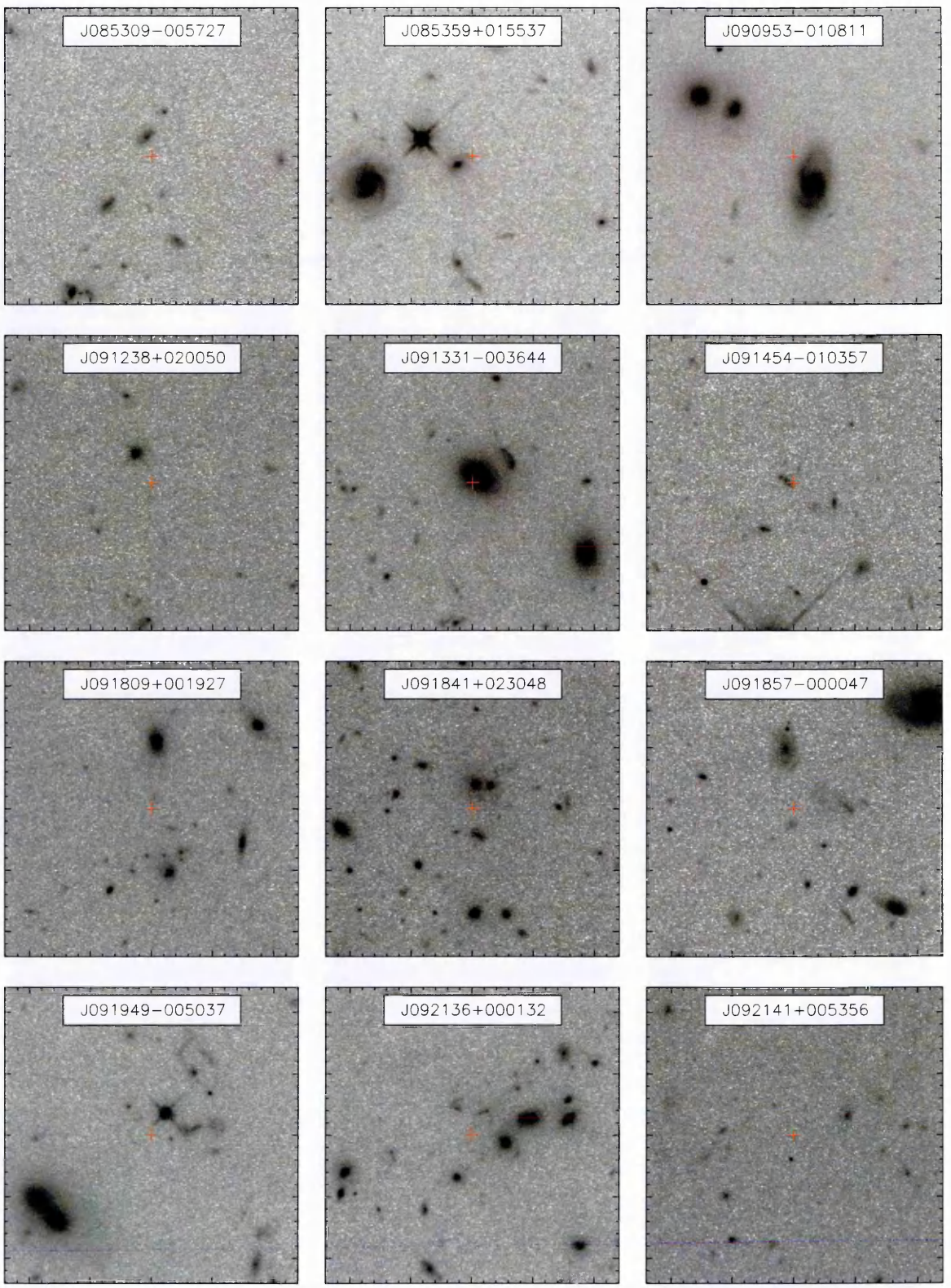

Figure B.1 (Continued): HST drizzled snapshots, images are 24" on a side centered at the SPIRE emission marked by the red cross.

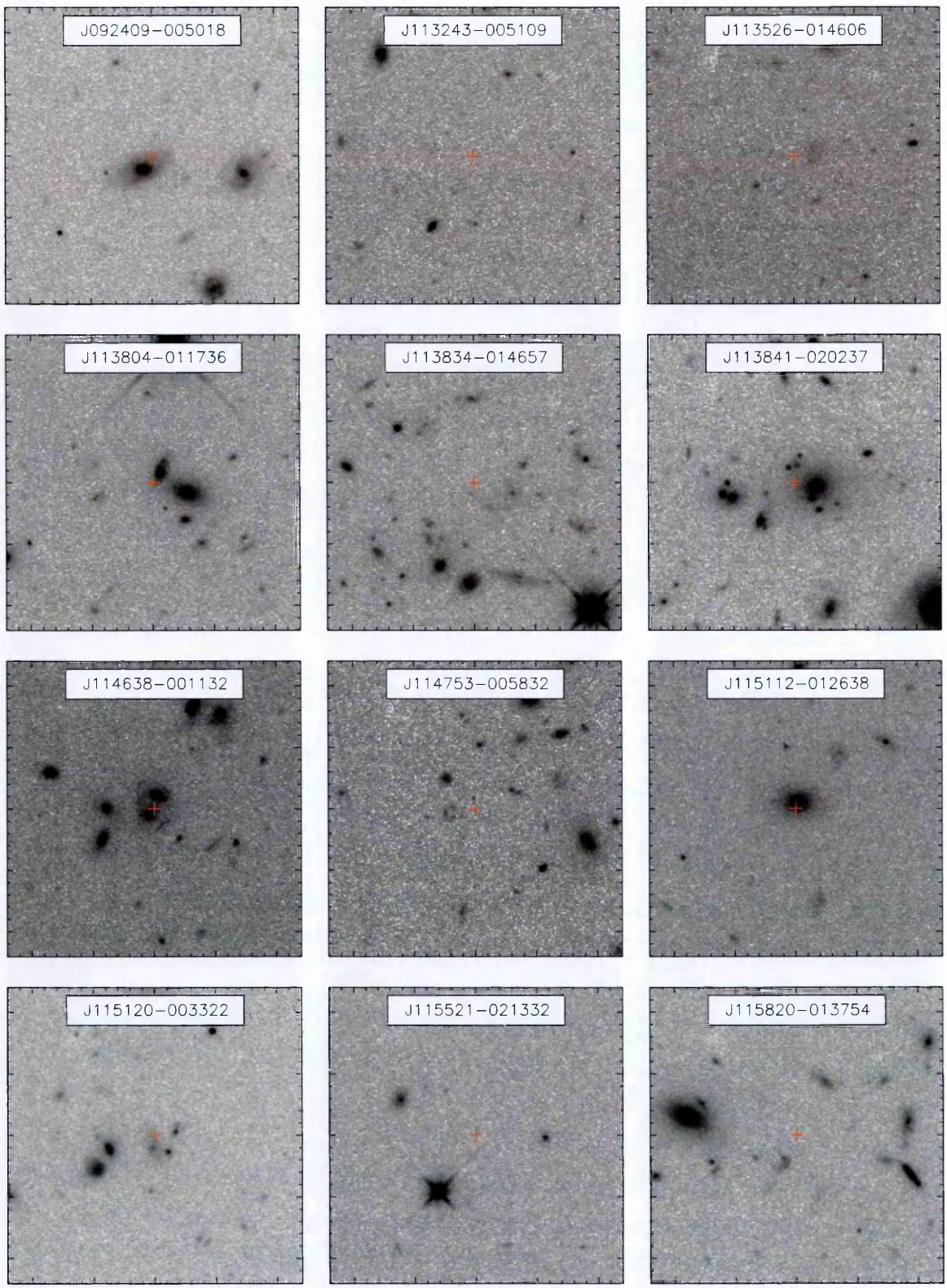

Figure B.1 (Continued): HST drizzled snapshots, images are 24" on a side centered at the SPIRE emission marked by the red cross.

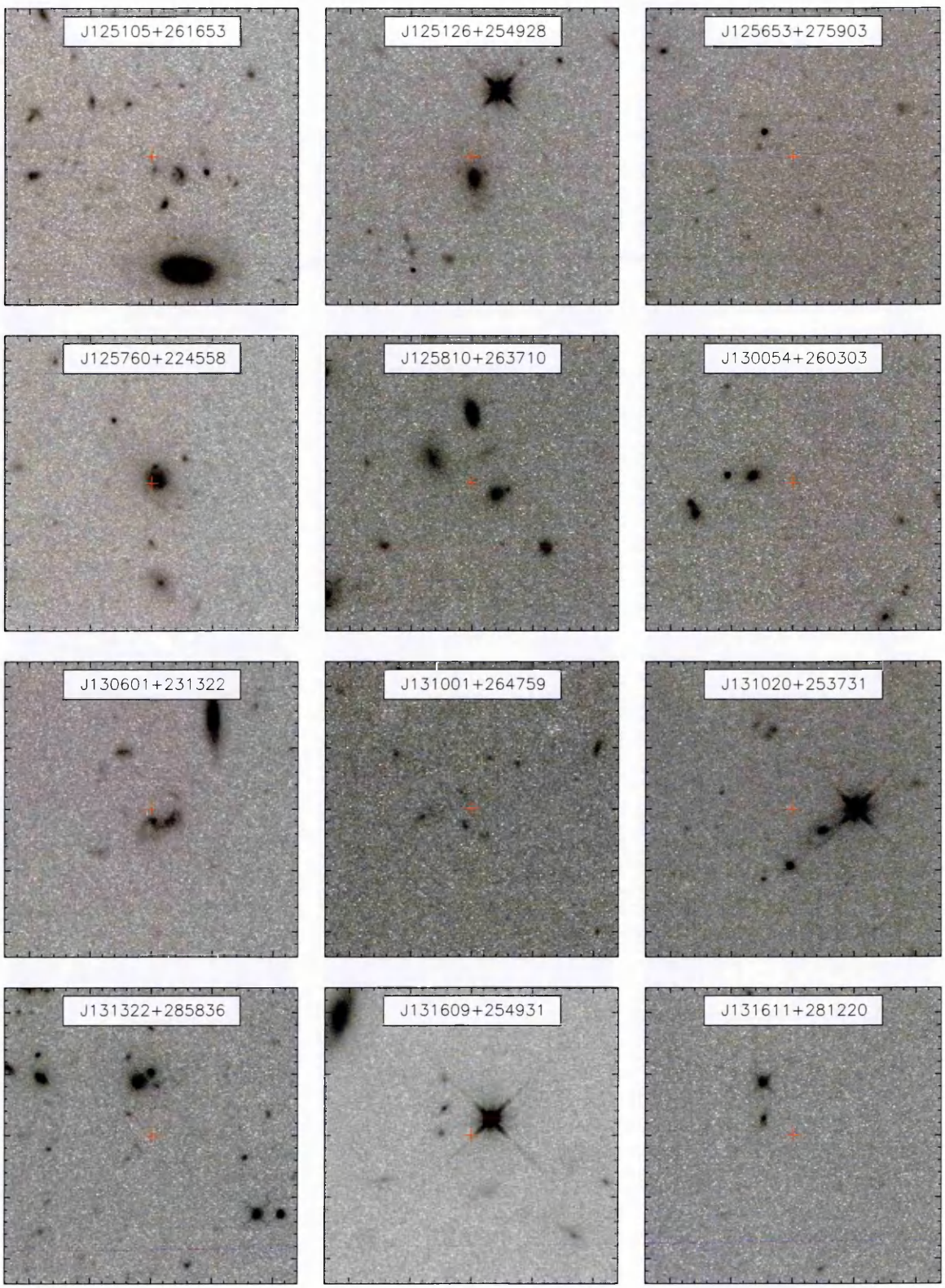

Figure B.1 (Continued): HST drizzled snapshots, images are 24" on a side centered at the SPIRE emission marked by the red cross.

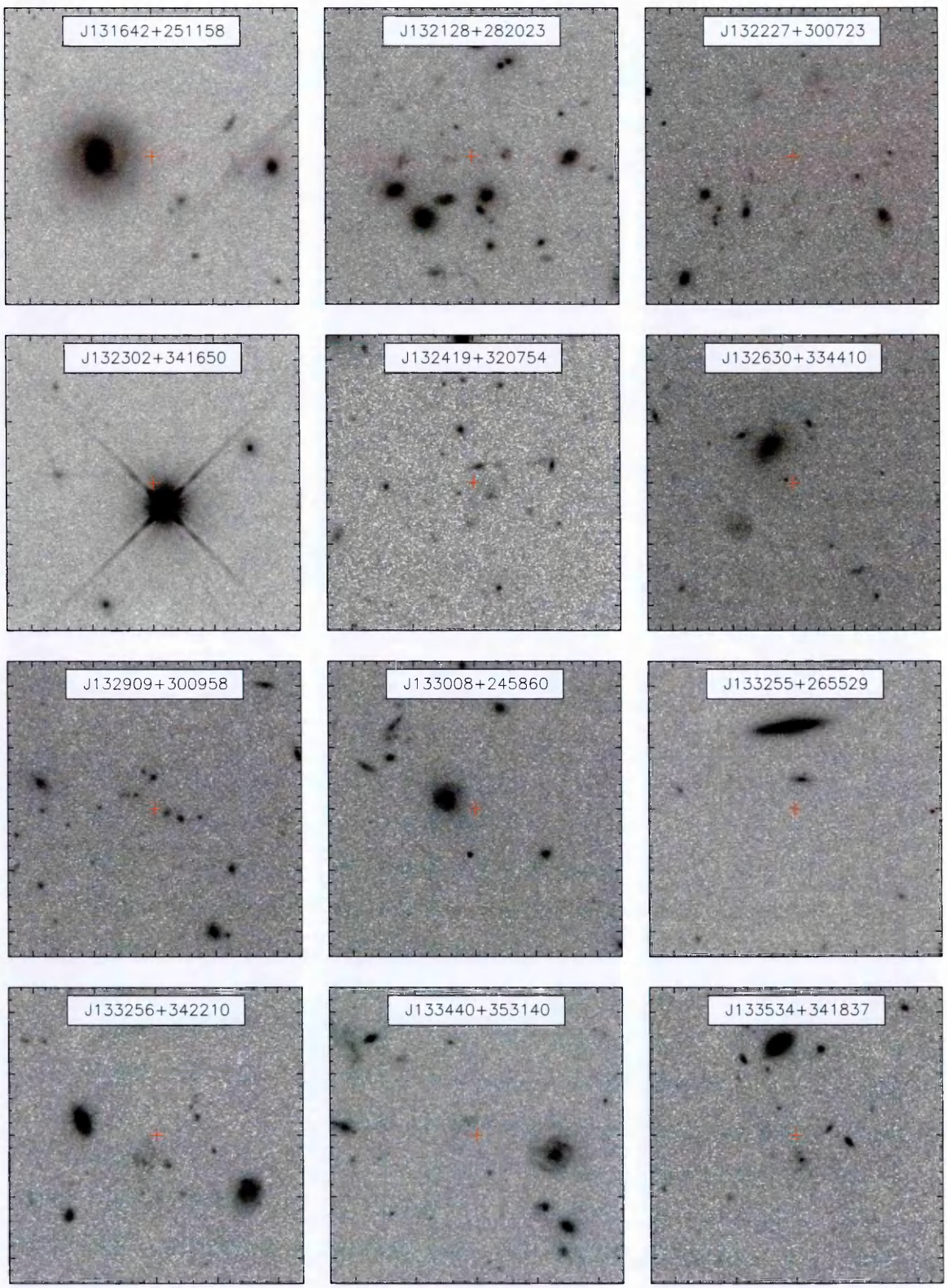

Figure B.1 (Continued): HST drizzled snapshots, images are 24" on a side centered at the SPIRE emission marked by the red cross.

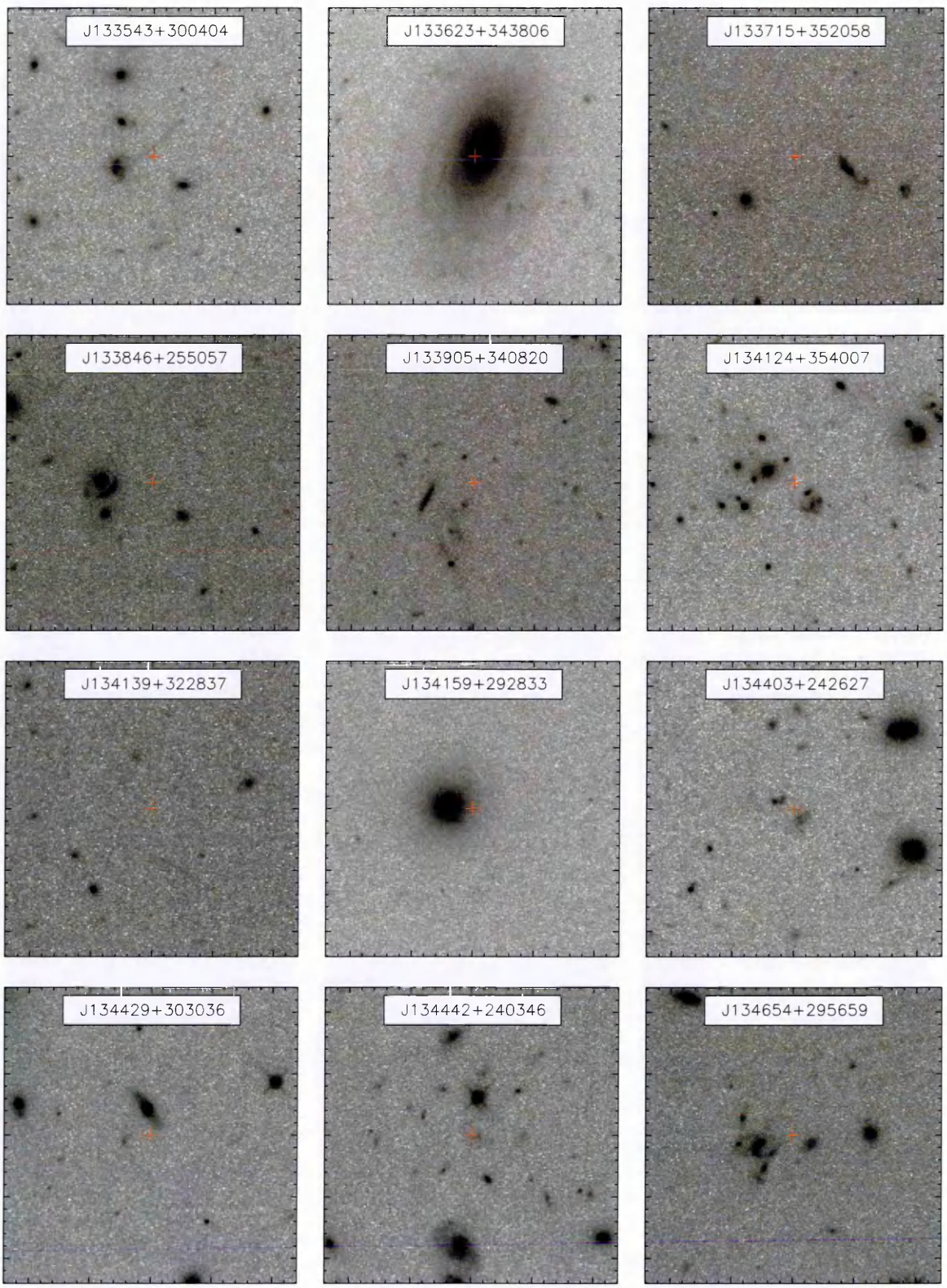

Figure B.1 (Continued): HST drizzled snapshots, images are 24" on a side centered at the SPIRE emission marked by the red cross.

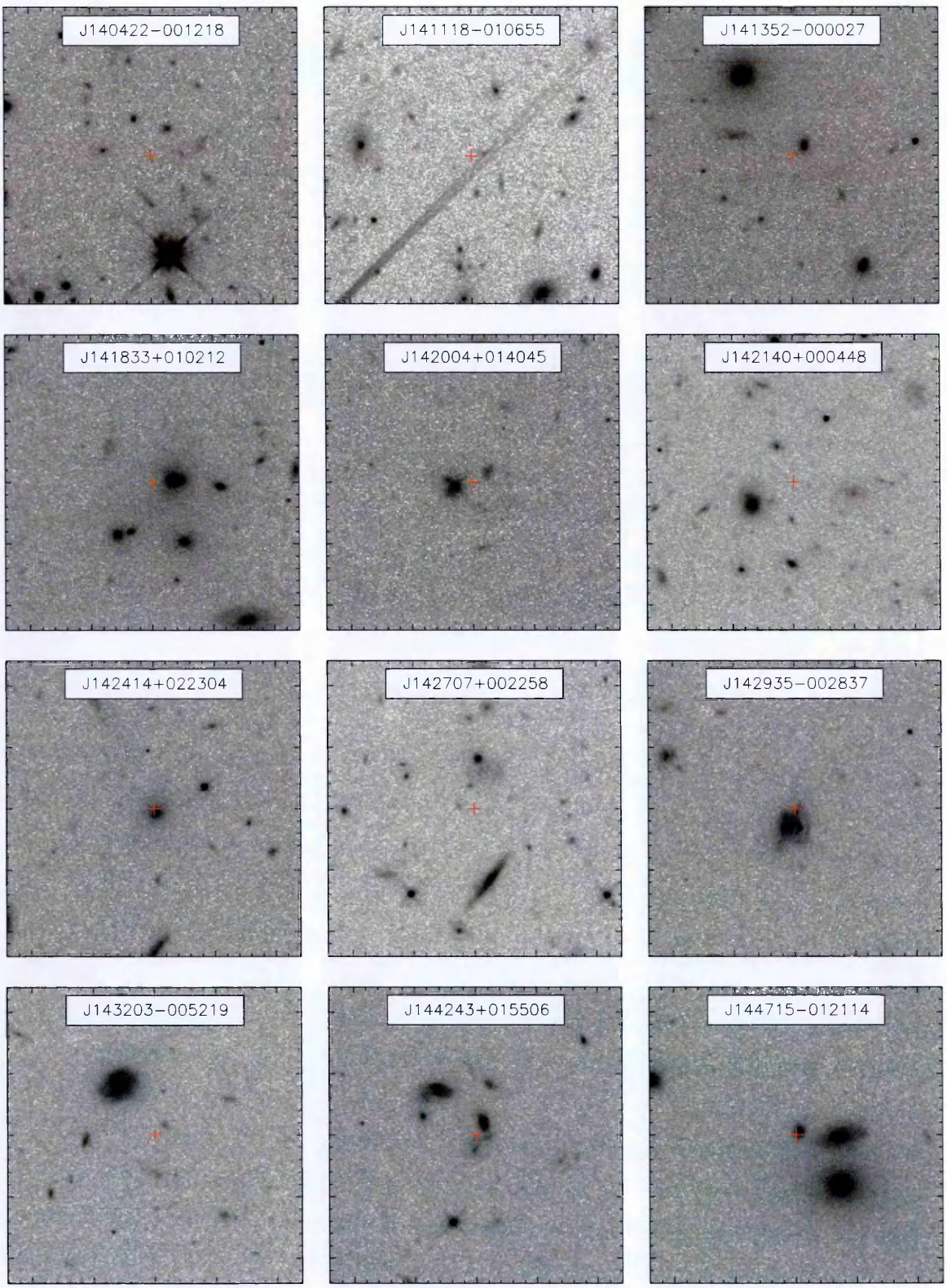

Figure B.1 (Continued): HST drizzled snapshots, images are 24" on a side centered at the SPIRE emission marked by the red cross.

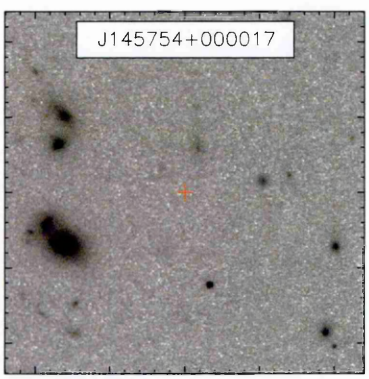

Figure B.1 (Continued): HST drizzled snapshots, images are 24" on a side centered at the SPIRE emission marked by the red cross.

Appendix C

H-ATLAS follow-up database

The H-ATLAS consortium maintain an internal wiki-based website acting as the repository for proposals, publications and additional information. All H-ATLAS members can create pages and upload information to coordinate and communicate on a single platform. Following the discovery of the efficient lens selection a large number of lens candidates were subject to multiple successful observations on over a dozen instruments. A catalog of the multi-wavelength data was initially based on a wiki table of links to individual pages containing the data. The wiki table consisting of row entries per lens candidate and columns for the observations, the table was populated by 'yes' or 'no' links to the corresponding target/observation page. The data format was inconsistent between observations, ranging from single numbers (e.g. redshift estimates) to arrays and figures (e.g. spectra and images). Management of the wiki table required the use of a text editor and wiki syntax to define the boundaries of each row and column on a cell-by-cell basis where each cell was a link to the specific page regarding the target/observations. The increasing number of lens candidates resulted in the editing of the wiki table becoming an inefficient and cumbersome task. An obvious alternative to this pseudo-database being maintained on the wiki was the internet standard SQL database with corresponding website, hereafter collectively referred to as the database, which could be embedded in the H-ATLAS wiki.

Figure C.1 represents the different elements of the database. All information is stored in SQL tables and user interactions with the frontend website automatically query and retrieve the required information. Interaction between the frontend and the server is performed using PHP/MySQL. To ensure the user experience did not change significantly

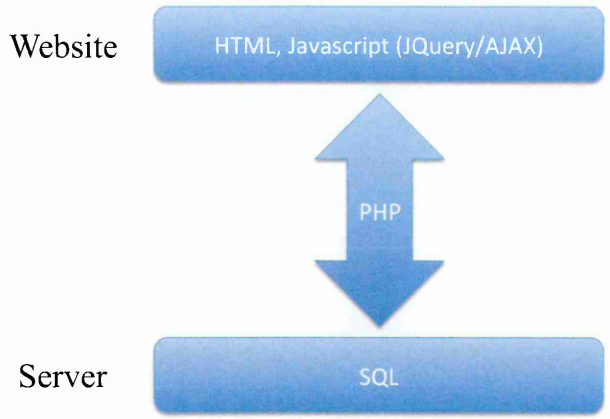

Figure C.1: Database schematic: The frontend website comprises of HTML and Javascript (pseudo-languages: JQuery and AJAX). PHP scripts translate the website commands and perform SQL queries on the server database.

the use of Javascript/JQuery/AJAX provides asynchronous data transfer and removes the need to refresh the frontend after every query.

The lack of any strict formatting, unlike the *fits* standard, limited the database to purely replicating the functionality of the wiki-based table but in a much more user-friendly manner. Each 'cell' was replaced by a pop-up box allowing the user to directly edit the information, the database was programmed to interpret wiki syntax allowing the user to continue to specify links or figures in a familiar manner. Figure C.2 shows a screenshot of a user's interaction with the database.

STATUS OF FOLLOWUP OBSERVATIONS

YES = observations have been awarded time (or, for FIRST, the source is detected) and info/results can be accessed through the corresponding link.
NO = observations have been proposed & awarded but were not carried out in the queue or were not successfully executed (follow link for more info).
NO = no observations have been proposed (or, for FIRST, the source is not detected).

Add row

Add column

HATLAS IAU ID	Alternate ID	Redshift	GBT/Zp	ZSpec	PdBI	CARMA	EVLA	SMA	MAMBO	FIRST	FTS	Keck	HST
J090740.0-004200	ID9	1.577	NO	YES	YES	YES	YES	YES	YES	YES	YES	YES	YES
J091043.1-000321	ID11	1.78									YES	YES	YES
J090302.9-014127	ID17	2.30									YES	YES	YES
J090311.6+003906	ID81	3.04									YES	YES	YES
J091305.0-005343	ID130	2.62									YES	YES	YES
J083051.0+013224	G09v1.97	3.63									YES	YES	YES
J084933.4+021443	G09v1.124	2.4									NO	NO	YES
J091840.8+023047	G09v1.326	2.58									YES	NO	YES
J083929.5+023536	G09v1.369										NO	NO	NO
J085111.7+004933	G09v1.427										NO	NO	YES
J084259.9+024958	G09v1.908										NO	NO	NO
J084957.6+010712	G09v1.1259										NO	NO	YES
J083344.9+000109	G09v1.1371	3.09									NO	NO	YES
J085358.9+015537	G09v1.40	2.09									YES	YES	YES

ZSpec: J090740.0-004200

Flag: YES NO

Link: id9-2

Estimated redshift: z=1.577±0.008 (published in Lupu et al. and Negrello et al.)

Update Close

Figure C.2: The website/database example for the target J090740.0-004200 from the ZSpec observation column. The user has the ability to update the text field (which can interpret wiki syntax), change the `yes` or `no` flag displayed in the cell and/or add a wiki link (in this case the wiki page titled 'id9-2'). The links at the top of the page for `Add row` and `Add column` allow the user to specify a new target (row) by either name or coordinate and to add a new column name.

Bibliography

Bartelmann, M. 2010, Classical and Quantum Gravity, 27, 233001 ADS 1

Becker, R. H., White, R. L., & Helfand, D. J. 1995, ApJ, 450, 559 ADS 32

Behroozi, P. S., Conroy, C., & Wechsler, R. H. 2010, ApJ, 717, 379 ADS 86, 90

Bertin, E., & Arnouts, S. 1996, A&AS, 117, 393 ADS 97

Blain, A. W. 1996, MNRAS, 283, 1340 ADS 26

Blandford, R. D., & Narayan, R. 1992, ARA&A, 30, 311 ADS 1

Bolton, A. S., Burles, S., Koopmans, L. V. E., et al. 2008, ApJ, 682, 964 ADS 12, 106, 109

Bonfield, D. G., Jarvis, M. J., Hardcastle, M. J., et al. 2011, MNRAS, 416, 13 ADS 25

Bonnarel, F., Fernique, P., Bienaymé, O., et al. 2000, A&AS, 143, 33 ADS 32

Bourne, N., Maddox, S. J., Dunne, L., et al. 2012, MNRAS, 421, 3027 ADS 23

Bracco, A., Cooray, A., Veneziani, M., et al. 2011, MNRAS, 412, 1151 ADS 26

Brownstein, J. R., Bolton, A. S., Schlegel, D. J., et al. 2012, ApJ, 744, 41 ADS 12

Bruzual, G., & Charlot, S. 2003, MNRAS, 344, 1000 ADS 57, 73, 86

Bussmann, R. S., Pérez-Fournon, I., Amber, S., et al. 2013, ApJ, 779, 25 ADS vi, 11, 55

Buzzoni, B., Delabre, B., Dekker, H., et al. 1984, The Messenger, 38, 9 ADS 59

Cabanac, R. A., Alard, C., Dantel-Fort, M., et al. 2007, A&A, 461, 813 ADS 12

Cai, Z.-Y., Lapi, A., Xia, J.-Q., et al. 2013, ApJ, 768, 21 ADS xii, xiii, xvii, 26, 27, 30, 47, 48, 49, 50, 51, 52, 53, 54, 55, 111, 112

Calanog, J. A., Fu, H., Cooray, A., et al. 2014, ApJ, 797, 138 ADS vii, 93, 110

Calzetti, D., Armus, L., Bohlin, R. C., et al. 2000, ApJ, 533, 682 ADS 23, 84

Chae, K.-H. 2003, MNRAS, 346, 746 ADS 11

Clements, D. L., Rigby, E., Maddox, S., et al. 2010, A&A, 518, L8 ADS 26, 28

Clowe, D., Bradač, M., Gonzalez, A. H., et al. 2006, ApJ, 648, L109 ADS 11

Colless, M., Dalton, G., Maddox, S., et al. 2001, MNRAS, 328, 1039 ADS 20

Condon, J. J., Cotton, W. D., Greisen, E. W., et al. 1998, AJ, 115, 1693 ADS 32

Connolly, A. J., Szalay, A. S., Dickinson, M., SubbaRao, M. U., & Brunner, R. J. 1997, ApJ, 486, L11 ADS 16

Coppin, K., Chapin, E. L., Mortier, A. M. J., et al. 2006, MNRAS, 372, 1621 ADS 23

Cox, P., Krips, M., Neri, R., et al. 2011, ApJ, 740, 63 ADS 35

de Graauw, T., Helmich, F. P., Phillips, T. G., et al. 2010, A&A, 518, L6 ADS 19

de Jong, J. T. A., Verdoes Kleijn, G. A., Kuijken, K. H., & Valentijn, E. A. 2013, Experimental Astronomy, 35, 25 ADS 20

di Serego Alighieri, S., Vernet, J., Cimatti, A., et al. 2005, A&A, 442, 125 ADS 103

Driver, S. P., Hill, D. T., Kelvin, L. S., et al. 2011, MNRAS, 413, 971 ADS 20

Dunlop, J. S., McLure, R. J., Yamada, T., et al. 2004, MNRAS, 350, 769 ADS 106

Dunne, L., Gomez, H. L., da Cunha, E., et al. 2011, MNRAS, 417, 1510 ADS 23

Dye, S., Dunne, L., Eales, S., et al. 2010, A&A, 518, L10 ADS 23

Dye, S., Negrello, M., Hopwood, R., et al. 2014, MNRAS, 440, 2013 ADS vi, 92

Dyson, F. W., Eddington, A. S., & Davidson, C. 1920, Royal Society of London Philosophical Transactions Series A, 220, 291 ADS 2

Eales, S., Dunne, L., Clements, D., et al. 2010, PASP, 122, 499 ADS 19

Eales, S. A. 2015, MNRAS, 446, 3224 ADS xiv, 11, 24, 57, 86, 88, 113

Einstein, A. 1936, Science, 84, 506 ADS 2

Emerson, J. P., & Sutherland, W. J. 2010, in Society of Photo-Optical Instrumentation Engineers (SPIE) Conference Series, Vol. 7733, Society of Photo-Optical Instrumentation Engineers (SPIE) Conference Series, 6 ADS 20, 32

Faber, S. M., & Jackson, R. E. 1976, ApJ, 204, 668 ADS 105

Feigelson, E. D., & Jogesh Babu, G. 2012, Modern Statistical Methods for Astronomy ADS 42

Fleuren, S., Sutherland, W., Dunne, L., et al. 2012, MNRAS, 423, 2407 ADS 25, 58

Franceschini, A., Hasinger, G., Miyaji, T., & Malquori, D. 1999, MNRAS, 310, L5 ADS 25

Frayer, D. T., Harris, A. I., Baker, A. J., et al. 2011, ApJ, 726, L22 ADS 24, 28, 35

Fruchter, A. S., & Hook, R. N. 2002, PASP, 114, 144 ADS xiv, 94

Fu, H., Jullo, E., Cooray, A., et al. 2012, ApJ, 753, 134 ADS 24

Gavazzi, R., Treu, T., Koopmans, L. V. E., et al. 2008, ApJ, 677, 1046 ADS 12

Gonzaga, S., & et al. 2012, The DrizzlePac Handbook ADS 94

González-Nuevo, J., Lapi, A., Fleuren, S., et al. 2012, ApJ, 749, 65 ADS 24, 57, 58, 60

González-Nuevo, J., Lapi, A., Negrello, M., et al. 2014, MNRAS, 442, 2680 ADS vii

Griffin, M. J., Abergel, A., Abreu, A., et al. 2010, A&A, 518, L3 ADS 19

Harris, A. I., Baker, A. J., Frayer, D. T., et al. 2012, ApJ, 752, 152 ADS 24, 35, 37

Herranz, D., González-Nuevo, J., Clements, D. L., et al. 2013, A&A, 549, A31 ADS 24

Hezaveh, Y. D., Marrone, D. P., Fassnacht, C. D., et al. 2013, ApJ, 767, 132 ADS 29, 112

Holwerda, B. W., Baldry, I. K., Alpaslan, M., et al. 2015, ArXiv e-prints, arXiv:1503.04813 ADS 12

Hopkins, P. F., Hernquist, L., Cox, T. J., et al. 2006, ApJS, 163, 1 ADS 15

Hughes, D. H., Serjeant, S., Dunlop, J., et al. 1998, Nature, 394, 241 ADS 16

Ivison, R. J., Swinbank, A. M., Smail, I., et al. 2013, ApJ, 772, 137 ADS vi, 26

Jaki, S. L. 1978, Foundations of Physics, 8, 927 ADS 2

Jarvis, M. J., Smith, D. J. B., Bonfield, D. G., et al. 2010, MNRAS, 409, 92 ADS 23

Kauffmann, G., Heckman, T. M., White, S. D. M., et al. 2003, MNRAS, 341, 33 ADS 73

Keeton, C. R. 2001, ArXiv Astrophysics e-prints, astro-ph/0102340 ADS 8, 10

Kormendy, J. 1977, ApJ, 218, 333 ADS 98

Kron, R. G. 1980, ApJS, 43, 305 ADS 97

Lapi, A., Negrello, M., González-Nuevo, J., et al. 2012, ApJ, 755, 46 ADS 10, 11, 30, 46, 53, 55, 112

Lapi, A., González-Nuevo, J., Fan, L., et al. 2011, ApJ, 742, 24 ADS 35, 46

Lawrence, A., Warren, S. J., Almaini, O., et al. 2007, MNRAS, 379, 1599 ADS 20

Leauthaud, A., Tinker, J., Bundy, K., et al. 2012, ApJ, 744, 159 ADS 86, 90

Longhetti, M., & Saracco, P. 2009, MNRAS, 394, 774 ADS 86

Longhetti, M., Saracco, P., Severgnini, P., et al. 2007, MNRAS, 374, 614 ADS xv, 98, 103, 105, 109

Lupu, R. E., Scott, K. S., Aguirre, J. E., et al. 2012, ApJ, 757, 135 ADS 24, 28, 35

Lynds, R., & Petrosian, V. 1989, ApJ, 336, 1 ADS 2

Madau, P., & Dickinson, M. 2014, ARA&A, 52, 415 ADS xi, 15

Maddox, S. J., Dunne, L., Rigby, E., et al. 2010, A&A, 518, L11 ADS 25

Messias, H., Dye, S., Nagar, N., et al. 2014, A&A, 568, A92 ADS vii, 24

Mortier, A. M. J., Serjeant, S., Dunlop, J. S., et al. 2005, MNRAS, 363, 563 ADS 17

Myers, S. T., Jackson, N. J., Browne, I. W. A., et al. 2003, MNRAS, 341, 1 ADS 12

Narayan, R., & Bartelmann, M. 1996, ArXiv Astrophysics e-prints, astro-ph/9606001 ADS 1

Navarro, J. F., Frenk, C. S., & White, S. D. M. 1996, ApJ, 462, 563 ADS 10

Negrello, M., Perrotta, F., González-Nuevo, J., et al. 2007, MNRAS, 377, 1557 ADS 26, 28

Negrello, M., Hopwood, R., De Zotti, G., et al. 2010, Science, 330, 800 ADS 24, 28, 34, 35, 37, 42, 58, 91

Negrello, M., Hopwood, R., Dye, S., et al. 2013, ArXiv e-prints, arXiv:1311.5898 ADS vi

Negrello, M., Hopwood, R., Dye, S., et al. 2014, MNRAS, 440, 1999 ADS vi, 92

Neugebauer, G., Habing, H. J., van Duinen, R., et al. 1984, ApJ, 278, L1 ADS 14, 33

Ochsenbein, F., Bauer, P., & Marcout, J. 2000, A&AS, 143, 23 ADS 33

Oguri, M., Inada, N., Pindor, B., et al. 2006, AJ, 132, 999 ADS 12

Oguri, M., Inada, N., Strauss, M. A., et al. 2012, AJ, 143, 120 ADS 11

Oke, J. B. 1990, AJ, 99, 1621 ADS 70

Oliver, S. J., Wang, L., Smith, A. J., et al. 2010, A&A, 518, L21 ADS 25, 28

Omont, A., Neri, R., Cox, P., et al. 2011, A&A, 530, L3 ADS 24

Pascale, E., Auld, R., Dariush, A., et al. 2011, MNRAS, 415, 911 ADS 31

Peebles, P. J. E. 1993, Principles of Physical Cosmology ADS 36

Peng, C. Y., Ho, L. C., Impey, C. D., & Rix, H.-W. 2010, AJ, 139, 2097 ADS 97

Petters, A. O., Levine, H., & Wambsganss, J. 2001, Singularity theory and gravitational lensing ADS 1

Pilbratt, G. L., Riedinger, J. R., Passvogel, T., et al. 2010, A&A, 518, L1 ADS 17

Planck Collaboration, Ade, P. A. R., Aghanim, N., et al. 2011, A&A, 536, A1 ADS 23

Poglitsch, A., Waelkens, C., Geis, N., et al. 2010, A&A, 518, L2 ADS 18

Polletta, M., Tajer, M., Maraschi, L., et al. 2007, ApJ, 663, 81 ADS 35

Press, W. H., & Schechter, P. 1974, ApJ, 187, 425 ADS 86

Reid, I. N., Brewer, C., Brucato, R. J., et al. 1991, PASP, 103, 661 ADS 32

Riechers, D. A., Cooray, A., Omont, A., et al. 2011, ApJ, 733, L12 ADS 35

Rigby, E. E., Maddox, S. J., Dunne, L., et al. 2011, MNRAS, 415, 2336 ADS 31

Rowan-Robinson, M., Broadhurst, T., Oliver, S. J., et al. 1991, Nature, 351, 719 ADS 15

Rowlands, K., Dunne, L., Maddox, S., et al. 2012, MNRAS, 419, 2545 ADS 23

Rybak, M., McKean, J. P., Vegetti, S., Andreani, P., & White, S. D. M. 2015, ArXiv e-prints, arXiv:1503.02025 ADS 55

Sand, D. J., Treu, T., Ellis, R. S., Smith, G. P., & Kneib, J.-P. 2008, ApJ, 674, 711 ADS 11

Sanders, D. B., & Mirabel, I. F. 1996, ARA&A, 34, 749 ADS 14

Serjeant, S. 2012, MNRAS, 424, 2429 ADS 105

Serjeant, S. 2014, ApJ, 793, L10 ADS 12

Serjeant, S., & Marchetti, L. 2014, MNRAS, 443, 3118 ADS 106

Serjeant, S., Bertoldi, F., Blain, A. W., et al. 2010, A&A, 518, L7 ADS 25

Sheth, R. K., & Tormen, G. 1999, MNRAS, 308, 119 ADS 46, 86

Short, J., Pearson, E., Coles, P., & Eales, S. 2012, ArXiv e-prints, arXiv:1206.4919 ADS 11, 24

Silva, L., Granato, G. L., Bressan, A., & Danese, L. 1998, ApJ, 509, 103 ADS 35

Smail, I., Ivison, R. J., & Blain, A. W. 1997, ApJ, 490, L5 ADS 16

Smith, D. J. B., Dunne, L., Maddox, S. J., et al. 2011, MNRAS, 416, 857 ADS 28, 60, 95

Soucail, G., Fort, B., Mellier, Y., & Picat, J. P. 1987, A&A, 172, L14 ADS 2

Springel, V., Frenk, C. S., & White, S. D. M. 2006, Nature, 440, 1137 ADS 25

Swinbank, A. M., Smail, I., Longmore, S., et al. 2010, Nature, 464, 733 ADS 11, 55

Tauber, J. A., Mandolesi, N., Puget, J.-L., et al. 2010, A&A, 520, A1 ADS 23

Thacker, C., Cooray, A., Smidt, J., et al. 2013, ApJ, 768, 58 ADS 25

Thompson, M. A., Smith, D. J. B., Stevens, J. A., et al. 2010, A&A, 518, L134 ADS 26

Tinker, J., Kravtsov, A. V., Klypin, A., et al. 2008, ApJ, 688, 709 ADS 86

Tody, D. 1986, in Society of Photo-Optical Instrumentation Engineers (SPIE) Conference Series, Vol. 627, Instrumentation in astronomy VI, ed. D. L. Crawford, 733 ADS 65

Tremonti, C. A. 2003, PhD thesis, THE JOHNS HOPKINS UNIVERSITY ADS 57, 73

Tremonti, C. A., Heckman, T. M., Kauffmann, G., et al. 2004, ApJ, 613, 898 ADS 73

Treu, T. 2010, ARA&A, 48, 87 ADS 11

Valls-Gabaud, D. 2006, in American Institute of Physics Conference Series, Vol. 861, Albert Einstein Century International Conference, ed. J.-M. Alimi & A. Füzfa, 1163–1163 ADS 1

Valtchanov, I., Virdee, J., Ivison, R. J., et al. 2011, MNRAS, 415, 3473 ADS 24

van Kampen, E., Smith, D. J. B., Maddox, S., et al. 2012, MNRAS, 426, 3455 ADS 25

Vieira, J. D., Crawford, T. M., Switzer, E. R., et al. 2010, ApJ, 719, 763 ADS 28

Vieira, J. D., Marrone, D. P., Chapman, S. C., et al. 2013, Nature, 495, 344 ADS 24, 29, 58

Walsh, D., Carswell, R. F., & Weymann, R. J. 1979, Nature, 279, 381 ADS 2

Wardlow, J. L., Cooray, A., De Bernardis, F., et al. 2013, ApJ, 762, 59 ADS xii, 24, 29, 37, 39, 42, 58

Weiß, A., De Breuck, C., Marrone, D. P., et al. 2013, ApJ, 767, 88 ADS 29, 35

White, R. L., Becker, R. H., Helfand, D. J., & Gregg, M. D. 1997, ApJ, 475, 479 ADS 32

Wijesinghe, D. B., da Cunha, E., Hopkins, A. M., et al. 2011, MNRAS, 415, 1002 ADS 23

York, D. G., Adelman, J., Anderson, Jr., J. E., et al. 2000, AJ, 120, 1579 ADS 20, 32

Zitrin, A., Fabris, A., Merten, J., et al. 2015, ApJ, 801, 44 ADS 11

Zwicky, F. 1937, ApJ, 86, 217 ADS 2